University of Bath

PHD

Laboratory studies of acoustic scattering: shape perturbations and material anisotropy

Chinnery, Paul Anthony

Award date:
1995

Awarding institution:
University of Bath

Link to publication

Alternative formats
If you require this document in an alternative format, please contact:
openaccess@bath.ac.uk

Copyright of this thesis rests with the author. Access is subject to the above licence, if given. If no licence is specified above, original content in this thesis is licensed under the terms of the Creative Commons Attribution-NonCommercial 4.0 International (CC BY-NC-ND 4.0) Licence (https://creativecommons.org/licenses/by-nc-nd/4.0/). Any third-party copyright material present remains the property of its respective owner(s) and is licensed under its existing terms.

Take down policy
If you consider content within Bath's Research Portal to be in breach of UK law, please contact: openaccess@bath.ac.uk with the details. Your claim will be investigated and, where appropriate, the item will be removed from public view as soon as possible.

Download date: 05. May. 2023

LABORATORY STUDIES OF ACOUSTIC SCATTERING: SHAPE PERTURBATIONS AND MATERIAL ANISOTROPY

submitted by Paul Anthony Chinnery
for the degree of Ph.D.
of the University of Bath.

1995

COPYRIGHT

'Attention is drawn to the fact that copyright of this thesis rests with its author. This copy of the thesis has been supplied on condition that anyone who consults it is understood to recognize that its copyright rests with its author and that no quotation from the thesis and no information derived from it may be published without the prior written consent of the author'.

This thesis may be made available for consultation within the University Library and may be photocopied or lent to other libraries for the purpose of consultation.

UMI Number: U070139

All rights reserved

INFORMATION TO ALL USERS
The quality of this reproduction is dependent upon the quality of the copy submitted.

In the unlikely event that the author did not send a complete manuscript
and there are missing pages, these will be noted. Also, if material had to be removed,
a note will indicate the deletion.

UMI U070139
Published by ProQuest LLC 2013. Copyright in the Dissertation held by the Author.
Microform Edition © ProQuest LLC.
All rights reserved. This work is protected against
unauthorized copying under Title 17, United States Code.

ProQuest LLC
789 East Eisenhower Parkway
P.O. Box 1346
Ann Arbor, MI 48106-1346

UNIVERSITY OF BATH
24 14 NOV 1995
PHD
509506

Abstract

The scattering of acoustic waves by objects in the underwater environment has long been of interest in both the civil and defence industries. This thesis addresses the problem of scattering by objects having complex geometry and material properties. The work reported here has two main strands, each associated with different complexities. Perturbations in the shape of cylindrical shells, and the anisotropic reinforcement of planar layers, are considered. Attention is focussed upon the resonances of objects.

A Schlieren technique is used to study the resonance behaviour of flooded cylindrical shells of varying geometry. A model for predicting the optical image obtained with the technique is developed and used to investigate to what extent the optical distribution can be considered to be an 'image' of the acoustic field. The fluid column resonances of circular and elliptical shells are investigated experimentally and are found to be in good agreement with theoretical predictions based upon the Normal Mode solution to the wave equation. Mode splittings and level crossings are observed in the resonance spectra as the eccentricity of the shell is varied. In addition to the main study, experimental results are presented for the resonance modes of another non-circular cylindrical cavity having a 'stadium' geometry. The backscattering properties of cylindrical shells have also been investigated using a parametric array facility and significant differences are observed between the properties of circular and elliptical samples.

The parametric array facility has been used to study the transmission properties of anisotropic panels. Results are presented for a uniaxial glass-reinforced plastic panel insonified at various angles of incidence. A theoretical model is developed for predicting the transmission properties of anisotropic laminates and good agreement is shown with the experimental measurements when the non-planar nature of the parametric source is included in the model. Both experimental and theoretical results show that the transmission properties of the anisotropic layer are dependent upon the angle between the plane of incidence and the fibre direction. The free modes of vibration of the anisotropic layer are also investigated numerically, and a similar dependence upon propagation direction in the layer is observed.

Shape perturbations and material anisotropy are both shown to result in a more complex acoustic behaviour than has previously been observed for simpler scattering geometries and materials.

Acknowledgements

I am grateful for the support and friendship of many members of the Underwater Acoustics Group, past and present. In particular I would like to thank Victor Humphrey for his guidance, advice and encouragement during the period of this research, and for having continued faith in the work. I also appreciated the comradeship of Jerry Holmes in the early years, when much of the work described here was actually done.

The Schlieren system employed in this work was originally developed by Sharon Knapp, and parts of the theoretical study built upon work begun by Carolyn Beckett. This work was carried out with the support of the Procurement Executive, Ministry of Defence and the Defence Research Agency.

I am especially grateful to Stephen Mark Smith for passing on his considerable knowledge of Unix and image processing, and for helping in many other ways over the years, both before and during my time at Bath.

Thanks are also due to Meghann Siobhán Mhairi O'Ryan, who, through her correspondence, has provided friendship and support during the final stages of the production of this thesis, and whilst waiting for the viva.

I am very grateful to my parents, my grandparents, and my sister Dee, for the encouragement, support, and interest they have shown in this venture. I also acknowledge the assistance of both my parents and my sister with the proof-reading of parts of the document.

Finally, I would like to thank Tessa Ford, Susan Clegg, Stephen Smith and Daniel Leonard for giving support, advice, encouragement, and many other things, during the years in which the work was done, and the period in which this document was written.

Table of Contents

1 Introduction

Discrete objects, whether they be man-made or naturally occurring in the marine environment, are often complex in shape and structure. The way that such objects scatter acoustic waves is of great importance in both the civil and defence industries; this is because acoustic waves remain the only viable means of detection, location and identification of objects in the sea, on the sea-bed or buried below it. Examples of such complex structures exist on all scales and include; submersible vehicles, fish, pipelines and sediments. Medical applications of ultrasound also encounter structural complexity in the human body; again from the microscopic, such as blood cells, to the larger organs and bones.

As the technologies involving acoustic systems develop, the capabilities of such systems increases and it becomes possible to detect, identify and measure the properties of objects with greater accuracy. There is, then, a need to interpret the acoustic signals returned from objects and to understand the factors contributing to those signals; not only for the purposes of identification but also because such an understanding is invaluable in the design of underwater systems.

There are many factors that contribute to the acoustic behaviour of an object and which affect the field scattered by that object, or emanating from it. The shape, size and material properties of an object are of particular importance. Simple geometries, such as spheres and cylinders, made of isotropic homogeneous materials, have been extensively studied in the past, providing valuable insight into scattering phenomena and the mechanisms responsible. In particular the role of target 'resonances' in acoustic scattering has been found to be of great significance. For scatterers of curved geometry - such as the spherical and cylindrical shells - resonances of both the internal fluid and the elastic shell influence the field scattered by the object. Similarly for the flat plate, Lamb waves are of central importance in determining the reflection and transmission properties of laminates. The size of a scattering object relative to that of the acoustic wavelength also significantly affects the response of the object to an acoustic field.

The acoustic properties of materials is also an area in which a great deal of research has taken place in recent years; it is well known that the properties of materials can significantly affect the acoustic behaviour of structures. Recent progress in the design and manufacture of advanced materials, such as viscoelastic and fibre-reinforced composites, makes the possibility of building strong lightweight structures with prescribed acoustic properties a realistic one.

There are other aspects of a scattering structure that influence its acoustic behaviour. These include: reinforcement with frameworks and ribs; surface structure (including rough and wedged surfaces); thickness variations; inhomogeneities; multiple scattering between different objects or different parts of the same object; and anechoic coatings and treatments. Most realistic scattering objects possess some, or all, of these complications and deviations from the simple 'model' problems which have been studied in the past (such as isotropic spheres and cylinders).

One consequence of such complexity is the increased number of parameters required to describe complex structures, and an associated increase in the number of variables in the acoustic problem. Consider for example a reinforced material with the fibres running in one direction (a uniaxial composite). Such a material requires at least five, often nine, elastic constants to describe its elastic behaviour, instead of the two required for isotropic materials. The scattering of a wave by a layer of the material is then dependent upon *two* angles of incidence instead of just one. Such an increase in the number of parameters and variables in an acoustic problem often accompanies the destruction of symmetry of the structure and the lifting of degeneracies in the acoustic response of the object to external excitation.

Theoretical investigation of the acoustics of objects incorporating such complexities have been severely limited in the past by the restrictions imposed by computing facilities. Low (or high) frequency approximations often had to be made to facilitate solution, severely restricting the range of applicability of many theories. With the ever increasing speed and power of modern computing facilities, such complex structures and materials are becoming amenable to solution by both analytic and numerical methods.

Theoretical modelling alone is of limited value unless experimental measurements are undertaken to validate the theories and demonstrate their range of applicability and their limitations; often some physical aspect of a problem, unaccounted for by theory, can have a significant influence on the acoustics of a structure. The huge expense and practical complications associated with sea trials highlights the need for good laboratory techniques for investigating scattering phenomena. Experimental studies have always been relatively few in comparison with theoretical investigations. Experimental studies involving all but the simplest geometries and materials, especially so. One reason for this is the difficulty of fabricating suitable objects for testing in the laboratory. The size and cost of suitable test objects is partly responsible for this. Fibre-reinforced shells, for instance, are not so readily available as simple metallic ones.

This gap between modelling (which is now quite advanced) and measurement is a wide one. It is one aim of the present study to narrow this gap by conducting parallel theoretical and experimental investigations into the acoustics of objects and materials of greater complexity.

Different aspects of a complex structure have different effects upon the acoustic (or elastic) behaviour of the structure as a scatterer, and the first step in any investigation must be to look at these different aspects independently. In this way we hope to obtain a better understanding of the phenomena associated with each added complexity, build up a picture of how a relatively complex object behaves, determine the causes of that behaviour and what can be done to alter that behaviour. So, for example, an axisymmetric shell made of fibrous material and reinforced with ring stiffeners will differ from a circular-cylindrical metal shell in its shape, its material (in this case anisotropic) and in the presence of the stiffening elements. All of these factors would be expected to influence the acoustics of the structure, which may be quite different from the simple metal shell whose properties are so well known.

In the present study two complexities have been introduced and studied separately; the introduction of anisotropy into a material, and the shape deformation of an object. Two complementary laboratory facilities, developed at the University of Bath

and previously used in investigations of planar, cylindrical and spherical geometries, have been used in this study. Between them these facilities permit accurate observations of scattering phenomena to be made over a wide range of frequencies.

A Schlieren technique has been used to locate and identify the resonances within cylindrical shells (or cavities) of circular and non-circular cross-section. The visualization system produces an 'image' corresponding to the acoustic field within the shell and has the advantage of allowing not only easy identification of resonances, but also the phenomena that cause them. A theory is presented that predicts the image obtained using the system. An investigation into the production of the optical field suggests that, under certain conditions, the optical image is a good approximation to the *square* of the pressure distribution in the acoustic field, but that in the experimental system the relationship between acoustic and optical fields is not so simple. The Schlieren technique is successfully used to study the resonance contribution to scattering by circular cylindrical shells and cylindrical objects of elliptical cross-section. A theoretical model for the fluid column modes of circular and elliptical cavities is derived. Experimental results for the high frequency fluid column modes of circular shells are also presented, and, complementary to the main body of work, preliminary results are given for a 'stadium' shaped cavity.

A parametric array facility has been used to make preliminary investigations into the backscattering from circular and deformed samples of the above mentioned cylindrical shells. However, the main application of this facility has been in measurements of the transmission properties of fibre-reinforced laminates.

The parametric array utilizes the non-linear propagation of high amplitude acoustic waves to produce a short, low frequency pulse, having a narrow beamwidth; ideal for measurements involving small test objects in a laboratory tank. This system has been adapted to make measurements over a wide range of frequencies ($10-250kHz$) and incident angles; the automation of the experimental technique and the use of asymmetrical pulses are of particular importance in this respect. The aim of this part of the study has been to investigate the effects that anisotropy have on the acoustic

performance of laminates, to validate the theoretical models used in predicting the properties of anisotropic layered media, and to test the limitations of the system as used to make measurements on small samples of such materials. The system has previously been used successfully to study the reflection and transmission properties of isotropic panels and its use in the present study follows naturally from that success. Results are illustrated for a uniaxial glass-reinforced plastic panel.

A theoretical model for anisotropic layered media is described. This theoretical approach can be used to study many aspects of acoustics pertaining to fibre-reinforced laminates, including the plate wave resonances and their contribution to the reflection and transmission properties of a layer. Experimental measurements made with a specific fibre-reinforced material are presented to illustrate the techniques and comparisons with theoretical predictions are made.

The work described in this thesis does not attempt to answer one particular question, but rather seeks to extend our understanding and knowledge in several areas; developing parallel theoretical and experimental techniques and procedures, and building up a knowledge and expertise of several key issues (shape perturbations and anisotropy) that will be needed in future studies involving complex scattering geometries. For this reason this document is not arranged in the traditional thesis format; the aims are different. In particular we are less concerned with one particular application of the work, and more concerned with the physics of scattering phenomena and the experimental techniques used to investigate them. Literature relevant to the study is reviewed in appropriate places throughout the document. Similarly, the theoretical models used, and results obtained, are divided between the main chapters of the document. Many of the theoretical details have been placed in appendices at the end of the document. With the exception of the occasional illustration that is more meaningful in the text, all figures are collected together at the end of each chapter.

Chapter 2 reviews the acoustics of *simple* structures pertinent to the work; both planar and cylindrical geometries are considered. This chapter provides the background and context for the remainder of the thesis. Chapter 3 describes the Schlieren visual-

ization system and Chapter 4 the parametric array facility. Chapter 5 describes the resonance behaviour and backscattering properties of circular and elliptical cylindrical shells, and Chapter 6 describes the work involving planar anisotropic layers. Chapter 7 summarizes the study, draws conclusions from this work, and discusses the future progression of the work, including the extension to other complexities.

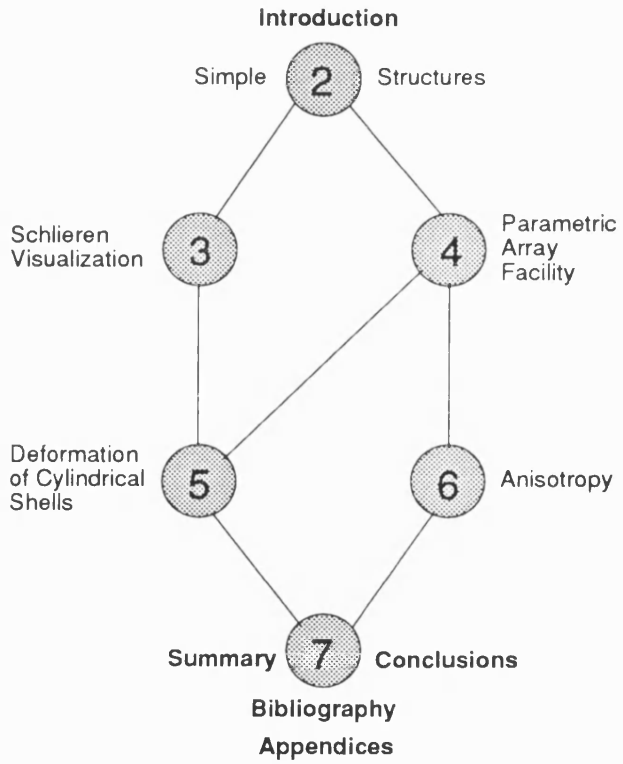

2 Acoustics of simple geometries

2.1 Introduction

Scattering from structures of simple geometry, such as infinite isotropic plates, cylinders and spheres, has been studied in great detail during this century. Recent reviews have been given by Veksler (1993) and Beckett (1992); other references of particular relevance will be given in later chapters. Although these 'idealized' or 'model' scatterers do not always exist in the marine environment, they provide valuable insight into scattering phenomena and without them we would have no idea what processes contribute to the scattering by more 'realistic' scatterers. Indeed without a knowledge of the scattering phenomena and mechanisms observed for simple structures, it would be difficult to even formulate, let alone solve, more complex problems. Sometimes the theoretical techniques developed for the solution of these model problems can be applied to more complex scattering problems. Often, however, the techniques must be extended, or new techniques developed - particularly where different wave phenomena occur.

Of particular importance in determining the acoustic behaviour of a structure are its *shape,* and its *material* properties. Many structures in the marine environment are comprised of elastic materials in the form of *layers* of material in various geometries.

In this chapter discussion centres upon two idealized problems; that of the infinite isotropic planar layer and the infinite isotropic circular cylindrical shell. These are essentially the simplest one-dimensional (flat) and two-dimensional (singly curved) 'layer' problems that can be envisaged; the three-dimensional doubly curved *spherical* geometry, equally simple and also much studied, is not considered here. The aim of this chapter is to introduce the important concepts involved in scattering from these structures, and to give some physical interpretation of the results. We concentrate here on the free modes of vibrations, plane wave excitation, and their interaction as 'resonances' of the scattering target. Simple theoretical models are used to predict the scattering behaviour and the results are illustrated with examples that are special cases of the scattering geometries discussed later in the thesis.

The remainder of this thesis concerns itself with the consequences of deforming the cylindrical shell, introducing anisotropy into the planar layers, and the two experimental techniques which have allowed us to investigate such complexities.

2.2 Planar geometry

The interaction of an acoustic wave with an isotropic layer is a much studied problem. Of particular importance are the reflection and transmission properties of layers. In many underwater applications structural components consist of flat layers, or can approximate flat, infinite, layers; although in practical situations the layers may be finite in extent and have edges or curvature that must also be considered.

It is within the context of the flat layer that the materials' influence upon the acoustics of a structure are often considered; layers having prescribed acoustic properties are often used in damping and anechoic applications. It is the properties of the material and the dimensions of the layer (relative to the wavelength) that determine the acoustic response of the layer, or structures incorporating the layer.

This section briefly summarizes the acoustics of the planar layer, concentrating on details pertinent to the study described in Chapter 6.

2.2.1 Acoustics of planar layers

The stiffness matrix[1] (C) for an isotropic material has only two independent elements and the elastic isotropy condition ($C_{12} = C_{11} - 2C_{44}$) ensures the material properties are the same in all directions (all directions are equivalent). For a plane wave of angular frequency ω propagating in any such general direction in a medium of density ρ, the elastic wave equation for displacement U,

$$C_{11}\nabla(\nabla \cdot U) - C_{44}\nabla \wedge (\nabla \wedge U) \quad = \quad \rho\ddot{U} \quad = \quad -\rho\omega^2 U, \tag{2.1}$$

1 A second rank tensor in the 'reduced subscript notation' described in Appendix C1.

allows two degenerate shear waves (U_s) and one compressional wave (U_l) to propagate. The shear waves have displacement vectors perpendicular to the direction of propagation and the compressional waves have displacement parallel to the propagation direction.

The zero curl property of U_l reflects the absence of tangential displacements and allows us to write U_l as the gradient of a scalar potential ($U_l = \nabla\zeta$), where ζ obeys Helmholtz' equation ($\nabla^2\zeta + k_l^2\zeta = 0$), with $k_l = \omega/c_l$ and $c_l = \sqrt{C_{11}/\rho}$. The zero divergence property of U_s reflects the absence of displacements normal to the wave-front and allows us to write U_s as the curl of a vector potential ($U_s = \nabla \wedge w$) which also satisfies Helmholtz' equation ($\nabla^2 w + k_s^2 w = 0$), with $k_s = \omega/c_s$ and $c_s = \sqrt{C_{44}/\rho}$. These equations can also be obtained by successive application of the curl and div operators to equation (2.1). The total solution is then written

$$U \;=\; U_l + U_s \;=\; \nabla\zeta + \nabla \wedge w. \tag{2.2}$$

Consider now a single layer of isotropic material (Figure 2.1). The displacements and stresses within the layer can be found from the potentials of the compressional and shear waves that propagate in the material. Within the layer, due to multiple reflections at the boundaries, there will exist waves with positive and negative z dependence, symmetric about the centre of the layer. For a planar layer the potentials can be written

$$\begin{aligned} \zeta &= \left(\zeta_+ e^{i\gamma_l z} + \zeta_- e^{-i\gamma_l z}\right) e^{i\alpha x} \\ w &= \left(w_+ e^{i\gamma_s z} + w_- e^{-i\gamma_s z}\right) e^{i\alpha x} \end{aligned} \tag{2.3}$$

where $\gamma_{l,s} = \sqrt{(k_{l,s}^2 - \alpha^2)}$. Using the definitions of (2.2) and (2.3), along with the stress - displacement relations, a matrix relation between displacements and stresses at the upper (1) and lower (2) interfaces can be derived (Brekhovskikh, 1980);

$$\begin{pmatrix} U^1 \\ T^1 \end{pmatrix} \;=\; \begin{pmatrix} \tau_{11} & \tau_{12} \\ \tau_{21} & \tau_{22} \end{pmatrix} \begin{pmatrix} U^2 \\ T^2 \end{pmatrix} \tag{2.4}$$

where $U^{1,2}$ and are vectors of the displacements of the upper and lower interfaces respectively, $\mathcal{T}^{1,2}$ are vectors of the corresponding stresses within the layer *at* the interfaces, and τ_{ij} are submatrices whose dimensions depend upon those of U and $\mathcal{T}$. For vertically polarized waves in an isotropic material only two components of displacement and stress need be considered; $U=(U_x,U_z)$ and $\mathcal{T}=(\mathcal{T}_{xx},\mathcal{T}_{zz})$. In this case, each submatrix (τ_{ij}) is of order two. The displacements and stresses at the upper and lower interfaces of a *multi*layered structure are easily obtained by successive application of (2.4). The plane wave reflection and transmission coefficients $(\Re,\Pi)$ of the layer can be calculated from the normal displacements of the upper and lower interfaces respectively;

$$\Re = 1 + \frac{\rho_f\omega^2}{i\gamma}U_z^1 \quad \text{and} \quad \Pi = -\frac{\rho_f\omega^2}{i\gamma}U_z^2 \tag{2.5}$$

where $\gamma=\sqrt{k^2-\alpha^2}$ and k is the wave number of the incident wave. The coefficients can be expressed on a log scale as reflection and transmission *losses* (e.g. $-20\log_{10}(\Pi)$).

To illustrate this analysis consider the transmission properties of an isotropic layer. Figure 2.2 shows the variation of transmission loss with both frequency and incident angle for an isotropic elastic layer of thickness $11.4mm$, density $1660kgm^{-3}$ and velocities $1474ms^{-1}$ and $2841ms^{-1}$. The material properties of this layer are essentially those of glass-reinforced plastic in one particular, rather special plane: the plane normal to the fibres (the transverse plane). This is the material that will be discussed fully in Chapter 6 when we consider anisotropic media. Only in this plane would the material be expected to behave like an isotropic material. The lighter portions of the figure represent regions of high transmission loss.

The plane wave transmission and reflection properties of the isotropic elastic layer have been much studied and are well understood. The dependencies on frequency and incident angle are associated with the excitation of plate waves, or *resonances* of the layer. A good interpretation of transmission and reflection by the isotropic layer has

been given by Fiorito, Madigosky & Überall (1979), and later extended by Freedman (1982). In this formalism transmission features are seen to arise from interference between overlapping resonances of the layer.

2.2.2 Resonances

The variations of transmission loss seen in Figure 2.2 are, in part, caused by the resonance behaviour of the layer. We shall consider here the case of the free waves, these being modes of vibration that exist without external excitation of any kind.

The simplest case which can be solved analytically is a single layer of isotropic material with free boundaries. There are two distinct kinds of free wave that can propagate in the unloaded layer; those having particle displacement parallel to the layer and perpendicular to the wave propagation direction, known as *Love* waves; and those having particle displacement in the plane normal to the layer, known as *Lamb* waves.

2.2.2.1 Love waves

A wave propagates along the plate in the x direction (Figure 2.1) and has particle displacement perpendicular to this in the plane of constant z, i.e. along the y axis. Such a wave is a shear type wave. Solutions of the wave equation with appropriate boundary conditions imply the existence of two cases; normal modes (labelled n) whose displacements are symmetric with respect to the midplane of the layer, occurring when $\gamma_s^n = n(\pi/d)$ $n = 0,2,4...$ etc, and antisymmetric modes occurring when $n = 1,3,5...$ etc. Here d is the layer thickness and $\gamma_s^n = \sqrt{(k_s^2 - \xi^{(n)2})}$, where ξ^n is the wave number of the n^{th} mode (propagating in the x direction). Thus for both symmetric and antisymmetric modes the phase velocity is given by

$$V^n = \frac{\omega}{\xi^n} = \frac{\omega}{\sqrt{k_s^2 - \left(\frac{n\pi}{d}\right)^2}} = \frac{c_s}{\sqrt{1 - \left(\frac{nc_s}{2dv}\right)^2}}. \qquad (2.6)$$

From this equation we deduce that there is a cutoff frequency ($\nu_n d = nc_s/2$) below which the mode cannot propagate (i.e. ξ^n becomes imaginary). Notice that Love waves are not damped by fluid loading; the normal components of displacement are zero and so waves cannot be generated in any bounding fluid due to the motion of the layer surfaces.

2.2.2.2 Lamb waves

Lamb waves are those plate waves propagating along the layer (x axis) with displacements in the vertical (xz) plane, i.e. $U_y = 0$. Solutions of the wave equation and boundary conditions again yield symmetric and antisymmetric solutions for the modal wave numbers ξ^n:

$$\begin{aligned} \text{(symmetric)} \quad & \frac{\tan\left(\frac{\gamma_l d}{2}\right)}{\tan\left(\frac{\gamma_s d}{2}\right)} + \frac{\left(\xi^2 - \frac{k_s^2}{2}\right)^2}{\xi^2 \gamma_s \gamma_l} = 0 \\ \text{(antisymmetric)} \quad & \frac{\tan\left(\frac{\gamma_l d}{2}\right)}{\tan\left(\frac{\gamma_s d}{2}\right)} + \frac{\xi^2 \gamma_s \gamma_l}{\left(\xi^2 - \frac{k_s^2}{2}\right)^2} = 0 \end{aligned} \tag{2.7}$$

where $\gamma_{s,l} = \sqrt{k_{s,l}^2 - \xi^2}$. These dispersion relations are known as the Rayleigh-Lamb equations, they can be solved numerically to find the phase velocity of each mode ($V^n = \omega/\xi^n$) at a given frequency. Each normal mode (n) can be considered to be the superposition of two compressional and two shear plane waves propagating along the plate with the same velocity and at a given angle to the midplane. For the case where $V^n > c_l > c_s$ all four waves are homogeneous and the plate wave propagates faster than compressional waves in the material. If $c_l > V^n > c_s$ then γ_l is imaginary and the two compressional waves will be *surface* waves. If $c_l > c_s > V^n$ then both compressional and shear waves are surface waves and the plate wave is concentrated near the boundaries of the layer.

The symmetric and antisymmetric dispersion equations each have one mode which exists for all values of frequency and layer thickness: the symmetric mode, denoted S_o, which is not dispersive as $\omega d \rightarrow 0$; and the antisymmetric mode A_o which is dispersive; the phase velocity tending to zero as the frequency tends to zero. All the higher order normal modes, S_i and A_i ($i \geq 1$) have cutoff frequencies below which the modes do not propagate (the phase velocity is imaginary). The cutoff frequencies are given by $\omega d/c_l = n\pi$ with n odd (symmetric), n even (antisymmetric) and $\omega d/c_s = n\pi$ with n even (symmetric) and n odd (antisymmetric); these correspond to waves having an integral number of wavelengths (compressional or shear) across the plate, and an infinite phase velocity.

Computer programs have been written to find the roots of (2.6) and (2.7) and hence obtain the dispersion curves for an isotropic layer. The elastic layer described earlier, whose transmission properties were given in Figure 2.2, was studied; the Lamb and Love wave dispersion curves are shown in Figure 2.3. The behaviour seen in this figure is well understood, and it is known that many of the modes of vibration can be excited by incident waves and are major contributors to the transmission and reflection properties of the layer. The free modes of vibration (resonances) of this elastic layer will be dealt with in greater detail in Chapter 6.

2.2.2.3 Fluid loading

As mentioned above the fluid loading of the layer has no effect on the Love waves that propagate in the plate. For this reason it is not possible to excite Love waves with an incident plane wave; the Love waves shown in Figure 2.3 do *not* influence the transmission behaviour shown in Figure 2.2. The Lamb waves however have components of displacement normal to the surface and so are able to transmit energy into the fluid. The normal modes are then known as 'Leaky Lamb' waves; the phase velocities are complex and the modes in the plate are 'damped' by the fluid loading. In this case the phase velocity is given by $V^n = \omega / Re(\xi^n)$ and the attenuation of the mode and 'width' of the resonance are characterized by $Im(\xi^n)$.

Dispersion equations for these 'leaky' modes have been obtained (see for example Plona, Behravesh & Mayer; 1975) and the theory implemented during this study, they will not however be presented here; a more general method for solving for the normal modes will be given in Chapter 6. In addition to the Leaky Lamb waves of the fluid loaded layer, there exist other waves known as Stoneley waves which are pure interface waves having exponential decay in both directions normal to the interface. Stoneley waves carry most of their energy in the fluid and propagate along the interface undamped. On the flat layer they can only be excited at glancing incidence and are therefore not generally excited by an incident plane wave. On curved surfaces, however, such modes *can* be excited.

The excitation of Leaky Lamb modes by an incident plane wave principally occurs when the trace of the velocity of the incident wave equals the plate wave velocity of a mode. This happens when the wave is incident at an angle θ to the layer normal, where

$$\theta = \sin^{-1}\left(\frac{c_f}{V^n}\right). \tag{2.8}$$

From this expression we note that an incident plane wave cannot excite modes having a Lamb wave velocity less than that of the velocity in the fluid (c_f).

2.3 Cylindrical geometry

If, instead of being flat, the scattering object has a curved geometry, the acoustic behaviour can be quite different to that described above and can be highly dependent upon the *shape* of the object. The simplest two-dimensional cases are those having a circularly cylindrical geometry.

2.3.1 Normal Mode Series approach

The first scattering problem of cylindrical geometry to be studied was the *rigid* circular cylinder. Solutions for *elastic* cylinders and circular cylindrical *shells* (both evacuated and fluid filled) were soon obtained and extensive theoretical and experimental

investigation has been undertaken in the last few decades. Both normal incidence and oblique incidence have been studied. All the important results have recently been collected together in a book by Veksler (1993). In the present work we are only interested in plane wave incidence *normal* to the cylinder axis. In this case the two-dimensional nature of the scattering geometry (Figure 2.4) results in a scattered field that is a function of both frequency and observation position and whose behaviour is commonly expressed in the 'form function';

$$f(r,\phi) = \sqrt{\frac{2r}{a}} e^{-ikr} \frac{P_{sc}(r,\phi)}{P_{in}}. \tag{2.9}$$

Here a is the outer radius of the cylinder, P_{in} is the incident pressure and P_{sc} is the scattered pressure. In underwater applications it is often the backscattered form function $f(\infty,\pi)$ that is of interest. One commonly used method for calculating the scattered pressure is the Normal Mode Series solution. Writing Helmholtz' equation in polar coordinates we obtain general solutions for the scattered pressure P_{sc} and the pressure in the fluid column P_{fl}

$$P_{sc} = P_o \sum_n \varepsilon_n i^n B_n(ka) H_n^1(kr) \cos(n\phi)$$

and (2.10)

$$P_{fl} = P_o \sum_n \varepsilon_n i^n A_n(ka) J_n(kr) \cos(n\phi)$$

where ε_n equals 1 if $n = 0$ and 2 if $n > 0$. The coefficients A_n and B_n are determined from the boundary conditions imposed at the inner and outer interfaces of the shell.

The Normal Mode Series approach is easily generalized to geometries comprising multiple layers, although the current study concerns itself only with single layered structures. Figure 2.5 shows the backscattered form function for a brass cylindrical shell having radii of (b) 14.25*mm* and (a) 15.85*mm* (hence $b/a = 0.90$). This is the same cylindrical shell that is the object of the study described in Chapter 5. As with the planar layer, many of the features are associated with *resonances* of the target.

2.3.2 Resonances

Resonance Scattering Theory (R.S.T.) (Flax, Gaunaurd & Überall, 1981) provides a connection between the normal modes of vibration (or resonances) of a target and the amplitude of the acoustic waves that the target scatters. In R.S.T. the scattered field is considered to be that due to a rigid target, except at frequencies that are equal (or close) to resonances of the target. In this case, the incident wave excites a resonance which in turn influences the scattered wave, manifesting itself as a sharp change in the scattering amplitude at that frequency. Thus the scattering amplitude as a function of frequency consists of a smooth background term (rigid scattering) with a series of sharp peaks and troughs (resonances) superimposed upon it.

Three distinct classes of resonance have been isolated; resonances of the fluid column, resonances of the elastic shell and resonances due to the propagation of Stoneley waves. The Stoneley waves are surface waves propagating around the cylindrical shell with most of their energy concentrated in the fluid. The Stoneley and shell resonances are closely related to the modes of vibration of a fluid loaded planar layer, as discussed in section 2.2.2. Of these three kinds of resonance, the fluid column resonances are the most abundant. In essence, the resonance behaviour of the cylindrical shell can be thought of comprising the resonance behaviour of a flat layer, bent into circular geometry, *plus* the resonance behaviour of the fluid column that this layer then encloses (except or course if the cylinder is evacuated).

In Figure 2.6 calculations of the magnitude of the pressure field are shown for the shell insonified by plane waves at different resonance frequencies. Examples of each kind of resonance mode are illustrated; the field in both the internal and the external fluids are shown. At resonance the pressure in the fluid column is far greater than that in the incident and scattered fields, and this provides a good way of locating and identifying the resonance modes of the shell.

2.4 Laboratory investigations

A variety of experimental techniques have been employed for investigating and characterizing the acoustic properties of materials and structures in the underwater environment.

Two laboratory techniques widely used for measuring the properties of materials are the impedance tube and free field measurements. Impedance tubes have the advantage that they can be pressurized, but do not conveniently allow measurements to be made on samples at different incident angles.

The use of a parametric array in free field measurements is now quite widespread. One advantage of this technique is the narrow beamwidth of the source, allowing measurements to be made using small test samples in a laboratory tank. The system developed at Bath has been used to study the transmission and reflection properties of isotropic panels, wedged materials, rib reinforced plates, and the scattering by spheres, solid cylinders and both air and water filled cylindrical shells. In all these applications the technique has proved itself to be of great value in understanding the acoustic properties of these structures. A fuller review of the experimental system and measurement technique are given in Chapter 4.

The acoustic behaviour of cylindrical shells has previously been studied mainly from a *scattering* perspective. Although, from theoretical work, it is known that target resonances are important in the scattering behaviour, there has been very little investigation into these resonance modes themselves.

One technique that has been developed at Bath and successfully used to study resonance behaviour of circular cylindrical shells is the Schlieren visualization technique. This technique allows the acoustic fields in, and around, a resonating structure to be directly visualized in a non-invasive manner. The experimental system and measurement technique are described in detail in Chapter 3.

2.5 Discussion

In the previous sections we have discussed the aspects of scattering by planar and cylindrical geometries that are pertinent to this work. In particular we have noted the role resonances play in determining the acoustic response of a structure. Any regularity or symmetry in a scattering system will give rise to resonances in the acoustic response to an incident wave. To a good approximation the resonances can be identified with the free vibrations of the object. For the flat plate and cylindrical shell resonances occur in the form of waves that travel along (or around) the elastic layer, or along the interfaces. For the circular cylindrical shell there also exist resonances of the enclosed fluid column, these being the most abundant.

As discussed in the introduction, realistic scattering objects are not perfectly circular cylindrical shells made of homogeneous, isotropic materials; for man-made structures it is not even desirable that they should be so. So the question arises; how are the physical phenomena observed for simple structures affected when we consider scattering by more complex structures? Conversely, how can the acoustics of a structure be altered by altering its *material* properties and its *geometry*. These two aspects in particular are of considerable importance in the design of structures in the marine environment.

The equivalence of all directions in the plane of the flat layer (i.e. the azimuthal incidence angle ϕ) means there is symmetry in the acoustics and suggests degeneracies exist in the free modes that propagate in the layer[1]. Similarly for the cylindrical shell; the circular symmetry results in an invariance with respect to ϕ and is expected to introduce degeneracies.

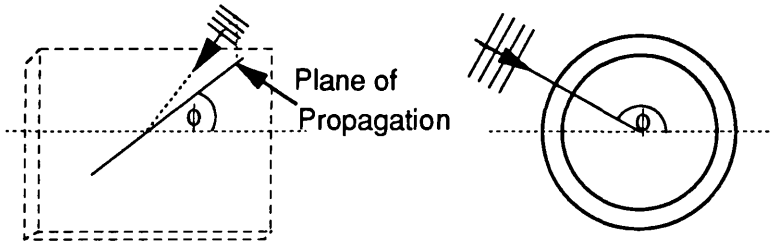

1 The same modes propagating in different directions are obviously identical in every respect.

In both cases the acoustics is invariant with respect to ϕ (i.e. all directions in the plane of the page are equivalent). The two cases that will be discussed in this thesis involve the destruction of these symmetries by introducing a ϕ dependence into the problem; for the circular case by deforming the shell, for the planar layer by reinforcement along one direction.

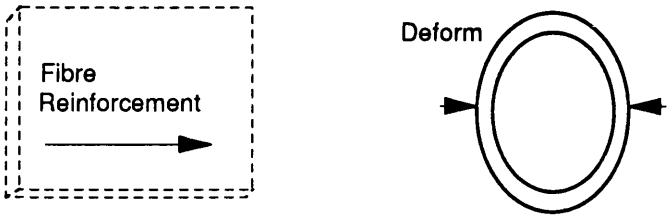

In scattering measurements involving such structures, the orientation (ϕ) of the object with respect to the incident beam is now of great importance.

The theoretical approaches described in this chapter cannot be applied directly to these problems, but must be either extended or replaced by other, more general methods. Although many numerical techniques exist which allow scattering from complicated geometries to be investigated, such techniques do not provide much insight into the mechanisms responsible for the behaviour predicted by the models. For this reason it was decided to follow analytical approaches to solving these problems.

Whatever mathematical methods and models are used in predicting the acoustic behaviour of structures, there is always a need for accurate experimental studies to validate and supplement the theories. In the next two chapters we describe the two experimental techniques used in the present study.

Figure 2.1 Isotropic elastic layer.

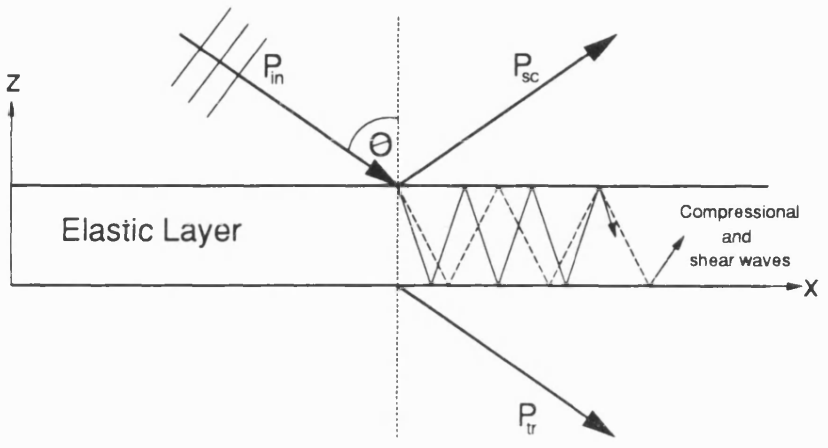

Figure 2.2 Transmission loss (dB) of an isotropic layer; variation with frequency and incident angle.

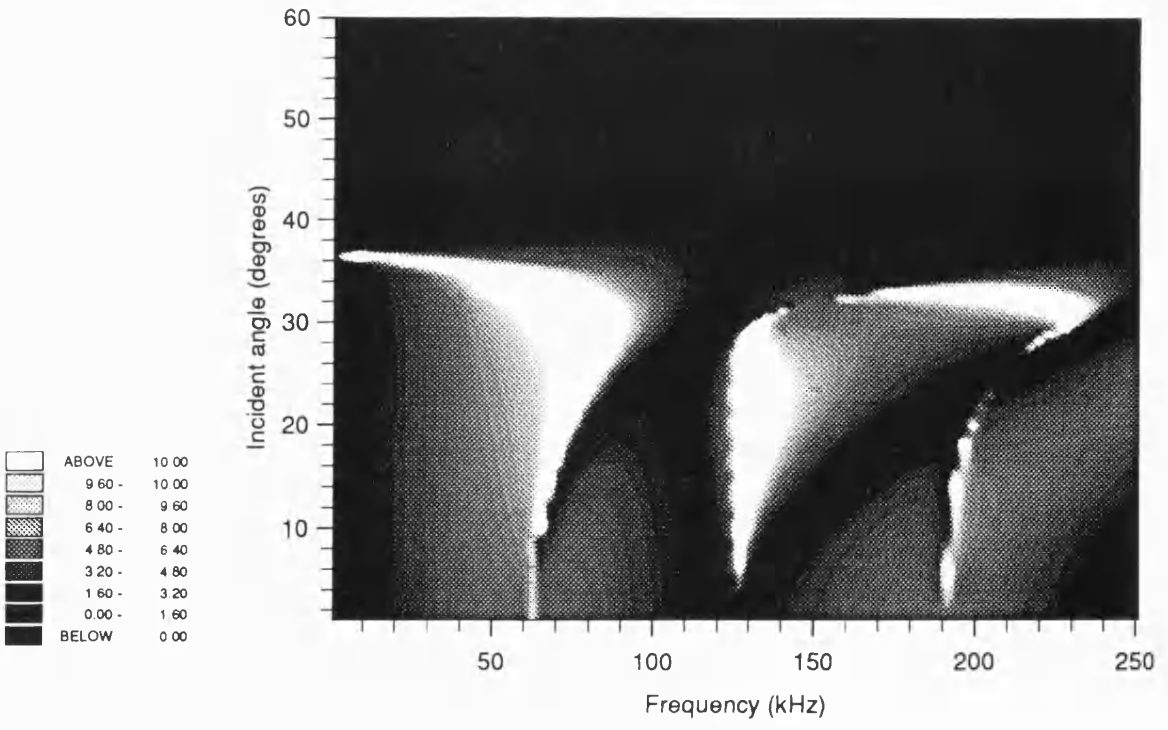

Figure 2.3 Dispersion curves for the isotropic layer; Lamb waves (S_i, A_i) and Love waves (T_i).

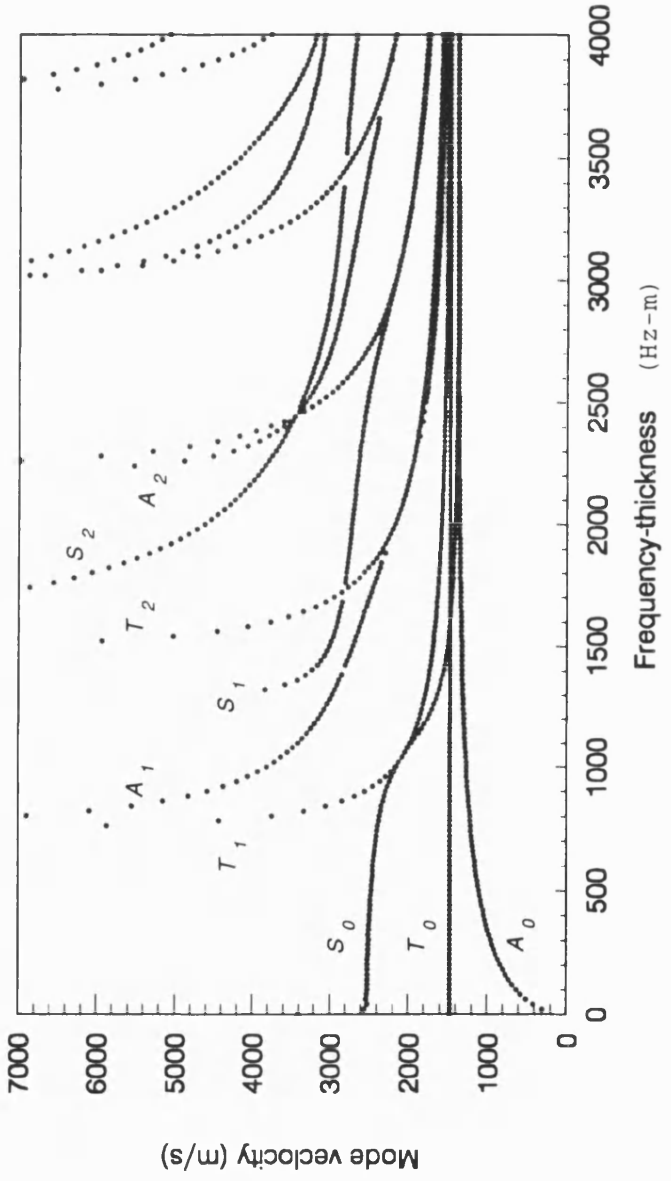

Figure 2.4 Scattering of a plane wave by a circular cylindrical shell.

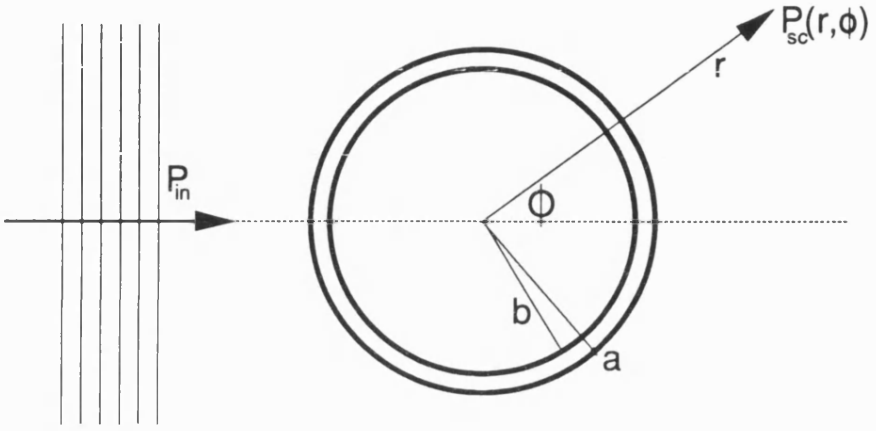

Figure 2.5 Backscattered form function ($f(\infty,\pi)$) for a brass cylindrical shell.

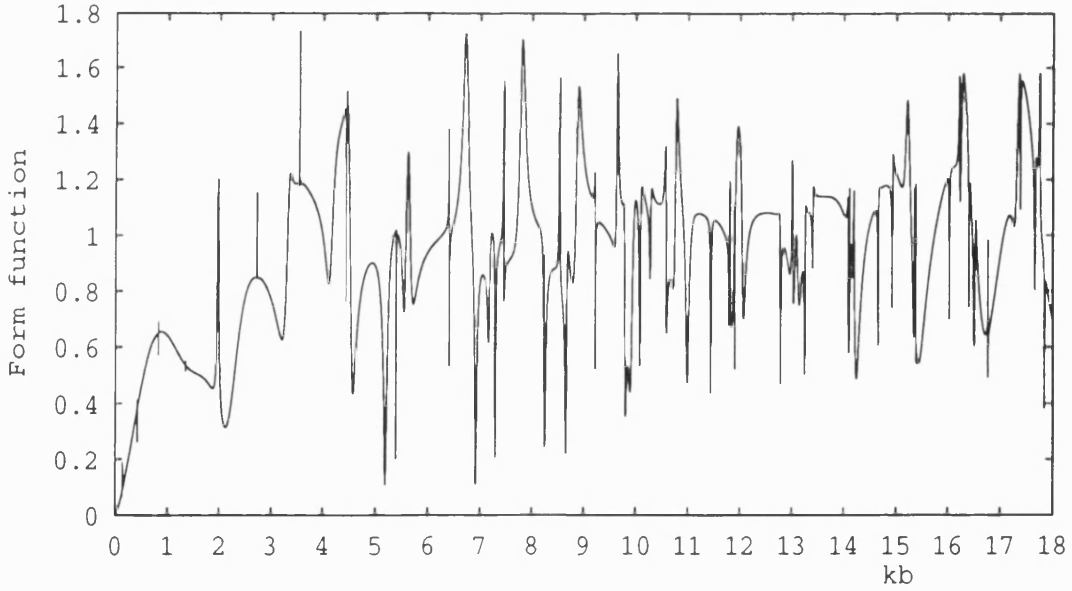

Figure 2.6 Resonance scattering by a brass cylindrical shell; theoretical predictions of pressure magnitude. Clockwise from top: (3,4) fluid column mode (kb = 14.66), (4,3) fluid column mode (kb = 12.78), n=3 shell resonance (kb = 7.29), n=6 Stoneley wave resonance (kb = 1.99) and (2,2) fluid column mode (kb = 6.92).

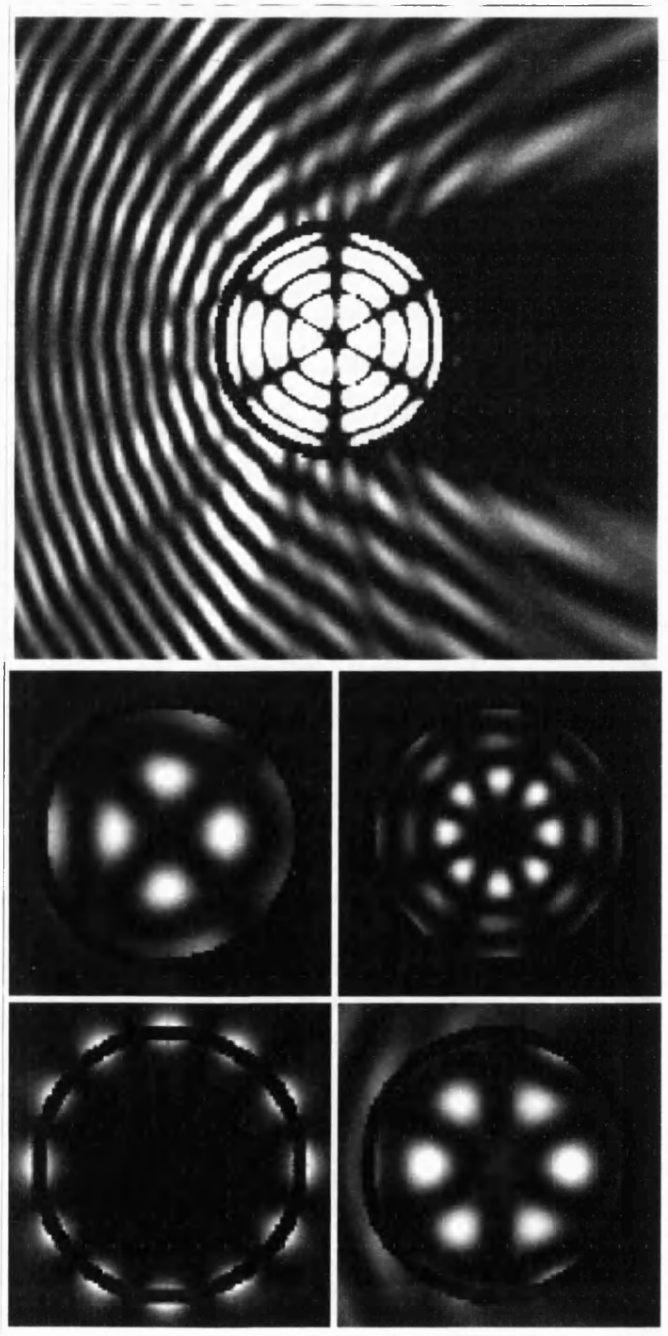

3 Schlieren visualization

3.1 Introduction

The Schlieren technique allows acoustic fields in a fluid to be 'visualized' optically. In particular it allows us to study the resonance and scattering behaviour of cylindrical objects in detail, and, importantly, in a *non-invasive* way. In the previous section we presented theoretical predictions of the acoustic fields both inside and outside insonified cylindrical shells at *resonance* (Figure 2.6). Very distinctive resonance patterns were evident; individual modes, and classes of resonance (fluid column modes, shell resonances and Stoneley wave resonances), can easily be identified by studying such images. For targets having translational symmetry the Schlieren technique potentially provides a means of obtaining such 'images' experimentally, and, therefore, of identifying the resonances and the resonance spectrum of the scattering object.

The Schlieren technique is sensitive to any phenomena that produce refractive index changes in the medium through which the light beam passes. It has mainly been used in the visualization of high speed air flow and in underwater ultrasonics. Toepler (1867) was the first to use the Schlieren technique to visualize the sound waves emitted by an electric spark (in air). The earliest known application to the visualization of ultrasound is Tawil (1930) who obtained images of ultrasonic waves in gasses. More recent applications of Schlieren in underwater acoustics have involved the visualization of acoustic scattering phenomena, see for example[1] Neubauer (1973) and Newman (1973). In particular, the pioneering work of Neubauer and colleagues provided valuable insight into the mechanisms involved in scattering by planar and curved surfaces, including cylindrical structures.

Much of the work involving Schlieren has been performed at frequencies well above a megahertz. Although visualization at these frequencies can be achieved with moderate ease, using a variety of experimental techniques (based upon Schlieren), individual wave-fronts have not normally been resolved. In addition, for *ka* ranges of interest

1 Other references to the use of Schlieren in scattering studies are given in Chapter 5.

in the marine environment, extremely small scale models of scattering objects would be required if studies were to be undertaken in the megahertz region. With the aim of studying scattering by discrete objects of reasonable size at low ka, a low frequency Schlieren system was developed at the University of Bath (Knapp; 1987, 1988a, 1988b,1988c, 1989). This system allows the visualization of pulsed and continuous acoustic fields down to about $100kHz$, and has been used to study scattering and resonance behaviour of circular cylindrical objects (Knapp & Humphrey, 1989; Humphrey, Knapp & Beckett, 1991). The same experimental system has been used in the current study.

There has always been some uncertainty as to how the images obtained with the Schlieren system are to be interpreted. Two aspects of particular concern are the effects that the spatial filtering arrangement and acoustic pressure have upon the image. Under certain conditions the optical field produced by an ideal Schlieren system is known to approximate the *square* of the acoustic pressure field. In previous studies (Humphrey, Knapp & Beckett, 1991) images obtained with the Schlieren technique have been compared directly with contour plots of the square of the pressure distribution. Unfortunately the acoustic pressure in the fluid column is unknown, and thus the validity of this comparison was uncertain. One of the major aims of the study described in this chapter is to investigate this relationship between acoustic and optical fields. We present a theoretical model for the optical distribution that constitutes the Schlieren image of an acoustic field. Computed results for the fluid column resonance modes of a circular cylindrical shell are presented and compared with images obtained from the experimental system. The theoretical results are compared with the pressure squared approximation to test its validity.

The use of the technique for studying the resonance behaviour of fluid filled cylindrical cavities of various geometries is discussed, prior to the use of the system for the more detailed study described in Chapter 5. Results are also presented for high frequency modes of the circular cavity, and, supplementary to the main body of work

described here, results for a cavity of 'stadium' geometry are presented and discussed.

The application of this technique to the study of cylindrical shells of elliptical geometry is postponed until Chapter 5.

3.2 Schlieren: principle and experimental system

In this section we discuss some of the aspects of the Schlieren technique and experimental arrangement pertinent to the present work.

The principle of Schlieren is that light is refracted as it passes through an acoustic wave-field in a fluid, since areas of different fluid density present a different refractive index to the light. This interaction of an optical wave with an acoustic wave has been the subject of much study since the effect was first explained by Raman and Nath in 1935. More recent discussions of the interaction include those by Klein and Cook (1967) and Van Den Abeele and Leroy (1990). It is known that if the intensity of the acoustic field is sufficiently low, the diffraction effect is small and the light suffers only phase variations (Raman-Nath diffraction). The acoustic field can then be considered to be a 'phase grating' which produces an interference pattern that contains information about the acoustic field. This information can be processed to produce an 'image' corresponding to the acoustic field. For a given wavelength of light, piezo-optic coefficient and interaction length, the relationship that this image has with the acoustic field depends upon the optical processing applied in the diffraction plane, and the amplitude of the acoustic pressure field through which the light passes.

The experimental arrangement (Figure 3.1) is based upon a standard 'Z' configuration. A pair of condensing lenses focus the light from a high power light emitting diode onto a pinhole[1], which acts as an 'effective' optical source. The light transmitted by the pinhole is collimated by the first parabolic mirror and passed through the water-filled tank containing the acoustic field. A cylindrical lens is placed between the pinhole and the mirror to help reduce the aberration caused by using parabolic mirrors off-axis.

1 Or an array of pinholes.

The source of acoustic waves in the water is a transducer placed with its axis perpendicular to the light beam. The light emerging from the tank is focussed by the second parabolic mirror, and forms a diffraction pattern in the focal plane of that mirror[1]. In the absence of an acoustic field an image of the pinhole is observed in the focal plane. If an acoustic field is present, the diffraction pattern contains side orders which contain the light that has been deflected out of the main beam.

The acoustic and optical components of the system electronics are shown in Figure 3.2. The system can be used in two different modes; continuous and pulsed. In the continuous mode of operation both the acoustic transducer and the optical source are driven continuously. In the pulsed mode, the light source is pulsed in synchronization with the acoustic source, allowing pulses to be visualized; by varying the delay between the acoustic and optical pulses an acoustic pulse can be observed as it propagates in apparent 'slow motion'. The pulsed mode of operation is particularly informative when studying scattering by hollow cylindrical structures, although results are not presented here.

If Raman-Nath diffraction is assumed then a uniformly bright image would be obtained were all the light in the focal plane used to form an image. This is because the light emerging from the tank has only *phase* variations and is not altered in amplitude. If, however, a part of the diffraction pattern is removed by a spatial filter, and the remaining light allowed to recombine, a meaningful 'image' can be obtained on film or video. The type of image produced, and its relationship to the acoustic field, is critically dependent upon the filtering applied in the focal plane. Two common filtering methods are zeroth order filtering and 'knife-edge' filtering (the removal of half of every diffraction order by a straight edge stop), both of which have advantages and disadvantages.

At low frequencies the resolution of the diffraction orders can become problematic. The separation of the orders (ℓ) in the focal (transform) plane is given by

1 The Schlieren diffraction effect is integrated along the optical path and so any variations of the acoustic wave-field along this path are averaged out in the diffraction pattern (and final image).

$$\ell = \frac{kh}{\kappa}, \tag{3.1}$$

where h is the focal length of the second mirror and κ is the optical wave number. Thus, for light of a fixed frequency and mirrors of fixed focal length, the order separation decreases with the acoustic frequency, and orders begin to overlap due to their finite size. Whilst the use of smaller pinholes results in narrower diffraction orders, it also reduces the amount of light passing through the system. For this reason arrays of pinholes are sometimes used to multiply the light and produce narrower orders[1]. Currently in use are an array of eight 100μm pinholes and an array of eighteen 50μm pinholes. The use of a laser as the optical source was investigated but was found to result in significant *optical* interference effects (due to the coherence of such a source). When multiple pinhole arrays are being used, zeroth order spatial filtering is achieved by using a matching array of spatial filters. Aberrations[2] in the system result in distorted diffraction orders, and so close-up photographs of the pinhole images *without* an acoustic field in the tank are used as spatial filters for the multiple pinhole arrays. The arrays had a random basis, so as to minimize the inevitable overlapping between the side orders of one pinhole pattern and those of another. Knife-edge filtering is not possible with multiple pinhole array sources.

A parallel theoretical and experimental investigation into the effects of spatial filtering, and the acousto-optic interaction, was previously undertaken by Knapp (1988a) for the case of a one-dimensional *progressive* wave. This study showed that as the acoustic pressure amplitude varies, the amount of light falling into the different orders in the diffraction plane varies, causing the image to change. For certain values of the pressure, the zeroth optical order completely disappears as all the light is diffracted into the higher orders. As this is tantamount to changing the spatial filtering arrangement, the optical distribution would be expected to change accordingly; this was shown to be the case. Results for zeroth order filtering indicated that, at *low* pressure

1 Incoherence of the light source prevents unwanted interference effects.

2 A discussion of the aberrations in the system and the steps taken to minimize them is given in Knapp (1987-1989).

amplitudes, the optical distribution varies as the square of the acoustic pressure, but changes markedly as the pressure is increased. Knife-edge filtering on the other hand produces an optical field whose intensity varies linearly with pressure over quite a broad range of pressures.

For standing waves the situation is not so simple. At certain places in an acoustic standing wave, the pressure amplitude is always zero, and we would expect that light will pass through the field undeflected in these regions, so that the zeroth order would never completely disappear. Additionally, in the standing wave fields of interest in the current study, the acoustic fields are two-dimensional and the pressure amplitude varies from place to place, potentially creating a very complex dependence of the optical field on the acoustic field. Additionally, there is a progressive wave component present, which further complicates matters.

For these reasons a more general theoretical investigation into the acousto-optic interaction, applicable to two-dimensional fields, was required. The details of this investigation, which is based, in part, upon that of Beckett & Humphrey (1989a), are now given.

3.3 Optical field: theoretical model

An exact theoretical expression for the optical image of any two-dimensional acoustic field visualized with an ideal Schlieren system is derived. Figure 3.3 shows the locations of the planes in which the various optical fields are calculated.

Any acoustic pressure field within the fluid can be written

$$P_{fl}(\underline{r},t) = e^{-i\omega t} p(\underline{r}) e^{i\delta(r)}, \tag{3.2}$$

where p is the spatial part of the pressure amplitude, and δ is its phase. Under Raman-Nath conditions, the acoustic pressure field produces *phase* variations (σ) in the light wave that passes through it. These phase variations are proportional to the real part of the pressure distribution;

$$\sigma(\underline{r},t) \propto Re\{P_{fl}\} = \nu_o(\cos\delta\cos\omega t + \sin\delta\sin\omega t), \tag{3.3}$$

where

$$\nu_o = \kappa\left(\frac{\partial\mu}{\partial p}\right)_s Lp, \tag{3.4}$$

and where κ is the optical wave number, $(\partial\mu/\partial p)_s$ is the adiabatic piezo-optic coefficient, and L is the acousto-optic interaction length (which is approximately equal to the width of the transducer face). The parameter ν_o, known as the Raman-Nath parameter, is dependent upon the acoustic pressure (p) and the strength of the acousto-optic interaction. It can be written $\nu_o = sp$, where $s = \kappa(\partial\mu/\partial p)_s L$ is a constant for a given experimental arrangement[1].

The optical field emerging from the tank (i.e. in the object plane) can then be written

$$E(\underline{r},t) = E_o e^{i\sigma} = E_o e^{isp\cos\delta\cos\omega t} e^{isp\sin\delta\sin\omega t}, \tag{3.5}$$

or, by expanding the exponentials in series of Bessel functions,

$$E(\underline{r},t) = E_o \sum_m i^m J_m(sp\cos\delta)e^{im\omega t} \sum_n J_n(sp\sin\delta)e^{in\omega t}. \tag{3.6}$$

After reflection in the mirror (M2) the optical field in the transform plane is given by the spatial Fourier transform (FT) of E,

$$E_T(\underline{\eta},t) = E_o \sum_{m,n} i^m e^{i(n+m)\omega t} FT\{J_m(sp\cos\delta)J_n(sp\sin\delta)\}, \tag{3.7}$$

where η is the coordinate vector in the transform plane. The diffraction pattern observed in the transform plane is given by $E_T E_T^*$, where E_T^* is the complex conjugate of E_T.

A spatial filter, $\Im(\eta)$, placed in the transform plane removes part of the optical field, leaving the transmitted field ($E_{T'}$);

1 Assuming L to be constant, which is not strictly true for divergent beams.

$$E_{T'}(\underline{\eta},t) = E_o \sum_{m,n} i^m e^{i(m+n)\omega t} \aleph_{mn} \quad ; \quad \aleph_{mn}(\underline{\eta}) = \Im(\underline{\eta}) FT\{J_m(sp\cos\delta) J_n(sp\sin\delta)\}. \tag{3.8}$$

The transmitted waves then pass through the imaging lens, to produce the final optical field in the image plane. This field (E_I) is the inverse Fourier transform of $E_{T'}$,

$$E_I(\underline{r}',t) \;=\; FT^{-1}(E_{T'}) \;=\; E_o \sum_{m,n} i^m e^{i(m+n)\omega t} FT^{-1}\{\aleph_{mn}(\underline{\eta})\}. \tag{3.9}$$

The intensity of the final image is given by

$$I(\underline{r}',t) = E_I E_I^* = E_o^2 \sum_{m,n,p,q} i^m e^{i(m+n-p-q)\omega t} FT^{-1}(\aleph_{mn}) [i^p FT^{-1}(\aleph_{pq})]^* , \tag{3.10}$$

but the actual image observed by the eye, or recorded on film, is the time average of I, $\frac{1}{T}\int^T I\,dt$, in which only terms having $m+n-p-q=0$ will contribute. The expression then reduces to

$$I(\underline{r}') = E_o^2 \sum_{m,n} FT^{-1}(\aleph_{mn}) \sum_l i^l FT^{-1^*}(\aleph_{m-l,n+l}) \quad ; \quad (l = m-p), \tag{3.11}$$

which can be shown to be real. This then is the final optical intensity distribution seen in the image plane, for different spatial filtering arrangements described by the function $\Im$.

3.4 Implementation

A computer code was written[1] to numerically implement the theory described above, and has been used to predict the optical distribution resulting from different acoustic fields, pressure levels, and spatial filtering arrangements. The fluid column resonances of the insonified cylindrical shell were chosen for comparison with experiment. It should be noted that the theory described contains no concept of a finite size pinhole, such as exists

1 This code was originally adapted from that written by C Beckett (Beckett & Humphrey, 1989a).

in the experimental system. Differences from the experimental results are expected for this, and other, reasons, including the aberrations that exist in the optical system.

Most significantly, although the acoustic field in the fluid column can be predicted using the Normal Mode Series approach described in Chapter 2, the amplitude of the incident pressure field is not known. The parameter v_o $(=sp)$ is dependent upon both the strength of the acousto-optic interaction $(s = \kappa(\partial\mu/\partial p),L)$ and the acoustic pressure. Taking the wavelength of the light to be $660nm$, the interaction length to be approximately equal to the diameter of the transducer face $(5cm)$, and the adiabatic piezo-optic coefficient for water to be $1.5\times10^{-10}Pa^{-1}$ (Raman & Venkataraman, 1939), we estimate the value of s to be $7\times10^{-5}Pa^{-1}$. The amplitude of the pressure field is, however, unknown. This means that the Raman-Nath parameter (v_o) cannot be calculated accurately. Estimates of the parameter are possible, by referring to the studies undertaken by Knapp (1988a) for the one-dimensional progressive wave, and these were used as a starting point.

In computing the image intensity distribution, the number of orders needed in the summation (3.11) increases with the value of v_o (and hence the pressure).

3.5 Results

In this section experimental results are presented, and comparison made with the theoretical predictions to test the validity of the theory. Results are illustrated by examining the fluid column resonances of a normally insonified brass cylindrical shell having radii of $14.25mm$ and $15.85mm$. The sample used in the experimental measurements was $100mm$ long. Measurements were made with the transducer driven in continuous mode.

3.5.1 Pressure levels

Figure 3.4 shows the (3,3) fluid column resonance found at a computed kb value of 11.448 and an experimental value of 11.46. The Schlieren image (Figure 3.4(a)) was obtained using an array of 18 pinholes of diameter $50\mu m$ and a matching spatial filter providing

zeroth order filtering. This is a typical Schlieren observation: the drive level was adjusted so that a reasonable image was obtained; too low a value and only the regions of highest amplitude are visible (or no image at all), too high a value and other effects complicate the image, as will be discussed. The computed fields are as follows. Figures 3.4(b-d) show the predicted optical distribution calculated with three different values of v_o. The three theoretical predictions are quite different, the experimental result bearing a closer resemblance to Figure 3.4(c) than either of the other predictions (Figures 3.4(b) and (d)).

Figure 3.4(b) was calculated with a low value of v_o (equal to 0.4) and is expected to result in an optical distribution approximating the *square* of the pressure distribution. In order to test this prediction, cross-sections of the optical distribution and pressure squared distribution are shown in Figure 3.5. The profiles are taken along the horizontal diameters of the fields and the vertical scales have been normalized for comparison. The agreement between the optical distribution calculated with $v_o = 0.4$ and the pressure squared variation is seen to be *exact*. Also shown in Figure 3.5 is a comparison of the magnitude of the pressure distribution with the optical distribution calculated with a value of $v_o = 3.4$. The agreement, although not exact, is quite good, suggesting that at a certain value of v_o the predicted optical image is a good approximation to the magnitude of the pressure distribution itself. The minor differences seen in the figure would not be observable in practice anyway. The complete images are compared in Figure 3.6, and in particular it is worth comparing Figure 3.6(c) with the experimental image given in Figure 3.4(a). It would appear that the experimental result is a closer approximation to the magnitude of the acoustic pressure than to its square. Care must be taken in interpreting these results however. For the standing wave-field inside the fluid column, different regions have different pressure amplitudes, and therefore different value of v_o (unlike the progressive plane wave). The value of v_o referred to here corresponds to the maximum value of pressure in the fluid column.

If the transducer is driven harder, the acoustic pressure in the fluid column increases and the optical image changes. An example of this effect is given in Figure

3.7. Figure 3.7(a) shows the appearance of the experimental image for a higher acoustic drive level. Experimentally, the higher pressure levels result in the diffraction orders of the individual pinholes in the array overlapping with adjacent pinhole side orders, so an array of $8 \times 100\mu m$ pinholes, more widely spaced, had to be used. This array, however, results in reduced clarity for low frequency fields due to overlapping of orders in the individual pinhole images, which results in the removal of part of the first side order by the filter designed only to remove the zeroth order. The predicted optical distribution (Figure 3.7(b)), calculated at an arbitrarily chosen value of $v_o(= 11.2)$, displays mostly the same features as the experimental image, although the agreement is not as good as previously. To generate the theoretical image, more orders needed to be considered in the calculation because the arguments of the Bessel functions are much larger. The brightest regions in the image are seen to broaden and split into several parts. This splitting, at high pressures, of each bright region into two bright regions, is described (in the one-dimensional case) by Knapp (1988b).

3.5.2 Spatial filtering

All the experimental and predicted images shown in the previous section involved zeroth order filtering. More dramatic changes to the Schlieren image of the acoustic field are evident when different spatial filtering is used in the transform plane. Figure 3.8 shows the (3,3) resonance again, this time produced using knife-edge filtering. A single pinhole of $400\mu m$ diameter was used to illuminate the acoustic field in the Schlieren system. Figures 3.8(a,b) show the appearance of the resonance when the knife-edge passes horizontally through the diffraction pattern; Figures 3.8(c,d) were produced with the knife in the vertical position. A razor blade was used as the knife-edge filter.

All the features seen in the experimental results can be seen in the theoretical plots if they are examined closely. The lack of symmetry between the two cases is due to the fact that the knife-edge passes along different symmetry planes in the diffraction pattern - these filtering arrangements are therefore fundamentally different.

Figure 3.9 shows the (4,4) fluid column mode visualized experimentally, again

using different spatial filtering in the stop plane. The result of zeroth order filtering is shown in Figure 3.9(a), whilst Figure 3.9(b) shows the result of using a filter that is larger than the zeroth order, and also blocks a part of the first side orders. Knife-edge filtering was used to produce the remaining images; Figures 3.9(c) and (d) are the result of using the knife-edge horizontally and vertically. Unlike the previous case considered (Figure 3.8), both of these images are the same, apart from a 90° rotation. This reflects the symmetry of the (4,4) resonance. To obtain a different image with the knife-edge it must be placed at some other angle, as is shown in Figure 3.9(e).

For zeroth order filtering, as described in section 3.5.1, the acoustic pressure level affects the appearance of the image considerably. For knife-edge filtering, however, the image does not change appreciably as the pressure is increased to moderate levels. This is of significance when we consider that the standing wave-field does not have a uniform pressure amplitude throughout the fluid column.

3.6 Location, identification and visualization of resonances

We now describe how the Schlieren system can be used as a tool to locate, identify and record the resonances of cylindrical shells. Being essentially an *optical* system, great care must be taken in aligning the system components accurately if acceptable images are to be obtained. The processes involved are quite complicated and only brief details will be given.

Although the use of a single pinhole source and a knife-edge filter is the easiest way of obtaining an image of the acoustic field, it does - as has been demonstrated - produce an image bearing a complicated, and unobvious, relation to the acoustic field. The use of zeroth order filtering produces images that are more easily interpreted (provided the pressure levels are not too high) and this method is now generally used with the present experimental system. The use of multiple pinhole arrays to increase the light level in the system also precludes the use of knife-edge filters.

With a test sample in place in the water tank, correctly aligned and insonified by the transducer, the frequency of the drive signal (continuous wave) is swept, either

manually, or automatically by the function generator. A video camera is placed immediately behind the spatial filter and connected to a television monitor (and optionally a video recorder). At frequencies corresponding to resonances of the test sample, acoustic standing waves are clearly seen in the fluid column. At other frequencies, where little energy penetrates the shell, only the scattered field is seen. There is also usually a standing wave between the transducer face and the test sample.

To record the resonance patterns, the video camera is replaced with a still camera, the frequency locked, the drive level adjusted until an acceptable image obtained, and several timed exposures made.

Care must be taken when interpreting the observed patterns and identifying resonance modes. If the drive level is too high, the image has an appearance such as that shown in Figure 3.7 and may be mistakenly identified. The possibility of other resonances being excited by overtones of the drive frequency must also me considered. This typically happens when a low frequency is applied to the transducer and the drive level increased in an attempt to visualize low frequency modes, these modes being harder to detect due to optical considerations.

Care must also be taken to correctly identify resonance modes differing in origin, but similar in appearance, such as certain fluid column modes and shell resonances (see Chapter 2). Also, resonance modes which are close in frequency may overlap, making identification of either mode difficult. This occurs particularly at high frequencies where the density of resonances is greatest. This will be discussed further in section 3.7.1.

The video recorder can be replaced with a personal computer incorporating a 'line-grabbing' digitization board and software. This facility allows the optical intensity at a point within the image to be monitored, and intensity profiles of the resonances to be obtained. Some aspects of this work are described in Scott & Wilcox (1992). The use of this facility, combined with the theoretical techniques described above, offers the potential of using the system to obtain more quantitative information from the Schlieren system than has hitherto been possible.

3.7 Cavity resonances: two supplementary studies using Schlieren

During the course of the study described here, the Schlieren technique has been used to study the resonance behaviour of flooded cylindrical structures of various geometry. In this chapter we have illustrated results for low frequency resonance modes of the circular cylindrical shell. Of particular interest to the present thesis is the resonance behaviour of structures that do *not* have a circular symmetry. In Figure 3.10 examples of resonance modes within two non-circular cylindrical cavities are presented; the elliptical geometry and the 'stadium'. A major part of this study will be presented in Chapter 5 where we consider the *elliptical* cylindrical shell in more detail.

In this section we present supplementary results concerning the *high* frequency behaviour of the circular cylindrical shell, and we briefly describe some work involving the stadium shaped cavity.

3.7.1 High frequency modes of the circular cylindrical shell

Most of the previous studies involving the resonances of fluid filled cylindrical shells have concentrated on the low frequency region ($100 - 400kHz$) where resonances are quite broad, but reasonably well separated in frequency. At higher frequencies the resonances become narrower, but closer together, and many tend to overlap, making the resolution of individual resonances impossible. Indeed at very high frequencies (several megahertz), the concept of a resonance as a single mode is not meaningful, as hybridization of modes becomes extensive. This effect is seen in the form function, and in calculations of the pressure in the fluid column itself. This higher density of resonances, and overlapping between them, is clearly seen at the higher frequency end of the form function shown in Figure 2.5. At the very highest frequencies *many* normal modes may contribute to the acoustic field at a given frequency.

The effect that this hybridization has upon the interior field is shown in the Schlieren photographs presented in Figure 3.11. New kinds of unexpected symmetry, such as the 3-fold symmetry seen here, can appear in the resonance patterns. Resonances having 5-fold and 7-fold symmetry have also been observed.

The appearance of some of these images is reminiscent of the classical 'ray' or 'orbit' concept that is applicable to wave-fields in the high frequency (short wavelength) domain. In particular, the association of some of the features of the resonance patterns with periodic (closed) orbits of a ray, or particle, 'bouncing' around within the enclosure, can be made. In the circular cavity, a typical orbit, such as that shown below (left), never repeats itself: every point on the circumference is 'hit' eventually, and a caustic is formed.

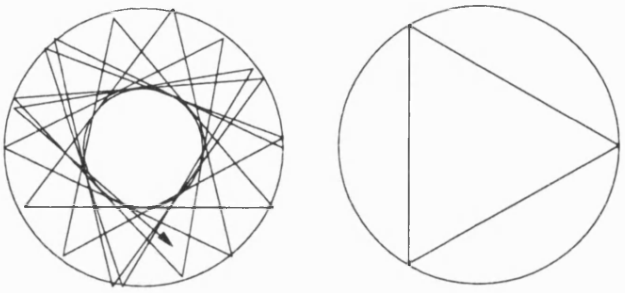

The rather special cases where the ray repeatedly traverses the same (periodic) orbit is shown on the right. Some of the acoustic resonance fields presented in Figure 3.11 clearly exhibit these kinds of behaviour. Even the comparatively lower frequency modes of Figure 3.11(a) and Figure 3.11(b) have a symmetry that can be associated with periodic orbits such as that illustrated above. Further discussion concerning rays and two-dimensional cavities is given in Appendix A1.

An alternative description of the behaviour manifest in Figure 3.11(a) and (b) can also be given. At these 'intermediate' frequencies only a couple of modes are interfering, and the new symmetry seen in the acoustic field is the highest *common* symmetry of the interfering modes; in this case six and three-fold symmetries respectively. This can also be thought of as a two-dimensional beating effect.

These observations made at high frequencies demonstrate how Schlieren can be used to provide insight into phenomena that could not easily be measured or observed

with a conventional acoustic approach using a hydrophone. Indeed, Schlieren is a valuable tool for studying many aspects of wave physics in general, as will be demonstrated in the following section.

3.7.2 The 'stadium' shaped cavity

In Figure 3.10 Schlieren images of the resonance modes of two *non*-circular cavities (having elliptical and stadium geometries) were presented. Although both of these geometries can be obtained by continuous perturbations of the circle[1], their properties are quite different: the stadium geometry has a classical mechanics that is *chaotic*, the elliptical geometry does not. There is currently great interest in the resonance and scattering properties of 'chaotic' systems, and in the work undertaken with Schlieren several geometries were initially investigated. In this section we briefly discuss the stadium geometry.

'Chaotic wave scattering' is defined by Doron, Smilansky and Frenkel (1990) as "the scattering of waves from systems for which the underlying classical (ray) dynamics is chaotic". In the context of the present work this description can be applied to any general deformation of a circular boundary whose solution is *not* integrable[2], as the perfect circle and ellipse described earlier are. The specific example we will discuss is that of the Bunimovich stadium which has been proved to be totally ergodic[3]. Our interest lies in the extent to which the chaotic behaviour of the classical mechanics influences the wave behaviour of a resonating system. The classical mechanics is discussed in more detail in Appendix A1.

3.7.2.1 Eigenstates of the stadium

The interest in chaotic scattering involving cavities such as the stadium originated in the semi-classical study of quantum systems. Since then studies of such systems have

1 In *principle* that is: the stadium cavity used experimentally was *not*, however, obtained in this way.

2 A solution of the classical mechanics is *integrable* if there exists a constant of the motion (conserved quantity). In classical mechanics this is the requirement that the Poisson bracket of a variable with the Hamiltonian vanishes, that variable being the constant of motion.

3 An *ergodic* system is properly defined in terms of the way a particle confined to motion within the system accesses the *phase* space. For the present purposes we can loosely equate ergodicity with an apparently 'random' motion.

been undertaken using microwaves, water-waves, and now *acoustic* waves; a review and references are provided in Appendix A2. The main difference between these different kinds of wave problems - and their solutions - is the different boundary conditions that are applicable. In this section we briefly explain what it is about the wave mechanics that is unexpected, and provoked such an interest in this geometry.

When the high energy wave functions of the stadium were calculated, they were found to have a non-uniform structure involving local enhancement of the wave functions in regions corresponding to the periodic (closed) orbits of the classical mechanics. These non-uniformities were unexpected because they had not been observed in the wave functions of integrable systems, such as the rectangular and circular cavities. The stadium, having been proved chaotic, was expected to exhibit even *less* detailed, non-uniform, structure than these integrable systems. A Gaussian random appearance was in fact expected of them. The influence of the periodic closed orbits of the classical mechanics is all the more surprising when we consider that they constitute the tiniest minority of all possible orbits within the stadium; they are of 'measure zero' with respect to the majority of orbits, which are chaotic. They are also, of course, highly unstable, and so would not be expected to be 'found' by any experiment. For these reasons it is initially surprising that the closed orbits have such a marked effect upon the wave functions of the stadium shaped cavity. More details are given in the paper included as Appendix A2, and the references therein.

3.7.2.2 Resonances of the stadium

Although the closed periodic orbits of classical mechanics are known to affect the quantum wave functions of chaotic scatterers, the question must be asked; do the periodic orbits affect other kinds of wave behaviour - such as electromagnetic, acoustic or water waves? In the acoustic case the resonance modes of the stadium shaped cavity are subject to hybridization in the same way as those of the circular shell, and periodic orbits could possibly manifest themselves in this way. We must stress that the influence of the periodic orbits in the quantum stadium is on *single* eigenstates.

Preliminary experimental investigations of the acoustic resonances within hollow stadium shaped cylinders (and quarter-stadiums) have been undertaken. Several different constructions using different materials have been investigated, the most successful being a cavity machined within an aluminium block, $95 \times 38 \times 63mm$ in size. The distance between the flats of the cavity is $26mm$. The acoustic impedance of aluminium is such that the outer boundary of the block makes a significant contribution to the appearance of the resonances within the cavity; the resonance 'sees' the outer boundary. For this reason the rectangular-sectioned block was eventually machined down to make a shell having an (approximately) constant thickness of $6mm$. This construction has the same symmetry for the outer and inner shell boundaries, although the finite impedance of the metal shell is of course unaltered, and the boundary conditions far from the simple Dirichlet boundary of the 'rigid' walled cavity.

The system was insonified with a transducer in the same way as the circular and elliptical cylinders; insonification at different angles being required to excite different resonances. One example of an observed resonance mode is shown in Figure 3.10(b), others are shown in Appendix A2 (Figure 2).

Isolation of individual resonances was only really possible at extremely low frequencies (below $100kHz$) where visualization is very poor (due to optical problems). However, it was possible to match some of these low lying states with computations performed at Bristol (Boasman, 1991).

Acoustic scattering aside, the greater importance of this work lies in the fact that it is the first known experimental demonstration of the influence of classical periodic orbits upon acoustic wave-fields within chaotic systems. It is in fact one of the first experiments of all to show the actual wave functions. Ways of reducing the widths of the stadium resonances were investigated in an attempt to resolve higher frequency states; this work may be continued in the future.

3.8 Summary

The application of the Schlieren visualization technique to the study of acoustic resonances within cylindrical shells has been discussed. A theoretical model of the optical intensity distribution in the image plane of an ideal Schlieren system has been presented.

The theory has been numerically implemented and tested for the resonance modes of cylindrical shells of circular cross-section. Calculations of the optical images of resonances within these shells have been presented and compared with experimental results obtained with the Schlieren system. The theory has been shown to be accurate in predicting the changes in the image associated with different values of v_o, and different spatial filtering arrangements in the transform plane.

The square of the pressure distribution has previously been used as an approximation to the Schlieren image (when zeroth order filtering is used). Comparison has been made between the pressure squared distributions and the exact predictions of the optical image. Good agreement has been found when very low pressures are present in the fluid column, but departures become obvious for more moderate pressures, and drastic for high pressures. It would appear that the experimentally obtained images correspond closer to the magnitude of the pressure distribution itself than to its square.

The results presented for different filtering arrangements in the transform plane are of particular interest. In this case, no approximations can be made and the exact theory provides the first theoretical predictions of these images.

The experimental system has been used to investigate many aspects of scattering and resonance behaviour involving cylindrical objects of various geometry, and is of particular value when considering those geometries that cannot easily be modelled. Of particular interest here are the hybridization of resonance modes at high frequencies, and the modes of *non*-circular cavities, such as the stadium.

Further applications of the techniques described in this Chapter are presented in Chapter 5 where we consider the elliptical cylindrical shell in depth.

Figure 3.1 The Schlieren visualization system.

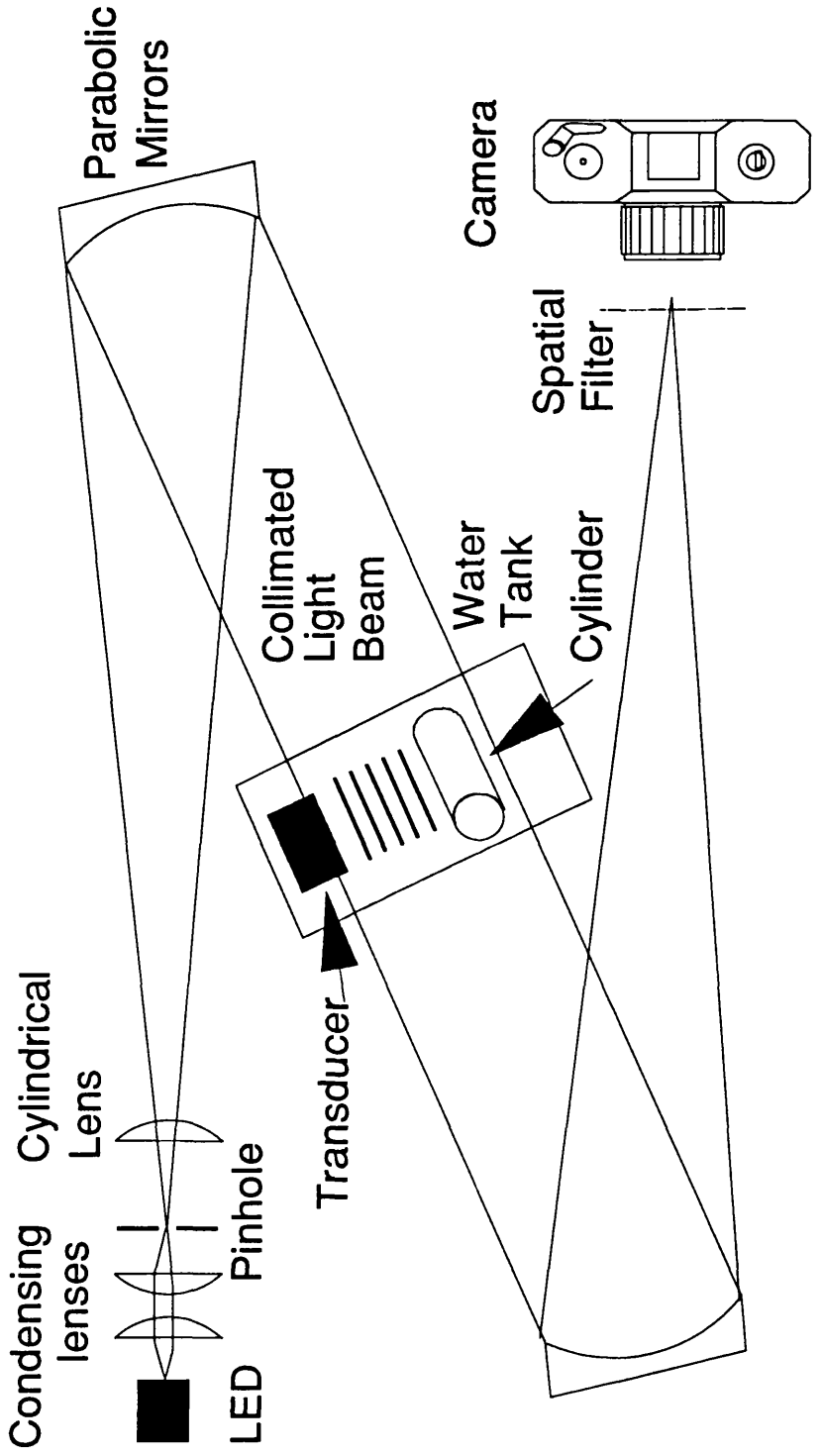

Figure 3.2 System electronics; acoustic and optical components of the Schlieren system.

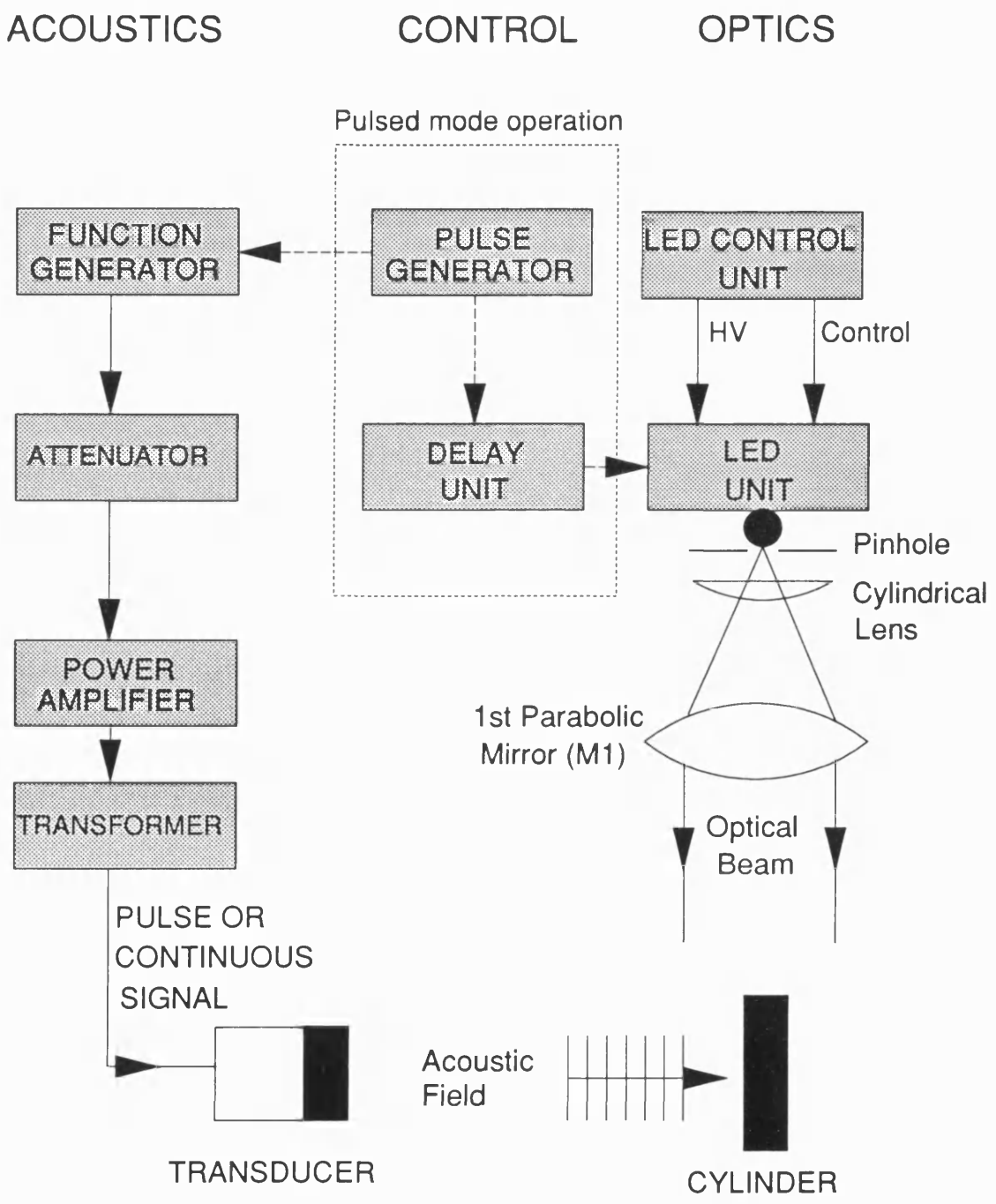

Figure 3.3 Location of the field planes in the Schlieren system.

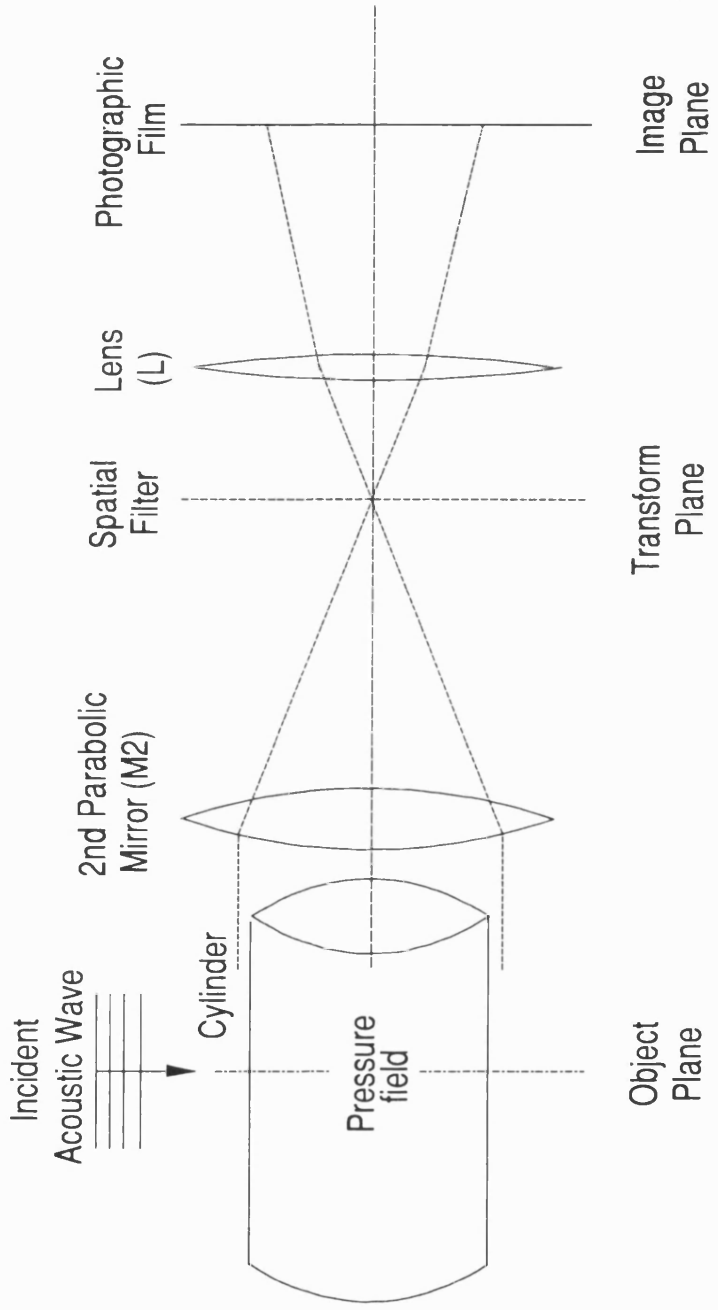

Figure 3.4 The (3,3) fluid column resonance mode; experimental observations (a) and theoretical predictions (b-d) for different values of the parameter ν_o.

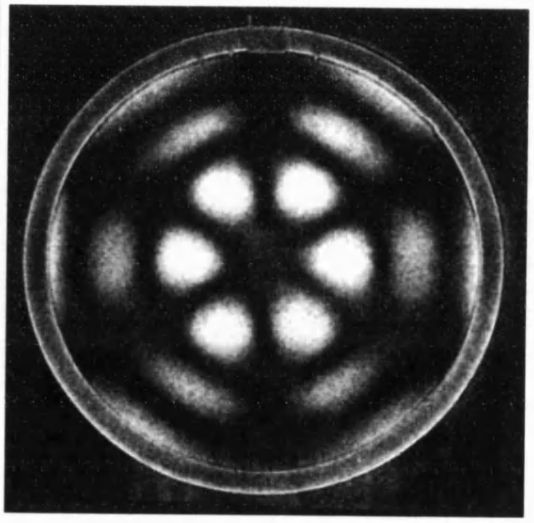

(a) Schlieren image

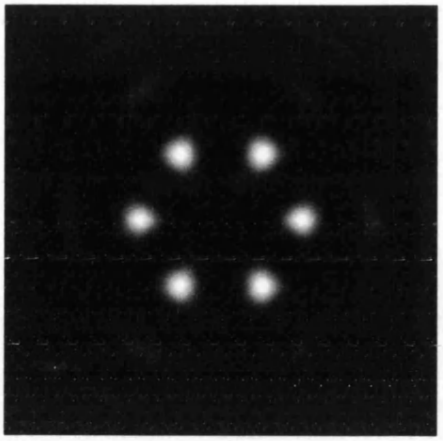

(b) $\nu_o = 0.4$

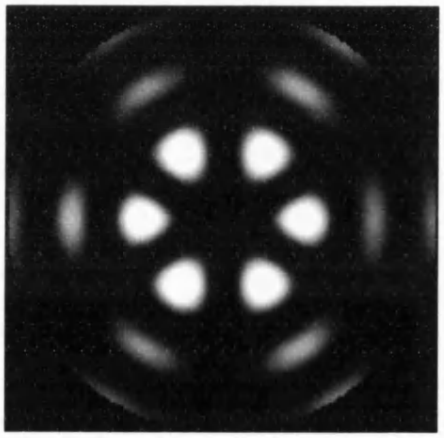

(c) $\nu_o = 4.3$

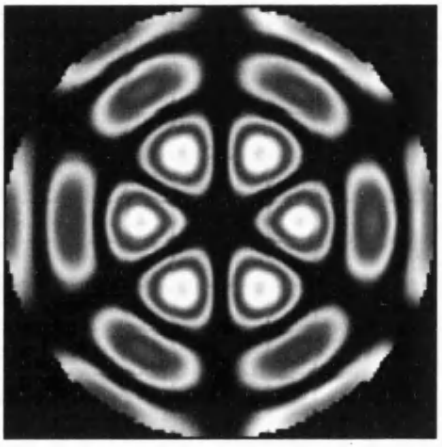

(d) $\nu_o = 11.2$

Figure 3.5 Computed cross-sections of the acoustic and optical fields for the (3,3) fluid column mode.

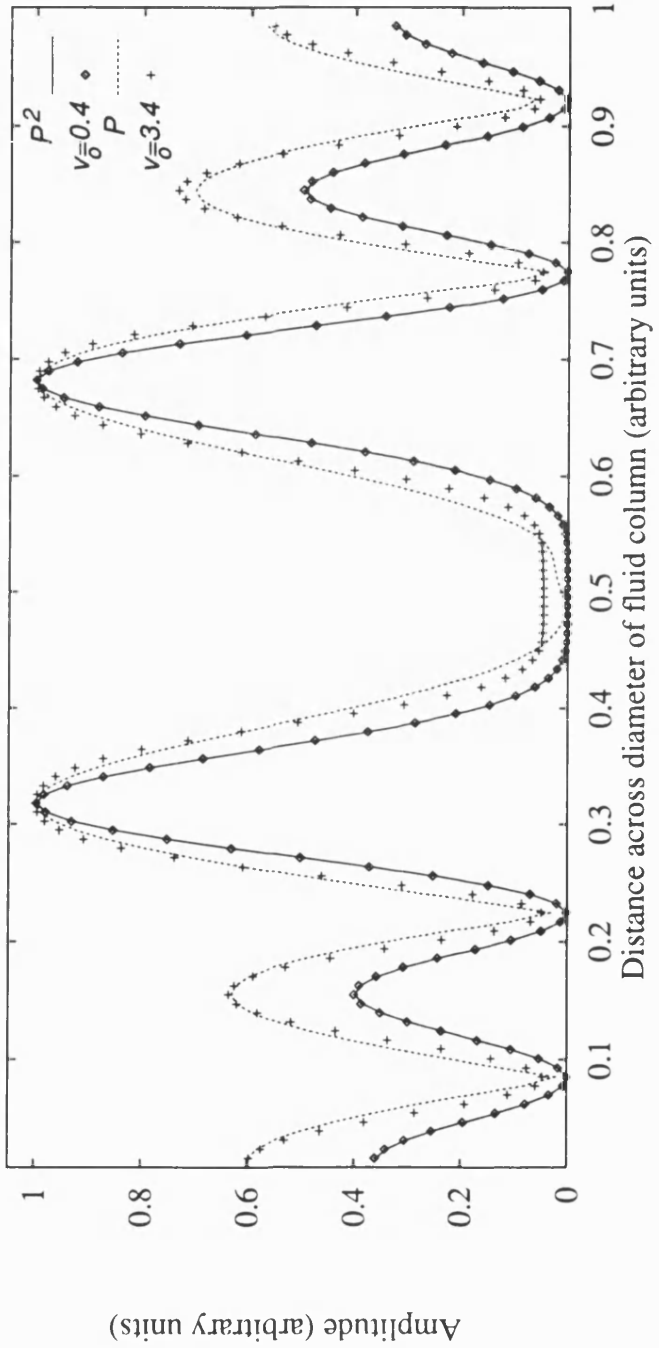

Figure 3.6 Comparison of predicted optical distributions with theoretical predictions of the magnitude of the *pressure* and pressure *squared* distributions.

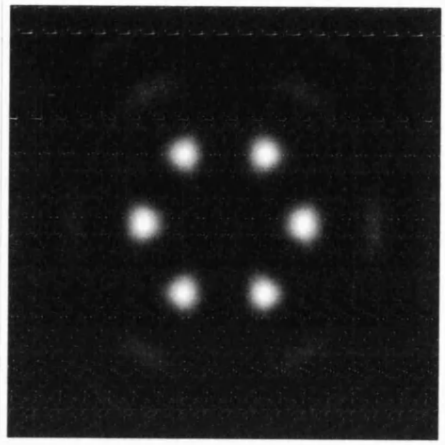

(a) P^2

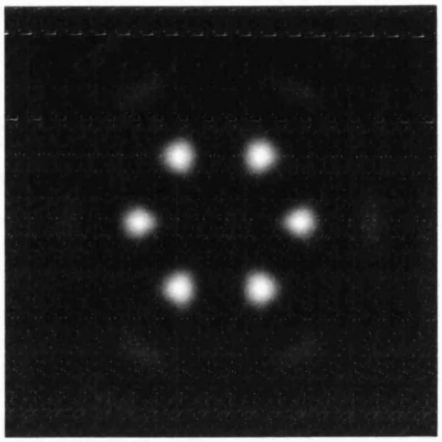

(b) $\nu_o = 0.4$

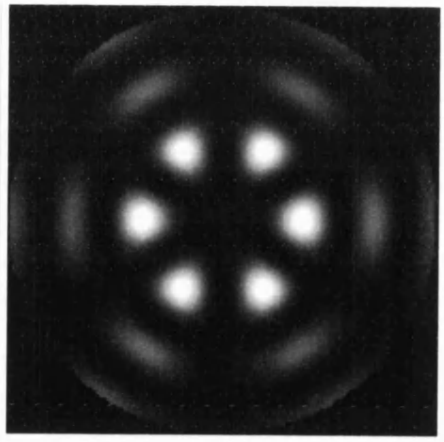

(c) P

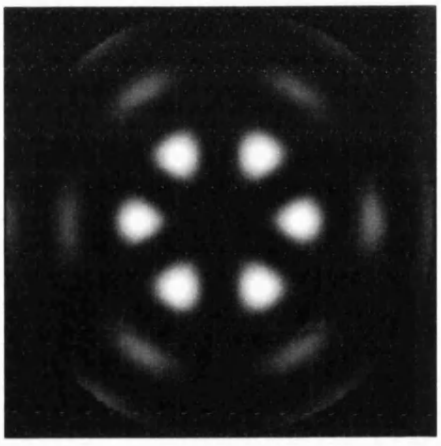

(d) $\nu_o = 3.4$

Figure 3.7 Experimental and theoretical results for high values of the acoustic pressure (experiment) and Raman-Nath parameter (theory).

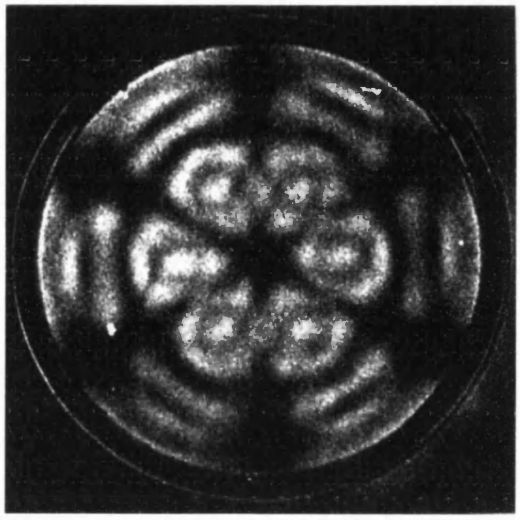

(a) Experiment

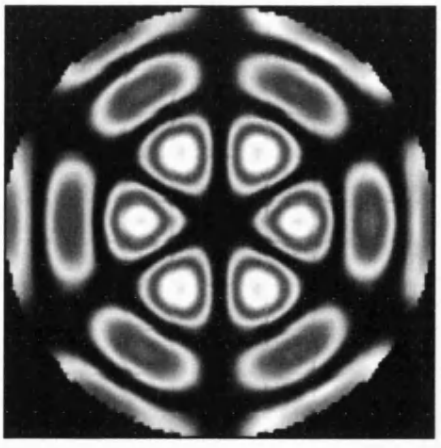

(b) Theory, $\nu_o = 11.2$

Figure 3.8 Knife-edge filtering; the (3,3) fluid column mode.

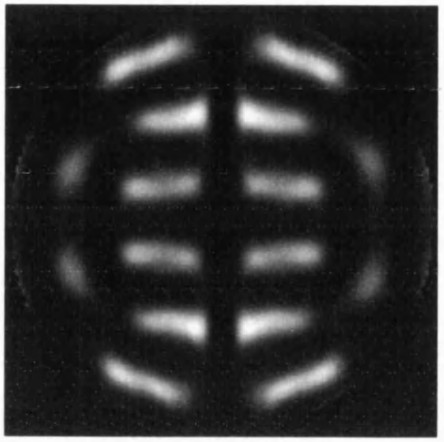

(a) Horizontal knife - theory

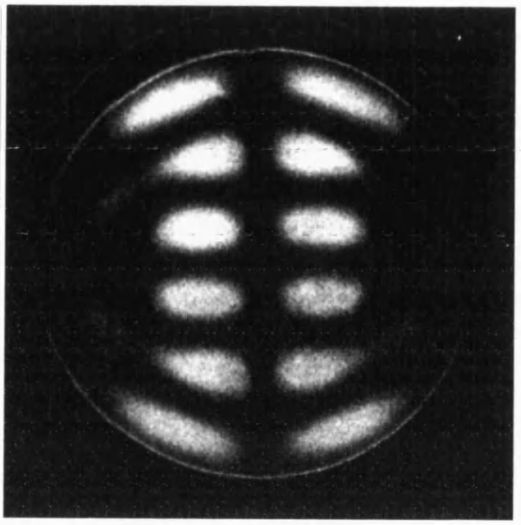

(b) Experiment

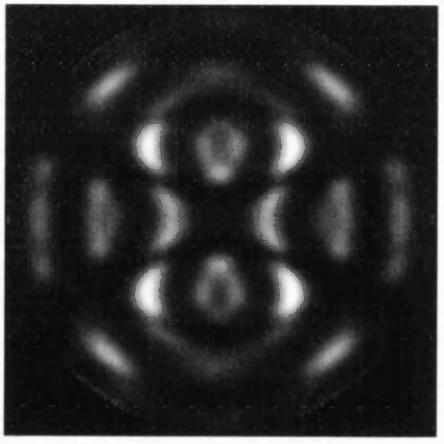

(c) Vertical knife - theory

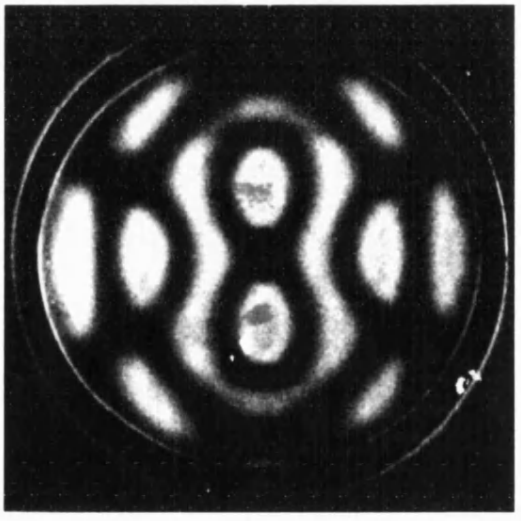

(d) Experiment

Figure 3.9 The (4,4) fluid column mode observed with different spatial filteing arrangements - experimental observations.

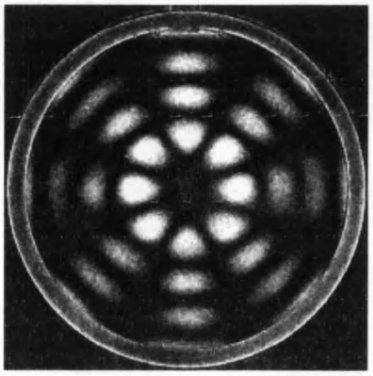

(a) Zeroth order filtering

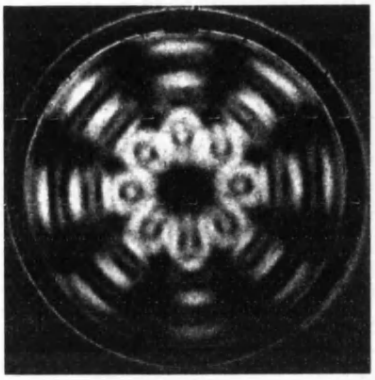

(b) Zeroth and part of 1st order

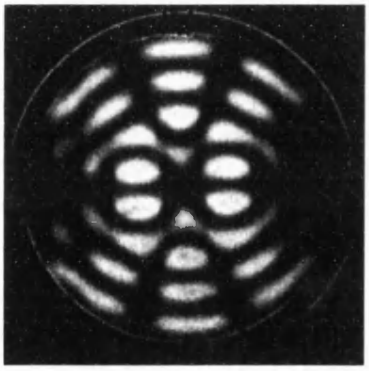

(c) Horizontal knife

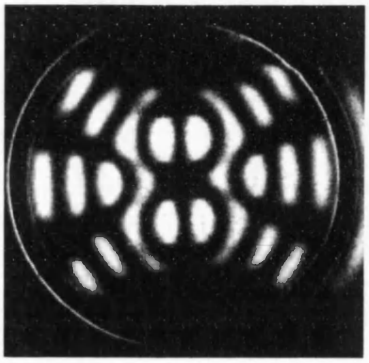

(d) Vertical knife

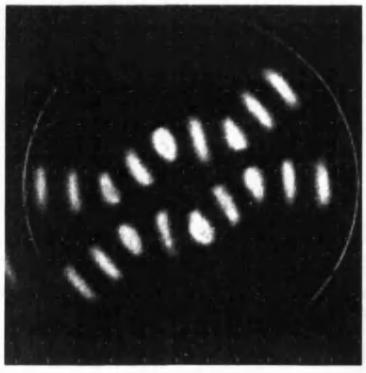

(e) Angled knife

Figure 3.10 Resonance modes of *non*-circular cylindrical cavities.

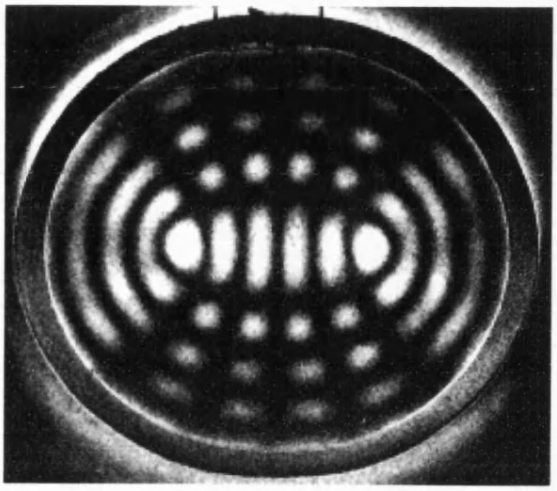

(a) Elliptical brass shell

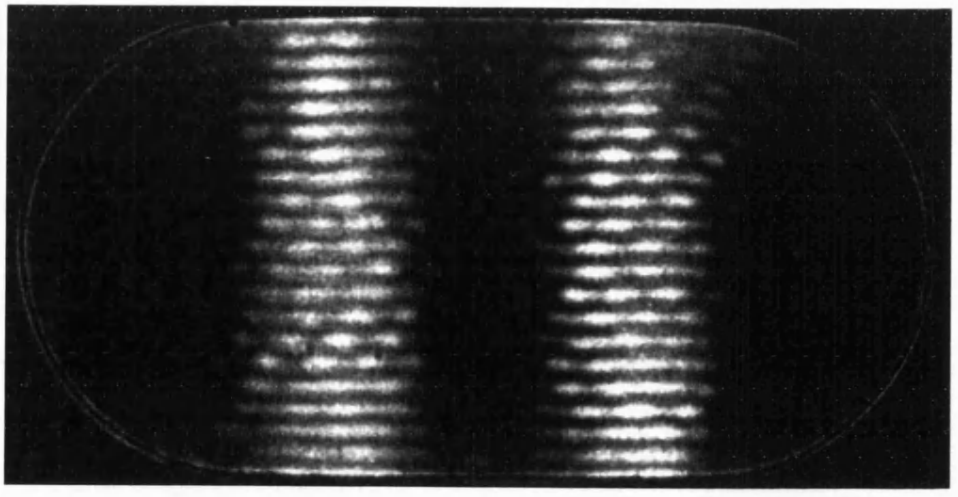

(b) Cavity with stadium shaped cross-section

Figure 3.11 High frequency resonance modes of the circular cylindrical shell.

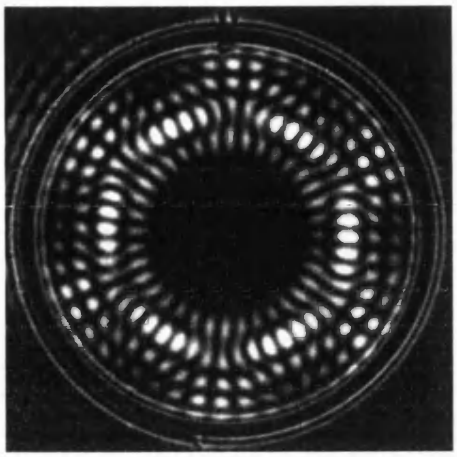

(a) 663.8 kHz

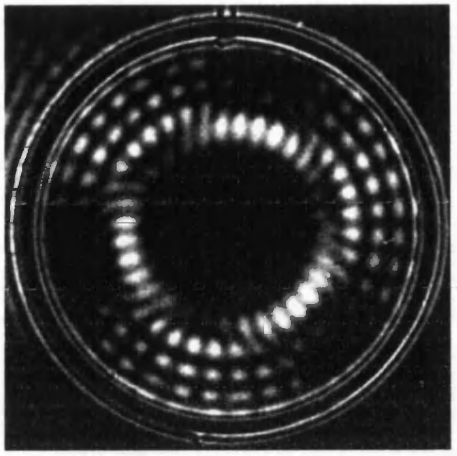

(b) 567.4 kHz

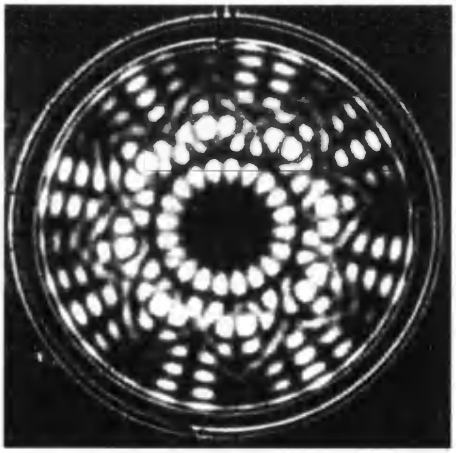

(c) 607.9 kHz

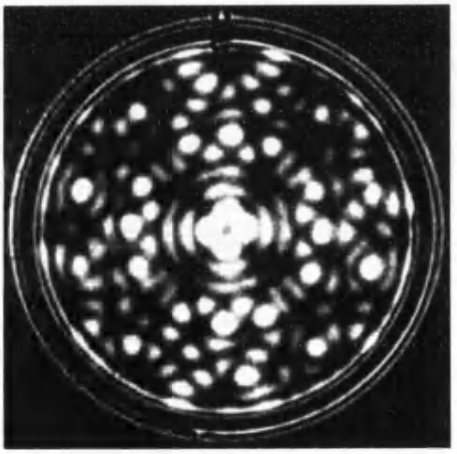

(d) 526.2 kHz

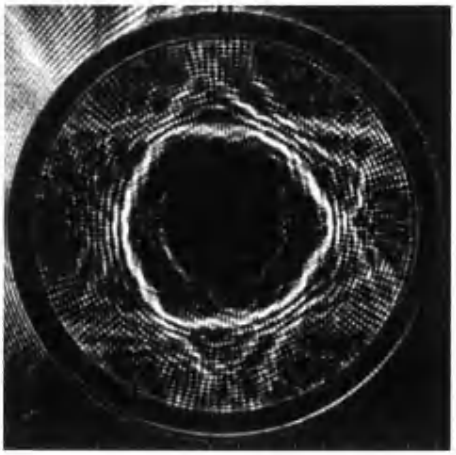

(e) 2.5 MHz

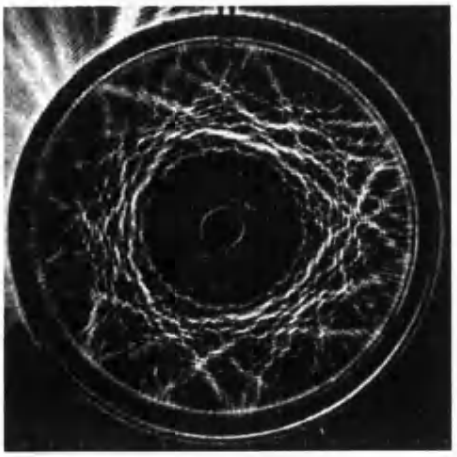

(f) 3.5 MHz

4 Parametric array facility

4.1 Introduction and review

This Chapter describes the parametric array facility used to make the backscattering and transmission loss measurements to be described in Chapters 5 and 6 respectively.

In underwater acoustics there is a need to make accurate, carefully controlled, laboratory measurements of the scattering behaviour and acoustic properties of objects in the underwater environment; both in order to validate theoretical predictions, and to investigate structures whose geometry or material properties are such that theoretical techniques cannot be used to model them. Such 'laboratory modelling' usually involves conducting experiments at ultrasonic frequencies with targets scaled down in size from those found in the marine environment itself.

Whilst high frequency ($> 300kHz$) transmission and reflection measurements are easily made in the laboratory using conventional source-receiver techniques, measurements at lower frequencies are more problematic, due to the broad beam of the conventional transducer, diffraction by the edges of finite test objects, and the difficulty in resolving the signals of interest from the reverberant field in the laboratory tank. An alternative approach that has been used with much success, and which is employed in the present study, is to use a parametric source.

Westervelt (1963) first proposed that the non-linear interaction of two *high* frequency waves could be used to generate a *low* frequency field in the region in which the waves interact. The discovery of this 'virtual source' followed from Westervelts earlier studies into scattering of sound by sound (Westervelt 1957) and marks the beginning of the application of non-linear acoustics in the underwater environment. The properties of this 'parametric acoustic array' were extensively investigated in the 1960's and 1970's (for a review see Bjørnø, 1975) and are now widely utilized in the underwater environment. The use of such a source was discussed by Berktay (1965) who proposed a transmitting technique, based upon the parametric array, and showed it to have the advantages of a broad-band signal, narrow beamwidth, and a pulse whose spectral

content could easily be controlled.

The proposed technique was further developed and employed by Humphrey (1981) and formed the basis of an experimental system and measurement technique that has been successfully used to measure the transmission and reflection properties of small panels (Humphrey 1985; Humphrey & Berktay, 1985) and the scattering properties of spheres (Humphrey, Murphy & Moustafa, 1987) and cylinders (Beckett & Humphrey, 1989b).

The non-planar nature of the parametric source was found to have significant implications for panel measurements, resulting in marked deviations from plane wave predictions (Humphrey & Berktay, 1985). This aspect is of particular importance in the current study involving transmission by plates, and is discussed in more detail in Chapter 6. In this Chapter we discuss the principle of the parametric array and describe the experimental system, the measurement technique, and the limitations of the system.

The experimental system used in the measurements described here is based upon that used by Beckett & Humphrey (1989b). The nature of the present study, involving scattering geometries of greater complexity than those studied in the past, has made certain improvements of the technique necessary. These include a higher degree of automation; permitting a sequence of measurements to be rapidly performed for different angles of incidence, and the use of a different modulating envelope for the pulse applied to the transducer. The latter enables scattering measurements to be made over a wider frequency range, without the need to repeat measurements using modulating envelopes of different length.

4.2 Experimental facility

In this section we discuss the basic operation of the parametric array and describe the experimental system as it is used in the current study.

4.2.1 Principle of a parametric array

The principle upon which the parametric array operates is the non-linear interaction of high amplitude waves to produce signals of different frequencies. A conventional piezo-electric transducer emits high amplitude, high frequency waves which propagate nonlinearly in the water and interact with each other to produce a signal containing additional frequency components to those of the 'primary' wave. If the primary wave contains high frequency components that are close together, then low frequency components are generated at the difference frequency (between primary wave components). This non-linear generation is a continuous process and the low frequency components are considered to come from secondary sources distributed throughout the whole interaction region insonified by the primary waves.

The simplest application of the technique involves the propagation of just two high frequency waves, the interaction between them producing a single low frequency component at the difference frequency. Components are also produced at the sum frequency, but these are of no importance. The two primary waves can be generated by two separate transducers, or by the same source. The distributed nature of the secondary sources, and the phasing between them, produces a behaviour similar to that of an end-fire array, resulting in an exceptionally narrow beam.

A more useful mode of operation is realized by applying an amplitude modulated *pulse* to the driving transducer. Such a pulse contains a broad spectrum of primary waves which interact to produce a broad-band low frequency pulse proportional to the second time derivative of the square of the modulating envelope. The resulting pulse has a spectrum which can easily be altered by adjusting the length and shape of the modulating envelope. This allows an extended frequency range to be covered with a single transducer.

The low frequency component generated in this way is not confined to the interaction region (in which it is generated) but continues to propagate. Thus by truncating the array with an acoustic filter a source free region is obtained in which measurements can be made.

4.2.2 Tank facility

The tank facility is shown in Figure 4.1. A large water-filled tank (approximately $2.5m \times 1.25m \times 1.5m$) contains the source transducer (resonant at approximately $930kHz$), the receiving hydrophone (B&K 8103), the acoustic filter, and the test object. Test objects are suspended from a rotation stage which is used, under computer control, to alter the angle that the object makes with the acoustic beam of the parametric array. The horizontal and vertical positions of the hydrophone, test object, and acoustic filter can all be varied manually. In all experiments discussed here the parametric array was truncated by an acoustic filter to terminate the non-linear generation of low frequency waves, and prevent the high frequency field from reaching the test object and hydrophone.

4.2.3 System electronics

The system electronics (Figure 4.2) can be divided into three parts; those associated with the signal applied to the transducer, those associated with the signal received by the hydrophone, and the components used to control the transmission and reception of these signals and the movement of the test object.

A continuous primary wave, typically $930kHz$, is generated by an oscillator and fed into a modulator where it is amplitude modulated by the 'envelope' function produced by a wave-form generator (Phillips PM5133). The exact form of this modulating envelope is described in detail in section 4.3. The amplitude modulated pulse is passed, via a buffer amplifier and attenuator, to the power amplifier, and then, via a matching transformer, to the transmitting transducer. The non-linear propagation of the modulated signal generates a low frequency pulse whose spectral content depends critically upon the length and shape of the modulating envelope.

The signal detected by the hydrophone is passed through a low pass ($250kHz$) filter before being amplified by a signal amplifier (Brookdeal 9452) and digitized by an Analogic Data 6000 signal processor. Typically between $0.25 - 1ms$ of signal was sampled at a $1\mu s$ sampling rate. The Data 6000 averaged 256 incoming signals and performed

further processing under computer control. The pulse repetition frequency of $20Hz$ was controlled by a pulse generator triggering the wave-form generator. The same trigger pulse was used to trigger the Data 6000 and oscilloscopes.

4.3 Pulse shape

Berktay (1965) showed that a short, amplitude modulated, pulse launched into the water will propagate non-linearly and produce a low frequency component proportional to the second time derivative of the square of the modulating envelope. In this paper Berktay presented predictions of the pulse resulting from the use of a Gaussian modulating envelope.

Previous applications of the parametric array have typically used a raised cosine bell as the modulating envelope (Humphrey, 1985). This is a single cycle of a cosine wave, phase shifted to produce a 'bell' shape envelope, similar in form to the Gaussian. Although the pulse produced by this method has a reasonably broad frequency spectrum, several measurements based upon envelopes of different length are often required to cover the frequency range of interest, particularly if *low* frequency ($< 30kHz$) measurements are to be obtained. Although the raised cosine bell is particularly simple to generate, many other envelope shapes can be considered. A raised triangular bell was used by Humphrey (1983), and found to result in a demodulated pulse whose spectrum was remarkably flat in frequency, although spectral levels at low frequency were a little lower than those observed with the cosine bell.

With a view to extending the frequency range over which a single measurement can be made, a study was undertaken by the author into the effects of modulating the carrier wave with envelopes having different shapes. Envelope functions were generated numerically using different mathematical functions, differentiated and Fourier transformed to obtain the spectra of the resulting pulse. Envelope shapes that looked promising were converted to binary form and downloaded onto a rewritable eprom that could then be used in a simple envelope generator built in-house[1]. The output from this

1 Designed and built by V. F. Humphrey & C. Cooper.

device was then used to modulate the carrier frequency in the experimental system. Signals were recorded and processed on the Data 6000 and their spectral content analysed. Of the envelope functions investigated in this way, smooth single cycle asymmetrical functions were found to produce the best results. Although this purpose built envelope generator was useful for investigating the effect of envelope shape upon the low frequency signal in the more realistic context of the experimental system, the output of the device was not stable enough to allow it to be used routinely in acoustic measurements. For detailed measurements, it was replaced with a conventional function generator (Phillips PM5133).

The modulating envelope used in the present study was an *asymmetrical* raised cosine bell, obtained on the Phillips generator by adding a dc offset to a single cycle, phase shifted, cosine wave; and then increasing the 'duty cycle' from 50% to approximately 90%. Experimentally obtained examples of the modulating envelope and demodulated pulse are shown in Figure 4.3, along with examples of the conventional symmetrical envelope. The corresponding spectra of these signals are shown in Figure 4.4. It can be seen that the asymmetrical envelope combines the best features of both the low and the high frequency symmetrical pulses. In the experiments performed so far with this pulse, the useful frequency range has been found to be several times that obtained with a pulse based upon the conventional raised cosine bell envelope. The main advantage is gained at the low frequency end of the spectrum: a higher frequency cosine bell produces a wider frequency range, but does not extend to the low frequencies.

This technique enables measurements to be obtained over a much wider frequency range in a single experiment. A theoretical investigation into the 'optimal' envelope function can be envisaged, although this would need to take into account the receiving system too: restrictions imposed by the response of the acoustic filter, and the sensitivity of the hydrophone, ultimately limit the high frequency behaviour of the system, irrespective of the type of envelope used to modulate the carrier wave.

4.4 Measurement technique

With the experimental system described above, accurate measurements can be made over a wide range of frequencies. In the present study this experimental system has been used to measure both the signal backscattered by cylindrical targets (Chapter 5) and the signals transmitted by panels (Chapter 6). In this section we describe elements of the experimental technique relevant to these measurements.

4.4.1 Processing and automation

The signals received by the Data 6000 are transferred to the computer via the GPIB interface bus for storage and further processing. The Data 6000 can be operated via front panel controls (for one-off measurements), or remotely - under computer control - when many consecutive measurements are being made. The rotational position of the test object can also be controlled remotely with the rotation stage being driven by a Digiplan stepping motor control unit connected to the same GPIB bus. Fortran programs were written to control both the operation of the Data 6000 and the stepping motor, via the GPIB interface. When a sequence of measurements is being made the operation of the entire system is automated in this way, with either the processing being performed on the Data 6000 or averaged time signals being transferred to the computer for later processing in a UNIX environment.

The averaged signals captured by the Data 6000 were windowed to remove unwanted multiples, and Fourier transformed to obtain their spectra. For both transmission loss and backscattering measurements the resulting spectra were divided by a 'reference' signal, obtained without the test object in position. Further details concerning the calculation of the form function (of cylindrical objects) and transmission loss (of panels) are given in sections 5.2.6 and 6.4.3 respectively.

With this experimental arrangement, a series of 50 consecutive measurements could typically be made on a test object in approximately 30 minutes, the object being rotated one or two degrees between each measurement. Reference signals were measured both before and after a sequence of measurements. In this way the two ref-

erence signals could be compared and any change in the pulse over the time taken to perform the experiment determined. The two factors limiting the time taken by each measurement were: the averaging speed of the Data 6000, and the time allowed between measurements for the mechanical arrangement to settle down - large panels in particular had a tendency to sway around after they had been rotated by the stepper motor. In these experiments 15 seconds was allowed. The averaging speed of the Data 6000 was increased substantially by turning the front panel display off during the averaging process. The time taken to process the averaged wave-forms was less than the allowed 'settling' time and therefore not significant.

A few experimental procedures and factors concerning the accuracy and interpretation of the results will now be discussed.

4.4.2 Support and location of components in the tank

For flat panels a simple connecting frame was rigidly fixed to the axis of the rotation stage and clamped to the edges of the test panel. Cylindrical objects were suspended from the rotation axis by nylon thread. The rotation axis could be adjusted to enable the vertical position of the samples to be easily varied. In this way the object could be suspended accurately such that its centre was on the acoustic axis. The distance of the whole supporting assembly from the transducer was chosen such that the objects could be rotated to the highest angle required without fouling on the acoustic filter.

The hydrophone was mounted in a hollow steel tube and fixed to an optical bench spanning the tank lengthways above the acoustic axis. In this way the distance between hydrophone and transducer could easily be varied. For panel measurements, a position was chosen close enough to the panel to prevent diffracted signals from the panel edges from reaching the hydrophone, yet far enough that multiples between the panel and the hydrophone were not problematic. For cylindrical targets the hydrophone was typically placed $25cm$ from the cylinder centre, a distance which is a close enough approximation to the far-field[1] and yet near enough that the signals reflected from the cylinder have a

1 For cylinders of the dimensions used here.

reasonable amplitude.

The stability and accuracy of this arrangement - and therefore the reproducibility of results - is limited mainly by the overhead fixings, and their necessarily large distance from the acoustic beam. Errors in the three angular orientations of the test objects are less than one degree and remain fixed throughout the course of a single experiment. The error in the (changing) orientation of a test object as it is rotated, is extremely small.

4.4.3 Array length and the angular spectrum of waves

The parametric array is truncated by the acoustic filter in order to isolate a source free region in the tank in which measurements can be made without problems associated with the non-linear response of the hydrophone (Moffet & Blue, 1980; Humphrey & Hsu, 1980) and the interaction of the primary waves with the target object itself.

The truncation length of the array, and the range at which the hydrophone is placed, both affect the angular spectrum of low frequency waves generated and received by the hydrophone. The non-planar nature of the beam precludes the existence of very narrow features in the angular response of a target, making measurement at sub-degree intervals unnecessary.

Also, beyond the acoustic filter the beam begins to spread - as it would from a conventional source - and so test objects must be placed reasonably close to the filter if the benefits of the narrow beam are to be utilized. Care must be taken, however, to avoid multiple reflections between components of the system. The location of the acoustic filter with respect to both the source transducer and the receiver is therefore of considerable importance.

4.5 Limitations and sources of error

The limitations of the experimental system and measurement technique are now briefly described, and the sources of some potential errors discussed.

By changing the modulation (envelope) frequency, the system can be used to make measurements down to $5kHz$, and up to approximately $250kHz$. The lower limit is

determined principally by the size of the water tank, the beam-width of the truncated parametric source and, in the case of panel measurements, the size of the panel. The hydrophone sensitivity and the attenuation of the acoustic filter are responsible for the upper frequency limit. Measurements can be made above $250kHz$, but signal levels are rather small.

For transmission loss measurements involving small test panels, the diffraction of low frequency fields by the panel edges is problematic; particularly when panels are rotated with respect to the incident beam. As the cross-sectional area decreases, it becomes harder to window out the edge diffracted pulse. The use of large area hydrophones (Humphrey, Simmonds & Green, 1994) for making transmission measurements was therefore investigated. Such receivers have good directionality and so avoid problems associated with waves diffracted by the edges of the panel. Unfortunately the hydrophones currently under development have a response that falls off at a lower frequency than the B&K hydrophone, and so does not permit measurements to be made at the higher frequencies of interest in this study. This kind of receiver does, however, look to be of great value for panel measurements involving small samples, and is expected to find application in this system in the near future.

The main limitation of the system as currently configured is the accuracy with which objects can be positioned (and orientated). The reproducibility of measurements is also largely limited by this factor. Also, the tendency of the test object to move around after rotation necessitates a pause in the measurement, which prolongs a sequence of experiments in time, leaving them open to other random and systematic errors.

In backscattering and reflection measurements the receiving hydrophone must be placed in the path of the incident beam and does therefore interfere with the field. This is obviously not a problem in the transmission loss measurements, but does affect measurements involving the cylindrical shells. A detailed discussion of this problem is given by Beckett (1992).

The signal detected by the hydrophone was found to change slightly with time. This 'drift' is thought to originate in the transmitting electronics and was found to be

more pronounced when the system was first powered up. It was overcome by allowing the whole system several hours to warm up before measurements were taken. With this precaution taken, the errors in transmission or reflection measurements over a 30 minute period are less than $0.1dB$ throughout the frequency range of interest. The origin of this drift is unknown, but the power amplifier and function generator can both be suspected; any change in the amplitude of the modulating envelope will change the spectra of the demodulated pulse, introducing errors into measurements made with respect to reference signals made some time later (or earlier) than the measurement itself.

4.6 Summary

The experimental system incorporating a parametric array has been described, and some of the details concerning the measurement technique have been discussed. The automation of a sequence of measurements permits investigations to be performed over a range of incident angles easily, and rapidly. The use of an asymmetrical modulating envelope results in a broad-band pulse, permitting measurements to be made over an extended range of frequencies in a single experiment. This obviates the need to perform several experiments, using different pulses.

The use of this system for making backscattering measurements involving cylindrical shells is described in Chapter 5, and in transmission loss measurements of anisotropic panels in Chapter 6.

Figure 4.1 Experimental system incorporating the parametric array.

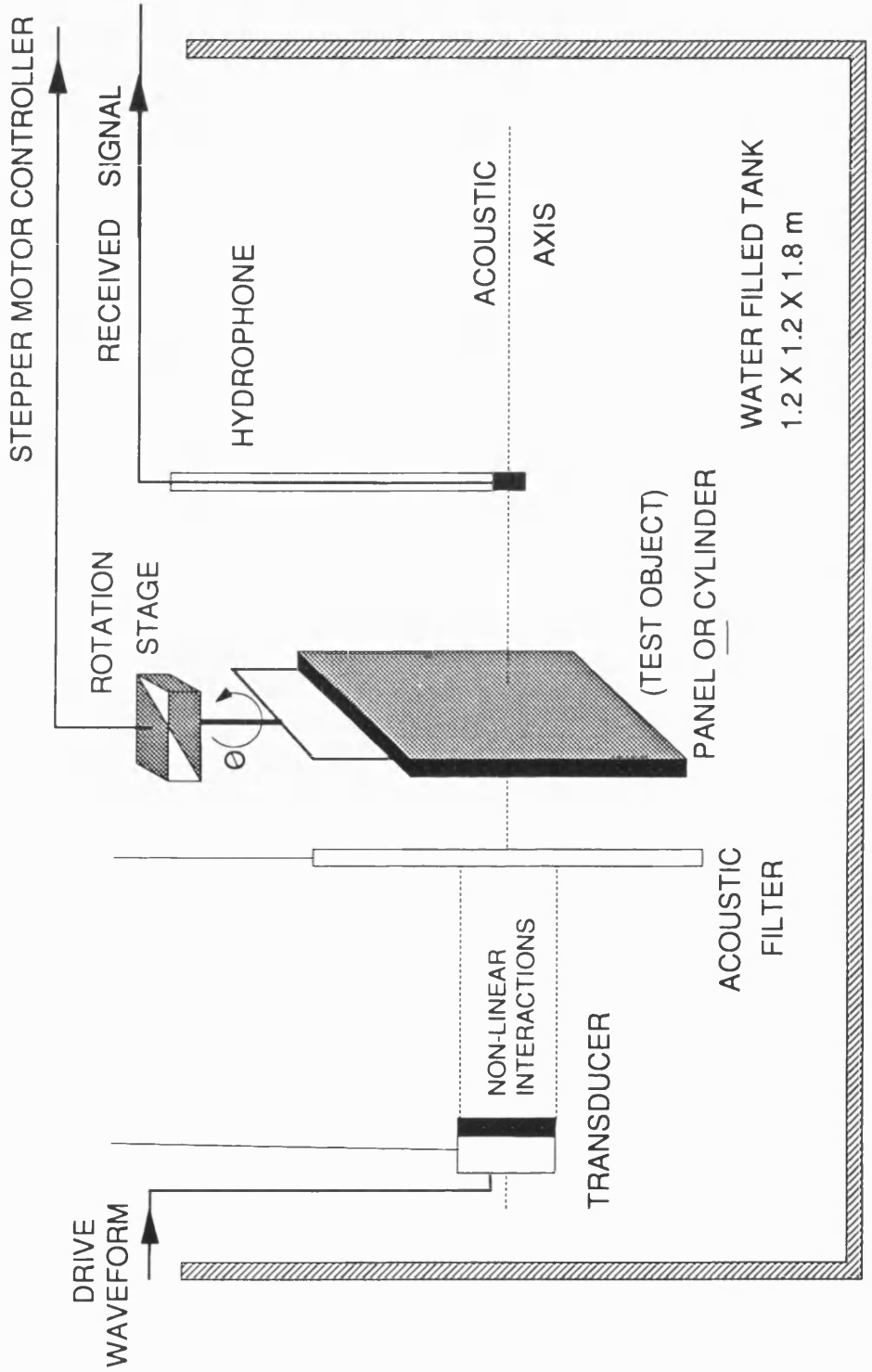

Figure 4.2 System electronics: generation of the parametric array, reception and processing of received signals and the automation of measurements.

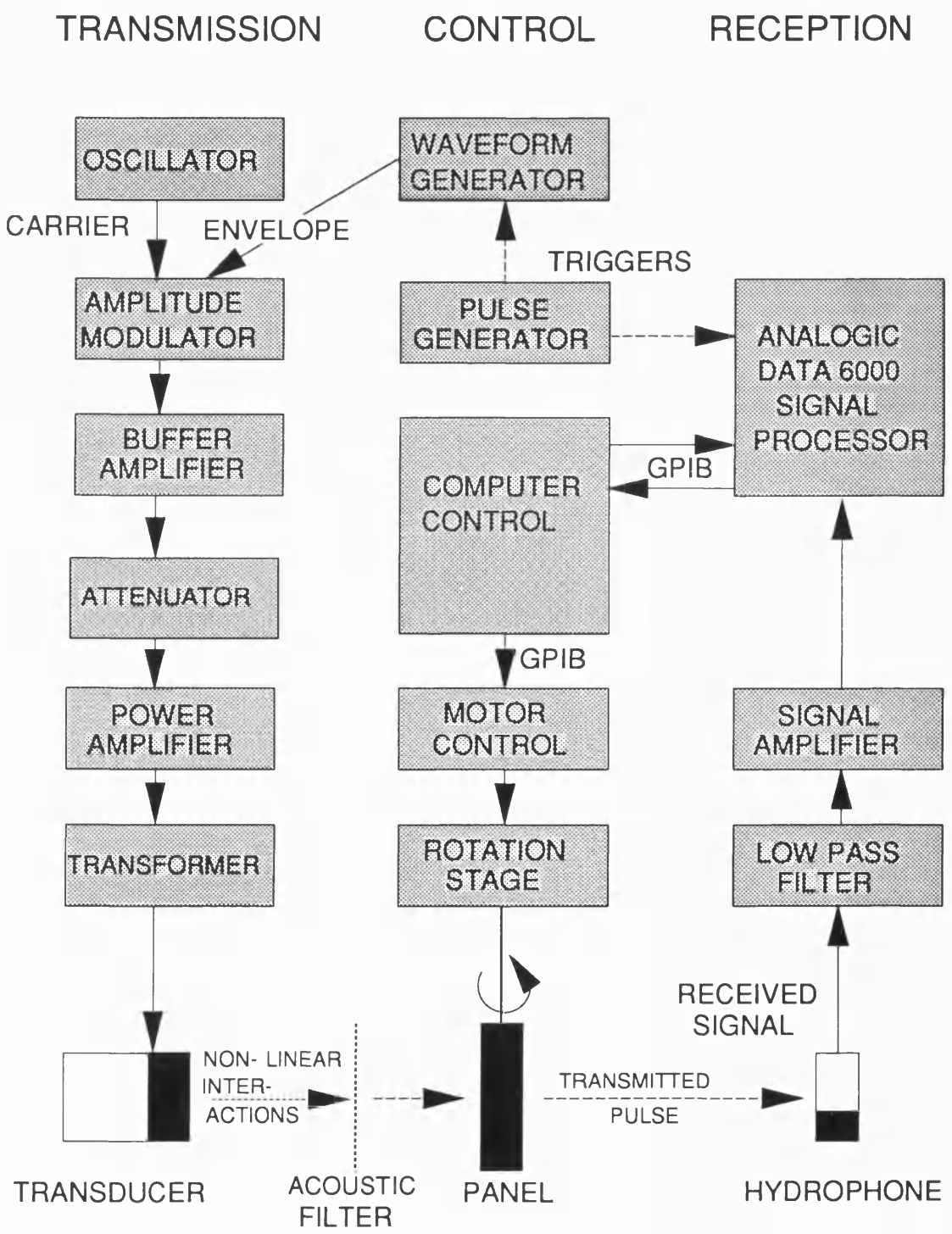

Figure 4.3 Examples of envelope shapes (above) and low frequency demodulated pulses (below) after passage through the receiving system. The asymmetrical envelope and its resultant pulse are shown in the centre, low and high frequency symmetrical pulses are shown to the left and right. The spectra are given in Figure 4.4.

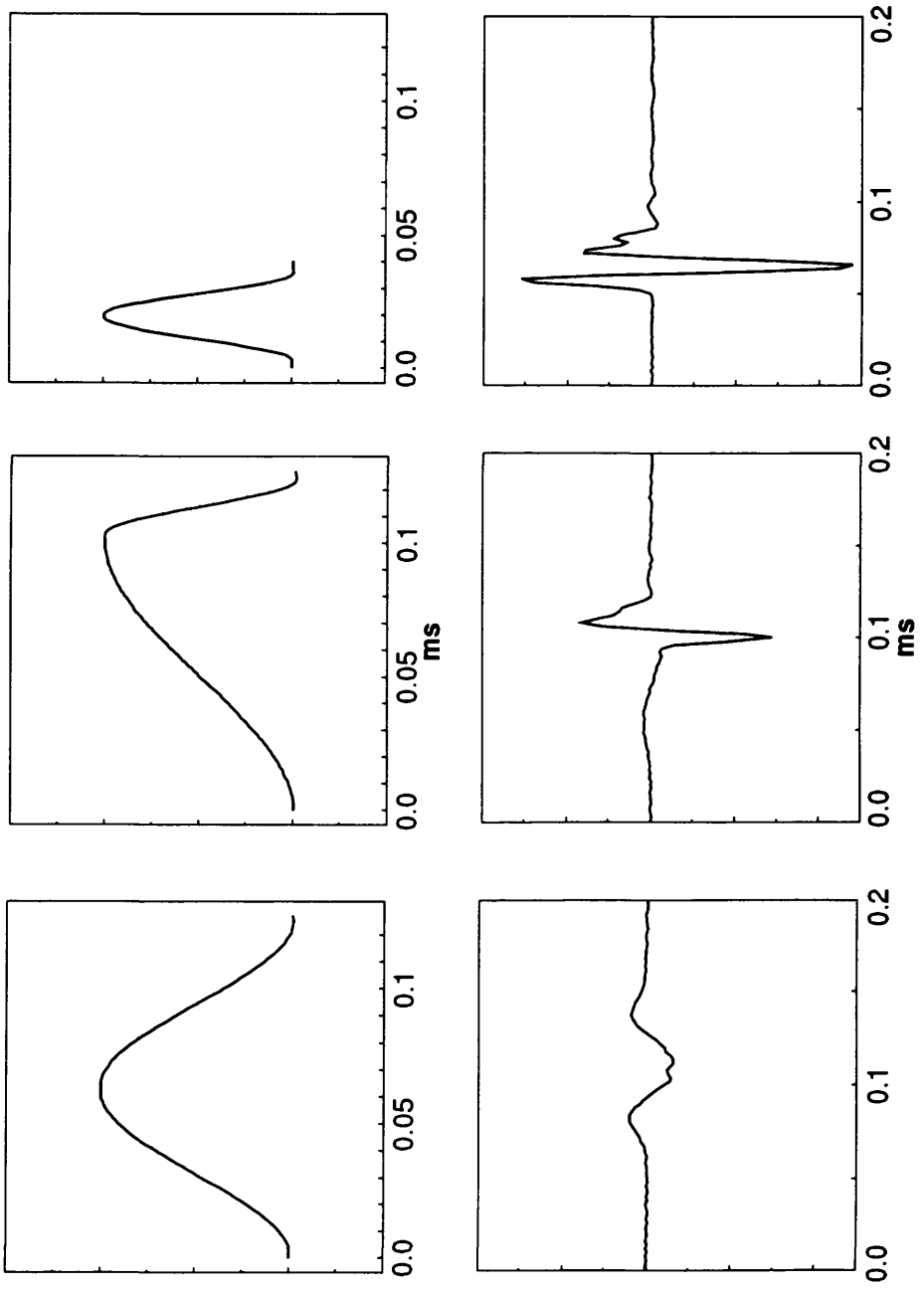

Figure 4.4 Normalized spectra of the demodulated pulses for the different envelopes shown in Figure 4.3.

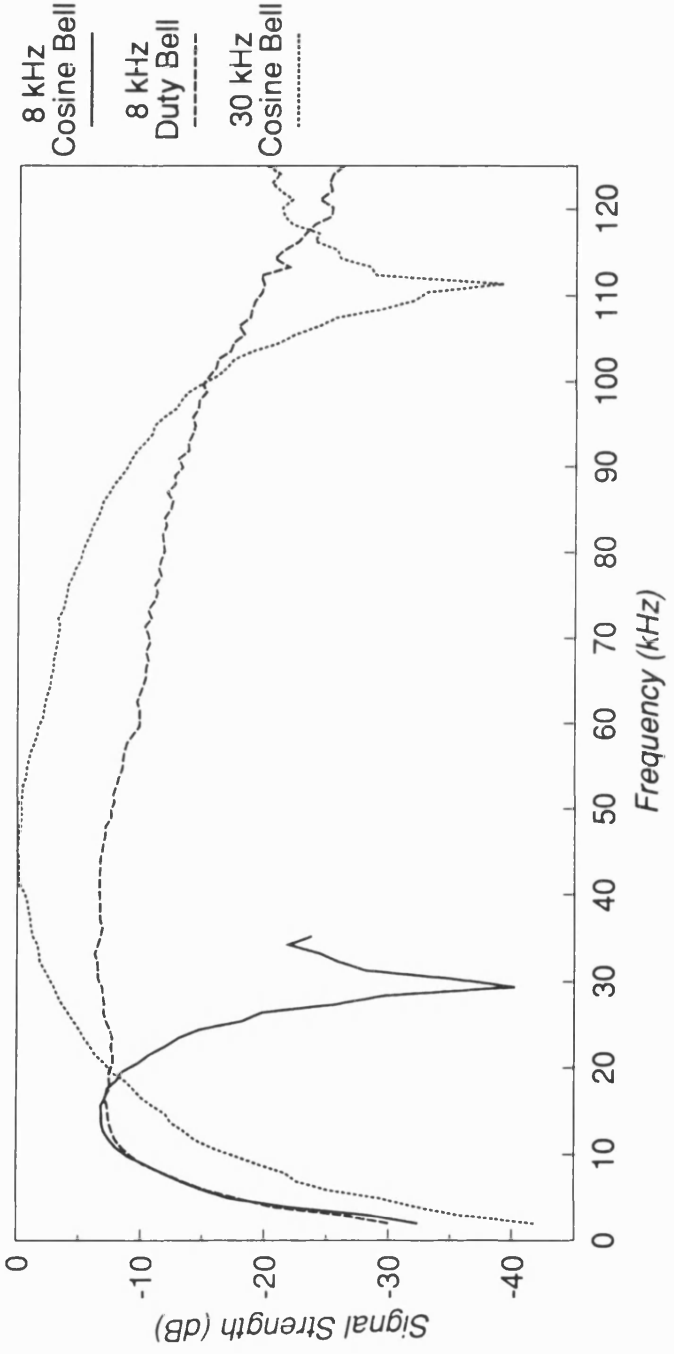

5 Cylindrical shells

5.1 Introduction and review

In this chapter experimental and theoretical studies of the backscattering and resonance behaviour of flooded cylindrical shells of circular and non-circular cross-section are presented. We are interested in the variation of the acoustic behaviour as the symmetry of the circular cylinder is broken by deforming it into the more general *elliptical* cylinder. The experimental study consisted of two parts. The resonance behaviour was investigated experimentally using the Schlieren technique described in Chapter 3, while the backscattering characteristics were investigated using the parametric array facility discussed in Chapter 4. This chapter brings these experimental techniques together and attempts to show how they complement each other in the investigation of resonance scattering by objects of regular or more complex geometry or material composition. The studies described here are a natural development of earlier work done at the University of Bath.

Considerable work has been performed on the scattering of waves from solid cylinders and cylindrical shells, but most of it has concentrated on the special case where the cylinders have circular cross-section. Theoretical models involving scattering by cylinders and shells of circular cross-section have commonly involved the Normal Mode Series expansion described in Chapter 2, although other techniques have been developed with a view to studying scattering by more complex structures. The vast body of work concerning scattering and resonance behaviour of such simple objects has recently been reviewed by Veksler (1993) and has been summarized in review articles by Flax, Gaunaurd & Überall (1981) and Gaunaurd (1989). Most of the early work involving cylindrical structures of circular cross-section concerned itself with the scattered field; the resonance behaviour itself received comparatively limited attention, until the Resonance Scattering Theory was introduced by Flax, Dragonette & Überall in 1978. The importance of the target resonances is now well established, and experimental techniques have been developed to isolate and identify resonances by analysing the

scattered field; see for example Tsui, Reid & Gaunaurd (1986) and Maze & Ripoche (1983).

The use of a parametric source for measuring the backscattering properties of discrete objects was described by Humphrey, Murphy & Moustafa (1987) and has been used to measure the scattering by a *solid* aluminium cylinder at normal and oblique incidence (Beckett & Humphrey, 1989b; Humphrey & Beckett, 1990). Results for both air filled and water filled steel *shells* were recently presented by Humphrey & Beckett (1994).

Comparatively little attention has been given to the more general case of the elliptical cylindrical geometries. The generalization of the Normal Mode Series approach to elliptical geometries involves the use of series of *Mathieu* functions, instead of the series of Bessel functions involved in the circular geometry, and is considerably more complex. Much of the early work involving scattering by infinite (two-dimensional) elliptical cylinders is described in Bowman, Senior & Uslenghi (1987) and references therein. Elliptical cylinders were considered by Burke (1964) who applied the Mathieu function solution to penetrable and inpenetrable elliptical cylinders and gave low frequency approximations. The Mathieu function approach was also used by Harumi (1961) who studied scattering by a ribbon. Goel & Jain (1981) consider the penetrable elliptical cylinder using a Greens function approach.

Whilst the Normal Mode Series approach is adequate for calculating the acoustics of structures having simple geometry, such as the circular cylindrical shell, it is of little use in the study of more complex geometries and other theoretical techniques must be employed. One such technique that has been applied to scattering problems involving elliptical cylindrical structures is the T-matrix approach (Varadan & Varadan, 1980). Simon & Radlinski (1982) investigated elastic wave scattering by an elliptical cylindrical shell by combining the T-matrix method with thin shell theory. Radlinski & Simon (1993) modified the previous formalism and applied it to cylindrical shells of arbitrary shape. Plastic, steel, and iron shells were considered, and a significant

dependence upon incident angle[1] was shown. Baskar, Varadan & Varadan (1984) also applied the coupled thin shell - T-matrix method to the scattering of acoustic waves from a thin elliptical cylindrical shell in a fluid. Other methods for thin shells include that by Borovikov & Veksler (1985) who used the geometrical theory of diffraction to study scattering by elliptical shells.

Thicker elliptical shells were studied by Pillai et al (1983), again using T-matrix methods. Shells of arbitrary cross-section were considered, with examples for circular and elliptical tubes being presented and compared with experimental results. Rigid and elastic cylinders of elliptical cross-section were previously studied by Pillai, Varadan & Varadan (1982) and scattering by rigid cylindrical objects of various cross-section by Varadan, Varadan & Tsao (1982).

Much of the interest in the elliptical cylindrical shells is due to their use in compliant gratings. Burke & Twersky (1966) studied a grating of elliptical cylinders and Brigham, Libuha & Radlinski (1977) studied the scattering by planar arrays of elliptical shells.

Other theoretical approaches to *non*-circular cylindrical geometries have recently appeared. The elliptical geometry has been investigated by Stepanishen & Ramakrishna (1994) using internal source distribution and singular value decomposition methods. A new method involving conformal mappings is described by DiPerna & Stanton (1994) and deals with scattering by cylindrical objects of non-circular geometries, including the elliptical cylinder. This latter method, referred to as the Fourier matching method (FMM), claims to be much more efficient than the T-matrix approach.

Analogous to the perturbations in the shape of a circular cylinder are problems involving deformation of spherical objects, and much can be learnt from the literature on scattering by spheroids and axisymmetric shells. Of particular interest is Werby et al (1990) and references therein, who discuss the resonances of elastic spheroids and the level crossing phenomena. James (1993) and Skelton (1993) present models for pre-

1 In the plane normal to the cylinder axis.

dicting the acoustics of axisymmetric structures made of composite materials.

Most of the literature described so far is concerned with the acoustics of evacuated, or air filled, shells, where the principal mechanisms contributing to the scattering behaviour are the propagation of surface waves around the cylinder perimeter, and vibrations of the elastic shell. The cylindrical shells described in this thesis are water filled, and so the possibility of fluid column resonances must be considered. Maze, Izbicki & Ripoche (1986) experimentally identified several kinds of resonance associated with the circular cylindrical shell. The majority of the resonances were modes of the fluid column. The resonances of the fluid column within cylindrical structures has not received as much attention as the external (scattering) problem. The use of a Schlieren technique for visualizing the interaction of acoustic waves with cylindrical objects was described by Knapp & Humphrey (1989) and Humphrey, Knapp & Beckett (1990). The use of this technique to identify several classes of resonance of the fluid filled circular cylindrical shell by examining the *interior* fluid was described by Humphrey, Knapp & Beckett (1991). Prior to this work the Schlieren technique had rarely been used to study the acoustic resonances of fluid filled cylindrical shells, although the visualization of elastic resonances of transparent solid cylinders had been achieved; see for example Dardy et al (1987) and Sittig & Coquin (1970).

No experimental results concerning visualization of the fluid column resonances of elliptical cylindrical shells (or cavities) are known to the author, although the focusing of a shock wave in an elliptical cavity was observed using a Schlieren technique by Gustafsson (1987). The modes of non-circular fluid-filled boreholes were considered by Randall (1991) who presented contour plots of fluid pressure within elliptical boreholes. The resonance modes of cavities of complex geometry can also be investigated using perturbation techniques. A recent book by Trusler (1991) gives a good overview of the acoustics of closed systems, focusing on perturbations in the shapes of cavities, and the impedance of the boundary. Perturbation methods were used by Aldoshina & Olyushin (1992) to calculate the resonance frequencies of enclosures having complex geometry and impedance boundaries.

5.2 Circular cylindrical shells

Before discussing the deformed (elliptical) cylindrical shells we will present a study of the behaviour of the undeformed cylindrical shell (of circular cross-section). We shall look at both the resonance behaviour and the backscattering properties of the shell, introducing theoretical models for the fluid column resonances, and presenting back-scattering results.

5.2.1 Theory: Normal Mode Series

The Normal Mode Series solution has been widely used to study the acoustic behaviour of targets of separable geometry (Veksler, 1993). The essence of the method is to expand all acoustic and elastic wave-fields as harmonic series; in the circular geometry these series involve products of Bessel functions and circular functions (see for example equation 2.10). The boundary conditions at the inner and outer interfaces of the shell require the continuity of normal stress ($\mathcal{T}$) and displacement (U), and the vanishing of all tangential stresses:

$$\begin{aligned} U_r(a) &= U_{ex}(a), & U_r(b) &= U_{fl}(b), \\ \mathcal{T}_{rr}(a) &= P_{ex}(a), & \mathcal{T}_{rr}(b) &= P_{fl}(b), \\ \mathcal{T}_{r\phi}(a) &= 0, & \mathcal{T}_{r\phi}(b) &= 0. \end{aligned} \tag{5.1}$$

Here, a and b are the outer and inner radii of the cylindrical shell, subscripts ex and fl refer to the external and internal fluids respectively, and variables on the L.H.S. of each equation refer to the elastic shell. The displacements within the shell are found by first expressing the displacement vector in terms of scalar and vector potentials (see equation (2.2)), each potential satisfying Helmholtz' equation and being expanded in Normal Mode Series. Stress-displacement relations then allow the components of the stress tensor ($\mathcal{T}$) to be calculated, and the boundary conditions solved to find the unknown coefficients in the Normal Mode Series (2.10). If there is an incident plane wave (P_{in}) the pressure and displacement in the external fluid are written $P_{ex} = P_{in} + P_{sc}$, $U_{ex} = U_{in} + U_{sc}$ where

$$P_{in} = e^{i(\underline{k}\cdot\underline{r})} = P_o \sum_n \varepsilon_n i^n J_n(kr)\cos n\phi. \tag{5.2}$$

In this way, expressions are obtained for the pressure fields in the fluid column and external fluid, and from this the form function of the cylindrical shell can be computed.

5.2.2 Cavity resonances: rigid boundary approximation

The above theoretical formalism constitutes an *exact* solution for the scattering of a plane wave from a circular cylindrical shell insonified normally to its axis. From a resonance scattering point of view, all the resonance modes of this coupled elas-to-acoustic scatterer are allowed for and can potentially be identified in the form function or interior pressure field.

For the fluid column resonances, however, a simpler technique is expected to yield the locations of the resonance modes. As the impedance mismatch between water and the metallic shell is large, the inner interface can be approximated to a rigid boundary so that the normal components of particle velocity (V) vanish;

$$V_r(b) = \dot{U}_r(b) = \frac{i}{\omega\rho_f}\frac{\partial P_{fl}}{\partial r}\bigg|_{r=b} = 0. \tag{5.3}$$

Substituting the Normal Mode expansion for P_{fl} (2.10) into (5.3) yields

$$J'_n(kb) = 0,$$

and the roots ($k_{n,m}$) are the free vibrational modes (n,m) of the fluid column (with rigid boundary) and might be expected to be good approximations to the fluid column resonances of an insonified shell.

The locations of resonance modes associated with the vibration of the elastic shell, or Stoneley wave propagation, cannot be found in this manner. For these, the full Normal Mode Series solution must be employed.

5.2.3 Location of resonances, theory and experiment

The experimental method of locating and identifying resonances has been described in section 3.6. In this section we discuss the theoretical determination of the resonance frequencies and identification of the different modes.

As has been demonstrated, the resonances manifest themselves in both the scattered acoustic field, and in the field within the fluid column. By calculating the partial wave amplitudes in the Normal Mode Series expansion, different families of resonance modes can easily be identified. Subtraction of an appropriate 'background' term, such as that of a rigid cylinder, makes identification even easier.

The Resonance Scattering Theory predicts that little energy penetrates the elastic shell, except at frequencies corresponding to a resonance of the structure. This is obviously particularly true of the fluid column resonances. Therefore, calculating or measuring the variation of pressure inside the fluid column gives another good indication of where the resonances lie, and what their widths are. This technique was discussed in section 3.6 where it was described how the Schlieren system can be used to obtain the spectra of resonances.

The locations of the cavity resonances can also be predicted using the rigid boundary approximation described in the previous section.

A comparison of these three theoretical approaches with the experimental technique has been given in Knapp & Beckett (1989) for a brass shell ($b/a = 0.87$). It was shown that predictions of resonance frequency made by examining the partial-wave form function amplitudes, and interior pressure distributions, were in good agreement with each other, and with experimental measurements made using Schlieren. The zeros of $J'_n(kb) = 0$ were also given and found to be, in general, slightly lower, revealing the extent to which the shell's finite impedance influences the resonance frequencies of the fluid column.

In the present study it was decided to investigate this aspect in greater depth. For

more complex targets, such as the deformed shell to be discussed later, full analytical solutions to the scattering problem are not easily obtained. Good approximations are therefore of great value.

5.2.4 Cavity resonances: impedance boundary

In an attempt to improve the agreement with experiment, a theory that predicts the resonance frequencies and accounts for the finite impedance of the shell is derived.

5.2.4.1 Theory

We consider the fluid loaded elastic shell to present a mechanical input impedance (Z_{inp}) to the acoustic fluid within the fluid column. At the inner interface (b), the boundary conditions require that the radiation impedance on the surface is equal to the input impedance of the shell. The radiation impedance in the fluid is P_{fl}/V_r where V_r is given by equation (5.3). The boundary conditions ($P_{fl}/V_r = Z_{inp}$) reduce to

$$Z_{inp}\left.\frac{\partial P_{fl}}{\partial r}\right|_b + i\omega\rho_f P_{fl}(b) = 0. \tag{5.4}$$

Using the Normal Mode Series expansion for P_{fl} (2.10) we obtain

$$J'_n(kb) + i\frac{\rho_f c_f}{Z_{inp}} J_n(kb) = 0 \tag{5.5}$$

having a series of roots $k_{n,m}$ which are the free modes (no incident field) of the fluid column, subject to finite impedance boundary conditions.

The exact mechanical impedance of the circular shell (Z_{inp}) can, of course, be derived from the formalism of section 5.2.1, but we here consider two approximations that will be employed later, and which result in greatly simplified expressions.

In the first case we approximate Z_{inp} to the normal input impedance of a planar

layer with a fluid half-space backing. In this case the layer is characterized only by its density, its compressional wave velocity, and its thickness. The derivation is well known (Brekhovskikh, 1980) and will not be repeated here. The resulting expression for Z_{inp} is

$$Z_{inp} = Z_L \frac{Z_w + iZ_L \tan(k_l d)}{Z_L + iZ_w \tan(k_l d)}, \tag{5.6}$$

where $Z_L = \rho c_l$ is the impedance of the layer material, $Z_w = \rho_f c_f$ is the contribution from the loading fluid half-space, k_l is the wave number in the layer and d is the layer thickness $(a-b)$.

In the second case we approximate the fluid loaded elastic shell to a fluid loaded fluid shell of circular cross-section, and the input impedance to the normal impedance of such a shell. The resulting expression is;

$$Z_{inp} = -iZ_L \frac{iZ_L[Y_n(k_l a)J_n(k_l b) - J_n(k_l a)Y_n(k_l b)] + Z_w[J_n(k_l b)Y'_n(k_l a) - Y_n(k_l b)J'_n(k_l a)]}{iZ_L[Y_n(k_l a)J'_n(k_l b) - J_n(k_l a)Y'_n(k_l b)] + Z_w[J'_n(k_l b)Y'_n(k_l a) - Y'_n(k_l b)J'_n(k_l a)]} \tag{5.7}$$

where the impedance of the external fluid (Z_w) is now derived from the expression for the 'scattered' field (P_{sc}, see equation 2.10);

$$Z_w = \left.\frac{P_{sc}}{V_r}\right|_{r=a} = -i\rho_f c_f \frac{H_n(ka)}{H'_n(ka)}. \tag{5.8}$$

It has been found that, in the limit whereby $ka \sim kb$ are sufficiently large that asymptotic expansions for J_n, Y_n and H_n are valid, the expression (5.7) reduces to that given above for a planar layer (5.6). The use of either of these impedances in the expression (5.5) yields an equation whose solutions are expected to better approximate the resonance frequencies of the fluid column than the roots of $j'_n(kb) = 0$ do.

5.2.4.2 Results

In order to test the validity of this model for the fluid column resonances, the brass shell previously investigated in Knapp & Beckett (1989) was studied, and the results are presented here in Table 5.1. The shell has an inner radius (b) of 8.25mm, an outer radius (a) of 9.50mm, and an inner to outer radius ratio (b/a) of 0.87. The experimental results are given in the second column, and theoretical predictions, made by examining the computed pressure distribution in the fluid column and in the far field form function, are given in the third and fourth columns. The fifth and sixth columns give results for the free vibrations of the fluid column with both infinite and finite impedance boundary conditions. The calculations involving the finite impedance boundary used the input impedance of a planar layer (5.6).

	Experiment	Plane Wave Theory		Free Vibrations	
Mode /kb	Schlieren	Pressure Distribution	Form Function	Rigid Boundary	Impedance Boundary
(2,2)	6.89	6.864	6.86	6.706	6.825
(2,3)	10.04	10.049	10.06	9.969	10.043
(2,4)	13.21	13.223	13.20	13.170	13.221
(3,2)	8.24	8.192	8.20	8.015	8.119
(3,3)	11.41	11.418	11.42	11.346	11.411
(3,4)	14.62	14.633	14.63	14.586	14.631
(4,2)	9.28	9.195	9.20	9.282	9.376
(4,3)	12.74	12.750	12.74	12.682	12.740
(4,4)	16.00	16.006	16.00	15.964	16.004

Table 5.1 Fluid column resonances of a brass cylindrical shell ($b/a = 0.87$) showing kb values determined experimentally and compared with different theoretical models. (Experimental data and plane wave results taken from Knapp & Beckett (1989).)

The results obtained using the finite impedance boundary model are seen to be in good agreement with the experimental results, and a significant improvement upon the rigid boundary approximation. There is an exception, however, in the case of the (4,2) mode, where the agreement is not so good. It has been noted (Knapp & Beckett, 1989) that agreement between theory and experiment is noticeably poorer for *all* the (n,2) modes; the reasons for this are unknown. The failure of the finite impedance model to provide significant improvement over the rigid boundary approximation in the (4,2) case, suggests that something other than the impedance of the shell may be an important factor in this case. It is possible that other (perhaps broader) resonance modes may be interfering with the fluid column mode, making identification of the resonance frequency more difficult.

5.2.5 Fluid column resonances of a brass cylindrical shell

Having established the validity of these theoretical techniques and discussed the experimental procedure for locating the resonances, we proceed to discuss the resonance behaviour and scattering behaviour of the circular brass cylindrical shell that has been used in the deformation study to be described later. This shell has radii of $14.25mm$ and $15.85mm$, giving a radii ratio (b/a) of 0.90 - slightly thinner than the shell discussed in the previous section. The sample used in the experimental measurements had a length of $100mm$.

Using the technique described in Chapter 3, the fluid column resonances of the brass shell lying in a limited frequency band were located. The frequency band stretches from the (3,3) mode to the (3,4) mode, representing an interval in which we expect to find a single representative of each order n (for low n). The results are given in Table 5.2. The temperature in the tank was 17°, corresponding to a velocity of $1473ms^{-1}$ in water.

Only the $n = 6$ mode (6,2) is absent from this data. There was some evidence for the existence of this mode, but it is thought to lie close to the (1,4) fluid column mode and is in the vicinity of both the $n = 5$ shell resonance and the $n = 16$ Stoneley wave resonance, making location of isolated modes extremely difficult.

Mode	(3,3)	(1,4)	(4,3)	(7,2)	(2,4)	(0,5)	(5,3)	(8,2)	(3,4)
kb	11.46	11.80	12.79	13.03	13.26	13.41	14.10	14.21	14.67

Table 5.2 Fluid column resonances of the brass cylindrical shell of circular cross-section ($b/a = 0.90$); values determined using the Schlieren system.

The resonant frequencies of the (2,4), (3,3), (3,4) and (4,3) modes can be compared with the data in Table 5.1 for the thicker shell. All four of these values are found to differ by only $0.05kb$, which is presumed to reflect the different thicknesses (and therefore impedances) of the shells.

A Schlieren image of the (3,3) fluid column resonance mode of this shell was presented in Figure 3.4(a), other examples of resonance modes of the circular shell are given in Knapp, Beckett & Humphrey (1995).

The variation of these resonance frequencies as the shell is deformed is the subject of section 5.3. We shall firstly present the *backscattering* results for the circular cylindrical shell.

5.2.6 Backscattering measurements

Although the Schlieren visualization system allows us to locate and identify the resonance modes of the cylindrical shell, and can provide valuable insight into scattering processes involving cylindrical structures, the technique provides no information about the amplitude of the scattered field. In Figure 2.5 the predicted backscattered form function of the brass cylindrical shell currently being discussed was presented. From this figure it can be seen that the shell is extremely resonant, exhibiting many features that are so narrow that they would require an incident field having a very narrow angular spectrum in order to resolve them. The level of detail shown in Figure 2.5 would not be expected to be measurable with any limited size laboratory tank facility.

The parametric array facility described in Chapter 4 has been used to measure the

backscattered form function of the circular cylindrical shell. The measurement technique was described in detail in section 4.4. Figure 5.1 shows the geometry used for making the backscattering measurements. All measurements were made at normal incidence (to the cylinder axis) and at a range (r) of $25cm$ from the centre of the cylinder. The reference measurement was made by rotating the hydrophone by 180° and relocating it at the position of the cylinder (Figure 5.1). The backscattered form function was calculated from the ratio of the backscattered signal to that of the reference signal, normalized as in equation (2.9).

Initially a $0.5m$ sample of the brass tube was used as the test object, but it was suspected that waves running down the length of the cylinder were being established by the off-normal components of the incident wave-field. To minimize this effect it was decided to use $1m$ samples.

An example of the backscattered time signal is shown in Figure 5.2. The long slowly decaying tail is characteristic of a resonant scatterer. The possibility of multiple reflections[1] was investigated in great detail and we are satisfied that no such signals of any significant level are present in this time window. The possibility of waves running along the length of the tube and reflecting from the ends cannot be discounted. Figure 5.3 shows the form function obtained using a long portion of this time signal ($0.43ms$ measured from the leading edge of the pulse) and a shorter portion ($0.13ms$). The result obtained using the shorter time signal shows a smoother variation and does not include many of the narrow features for which the long resonant tail is responsible. The experimental results obtained with the long time signal are compared with the theoretical predictions in Figure 5.4. The absence, in the experimental data, of the very narrowest resonance features at low frequencies is to be expected considering the now well known property of the parametric source - as an angular spectrum of plane waves - to smooth out such features in the form function. Even so, with this length of signal, the fluid column modes, such as the (3,4) mode marked in the figure, *are* being resolved in this measurement. An uncertainty in the shear wave velocity of brass, discussed in

1 Between cylinder and hydrophone, side walls, water surface etc.

Knapp, Beckett & Humphrey (1995), may be giving rise to other discrepancies between theory and experiment in this figure. Figure 5.5 shows the narrow region between $kb = 11$ and $kb = 15$. From the theoretical curve we see that a great many narrow modes exist, some of which are evident in the experimental data obtained with the parametric array (Figure 5.4), and most of which are in good agreement with the data obtained using the Schlieren technique (also shown in the figure).

5.2.7 Discussion

A theoretical model has been presented that predicts the frequencies at which the fluid column modes of a flooded circular cylindrical shell are excited. Good agreement has been obtained with experimental data obtained using the Schlieren technique. These predictions also agree with those of the Normal Mode Series approach for the scattering of a plane wave by a circular cylindrical shell. In the next section (5.3) the fluid column model is extended to the more general case of the elliptical cylindrical shell. With this aim in mind we have presented experimental data (Table 5.2) for the fluid column modes of the undeformed (circular) brass shell ($b/a = 0.90$) that is used in the elliptical study. The backscattering form function of the circular sample was also measured using the parametric array facility. Narrow resonance features (such as the fluid column modes) can just about be resolved with this system, but not so easily as with the Schlieren system, and not in a way that allows easy identification of individual modes.

Both of these experimental techniques will now be applied to the study of deformed (elliptical) samples of this same cylindrical shell.

5.3 Elliptical cylindrical shells: cavity resonances

In this section we discuss the results of a parallel theoretical and experimental investigation into the resonance behaviour of a deformed cylindrical shell. The back-scattering results are presented in section 5.4. As the deformed samples were approximately elliptical in cross-section, it was decided to model them as infinite elliptical cylindrical shells.

Of the nine fluid column modes located in the circular sample (Table 5.2, section 5.2.5), six were chosen for investigation. The six modes, in ascending order of frequency, were (3,3), (1,4), (4,3), (2,4), (0,5) and (3,4). Thus all the orders between 0 and 4 are represented. All of these resonances were found between 190 and 250 *kHz* in a water medium.

5.3.1 Experimental results

The resonances within five brass cylindrical shells of differing eccentricity were located and photographed using the Schlieren system, and compared with theoretical predictions made using a generalization of the models presented in section 5.2. Taking the internal semi-minor axis of each sample to be s, and defining a deformation parameter $\gamma = 1 - s/b$, the five samples had deformations of $\gamma = 0\%, 3.4\%, 6\%, 8\%$ and 10.4%. All the samples were 100*mm* long and made by distorting samples of the same cylindrical shell as that described in section 5.2.5.

The experimental procedure used to locate the resonances of the shell was discussed in Chapter 3 and is the same as that used for the circular sample described above. The angle that the acoustic beam made with the major axis of the elliptical cylinder was varied depending on the symmetry of the resonance sought: all even solution resonances were found by insonifying along the major axis; the odd solution resonances required insonification at other angles in order to excite the modes.

The results are given in Table 5.3 and shown in Figure 5.6, relative to those of the circular sample. The distribution of resonances within the deformed shells was initially very confusing; many more modes were detected than for the circular sample, and the

resonance patterns of many of these modes did not resemble those of the circular shell, and could not be easily classified. The ordering and classification of the data given in Table 5.3 was only possible after the theoretical investigations described in the next section had been performed. Further interpretation of the results will be postponed until then.

γ	0%	3.4%	6.0%	8.0%	10.4%
eccentricity	0	0.36	0.46	0.52	0.59
Mode/	*kb*	*kb*	*kb*	*kb*	*kb*
(3,3,o)	11.46	11.46	11.48	11.52	11.59
(3,3,e)	"	11.37	11.28	11.21	11.17
(1,4,o)	11.80	12.12	12.32	12.55	12.86
(1,4,e)	"	11.76	11.84	11.94	12.11
(4,3,o)	12.79	12.77	12.75	12.75	12.79
(4,3,e)	"	12.74	12.63	12.52	12.45
(2,4,o)	13.26	13.36	13.48	13.63	13.83
(2,4,e)	"	13.12	13.12	13.18	13.29
(0,5,e)	13.41	13.74	13.97	14.25	14.57
(3,4,o)	14.67	14.69	14.75	14.84	14.99
(3,4,e)	"	14.52	14.44	14.42	14.50

Table 5.3 Experimental locations of fluid column resonance modes of deformed shells.

5.3.2 Rigid boundary approximation

The fluid column resonances of a circular shell were shown above to lie close to the free modes of vibration of the fluid column within a *rigid* boundary. An analogous approach was initially chosen to solve for the deformed shells. The 'free' modes of vibration (i.e.

with no incident wave) of a fluid column with elliptical boundary were calculated as solutions of the wave equation in elliptical coordinates. The geometry and parameters of the problem are given in Figure 5.7.

5.3.2.1 Elliptical coordinates

The coordinates μ,ν represent families of confocal ellipses and hyperbolae respectively (Appendix B1). An ellipse having 'pseudo-radial' coordinate μ has an eccentricity $e = sech(\mu)$ and the distance between foci is $f = 2le$, where, for all ellipses having the same circumference, the semi-major axis (l) and semi-minor axis (s) are related by $(s + l)/2 = b$, where b is the radius of the limiting circle ($e = 0$) from which the ellipse is deformed. If the inner and outer boundaries of the shell (denoted b and a respectively) are parallel, then $\mu_a = \mu_b = \mu_o$ and the boundaries have the same eccentricity, but different interfocal distances f_a, f_b. In the circular limit, $\cosh(\mu_o) \to \infty$, $f_a \cosh(\mu_o)/2 \to a$ and $f_b \cosh(\mu_o)/2 \to b$ as the foci coalesce; a and b are then the outer and inner radii of the circular shell.

5.3.2.2 Wave equation and its solutions

Writing Helmholtz' equation in elliptical coordinates we obtain

$$\frac{\partial^2 P}{\partial \mu^2} + \frac{\partial^2 P}{\partial \nu^2} + \frac{f^2}{4} k^2 (\cosh^2 \mu - \cos^2 \nu) P = 0. \tag{5.9}$$

Separation of variables ($P(\nu,\mu) = \Theta(\nu) j(\mu)$) yields the two equations

$$\frac{\partial^2 \Theta(\nu)}{\partial \nu^2} + \left(\iota - \frac{f^2 k^2}{8} \cos 2\nu \right) \Theta(\nu) = 0 \tag{5.10}$$

and

$$\frac{\partial^2 j(\mu)}{\partial \mu^2} - \left(\iota - \frac{f^2 k^2}{8} \cosh 2\mu \right) j(\mu) = 0, \tag{5.11}$$

where ι is the separation constant. Equation (5.10) is Mathieu's equation (Appendix B2) and has solutions

$$\Theta = \begin{Bmatrix} ce_n(q,\nu) \\ so_n(q,\nu) \end{Bmatrix} \tag{5.12}$$

where ce_n are *even* Mathieu Functions of order n, so_n are *odd* Mathieu Functions, and q is a dimensionless parameter given by

$$2q = \frac{f^2 k^2}{8}. \tag{5.13}$$

Periodicity in the coordinate ν implies that n must take integer values. The even/odd property refers to symmetry about the major axis ($\nu = 0$).

For the same value of ι, equation (5.11), known as the 'Modified Mathieu's equation', has corresponding solutions

$$j = \begin{Bmatrix} je_n(q,\mu) \\ jo_n(q,\mu) \end{Bmatrix}, \tag{5.14}$$

where je_n and jo_n are 'Radial Mathieu Functions' of order n, and even and odd symmetry respectively. The Mathieu Functions are infinite series of circular functions, and the Radial Mathieu Functions are infinite series of hyperbolic functions. Each even/odd Mathieu Function has either π or 2π periodicity, so there are four 'kinds' of solution to Mathieu's equation, and four corresponding solutions to the Modified equation. Therefore, the solution of Helmholtz' equation for the pressure P consists of the functions

$$P_n(\nu,\mu) = \begin{Bmatrix} ce_n(q,\nu)je_n(q,\mu) \\ so_n(q,\nu)jo_n(q,\mu) \end{Bmatrix}, \tag{5.15}$$

each product being associated with a particular value of ι, which is in turn dependent upon n and q (and hence k). In the limit $q \to 0$,

$$\begin{aligned} ce_n(q,\nu) &\rightarrow \cos n\phi \\ so_n(q,\nu) &\rightarrow \sin n\phi \\ je_n(q,\mu) \rightarrow jo_n(q,\mu) &\rightarrow J_n(kr), \end{aligned} \tag{5.16}$$

the functions become the familiar circular functions ($q = 0 \Rightarrow f = 0$) and the notation has been chosen to reflect this behaviour.

Boundary conditions applied at $\mu = \mu_0$ limit the values of q to a discrete set of real eigenvalues.

5.3.2.3 Boundary conditions

At a rigid boundary the component of particle velocity normal to the inner surface of the shell must vanish. In a manner analogous to that of section 5.2.2 the resonance modes ($q_{n,m}$) of the elliptical cavity are calculated as solutions of

$$\begin{aligned} je'_n(q_b,\mu_o) &= 0 \\ jo'_n(q_b,\mu_o) &= 0 \end{aligned} \tag{5.17}$$

where

$$q_b = \frac{f_b^2 k^2}{16},$$

from which the wave numbers can be calculated. The fact that $je \rightarrow jo$ as $q \rightarrow 0$ implies that $q_{n,m}^{(e)} \rightarrow q_{n,m}^{(o)}$ and hence

$$k_{n,m}^{(e)} \rightarrow k_{n,m}^{(o)} \quad \text{as} \quad f \rightarrow 0, \tag{5.18}$$

which is simply the statement that the odd and even resonance frequencies are equal in the circular limit. For the n=0 case, only even solutions exist.

In summary then, the pressure distribution can be seen to consist of a series of normal modes characterised by their symmetry, and by the integers n and m. We denote these normal modes (n,m,e) (even solutions) and (n,m,o) (odd solutions), and we can write the pressure distributions of these modes

$$\begin{aligned} P^{(e)}_{n,m}(\nu,\mu) &= ce_n(q^{(e)}_{n,m},\nu)je_n(q^{(e)}_{n,m},\mu) \quad ; \quad (even) \\ P^{(o)}_{n,m}(\nu,\mu) &= so_n(q^{(o)}_{n,m},\nu)jo_n(q^{(o)}_{n,m},\mu) \quad ; \quad (odd). \end{aligned} \tag{5.19}$$

Common to both the calculation of the resonance frequencies and the acoustic pressure fields is the determination of the coefficients in the Mathieu Function series, and it is the computation of these that proves to be most problematic. Further details are given in Appendix B2.

5.3.3 Preliminary theoretical results

The model described above can be used to predict the behaviour of the fluid column modes as the eccentricity of an initially circular cavity is increased.

An ellipse has two degrees of freedom with respect to changes in its shape; both its eccentricity and its overall size can be altered. This means that the wave number for a particular mode will be a function of two variables. Ultimately we are really only interested in the variations with eccentricity. We choose $b = (s+l)/2$ to be the variable describing the 'size' of the cylinder, where b is the radius of the circle having the same circumference as the ellipse, i.e. the circle from which the ellipse was deformed. Thus, for deformations that keep the circumference constant, b will be constant. Code was written to find the solutions of (5.17) and to calculate the pressure distribution in the fluid column (5.19).

Concentrating on the six modes that were the subject of the experimental investigation, the model was used to calculate the frequencies of the modes at different eccentricities and to calculate the acoustic field in the cavity. The variation of resonance frequency with deformation is shown in Figure 5.8 where it is seen that each resonance

of the circular shell splits into two as the symmetry is broken; except for an $n = 0$ resonance at $kb \approx 13.4$, which is isolated. The agreement between theory and experiment is good enough to allow the experimental data to be interpreted; each of the experimentally observed resonances can be associated with a particular branch of the plot, and thus with a resonance of the circular (undeformed) fluid column. Further comment upon this behaviour is postponed until section 5.3.5 where a more accurate model is used in the predictions.

In Figures 5.9 and 5.10 theoretical predictions of the Schlieren images are presented alongside experimentally obtained results for the field inside the fluid column. The theoretical plots show the optical distribution calculated using a value of the Raman-Nath parameter (v_o) of 3.4, which was shown in Chapter 3 to give a reasonably accurate representation of both the pressure distribution and the experimental images. The (3,4) fluid column mode is shown for three of the deformed samples of differing eccentricity. Modes lying on the odd branch (Figure 5.9) are seen to resemble the (3,4) mode of the circular cavity; but the even modes (Figure 5.10) are very different in appearance to anything previously seen in the circular cavity. Only small deformations are necessary to alter the appearance of many resonances significantly. The agreement between theory and experiment is very good, validating the theoretical approach of the previous section, and the approximation of the deformed shells to elliptical cylinders.

The agreement between the experimentally measured wave numbers ($k_{n,m}$) and the predictions of the rigid body approximation was not considered satisfactory by the author and improvement was sought. The differences are attributed to the finite impedance of the brass shell and the non-elliptical nature of the cavity. The latter cannot easily be dealt with; either high precision elliptical shells would have to be manufactured or numerical techniques employed to solve for general two-dimensional boundaries. The finite impedance of the elliptical shells, however, can potentially be allowed for in a manner analogous to that used for the circular shell.

5.3.4 Impedance boundary

The solution of the internal problem involving a finite impedance boundary was alluded to in section 5.2.4, where it was shown (for the circular geometry) to give greatly improved agreement with the experimental measurements. We shall now apply this technique to the elliptical geometry. As with the rigid boundary formalism, solutions of even and odd parity, and period π and 2π, exist; but for brevity we shall suppress reference to them, and their arguments, referring only to a solution denoted $P(x)$, where x is a or b and the arguments may be deduced from the context of the equation.

At the inner boundary (b) the normal component of velocity in the fluid column (V_r) is related to the pressure (P_{fl}) by

$$V_r(b) = \frac{i}{\omega\rho_f}\frac{dP_{fl}(b)}{dn} = \frac{i}{\omega\rho_f}\frac{1}{h_\mu}\frac{dP_{fl}(b)}{d\mu} \tag{5.20}$$

where ω is the angular frequency, $dn = h_\mu d\mu$ is normal to the ellipse, and the metric $h_\mu = f_b\sqrt{(\cosh(2\mu_o) - \cos(2\nu))/8}$ is a function of the angular coordinate (v). The boundary conditions at b can be written

$$\frac{P_{fl}(b)}{V_r(b)} = Z_{inp} \tag{5.21}$$

where Z_{inp} is the mechanical surface impedance of the shell and P_{fl}/V_r is the radiation impedance on the inner surface. Combining (5.20) and (5.21) we obtain

$$\frac{dP_{fl}(b)}{d\mu} + i\frac{\omega\rho_f h_\mu}{Z_{inp}}P_{fl}(b) = 0. \tag{5.22}$$

The actual impedance of the shell (Z_{inp}) is properly given by

$$Z_{inp} = \frac{P_{lay}(b)}{V_{lay}(b)} = \frac{P_{lay}(b)}{\left.\frac{i}{\omega\rho}\frac{1}{h_\mu}\frac{dP_{lay}}{d\mu}\right|_b} \tag{5.23}$$

where P_{lay}, the pressure in the layer, depends upon boundary conditions at the outer boundary a. Substituting this expression into (5.22) yields

$$P'_{fl}(b)+i\frac{\omega\rho_f}{X_{inp}}P_{fl}(b)=0 \qquad \text{where} \quad X_{inp}=\frac{P_{lay}(b)}{\frac{i}{\omega\rho}\frac{dP_{lay}}{d\mu}\Big|_b}, \tag{5.24}$$

this equation having no angular dependence. Knowledge of Z_{inp} (or X_{inp}) would constitute a complete solution of the scattering problem. Unfortunately Z_{inp} is unknown, and its computation rather problematic. In the present study we do not calculate X_{inp} exactly, but seek an approximation, as follows. In the circular limit ($f_b \to 0$), $d\mu \to dn/b$ and $X_{inp} \to Z_{circ}/b$, where Z_{circ} is the input impedance of a circular shell of inner radius b. The use of Z_{circ} in equation (5.24) for eccentricities greater than zero, amounts to the approximation that the input impedance is that of a circular shell irrespective of eccentricity. The impedance of the circular shell can be approximated to that of an 'acoustic' shell characterized by only one velocity (as in equation 5.7);

$$Z_{circ}=\rho c_l\frac{4/\pi^2k_l^2ab-i(\chi r_n s_n+p_n q_n/\chi)}{\chi^2+q_n^2/\chi}, \tag{5.25}$$

where $\chi=Z_w/\rho c_l$, $Z_w=-i\rho_f c_f H_n(ka)/H'_n(ka)$, and r_n, s_n, p_n and q_n are products of Bessel functions and their derivatives, as shown in equation (5.7) and defined in Abramowitz (1972, p.361). As in section 5.2.4 we can further approximate the surface impedance to the input impedance of a planar layer having the same thickness;

$$Z_{inp}=\rho c_l\frac{\rho_f c_f+i\rho c_l\tan(k_l[a-b])}{\rho c_l+i\rho_f c_f\tan(k_l[a-b])}. \tag{5.26}$$

Both expressions (5.25) and (5.26) have been found to give very similar values for the surface input impedance, and produced insignificant differences in the final results. Therefore in the present study, the simpler expression for the planar layer is used throughout. With these approximations, equation (5.24) becomes

$$P'_{fl}(b)+i\frac{\rho_f c_f kb}{Z_{inp}}P_{fl}(b)=0\,. \tag{5.27}$$

The roots of (5.27) are $q^{e/o}_{n,m}$ and the corresponding wave numbers are $k^{e/o}_{n,m}$ (found from (5.13)). As in section 5.3.2 each (n,m) labels a pair of resonances (*e*ven and *o*dd) that are degenerate in the circular limit. The results of the rigid boundary approximation emerge from the above formalism (5.27) as the special case $Z_{inp}=\infty$; i.e. $P'_{fl}(b)=0$.

5.3.5 Results and discussion

This modified theory was used to recalculate the resonance frequencies of the elliptical cavity and found to provide better agreement with the experimental results than the rigid boundary approximation did. The results are shown in Figure 5.11.

All of the even solutions (except (0,5)) have an initial decrease in the *kb* value as the shell is initially deformed. As it is deformed still further however, the *kb* values begin to increase again and eventually become greater than the initial values for a circular shell. It would seem that the modes having lower values of n do not have as great a decrease in *kb* as do the higher order modes. Compare (1,4,e) and (3,4,e) for example. The (0,5,e) mode does not decrease at all. Comparison of the (3,3,e) and (3,4,e) modes show that the number of wavelengths across the diameter (m) does not play such a large part in the variations as does the order (n).

The odd solutions behave differently. The $n=3$ and $n=4$ resonances show a slight decrease before k begins increasing, while the lower order modes begin increasing immediately.

So it is seen that the nature of the splitting, for low eccentricity, is largely dependent upon the number of wavelengths (n) around the cylinder in the angular direction. Degeneracies can be seen to exist at certain eccentricities where the curves cross. These are known as 'level crossings'. As the deformation increases to high values, all the resonance frequencies increase, as might be expected considering that the volume decreases as the eccentricity increases (since the circumference is constant).

The remaining differences between the experimental results and the theoretical predictions are thought to be mainly due to a certain amount of 'flattening' that occurred along the portions of the ellipse in contact with the jaws of the press with which they were produced. This flattening is only noticeable for the highly eccentric samples. It was this tendency to flatten and buckle that prevented samples of higher eccentricity from being produced.

5.3.5.1 Theoretical predictions for highly eccentric cavities

As we have already seen in Figure 5.11, all of the resonance frequencies, whether they be even or odd solutions, ultimately increase with eccentricity. Although experimental results could not be obtained for higher eccentricities, the theoretical calculations have been extended to predict the behaviour of the wave numbers, and the acoustic field, at these much higher eccentricities.

Figures 5.12 shows a sequence of images for the (1,4) resonance modes, of both even and odd symmetry, as the ellipse is deformed to high eccentricities. It is seen that the pressure variations become increasingly confined to the central portion of the enclosure, bounded by the sections of perimeter having the least curvature; there being no pressure variations near the highly curved ends of the ellipse. The ellipse begins to act as a pair of parallel plates with respect to wave-fronts parallel to the major axis (i.e. variations along the minor axis) and we would expect the kb values of the resonances to behave accordingly (i.e. to vary linearly with $1/s$; s = semi-minor axis) as has been shown to be the case (Chinnery, 1990).

5.4 Backscattering by an elliptical shell

Backscattering measurements were made with a $1m$ brass cylindrical shell of the same dimensions as that used in the resonance study, and in the backscattering measurements of section 5.2.6. The sample was initially circular and was deformed by 5%. The cylinder was suspended from the rotation stage by nylon thread, and could be rotated to any angle (θ) with respect to the incident beam (Figure 5.13). At each angle θ the

averaged time signals were recorded, and the form function calculated in the same way as were those of the circular sample.

Results for the two principle orientations of the deformed sample, $\theta = 0°$ and 90°, are compared with the form function of the undeformed sample in Figure 5.14. These two orientations involve insonification of the shell 'end on' and 'side on' respectively. Significant differences can be seen between all three measurements, in particular in the locations of the peaks and troughs in the form function (e.g. kb~7). At certain frequencies (e.g. kb~14.2) the amplitude of the backscattered signal is seen to differ greatly between the two orientations of the deformed shell. These results indicate the sensitivity of the scattering to orientation of the cylindrical shell, and are thought to be due to the excitation of resonances (i.e. peripheral waves).

The complete angular dependence of the backscattered signal is shown in Figure 5.15 for the narrow band of frequencies discussed in section 5.3. The cylinder was rotated in 2° steps under computer control, 0° corresponding to the incident beam parallel to the major axis of the ellipse. The strongest reflections are seen to occur when the cylinder is insonified side-on (90°), but at some frequencies the maxima occur at other angles. There is a general tendency for features to move up in frequency as the cylinder is rotated. This is to be expected from simple considerations involving the changing dimensions of the cylinder 'seen' by the incident beam. Examples of the variation of form function with incident angle are given in Figure 5.16 for two frequencies. The variations in backscattered amplitude are quite large considering the extent to which the cylinder has been deformed.

5.5 Summary

This chapter has presented experimental evidence of how the fluid column resonances of circular cylindrical shells behave as they are deformed, and how the backscattering properties of a deformed shell differ from those of the circular (undeformed) sample. Both the Schlieren visualization technique and the parametric array facility have been employed in these studies with great success.

Six fluid column resonances were located in five 'deformed' shells of differing eccentricity. The resonances were located using Schlieren and photographs of the resonance patterns obtained with the system.

Simple theoretical models for the standing waves within rigid circular and elliptical boundaries have been described, implemented numerically, and used to predict resonance frequencies and acoustic wave-fields of the fluid column modes of the cylinders. Good agreement with experiment has been obtained, despite the simplicity of the model (which assumed the boundaries to have infinite impedance) and possible differences caused by the non-elliptical nature of the shells prepared experimentally. Theses models were extended by including the effects of a *finite* impedance boundary, and substantially improved agreement was obtained.

Theoretical predictions were extended to predict the behaviour of the resonance frequencies and acoustic fields within highly deformed cavities, but shells of such high eccentricity could not be prepared for experimental investigation.

Other types of resonance of the cylindrical shells (shell resonances and Stoneley wave resonances) have not been discussed, although they have all been observed within the elliptical shells using the Schlieren system. The full theoretical calculations for insonified shells would need to be implemented in order to provide detailed information about these resonances.

Both experimental systems have proved to be very useful tools in the study of resonance scattering from cylindrical shells with non-circular symmetry, and would be expected to provide valuable insight into the resonance and scattering behaviour of other complex targets, such as the fibre-reinforced cylinder and the rib-reinforced cylindrical shell.

Figure 5.1 Scattering geometry.

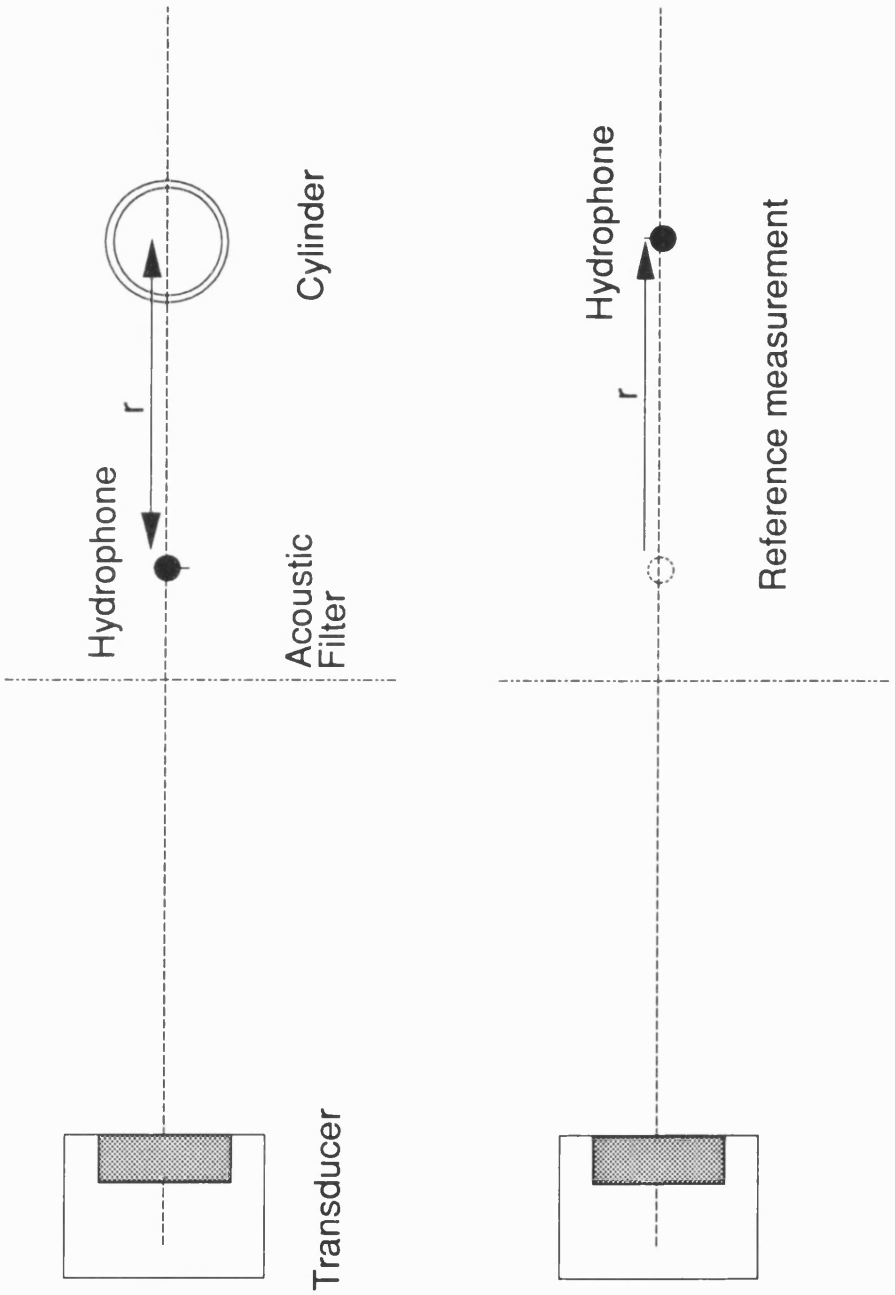

Figure 5.2 Signal backscattered by a brass cylindrical shell of circular cross-section.

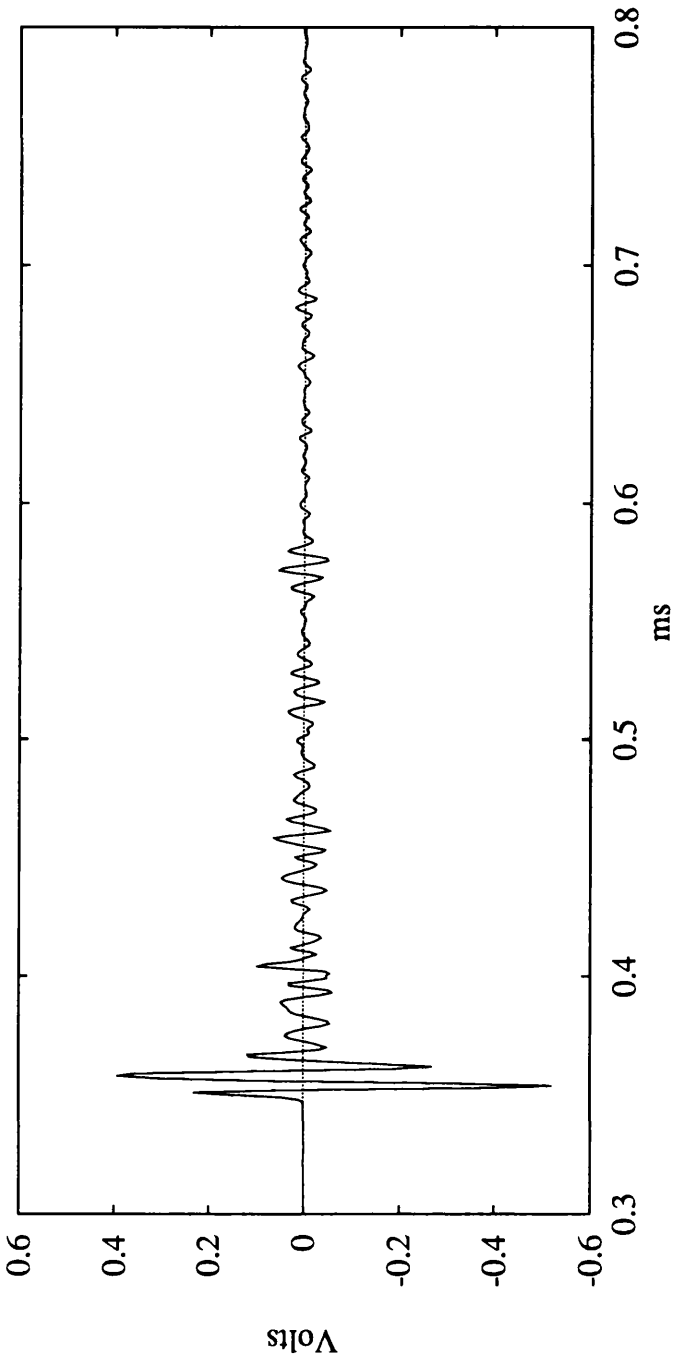

Figure 5.3 Backscattered form function of circular shell; measurements made by analysing long and short portions of the captured time signals.

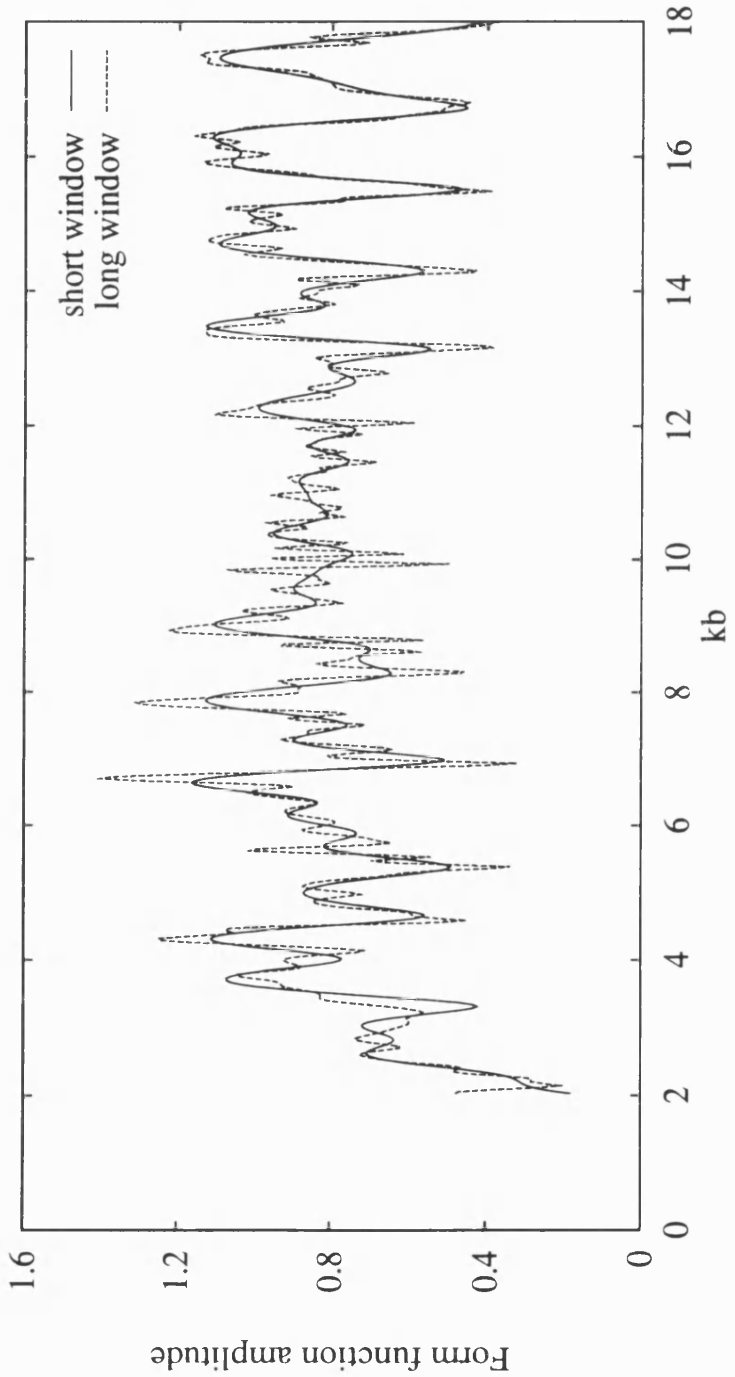

Figure 5.4 Backscattered form function; comparison of experiment (points) with theory (lines).

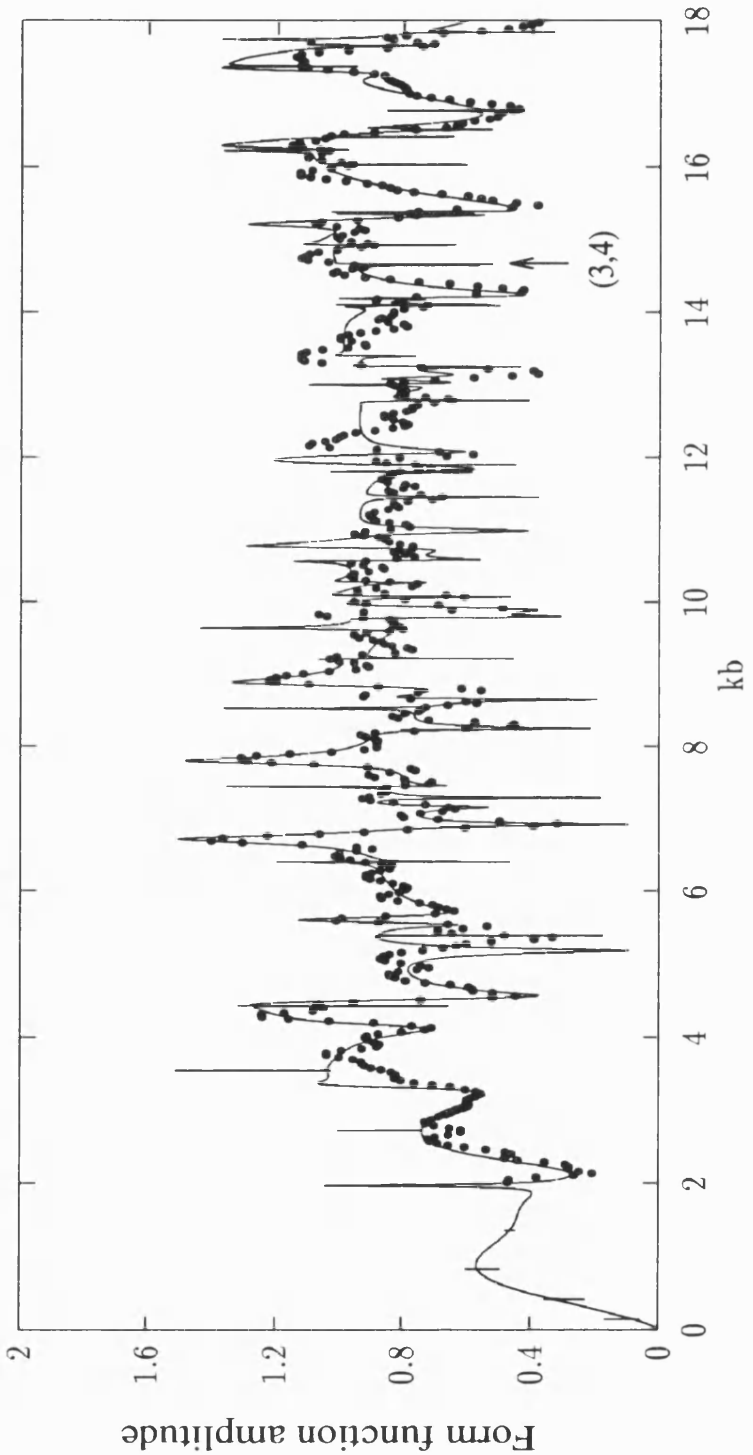

Figure 5.5 Resonances located with the Schlieren technique; comparison of experimentally determined frequencies (impulses) with the predicted plane wave form function (solid line).

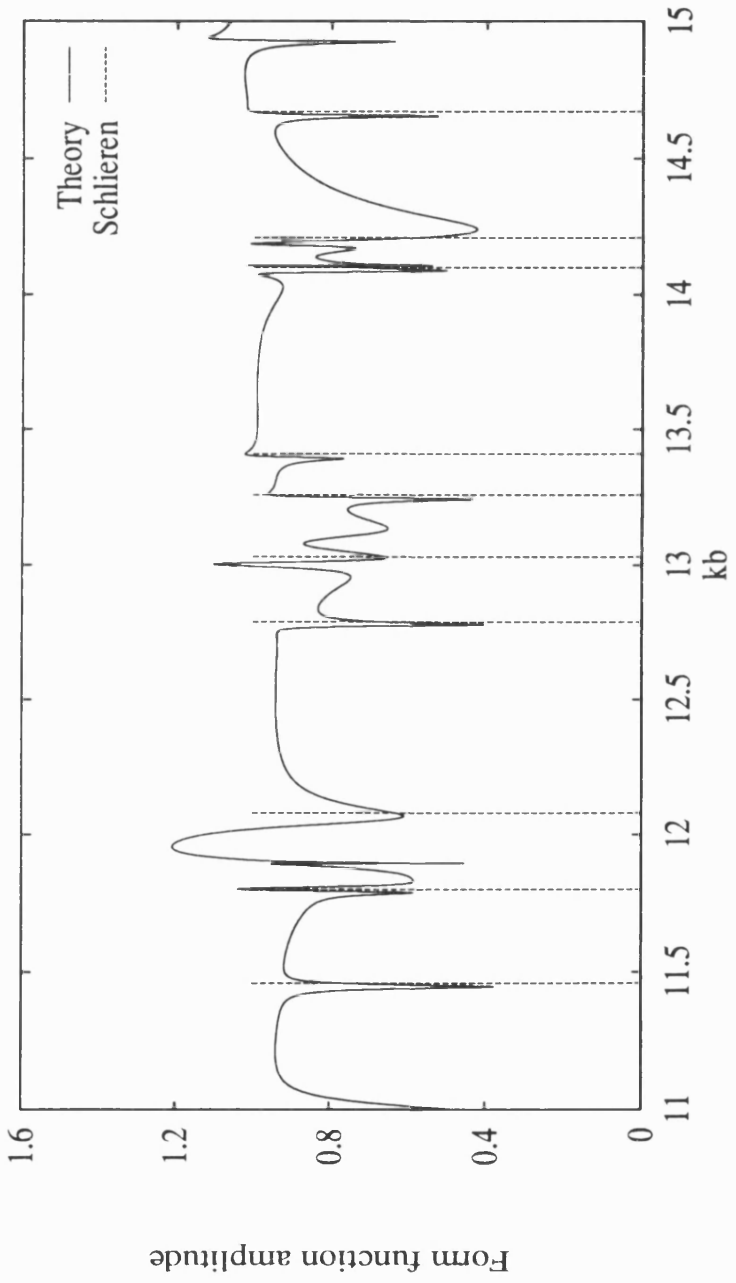

Figure 5.6 Experimental locations of resonances in *deformed* shells (points) compared with locations for undeformed shells (impulses).

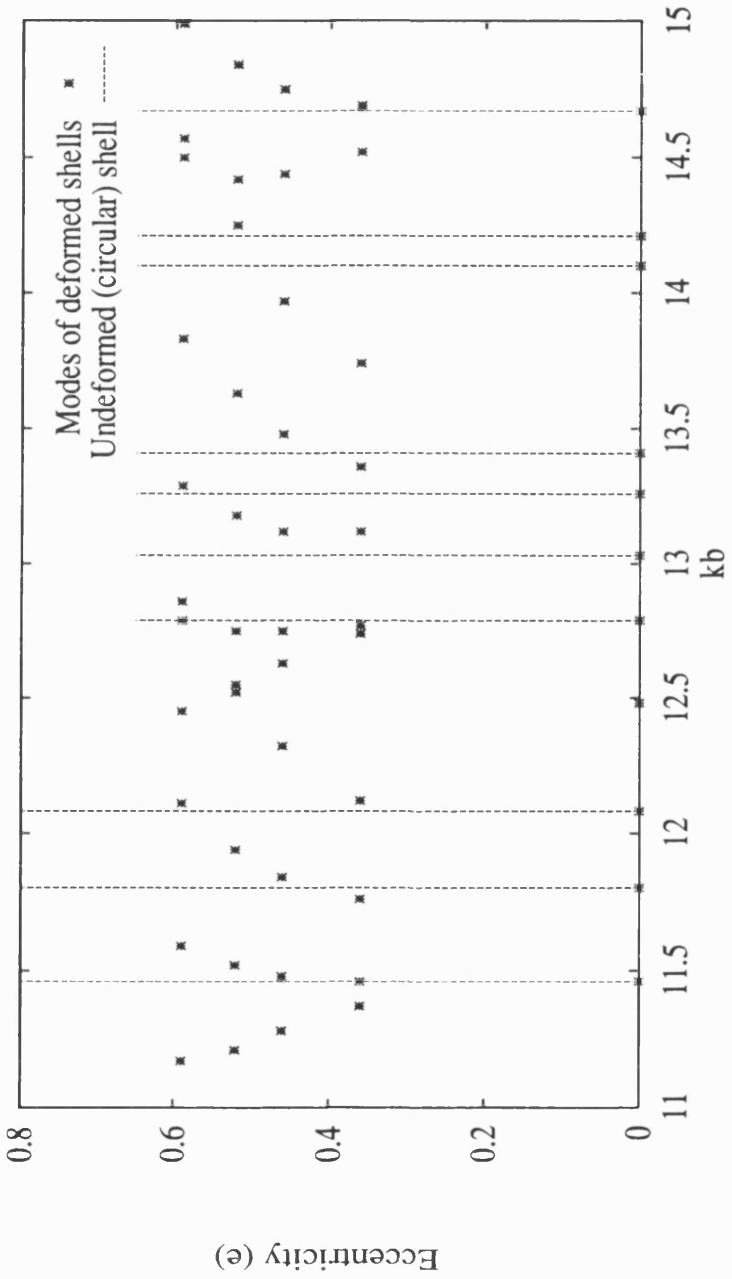

Figure 5.7 Elliptical coordinate system and geometry of the elliptical shell.

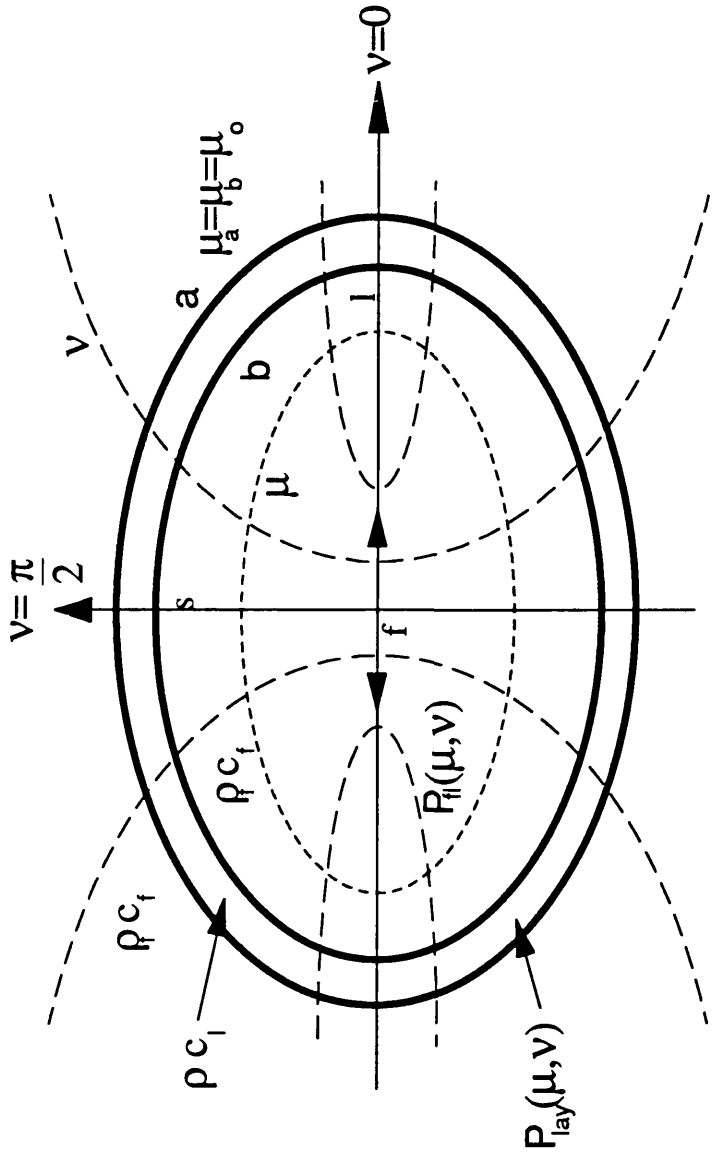

Figure 5.8 Variation of resonance frequencies with eccentricity; rigid boundary approximation and experimental results.

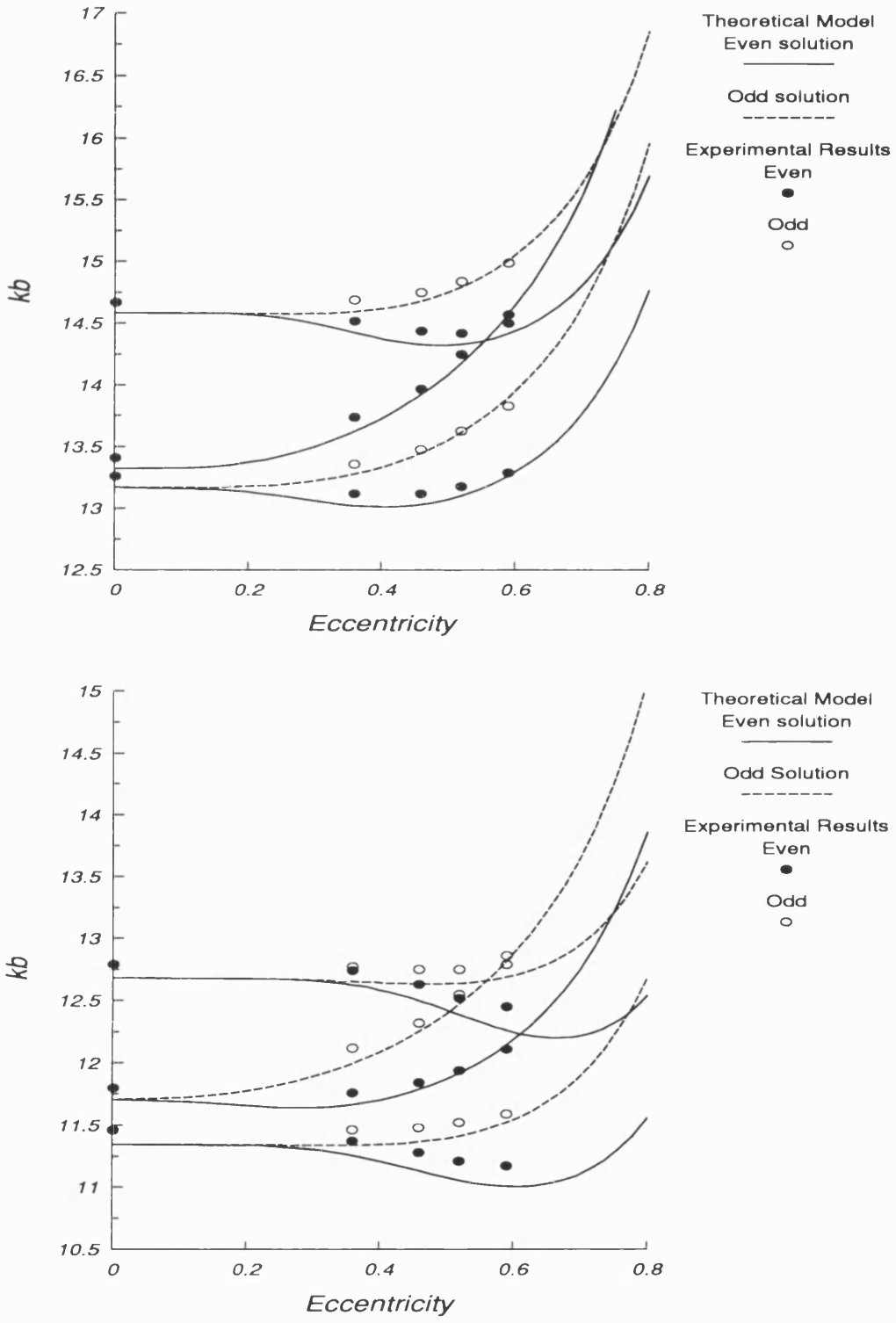

Figure 5.9 (3,4,$\underline{\mathbf{o}}$) fluid column resonances of elliptical shells of different eccentricity e (% deformation γ). Theoretical model (left) and Schlieren images (right).

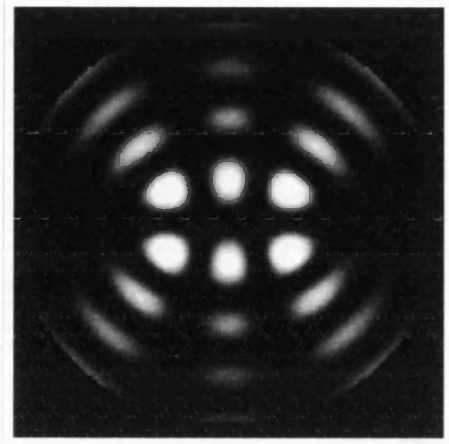

$e = 0.36$

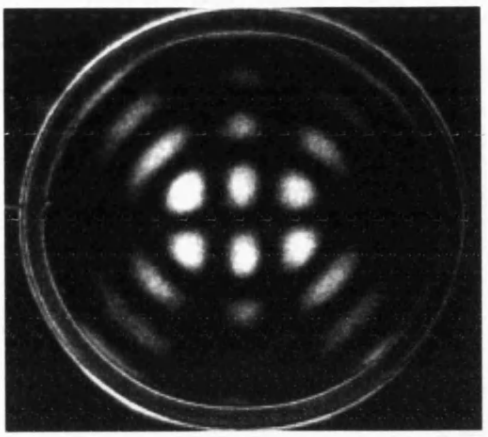

$\gamma = 3.4\%$

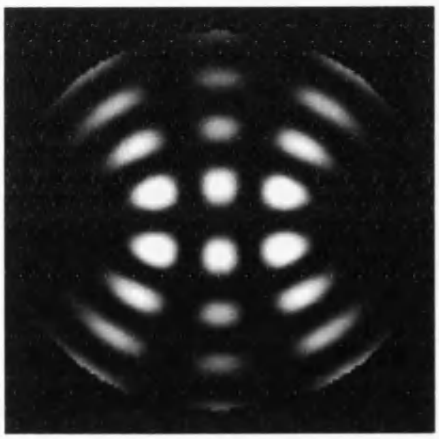

$e = 0.46$

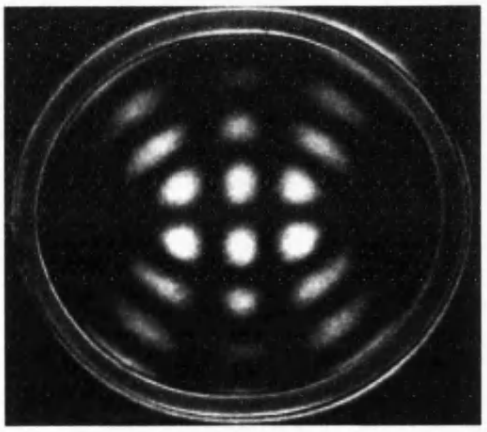

$\gamma = 6.0\%$

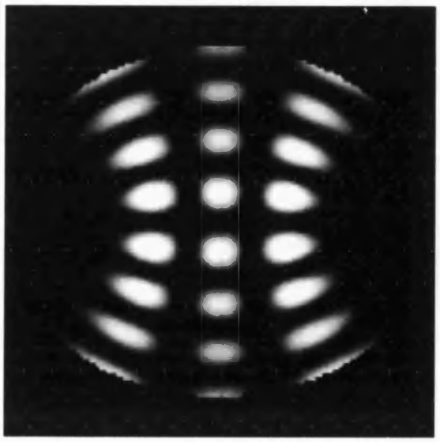

$e = 0.59$

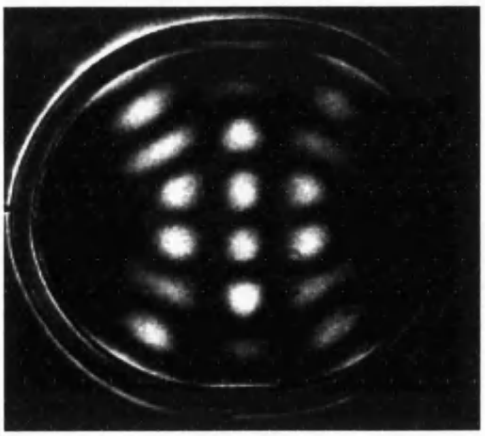

$\gamma = 10.4\%$

Figure 5.10 (3,4,**e**) fluid column resonances of elliptical shells of different eccentricity e (% deformation γ). Theoretical model (left) and Schlieren images (right).

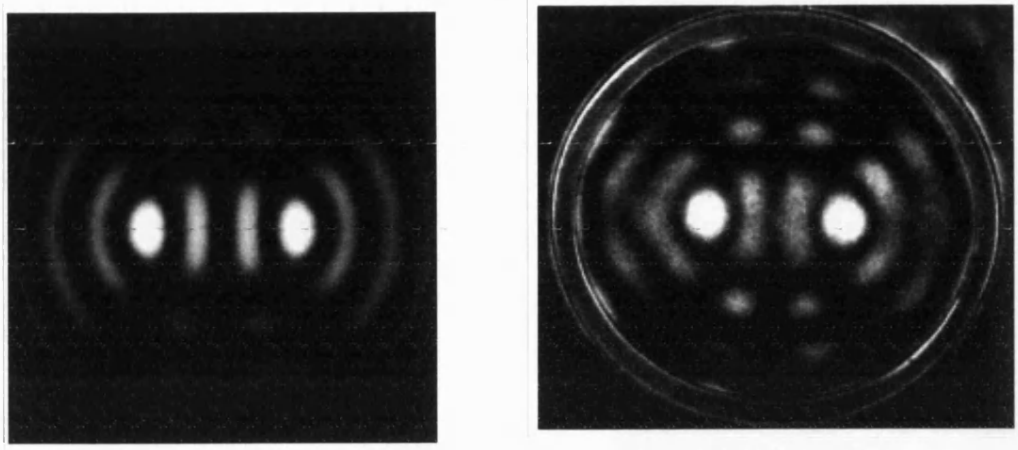

$e = 0.36$ $\gamma = 3.4\%$

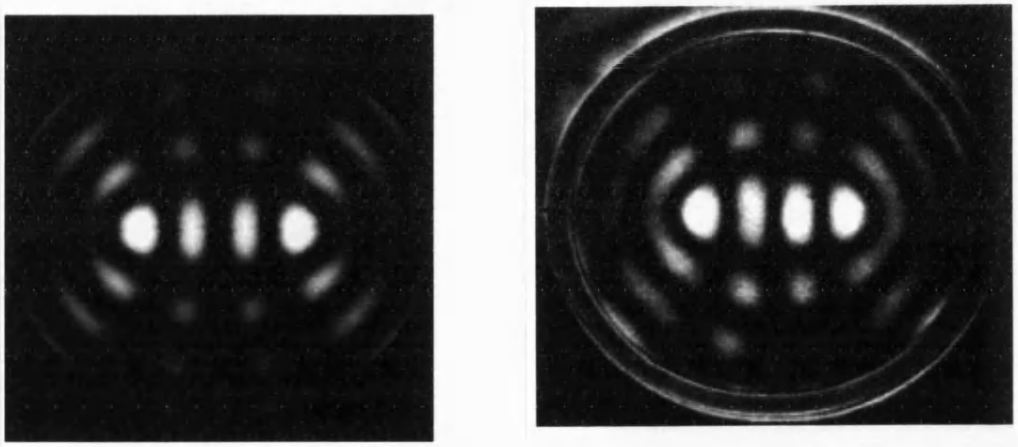

$e = 0.46$ $\gamma = 6.0\%$

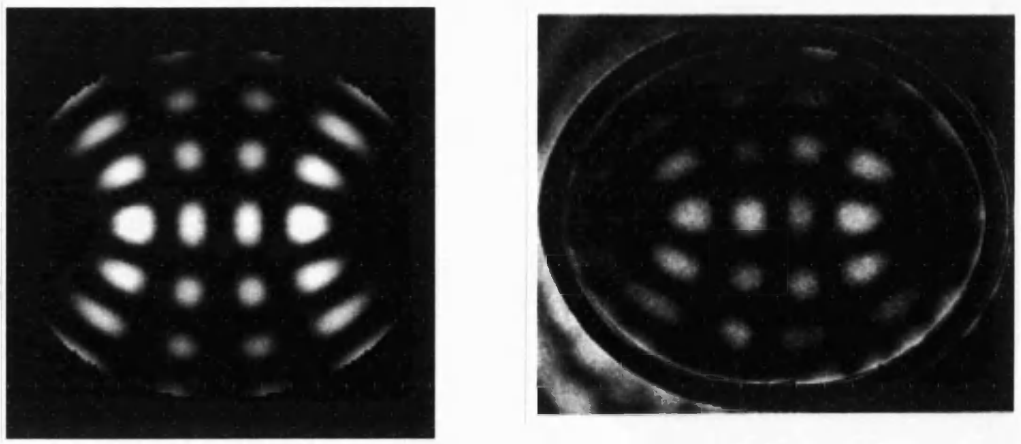

$e = 0.59$ $\gamma = 10.4\%$

Figure 5.11 Variation of *kb* with deformation (γ) for selected fluid column resonance modes (n,m,e/o). Theory (lines) and experimental observation (points; even (•) and odd (o) modes).

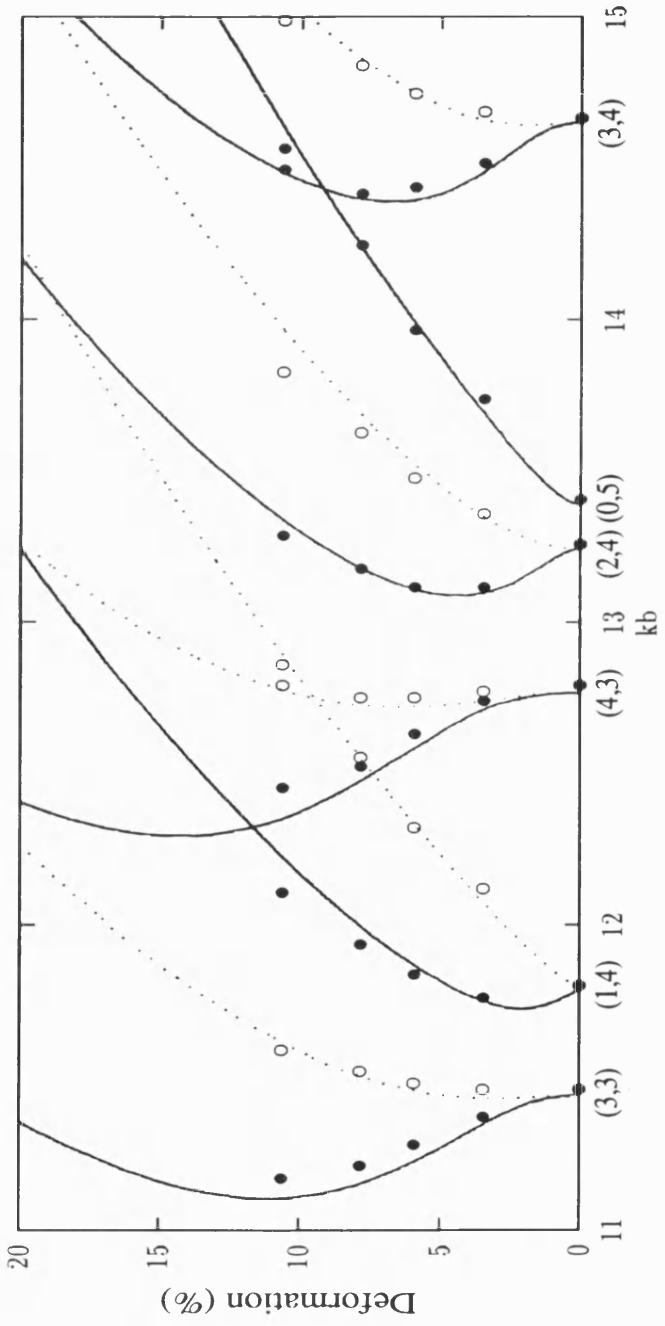

Figure 5.12 Predicted pressure distribution of the (1,4) fluid column modes in elliptical cavities of different eccentricity. Odd (left) and even (right) solutions.

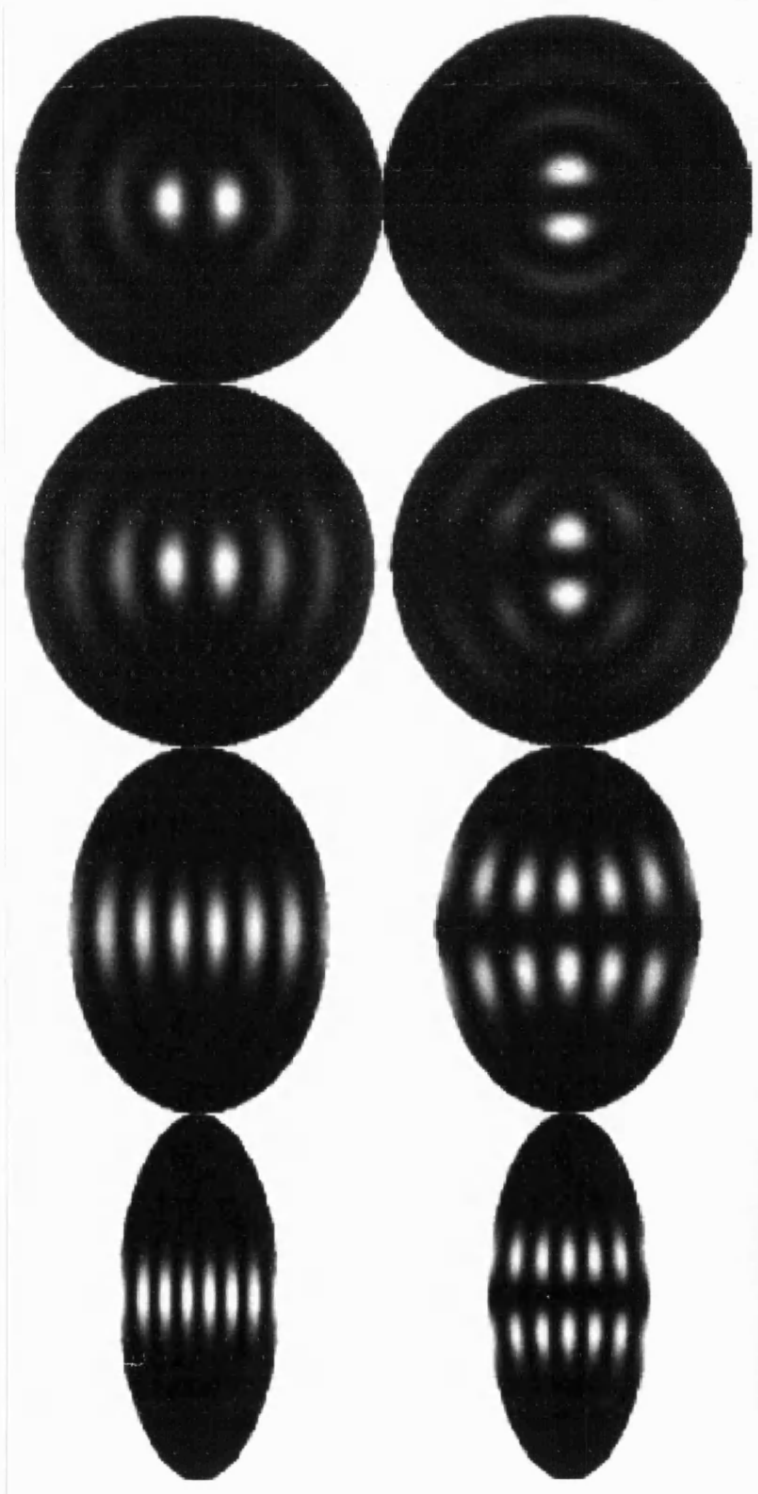

Figure 5.13 Scattering geometry for backscattering measurements involving the deformed brass cylindrical shell.

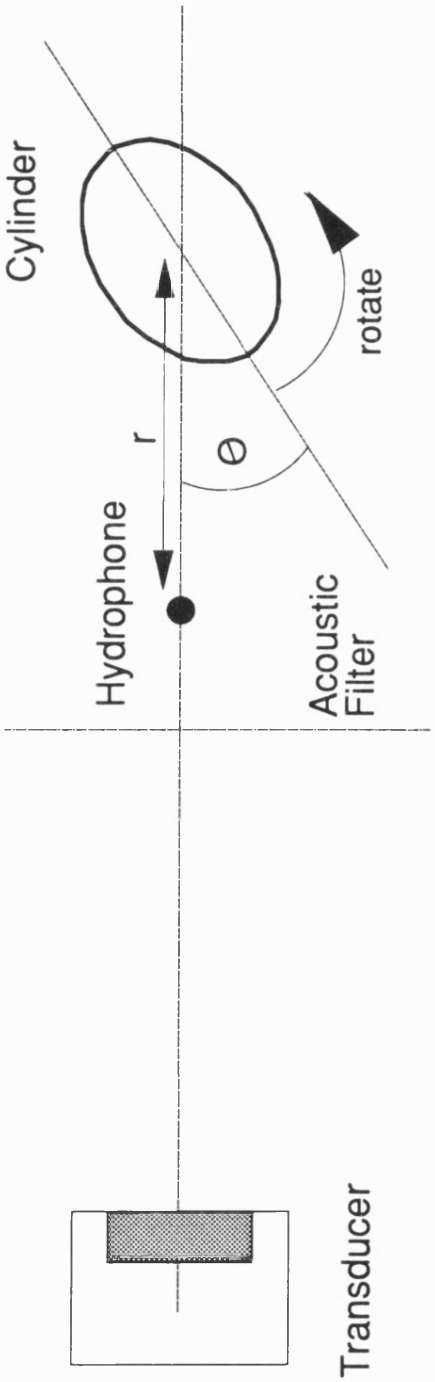

Figure 5.14 Measured form function of deformed brass cylindrical shell; deformation (γ) of 5%. Incident beam 90° to major axis (-------), 0° (.....) and circular sample (——).

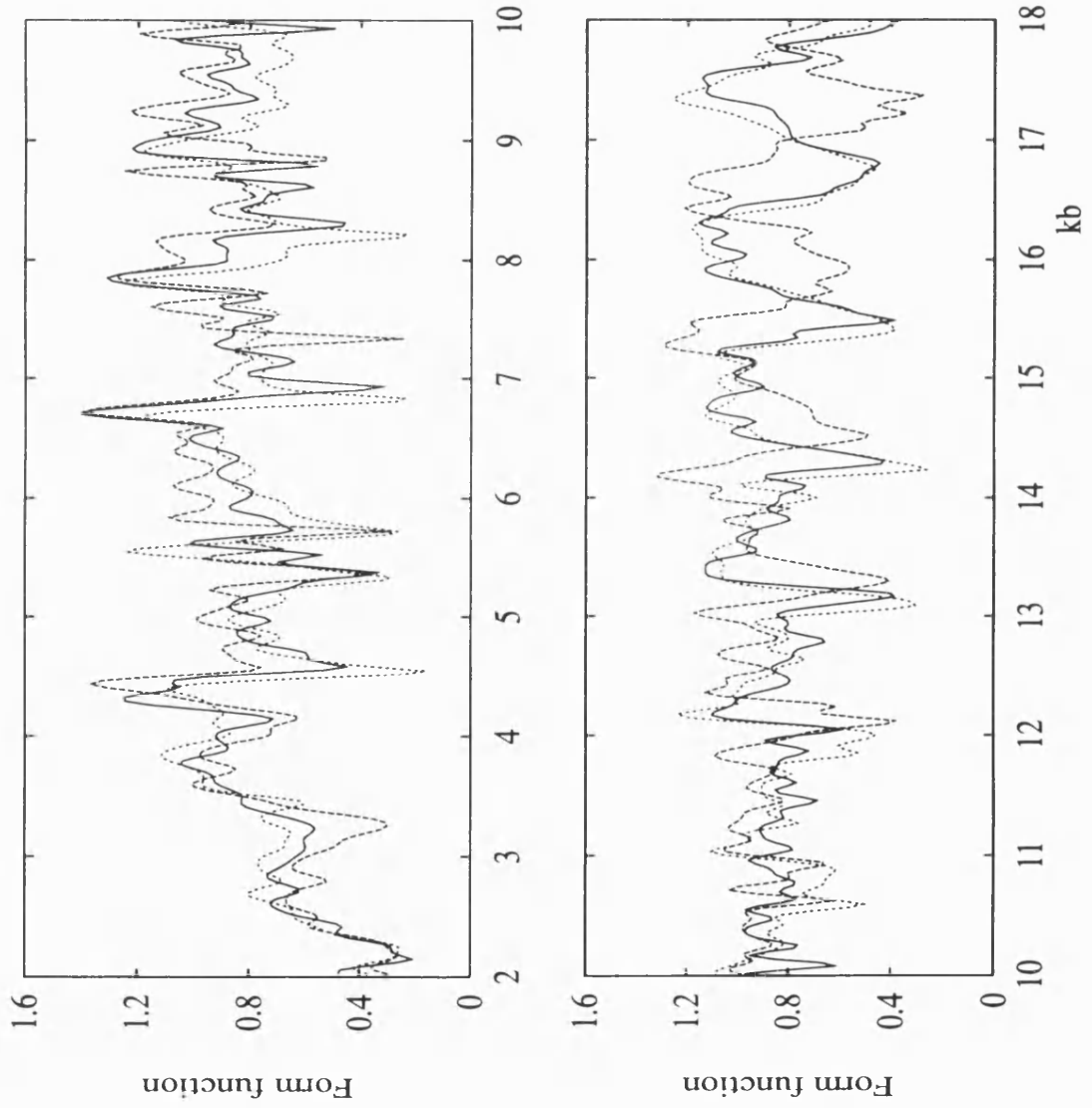

Figure 5.15 Variation of measured form function with frequency (*kb*) and incident angle (θ); *kb* range 11 – 15.

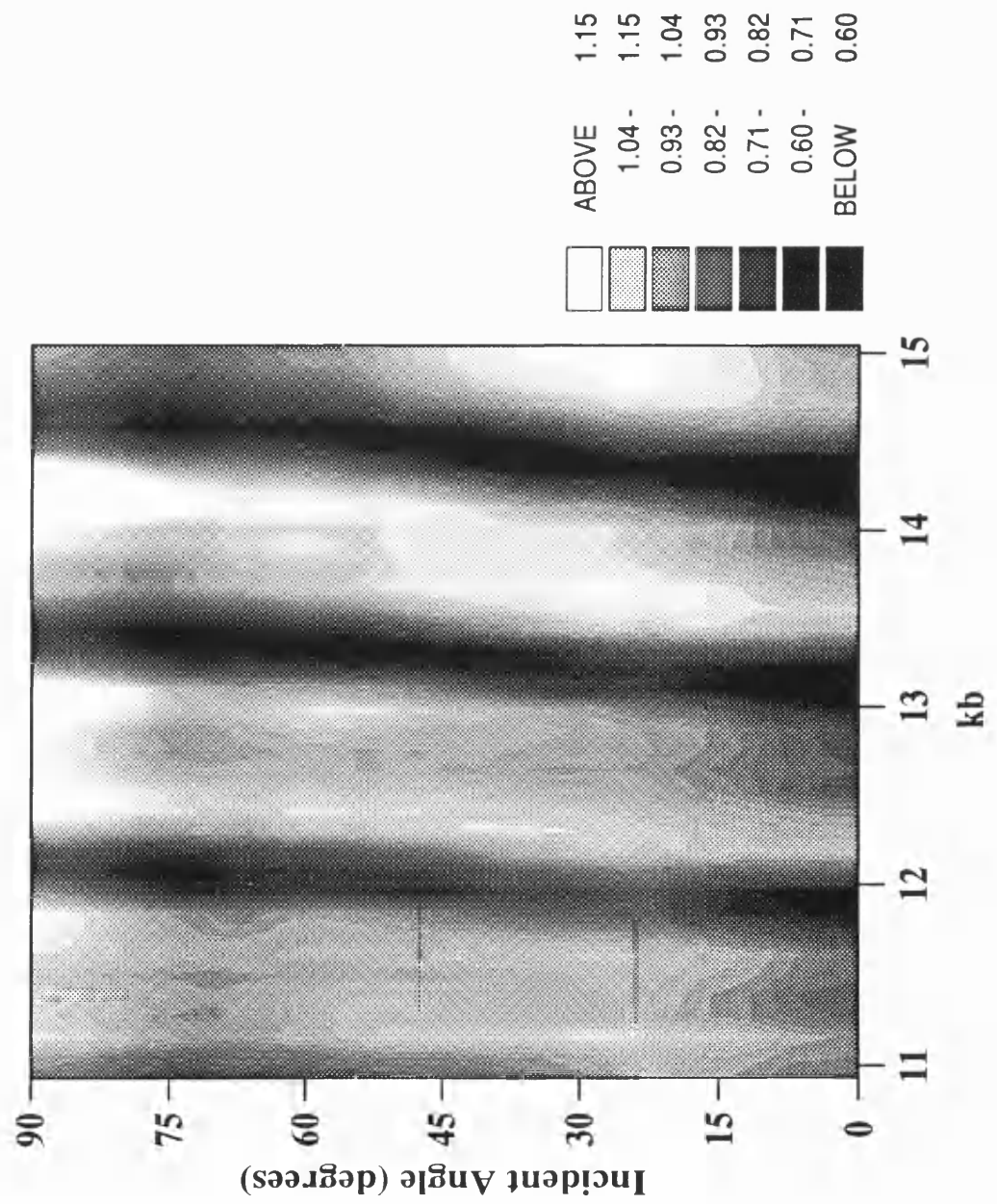

Figure 5.16 Variation of measured form function with incident angle at two frequencies; kb = 10.1 (o) and kb = 14.2 (•).

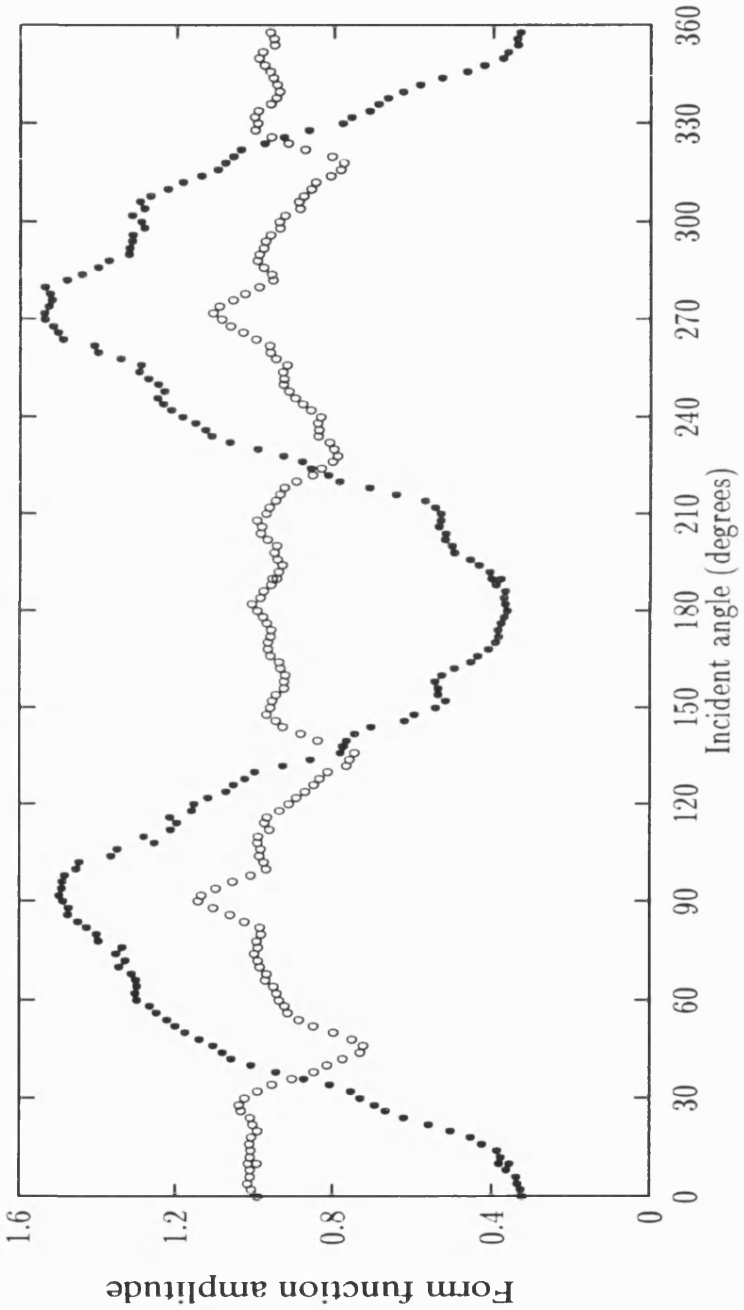

6 Anisotropy

6.1 Introduction

The scattering of acoustic waves by objects of various geometry, made of isotropic materials, has been extensively studied over the years. Many structures of interest in the underwater environment are comprised, in part at least, of panels or layers of material. A brief review of the theoretical aspects of isotropic layers has been given in Chapter 2. Less attention has been paid to materials which are *anisotropic*, such as fibrous composites. For anisotropic media the theoretical approaches described in Chapter 2 are not applicable, and other models must be sought. One reason for the comparative paucity of research on scattering from objects made of such complex materials is the greatly increased complexity of the equations describing propagation in anisotropic elastic media, and the resultant computational problems, which often prohibit solution. With the current trend towards faster and more powerful computing systems, it becomes possible to computationaly investigate scattering problems that involve anisotropy (and other complexities).

Fibre-reinforced materials are increasingly being used in the marine environment for the construction of strong, lightweight, structures. One advantage of these, and other composite materials, is that their acoustic and elastic properties can potentially be determined at the design stage; allowing structures with prescribed (or optimal) acoustic performance to be built. A good introduction and review of the use of composites in marine structures is given by Smith (1990).

Much of the study reported in this thesis has concerned itself with the acoustics of cylindrical shells made of isotropic materials. The question arises, what effect does anisotropy have upon the acoustic behaviour of such cylindrical objects (or other axisymmetric structures) ? However, before the acoustics of such complex structures can be investigated it is necessary to develop theoretical models and experimental techniques to investigate the simpler case of the planar geometry. Obviously this case is also of importance in its own right. What we ultimately wish to know is how the

presence of anisotropy affects the acoustics of structures of various geometry, and how it can be used to advantage. This Chapter concerns itself with the anisotropy of *planar* layered media.

Advanced composites, such as fibre-reinforced materials, are both anisotropic and inhomogeneous. For low frequencies where the wavelength is much greater than the fibre dimension, the material can be assumed to be homogeneous, although this assumption may break down in certain composites due to the presence of voids, bubbles and other defects resulting from the manufacturing process. Assuming the materials to be homogeneous, we can use theories of anisotropic elasticity to model the acoustics of fibrous materials, and the structures that incorporate them.

In the case of the flat anisotropic plate the main differences from the isotropic case, described in Chapter 2, are (i) the type of waves that propagate, (ii) the number of waves that propagate, (iii) the variation of velocity with direction, (iv) the deviation of the direction of energy flow from the direction of the wave vector, and, (v) the interaction of three distinct modes at the boundaries of the layer.

In this chapter we shall present the results of an experimental study into the acoustic behaviour of a glass-reinforced plastic panel. The parametric array facility described in Chapter 4 has been employed in this study. In order to interpret experimental measurements made in the laboratory, it is important to develop theoretical models that predict the acoustics of such anisotropic laminates. In this way we can hope to discover which features in the experimental results can be attributed to anisotropy, and which should be attributed to other causes. The model used here for wave propagation involving anisotropic layered media was based upon that of James (1990) which has subsequently been published (Skelton & James, 1992).

We discuss wave propagation in anisotropic materials and the acoustics of planar anisotropic laminates. We illustrate theoretical and experimental techniques by presenting results for a unidirectional layer which clearly illustrates the differences in acoustic behaviour between isotropic and anisotropic materials.

Our primary interests in this chapter are: the application of the parametric array facility; the development and validation of the theory; and the differences in acoustic behaviour from that of the isotropic layer.

Musgrave (1954a) was one of the first to study in detail the propagation of waves in anisotropic media, paying particular attention to hexagonal media (Musgrave, 1954b). Good introductions to wave propagation in unbounded anisotropic media are given in the books by Musgrave (1970) and Auld (1990).

One reason that the anisotropic layer is of interest is due to the 'free modes' of vibration of such layers, and their effect upon the scattering behaviour of the layer. Although such guided waves in the isotropic layer are well understood, the anisotropic layer has received much less attention. The propagation of waves in anisotropic layers was first studied by Solie & Auld (1973). The main interest lies in the field of ultrasonic testing of materials. A more recent introduction and review of the plate wave modes of the anisotropic layer is contained in Li & Thompson (1990).

Transmission and reflection by the anisotropic layer have been dealt with by Chedid-Helou & Hemann (1991), Mal & Ting (1988) and Nayfeh & Chimenti (1991), among many others. The characterization of anisotropic materials and determination of their elastic constants is a field that has attracted enormous interest in the last few decades, but this aspect is not dealt with here. An example of the techniques used to obtained elastic constants for orthotropic materials is given by Hosten (1991).

A new approach to the acoustics of anisotropic planar layered media was proposed by James (1990), for orthotropic media, and Skelton & James (1992), for general (triclinic) media. This approach, to be described in this thesis, is currently being applied to fibre-reinforced laminates of other geometry (Skelton, 1993), such as the anisotropic cylindrical shell.

The use of a parametric array facility for making reflection and transmission measurements on flat plates was mentioned in Chapter 4. Of the work reviewed there, Humphrey (1985) gave a single experimental result for a glass-reinforced plastic panel

at normal incidence. This result does, in a sense, mark the very beginning of the investigations into anisotropic layered media undertaken at Bath, of which the current work is a part.

6.2 Theory

The theoretical model used in our study of the acoustics of anisotropic laminates is developed in stages, in a manner that hopefully gives insight into the way the acoustics of fibrous layered media differ from those of isotropic materials described in Chapter 2. Firstly we discuss how fibrous composites can be modelled as anisotropic media, and how wave propagation in such anisotropic media can be modelled. We then discuss wave propagation involving a *layer* of anisotropic material, the *free* vibrations of the layer, and, finally, the interaction of a *plane wave* with the layer. The non-planar nature of the parametric source will be discussed in a subsequent section (6.4.4), after the experimental results have been presented.

6.2.1 Modelling fibrous composites

Under certain conditions a composite material can be modelled as a crystalline medium possessing a set of 'effective elastic constants'. These effective constants can be measured experimentally, or predicted theoretically if the composite is modelled correctly. Models of fibre-reinforced composites make certain assumptions about the fibres, the matrix, and the interaction between them. These assumptions must be remembered when using effective elastic constants in mathematical models involving the composite.

We first assume that the fibres are straight, parallel, of uniform cross-section, and extend continuously through the matrix. We also assume that the matrix is homogeneous and free of defects (Tewary, 1978). If we assume that the fibres are distributed randomly throughout the matrix then the composite possesses 'transverse isotropy' and can be modelled as a hexagonal medium, having five independent elastic constants. In practice, due to manufacturing techniques, the composite may not possesses transverse isotropy, and is better modelled as orthotropic, as Nayfeh & Chimenti (1988) have found.

6.2.1.1 Experimental determination of effective elastic constants.

Because the velocities of waves in a material are related to the elastic constants, ultrasonic velocity measurement techniques can be used to determine the constants. In general, the greater the number of constants to be determined, the more ultrasonic velocity data must be obtained, and the more complex is the mathematical manipulation of the data required to extract the constants. The material used in the measurements described in this thesis was modelled as a hexagonal medium; the five stiffness constants (C_{ij}) were previously determined (Sutton & Ryall, 1986) using the velocity technique. The data obtained is shown in Table 6.1 and is used throughout the chapter.

C_{11} (GPa)	C_{12}	C_{23}	C_{44}	C_{33}	Density (Kgm^{-3})	Thickness (mm)
13.2	6.2	6.4	3.6	27.0	1660	11.4

Table 6.1 Material properties of glass-reinforced plastic (Sutton & Ryall, 1986).

6.2.2 Waves in anisotropic media

In this section we consider the case of wave propagation in bulk anisotropic media. We concentrate first on the characterization of an anisotropic media, the propagation of waves in an unbounded anisotropic media, and then discuss some predicted properties of the fibrous composite material of interest in the present study.

In Chapter 2, wave propagation in isotropic media was discussed, and it was seen how the displacements could be expressed in terms of two potentials governing the propagation of compressional and shear waves. This is not the case for general anisotropic media, and an alternative approach must be taken.

6.2.2.1 Characterisation of anisotropic media

Mathematically, the elastic properties of a material are described by the elastic stiffness constants (c_{ijkl}) which relate the stresses in the material ($\mathcal{T}$) to the strains (Σ):

$$\mathcal{T}_{ij} = c_{ijkl}\Sigma_{kl} \qquad [i,j,k,l = x,y,z] \ . \tag{6.1}$$

Although c is a fourth rank tensor having 81 elements, only 21 of them are independent. Using the reduced subscript notation (Appendix C1) these 21 elements can be written as the elements of a sixth order symmetric matrix C. In this notation the stress tensor reduces to a vector with six elements $[\mathcal{T}_1, \mathcal{T}_2, \mathcal{T}_3, \mathcal{T}_4, \mathcal{T}_5, \mathcal{T}_6]^t$, representing the six independent elements of stress. Similarly there is a corresponding vector of strains. The stress - strain relation (6.1) can then be written

$$\mathcal{T}_i = C_{ij}\Sigma_j \qquad [i,j = 1 \rightarrow 6] \tag{6.2}$$

and the strain - displacement relation is

$$\Sigma_j = \nabla_{jk}U_k \qquad \left[\begin{smallmatrix} j = 1 \rightarrow 6 \\ k = 1 \rightarrow 3 \end{smallmatrix}\right] \tag{6.3}$$

where the differential operator (∇) is defined in Appendix C1.

The case where all 21 elastic constants are independent corresponds to media whose symmetry are described by the triclinic point group. For media possessing greater symmetry the elastic stiffness matrix simplifies, as many of the elements are interdependent. For hexagonal materials there are five independent elements. In a coordinate system in which the principal axis of symmetry is the z-axis (Figure 6.1) the stiffness matrix for hexagonal media is

$$C = \begin{pmatrix} C_{11} & C_{12} & C_{13} & 0 & 0 & 0 \\ C_{12} & C_{11} & C_{13} & 0 & 0 & 0 \\ C_{13} & C_{13} & C_{33} & 0 & 0 & 0 \\ 0 & 0 & 0 & C_{44} & 0 & 0 \\ 0 & 0 & 0 & 0 & C_{44} & 0 \\ 0 & 0 & 0 & 0 & 0 & \frac{1}{2}(C_{11} - C_{12}) \end{pmatrix} . \tag{6.4}$$

The term $C_{66} = (C_{11} - C_{12})/2$ reflects the transverse isotropy of hexagonal media. In a coordinate system (x', y', z') rotated with respect to this system, elements of the stiffness matrix are given by

$$C'_{ij}(x', y', z') = M_{ik} M_{jl} C_{kl}(x, y, z), \tag{6.5}$$

where M is the Bond stress transformation matrix (Appendix C1). For the case of a fibre-reinforced layer in which the principal axis (fibre direction) is the y-axis the transformed matrix is

$$C' = \begin{pmatrix} C_{11} & C_{13} & C_{12} & 0 & 0 & 0 \\ C_{13} & C_{33} & C_{13} & 0 & 0 & 0 \\ C_{12} & C_{13} & C_{11} & 0 & 0 & 0 \\ 0 & 0 & 0 & C_{44} & 0 & 0 \\ 0 & 0 & 0 & 0 & \frac{1}{2}(C_{11} - C_{12}) & 0 \\ 0 & 0 & 0 & 0 & 0 & C_{44} \end{pmatrix}. \tag{6.6}$$

Both (6.4) and (6.6) are degenerate forms of the *orthotropic* stiffness matrix;

$$C = \begin{pmatrix} C_{11} & C_{12} & C_{13} & 0 & 0 & 0 \\ C_{12} & C_{22} & C_{23} & 0 & 0 & 0 \\ C_{13} & C_{23} & C_{33} & 0 & 0 & 0 \\ 0 & 0 & 0 & C_{44} & 0 & 0 \\ 0 & 0 & 0 & 0 & C_{55} & 0 \\ 0 & 0 & 0 & 0 & 0 & C_{66} \end{pmatrix} \tag{6.7}$$

having *nine* independent elements.

6.2.2.2 Wave propagation in anisotropic media

Having characterized fibre-reinforced materials by the elastic stiffness constants of anisotropic crystalline media, we now turn our attention to the propagation of waves in such media. We will develop the theory for an orthotropic medium; hexagonal and isotropic media being just special cases involving degenerate stiffness constants.

In a source free medium acoustic waves must satisfy the acoustic field equation

$$\frac{\partial \mathcal{T}_{ij}}{\partial x_j} = \rho \frac{\partial^2 U_i}{\partial t^2} = -\rho\omega^2 U_i \qquad [i,j = 1,2,3] \tag{6.8}$$

where U is the displacement vector, ρ is the density of the medium and ω is the angular frequency of waves, assumed to have a time dependence $e^{i\omega t}$. In reduced subscript notation the equation is written

$$\nabla_{ij} \cdot \mathcal{T}_j = -\rho\omega^2 U_i \qquad \left[\begin{smallmatrix} i=1\to 3 \\ j=1\to 6 \end{smallmatrix}\right] \tag{6.9}$$

where the differential operator $\nabla\cdot$ is defined in Appendix C1. Substituting (6.2) and (6.3) into (6.9) we obtain

$$[\nabla_{ij} \cdot C_{jk} \nabla_{kl} + \rho\omega^2 \delta_{il}] U_l = 0 \tag{6.10}$$

which is the anisotropic equivalent of equation (2.1). Equation (6.10) is more usually written

$$[k^2 \Gamma_{il} - \rho\omega^2 \delta_{il}] U_l = 0 \qquad [i,l = 1,2,3] \tag{6.11}$$

where k is the wave number, δ is the Kroneker delta and Γ is the symmetric 'Christoffel Matrix' whose elements are functions only of the direction of propagation of the wave in the medium. For an orthotropic medium the elements of Γ are given in Appendix C2. For (6.11) to be true requires that the characteristic determinant vanish;

$$| k^2 \Gamma - \rho\omega^2 \delta | = 0. \tag{6.12}$$

For fixed ω this is a cubic equation in k_x^2, k_y^2 and k_z^2. It is a dispersion relation that describes how k varies with its direction in the medium, the roots $\pm k^l$ ($l = 1,2,3$) representing three distinct waves. The dispersion relation therefore has three sheets, in k-space, known as the wave vector surfaces. The displacements, found by back-substituting the roots k^l into (6.10), have components both parallel and perpendicular to the direction of propagation, and so cannot be described as pure compressional or pure shear waves. However, the displacement vectors of the three waves are mutually orthogonal,

so that there exists one wave with displacement vector closer to the direction of propagation than to a plane normal to it; the remaining two waves having displacements closer to the plane normal to the propagation direction. The former wave can be described as 'quasi-compressional' and the latter as 'quasi-shear' waves. Only in special directions in the medium will waves be pure shear or pure compressional; these directions are called 'Pure Mode Directions' and can include *non*-symmetry as well as symmetry directions (Auld, 1990). Instead of the 'wave vector surface', the directional dependence of the propagation characteristics of a medium are usually illustrated by the 'slowness surface', or, inverse velocity surface, which shows how k/ω $(= 1/velocity)$ varies with direction for each of the three different waves.

6.2.2.3 Slowness curves for glass-reinforced plastic

Using the measured data for glass-reinforced plastic (Table 6.1, section 6.2.1) we are able to calculate sections of the slowness surface for this material. Figures 6.2-6.4 show sections of the slowness surface for three planes orientated at different angles to the fibre direction.

Figure 6.2 shows the variation in slowness of the three waves when they propagate in the plane of transverse isotropy. S_n is the component of slowness normal to the symmetry axis of the material and S_r is the component perpendicular to this in the plane of propagation of the waves; in this case S_r is *also* normal to the symmetry axis and so both directions are equivalent. All the waves are *pure* waves; the innermost curve representing the compressional wave and the outer curves representing the shear waves. In general the shear wave whose displacement vector is normal to the plane of incidence (along the symmetry axis) has a different velocity to that of the shear wave whose displacement is in the transverse plane itself, and this is reflected in differing magnitudes of the (constant) slowness for the two waves (i.e. different radius circles) as shown in Figure 6.2. For this particular material the difference is rather small.

Figure 6.3 shows how the slowness of the three waves vary when propagation is in a plane containing the symmetry axis, i.e. a *zonal* plane. Here S_r is the slowness

component along the fibre axis. In this case only the wave whose displacement vector is normal to the plane of propagation, and thus normal to the symmetry axis, will be pure shear, the other two waves being quasi-shear and quasi-compressional, as is reflected in the varying magnitude of their slowness as a function of propagation direction. It can be seen that the two 'shear' wave velocities are the same when propagation is along the symmetry axis itself, this is because both displacements vectors are again in the transverse plane. These shear waves propagate with a velocity equal to that of the shear wave which propagates in the direction normal to the fibres with displacement vector parallel to the fibres (Figure 6.2).

The more general case of waves propagating in the plane orientated at 45° to the symmetry axis is shown in Figure 6.4. None of the waves are pure here, the constancy of one of the shear branches is due to the near degenerate nature of the measured elastic constants.

It would appear that for the material characterized by the measured effective elastic constants there is a shear wave that is pure for propagation in all directions, this may be due to the method by which the constants were obtained.

6.2.3 Waves in an anisotropic layer

In this section we present the theory for propagation of waves in a planar layer of anisotropic solid. The elastic layer is characterized by a 'stiffness matrix' which relates the stresses and displacements at the surfaces of the layer. The theoretical details pertaining to the fluid loading of a layer, the free vibrations of a layer, and the reflection and transmission of waves by the layer, are not directly dependent on the layer constitution (i.e. isotropic or anisotropic); only the stiffness matrix for the layer need be known. So although the properties of anisotropic and isotropic layers will obviously be quite different, having obtained expressions relating the displacements and stresses at the surfaces of a given layer, subsequent theoretical development is essentially the same as for the isotropic layered media. The theoretical development presented here is based upon that of James (1990).

6.2.3.1 Stiffness relation for an anisotropic layer

For the anisotropic layer we must solve the Christoffel Equation (6.10) to obtain the surface displacements and again use equations (6.2) and (6.3) to obtain the surface stresses. The derivation is rather lengthy; details are summarized in Appendices C3-C5. The equation is solved in the *spectral* domain[1] where the differential equations are reduced to algebraic equations facilitating a simpler solution. The equations are solved for media possessing orthotropic symmetry. The geometry is as shown in Figure 6.5. A relationship between surface spectral stresses ($\overline{T}^{1,2}$) and surface spectral displacements ($\overline{U}^{1,2}$) is obtained;

$$\begin{pmatrix} \overline{T}^1 \\ \overline{T}^2 \end{pmatrix} = \begin{pmatrix} \mathcal{S}_{11} & \mathcal{S}_{12} \\ \mathcal{S}_{21} & \mathcal{S}_{22} \end{pmatrix} \begin{pmatrix} \overline{U}^1 \\ \overline{U}^2 \end{pmatrix} \tag{6.13}$$

where $\mathcal{S}_{ij}$ are 3 by 3 submatrices. This relationship is the analogue of equations (2.4) for the isotropic layer.

This then is the relationship between the stresses in the layer at the upper and lower interfaces and the displacements of these interfaces. At a given frequency ω and given wave numbers (k_x and k_y), the elements of the matrix $\mathcal{S}$, known as the 'stiffness coupling matrix', are functions of the elastic constants, density, and thickness of the layer.

The anisotropic layer thus described, is essentially an elastic 'finite element', and can be easily incorporated into various planar scattering systems. As yet, no mention has been made of the fluid loading to which the anisotropic layer is subjected.

6.2.3.2 Fluid loading and the 'stiffness relation' for the layer

Similar relationships between the stresses (pressures) and displacements in the fluid half-spaces can be derived; details are given in Appendix C6. Denoting the stresses in the fluid at the upper and lower interfaces T^1 and T^2 respectively, relations of the form

1 Spectral forms of variables are defined in Appendix C3.

$$T^{1,2} = \mp S_f U^{1,2} \tag{6.14}$$

are obtained where S_f is the 'stiffness matrix' for the fluid half-spaces and has only one non-zero element, as would be expected.

The formulation so far has made no mention of any coupling between the elastic layer and the loading acoustic half-spaces, neither of any means of exciting the system. We will here introduce excitations as we 'assemble' the system (layer and fluid half-spaces) by asserting conditions of joint equilibrium at the upper and lower interfaces (Figure 6.5). In what follows we will omit the notation for spectral forms of variables.

At the upper interface, for equilibrium to be maintained, we must have

$$F^1 = \mathcal{T}^1 - T^1 \tag{6.15}$$

where F^1 is a vector describing the external force applied to interface (1). Such forces are defined to be positive when acting in the positive z direction. Substituting for $\mathcal{T}$ and T using (6.13) and (6.14) we obtain

$$F^1 = \mathcal{S}_{11} U^1 + \mathcal{S}_{12} U^2 + S_f U^1, \tag{6.16}$$

where $[S_f]_{33} = \rho_f \omega^2 / i\gamma$ is the contribution from the fluid loading half-spaces (all other $[S_f]_{ij}$ are zero). Similarly, at the lower interface (Figure 6.5)

$$F^2 = -\mathcal{T}^2 + T^2, \tag{6.17}$$

from which

$$F^2 = -\mathcal{S}_{21} U^1 - \mathcal{S}_{22} U^2 + S_f U^2. \tag{6.18}$$

Equations (6.16) and (6.18) together constitute a matrix relation between the applied stresses $F^{1,2}$ and the interfacial displacements $U^{1,2}$;

$$\begin{pmatrix} F^1 \\ F^2 \end{pmatrix} = \underline{\underline{\mathcal{S}}} \begin{pmatrix} U^1 \\ U^2 \end{pmatrix} \tag{6.19}$$

where

$$S = \begin{pmatrix} \mathcal{S}_{11}+\mathcal{S}_f & \mathcal{S}_{12} \\ -\mathcal{S}_{21} & -\mathcal{S}_{22}+\mathcal{S}_f \end{pmatrix}. \tag{6.20}$$

Defining a vector of interfacial applied stresses, or excitations; $\mathcal{F}=(F^1,F^2)$ and displacements $\mathcal{U}=(U^1,U^2)$, we can write

$$\mathcal{F} = S\,\mathcal{U} \tag{6.21}$$

which is a 'stiffness relation' between applied interfacial stresses and interfacial displacements. We note that (6.21) can be used to model waves in *unloaded* layers by setting $\rho_f=0$ in the term for $\mathcal{S}_f$.

6.2.3.3 Résumé

In this section (6.2.3) we have derived a stiffness relation for a layer of anisotropic material having orthotropic symmetry. For the anisotropic layer we have solved the Christoffel equation for orthotropic media in the spectral domain. Similar relations have been obtained for the fluid half-spaces that bound the layer above and below, and the system was 'assembled' to produce a final 'stiffness relation' in terms of interfacial excitations, which could take any form. A following section will describe excitation by plane wave; other excitations are described by Skelton & James (1992). The method of solution outlined in this section is easily generalized to multilayered media by asserting conditions of joint equilibrium at *all* the interfaces between the layers. The matrix $\mathcal{S}$ is then of a higher order and $\mathcal{U}$ and $\mathcal{F}$ are vectors of interfacial displacements and applied forces for the whole multilayered system. This generalisation has been undertaken by the author and results were presented in Chinnery (1991).

Before considering the excitation of the system by an incident plane wave we will discuss the free modes of vibration of the system.

6.2.4 Plate waves

In Chapter 2 we discussed the free modes of vibration of the isotropic elastic layer. In this section the solution for the free modes of a general anisotropic layer is given in terms of the stiffness matrix derived above. This method allows us to calculate the dispersion curves for the free modes of a fluid loaded elastic plate.

We consider the stiffness relation (6.21) relating the applied stresses at the surface of the layer to the displacements of the layer boundaries. The very nature of a 'free' wave is simply the requirement that there be no applied stresses ($F^1 = F^2 = 0$) at the layer surfaces. From (6.21) this implies

$$det[S(\xi^n, \omega)] = 0. \tag{6.22}$$

The roots ξ^n are the wave numbers of the propagating modes. In the general case of a fluid loaded plate the phase velocities of free waves are found from

$$V^n = \frac{\omega}{Re(\xi^n)}, \tag{6.23}$$

and the attenuation of leaky modes is given by $Im(\xi^n)$. The complex solutions (ξ^n) of (6.22) can be found by using Newtons Secant method or Reguli Falsi for complex variables.

An angular variable (θ) can be associated with a given free mode in the plate. From Snells law connecting the angles of wave propagation in the fluid and the layer we have

$$\frac{\sin(\theta)}{c_f} = \frac{\sin\left(\frac{\pi}{2}\right)}{V^n}, \tag{6.24}$$

whence

$$\theta = \sin^{-1}\left(\frac{c_f}{V^n}\right). \tag{6.25}$$

This is the angle at which leaky modes radiate waves into the fluid. It is also the angle at which plate waves are excited by an incoming plane wave.

When no fluid loading is present (plate in vacuum) the same method can be applied with fluid half-spaces of zero density. The solutions ξ^n are then *real,* reflecting the fact that modes are not attenuated and there is no leakage into the half-spaces.

6.2.5 Plane wave incidence

In this section the elastic layer, characterized by its stiffness matrix, is excited by a plane wave disturbance at the first interface ($z = d$). The reflection and transmission coefficients of the layer are calculated from the stiffness relation (6.21) with appropriate applied stresses.

6.2.5.1 Waves in the fluid

A plane wave,

$$P_{in} = e^{i(\underline{k}_{in} \cdot \underline{r} - \omega t)} \quad ; \quad \underline{k}_{in} \cdot \underline{r} = \alpha x + \beta y + \gamma(z - d), \tag{6.26}$$

with

$$\alpha = -k_{in} \sin\theta \cos\phi \qquad \beta = -k_{in} \sin\theta \sin\phi \qquad \gamma = -k_{in} \cos\theta, \tag{6.27}$$

is incident upon the layer (Figure 6.6). The 'angle of incidence' is θ and the 'plane of incidence' makes an angle ϕ with the fibre direction. Here k_{in} is the wave number of the incident wave whose components are α, β and γ. The reflected and transmitted waves are

$$\begin{aligned} P_{rf} &= \Re\, e^{i(\underline{k}_{rf} \cdot \underline{r} - \omega t)} \quad ; \quad \underline{k}_{rf} \cdot \underline{r} = \alpha x + \beta y - \gamma(z - d) \\ P_{tr} &= \Pi\, e^{i(\underline{k}_{tr} \cdot \underline{r} - \omega t)} \quad ; \quad \underline{k}_{tr} \cdot \underline{r} = \alpha x + \beta y + \gamma z \end{aligned} \tag{6.28}$$

where $\Re$ and Π are the reflection and transmission coefficients respectively; yet to be determined.

6.2.5.2 Elastic layer: applied stresses

The only applied stress is the normal pressure at the first interface;

$$\begin{aligned} F_x^1 &= F_y^1 = 0 \\ F_z^1 &= -P^{applied} = -\,e^{i(\alpha x+\beta y)}(e^{-i\gamma(z-d)}+e^{i\gamma(z-d)})\,|_{z=d} = -2e^{i(\alpha x+\beta y)} \\ F^2 &= (0,0,0)^t. \end{aligned} \tag{6.29}$$

In the spectral domain this gives

$$\begin{aligned} \overline{F}_z^1(k_x,k_y,d) &= -2\int\int e^{i(\alpha x+\beta y)}e^{-i(k_x x+k_y y)}dxdy \\ &= -2\int e^{i(\alpha-k_x)x}dx\int e^{i(\beta-k_y)y}dy, \end{aligned} \tag{6.30}$$

yielding

$$\overline{F}_z^1 = \begin{cases} -2 & if \quad k_x=\alpha \quad \text{and} \quad k_y=\beta \\ 0 & if \quad k_x\neq\alpha \quad \text{or} \quad k_y\neq\beta \end{cases}. \tag{6.31}$$

This result reflects the 'monochromatic' nature of the incident plane wave. Substituting these values into (6.19) results in

$$U^2 = [S_{12}-(S_{11}-S_f)S_{21}^{-1}(S_{22}+S_f)]^{-1}\begin{bmatrix} 0 \\ 0 \\ -2 \end{bmatrix}, \tag{6.32}$$

and

$$U^1 = -S_{21}^{-1}(S_{22}+S_f)U^2. \tag{6.33}$$

These then are the displacements of the first and second interfaces when the fluid loaded layer is excited by a plane wave disturbance at the first interface. Values of $k_x=\alpha$ and $k_y=\beta$ are used in the calculation of the elastic layer stiffness matrix S. The transmission coefficient is then obtained by solving

$$U_z^2=\left(\frac{1}{\rho_f\omega^2}\right)\frac{\partial P_{tr}}{\partial z}\bigg|_{z=0} \tag{6.34}$$

to obtain

$$\Pi = -\frac{\rho_f \omega^2}{i\gamma} U_z^2, \tag{6.35}$$

and similarly for the reflection coefficient.

6.3 Implementation

Computer programs were written in Fortran to implement the theories described in this chapter. Plane wave transmission and reflection losses can be calculated for a wave of given frequency, incident at any angle upon a multilayered system composed of any number of elastic layers, bounded above and below by fluid half-spaces. Each layer is described by a set of stiffness constants, a thickness, and a density. The elastic constants of each layer are transformed such that they describe the properties of that layer in the global coordinate system defined by the geometry of the incoming wave. Loss can be incorporated by using complex stiffness constants for the elastic material. The free waves in the layer can also be calculated, with and without fluid loading.

Prior to the experimental investigation, preliminary theoretical studies of the transmission properties of anisotropic layers, and multilayered systems, were undertaken using this implementation of the theory (Chinnery, 1991). Results were obtained for aluminium, boron-reinforced aluminium, titanium, glass-reinforced plastic, and graphite-reinforced plastic layers. Titanium is of particular interest as it is a metal having a hexagonal crystal structure and would be expected to exhibit some differences in behaviour from more conventional metals such as aluminium or steel. The benefits of using titanium in construction of structures in the marine environment include its non-magnetic property and its resistance to corrosion (Chalmers, 1988).

The effect of stacking multiple layers of glass-reinforced plastic in different configurations has also been investigated (Chinnery, 1991). Results for anisotropic layers indicated that significant deviations from the behaviour of an isotropic layer were to be expected, in particular with regard to the plane of incidence (with respect to the fibres of a uniaxial layer).

The theory was extended in an attempt to incorporate the effects of the non-planar wave-field produced by a parametric source. The model for this is described later. Again, notable differences were observed between the results for the parametric source and plane wave incidence.

The model could easily be generalized to allow materials of triclinic symmetry to be included. Fluid layers could also be included in the implementation (Skelton & James, 1992).

After obtaining the preliminary results presented in Chinnery (1991) it was decided to focus attention on fibrous composites such as glass (and carbon) reinforced plastics. With this agenda in mind a series of parallel theoretical and experimental studies were undertaken, some of which are described in the following section.

6.4 Results

In this section we present theoretical and experimental results for a single uniaxial glass-reinforced plastic layer. The aims of this study are: to validate the theoretical predictions; to illustrate the problems involved in making measurements on anisotropic panels; to demonstrate the differences in behaviour of fibrous composites; and to investigate the consequences of the non-planar nature of the parametric source. Experimental results for other fibrous composites, both uniaxial and biaxial, have been given in Chinnery (1992).

6.4.1 Introduction

The panel used in these measurements was $450mm \times 450mm \times 11.4mm$ in size. The five elastic constants describing this hexagonal material had previously been obtained from velocity measurements made at $500kHz$ using the immersion technique (Table 6.1, section 6.2.1). As no attenuation data for this material was available, damping was simulated by using complex stiffness constants with a small imaginary part ($C_{ij}(1-0.01i)$). Theoretical and experimental results are presented for the cases where the plane of incidence (ϕ) is at 0, 90 and 45 degrees to the fibre direction. In each case

the incident angle (θ) was varied from 0° to 60° in 1° steps. This panel was chosen for detailed investigation and comparison with theoretical predictions because it was a particularly well made sample. It was free of inhomogeneities, bubbles and defects; it was exceptionally flat; and it was well characterized. Other samples obtained for testing were not so good in these respects. The geometry is shown in Figure 6.6.

6.4.2 Theoretical predictions

In Figure 6.7 we present theoretical predictions of the plane wave transmission characteristics of the layer for the three cases. The contour plots show transmission loss of the layer as a function of both incident angle (θ) and frequency. The light areas are regions of high transmission loss. The behaviour seen in Figure 6.7(a) is what we expect for an isotropic layer; in this case wave propagation is in the plane of transverse isotropy, and all the waves are pure compressional or pure shear waves. Comparison with the predictions for an isotropic layer (Figure 2.2) show that the acoustics in the transverse plane is, as we expect, essentially that of an isotropic layer.

In Figure 6.7(b), for propagation in the plane orientated at 45° to the fibre direction, the behaviour is considerably more complex; more 'resonance' features appear in addition to those seen in the transverse plane. The case of propagation in the plane parallel to the fibres is shown in Figure 6.7(c). This is again a symmetry direction of the material and the transmission behaviour is again as simple as case (a), but resonance features occur at different frequencies and incident angles.

The dispersion curves of the free modes of vibration of the layer (in vacuum) are given in Figure 6.8 as a function of the frequency thickness product. It is known that these modes, and the interactions between them, are largely responsible for the resonance features seen in the transmission and reflection behaviour of the layer; indeed many of the modes can be associated directly with features in the transmission loss plots (Figure 6.7). We note that the subsonic modes (where $V^n < c_f$) will *not* be excited by plane wave incidence ($\theta = 90°$ when $V^n = c_f$). Figure 6.8(a) can be compared with the predictions for the free modes of an isotropic layer shown in Figure 2.3. All the modes of the ani-

sotropic layer are present in the isotropic case, and are coincident with them, again confirming that the layer is behaving as an isotropic layer in this plane. The modes shown in Figure 2.3 that are *absent* from Figure 6.8(a) are the *Love* waves. These modes result in no normal displacement of the layer interfaces, thus no loss of energy into the fluid; making the modes, as defined by equation (6.22), infinitely narrow and thus undetectable by this numerical method[1]. As these modes play no part in the transmission behaviour of the layer this is not a problem.

The situation shown in Figure 6.8(b) is completely different. Not only do the modes occur at different frequencies (or have different velocities) from those of the transverse case (and the isotropic layer), but additional modes are present. These additional modes are reminiscent of the Love waves of Figure 2.3, and have been shown to be of a 'Love-like' nature. In essence, what we see here are quasi-Lamb waves and quasi-Love waves; modes having mixed displacement vectors. The quasi-Love modes, for instance, have a non-zero component of displacement normal to the interfaces, which is why they are being detected by the numerical search. In comparing the two cases, the different distribution of modes and the presence of additional modes in Figure 6.8(b) is thought to be responsible for the new features seen in Figure 6.7(b). Thus the previously unimportant shear type waves of an isotropic plate are now of great importance in determining the acoustic properties of the anisotropic layer. In particular, the presence of a low velocity mode ($\sim 1800 m/s$) at low frequencies (frequency-thickness < 1500) gives rise to effects seen at high incidence angles. This behaviour reflects the destruction of symmetry of the material and the independent propagation of three quasi-compressional/shear waves, and their mode conversions at the interfaces.

Figure 6.8(c) shows the free wave dispersion curves for propagation in the plane parallel to the fibre direction. The additional modes are not present here, but the quasi-Lamb waves occur at different locations to those of the transverse case, again explaining the difference in form of the plane wave transmission properties of the layer in the two orientations shown in Figures 6.7(a) and (c).

1 These modes *can* however be detected if an extremely fine search interval is employed, as the necessarily finite precision of the computer gives the modes a small, but finite, width.

6.4.3 Experimental results

Transmission loss measurements were made using the system and procedures described in Chapter 4. The panel was suspended from the rotation stage in different orientations such that the fibres cut the plane of incidence at different angles (ϕ). The array was truncated at a distance of $0.48m$ from the transducer face and the hydrophone placed $1.18m$ from the transducer (see Figure 4.1). A sequence of measurements was made with the panel being rotated in 1° steps. A reference measurement was made without the panel in position, and the transmission coefficient calculated by dividing the spectrum of each averaged signal by the spectrum of the reference measurement. The experimental results are given in Figures 6.9.

The main differences between the plane wave predictions of Figure 6.7 and the experimental results are (i) a broadening of the transmission loss features and (ii) a slight variation in the angles at which features occur, particularly at low frequencies. These are similar to the effects that have been observed for isotropic panels when using a non-planar source, such as the parametric array. With this in mind, the theoretical model was extended to take into account this aspect of the incident wave-field. This extended model will be presented in the following section.

The 'banding' at low frequencies is thought to be due to the presence of a multiple signal in the time window analysed. The most likely cause for this signal is either diffraction by the edges of the plate, or re-radiation of signals travelling along the plate and reflecting from the edges. Such unwanted signals have been observed in other measurements involving anisotropic panels (Humphrey, Anastadiasis & Dyer, 1992) and are found to be more pronounced than for metal plates.

6.4.4 Plane wave spectrum of the parametric array

The acoustic field produced by a parametric array is not an infinite plane wave but a finite beam having an angular spectrum of plane waves. This aspect of the parametric source and its influence upon transmission and reflection loss measurements has been described in detail by Humphrey & Berktay (1985) for the isotropic layer. In this section

we discuss how the transmission coefficient of an anisotropic layer measured with such a source can be predicted. The 'line array' model of the parametric array is used (Berktay, 1965).

6.4.4.1 Field of a parametric array

The field at a point R on the axis of parametric array of length L inclined at angles θ_0 and ϕ_0 to the coordinate axis (Figure 6.10) is given by

$$\psi(\theta_0, \phi_0, R) = \int_0^L e^{ikr} \frac{e^{ik(R-r)}}{R-r} \, dr \tag{6.36}$$

where r is measured along the array axis, and k is the wave vector inclined at angles (θ, ϕ) to the coordinate axis. The first term (e^{ikr}) is the initial phase of the secondary spherical sources. The integral is calculated over the entire length of the array (all sources).

We expand the spherical term as a spectrum of plane waves;

$$\frac{e^{ikr'}}{r'} = \frac{ik}{2\pi} \int_0^{\pi/2 - j\infty} \int_0^{2\pi} e^{i\underline{k} \cdot \underline{r}'} \sin\theta \, d\theta \, d\phi \tag{6.37}$$

where $r' = R - r$. Inspection of Figure 6.10 shows that, for this geometry,

$$\underline{k} \cdot \underline{r}' = kr'\Lambda(\theta, \phi), \tag{6.38}$$

where

$$\Lambda = \sin\theta \sin\theta_0 \cos(\phi - \phi_0) + \cos\theta \cos\theta_0. \tag{6.39}$$

Thus

$$\frac{e^{ik(R-r)}}{R-r} = \frac{ik}{2\pi} \int_0^{\pi/2 - j\infty} \int_0^{2\pi} e^{ik(R-r)\Lambda} \sin\theta \, d\theta \, d\phi. \tag{6.40}$$

Substituting this into equation (6.36) gives

$$\psi(\theta_0,\phi_0,R)=\frac{ik}{2\pi}\int_0^L e^{ikr}\int_0^{\pi/2-j\infty}\int_0^{2\pi} e^{ikR\Lambda}e^{-ikr\Lambda}\,dr\,\sin\theta\,d\theta\,d\phi$$
$$=\frac{ik}{2\pi}\int_0^{\pi/2-j\infty}\int_0^{2\pi} e^{ikR\Lambda}\int_0^L e^{ikr(1-\Lambda)}\,dr\,\sin\theta\,d\theta\,d\phi. \tag{6.41}$$

The integral over r is the 'Plane Wave Spectrum' $\Omega(\theta,\phi)$ of the parametric source and can be solved analytically:

$$\Omega(\theta,\phi) = \int_0^L e^{ikr(1-\Lambda)}\,dr = \left[\frac{e^{ikr(1-\Lambda)}}{ik(1-\Lambda)}\right]_0^L = \frac{e^{ikL(1-\Lambda)}-1}{ik(1-\Lambda)}. \tag{6.42}$$

Equation (6.41) can now be written:

$$\psi(\theta_0,\phi_0,R)=\frac{1}{2\pi}\int_0^{\pi/2-j\infty}\int_0^{2\pi}\frac{e^{ikR\Lambda}}{1-\Lambda}(e^{ikL(1-\Lambda)}-1)\sin\theta\,d\theta\,d\phi. \tag{6.43}$$

An investigation was undertaken which found that the contribution from the imaginary part of the contour has little effect on the calculations, except at very low frequencies. The integral can therefore be taken over the real part of the contour alone.

6.4.4.2 Transmission coefficient

When a panel is inserted between the source and the observation point, normal to the z-axis, equation (6.43) must be modified to account for the transmission through the panel of each plane wave component in the angular spectrum. The field observed at R is then given by

$$\psi(\theta_0,\phi_0,R)=\frac{1}{2\pi}\int_0^{\pi/2}\int_0^{2\pi}\tilde{\Pi}(\theta,\phi)\frac{e^{ikR\Lambda}}{1-\Lambda}(e^{ikL(1-\Lambda)}-1)\sin\theta\,d\theta\,d\phi\,, \tag{6.44}$$

where $\tilde{\Pi}$ is the transmission coefficient of the plane wave component travelling in the (θ,ϕ) direction;

$$\tilde{\Pi}(\theta,\phi) = \Pi(\theta,\phi)e^{-ikd\cos\theta} \tag{6.45}$$

here Π is the plane wave transmission coefficient calculated in section 6.2, and the phase term accommodates the time delay of the fluid path that has been replaced by the layer.

The field that would be measured at R in the absence of the layer is found by integrating equation (6.43) (setting $\theta_0 = \phi_0 = 0$ in the expression for Λ, equation (6.39)). The result is

$$\psi_0 = e^{ikR}\ln\left(\frac{R}{R-L}\right). \tag{6.46}$$

The total transmission coefficient of the panel, as measured with a parametric source, is then given by

$$\Pi_{pws} = \frac{\psi(R)}{\psi_0(R)}. \tag{6.47}$$

6.4.5 Results of the full theory

This modified theory was used to predict the transmission loss of the glass-reinforced plastic panel whose measured results were presented in Figure 6.9. The array length (L) was $0.48m$ and the range (R) $1.18m$, corresponding to the positions of the acoustic filter and hydrophone in the tank facility. Simpsons rule was used to evaluate the integrals in (6.44).

The results are shown in Figure 6.11, again for the same three orientations that have previously been discussed. Comparison of these results with the experimental results of Figure 6.9 reveals a very good agreement. Most of the differences observed between the plane wave predictions and experiment have disappeared.

Preliminary attempts were made to optimize the stiffness constants (C_{ij}) used in the model with a view to using transmission loss data to infer the material properties of other samples of fibre-reinforced material. In principle, by studying the changes in

transmission loss that result from varying individual elastic constants, it should be possible to estimate values for C_{ij}. This proved to be impracticable and the attempt was abandoned. However, it was found that if the value of C_{33} is increased to $29.0GPa$ then the theoretical predictions agree a little more closely with the experimental results. Considering that C_{33} is the constant associated with wave propagation *along* the fibres, and that the velocity in this direction is subject to the greatest error in measurement, it may well be that the measured value is inaccurate, and that this is a more appropriate value for the constant. Velocity measurements *along* the plate would need to be made to confirm the value of this constant. This would require the compressional wave to be coupled into the edge of the panel, which is possible - but not using the immersion technique.

Finally in this section, a comparison of both theory and experiment is given at a single frequency ($150.4kHz$). The results are shown in Figure 6.12. The theoretical predictions shown here were made using the modified value of C_{33} mentioned above. Again, the theory, modified to include the plane wave spectrum of the source, is in far better agreement with the experimental results than are the plane wave predictions.

6.5 Conclusions

The introduction of anisotropy into a planar elastic layer has been investigated both experimentally, using a parametric source, and theoretically. A well characterized uniaxial glass-reinforced plastic panel was chosen for the investigation. This material is modelled as an homogeneous, but anisotropic, medium having hexagonal symmetry. A theoretical model for wave propagation in anisotropic media has been discussed and sections of the slowness surface for the material presented. Significant variations in velocity with propagation direction are evident in these curves.

A model has been presented that deals with all aspects of the acoustics of anisotropic layered media. This model has been used to predict the dispersion characteristics of the plate waves propagating in the anisotropic layer used to model the glass-reinforced plastic panel. Again, significant differences are observed between

propagation in the principal planes (parallel and normal to the fibres) and in a general plane (45° to the fibres). The plane wave transmission coefficient of the layer was calculated as a function of frequency and incident angle for these three planes of incidence. Significant differences were observed, particularly in the 45° case. The excitation of additional modes of vibration of the anisotropic layer are thought to be partly responsible for the observed behaviour.

Measurements on a glass-reinforced plastic test panel are in good agreement with theoretical predictions when the model is extended to incorporate the effects of the plane wave spectrum of the parametric source. The experimental results would seem to validate the theoretical models used, and suggest that both the theoretical and experimental techniques can be used to study the acoustics of other, possibly more complex, anisotropic laminates.

The need to perform many more measurements on an anisotropic panel than was previously necessary for isotropic materials has resulted in alterations to the experimental technique that have improved the performance of the system, as discussed in Chapter 4. It is expected that the experimental system will be used to study the scattering properties of anisotropically reinforced cylindrical structures, and other complex scattering geometries.

Figure 6.1 Local coordinate system for the hexagonal crystal class.

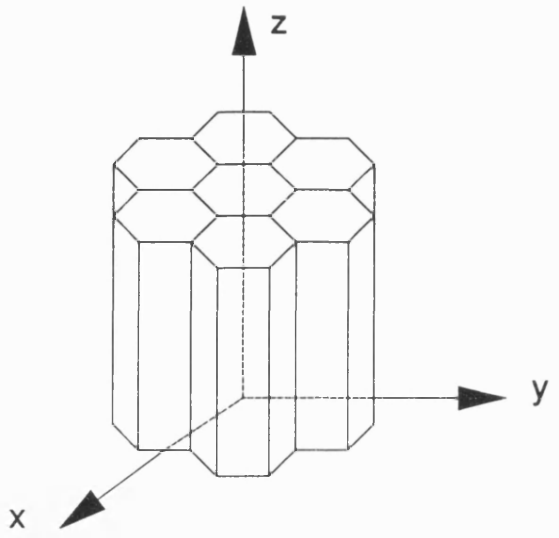

Figure 6.2 Slowness curves for propagation in the transverse plane ($\phi = 90°$).

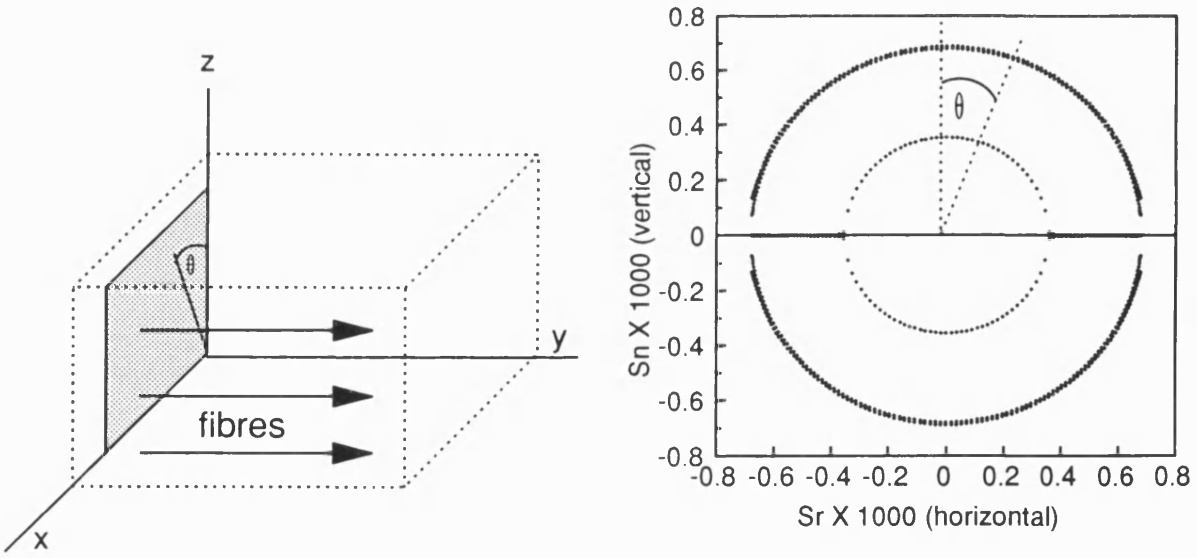

Figure 6.3 Slowness curves for propagation in the $\phi = 0°$ plane.

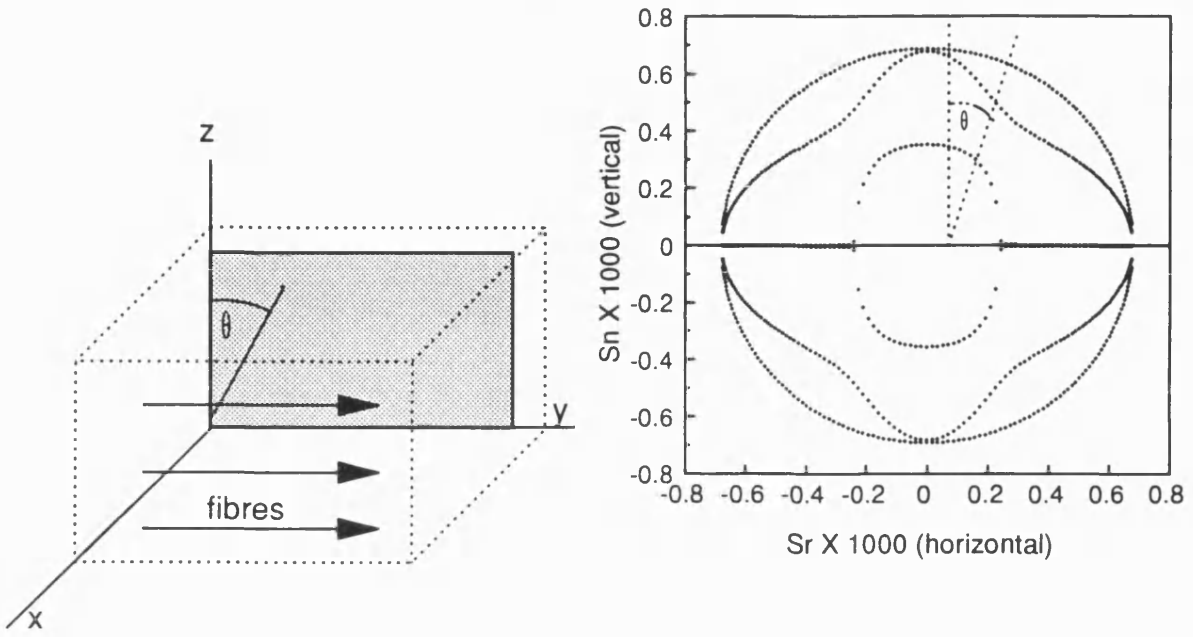

Figure 6.4 Slowness curves for propagation in the $\phi = 45°$ plane.

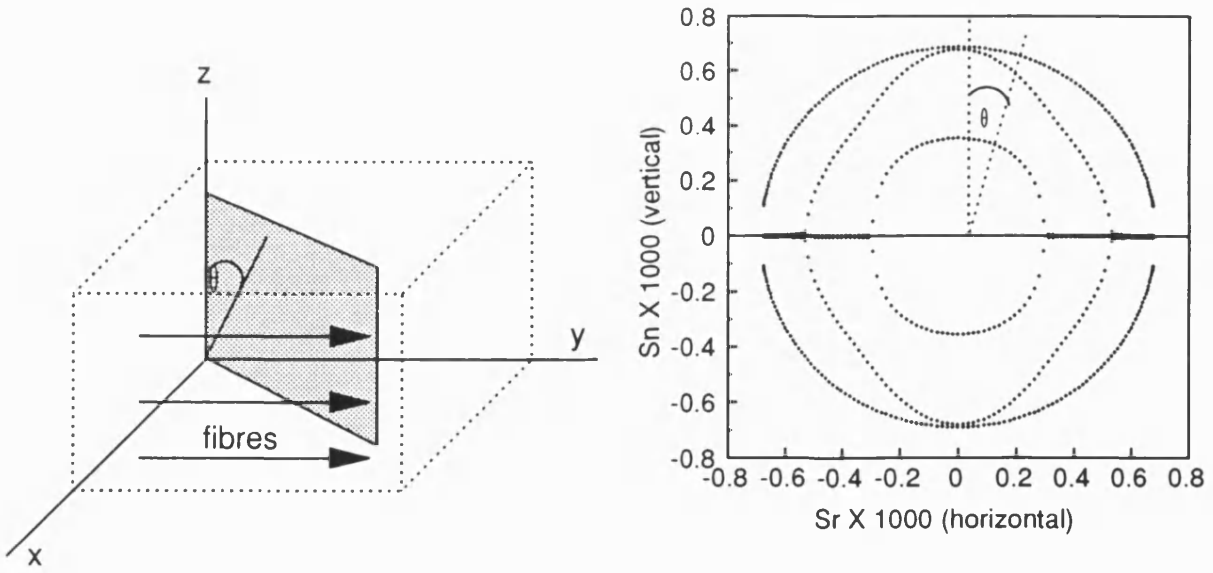

Figure 6.5 Stresses and displacements at the interfaces of the elastic layer and fluid half-spaces.

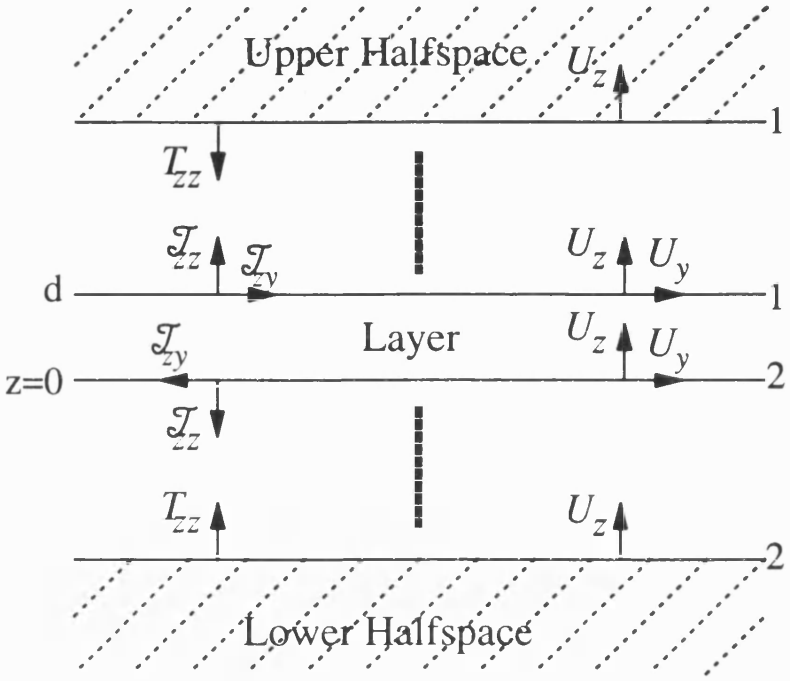

Figure 6.6 Scattering geometry; acoustic wave incident upon an anisotropic layer.

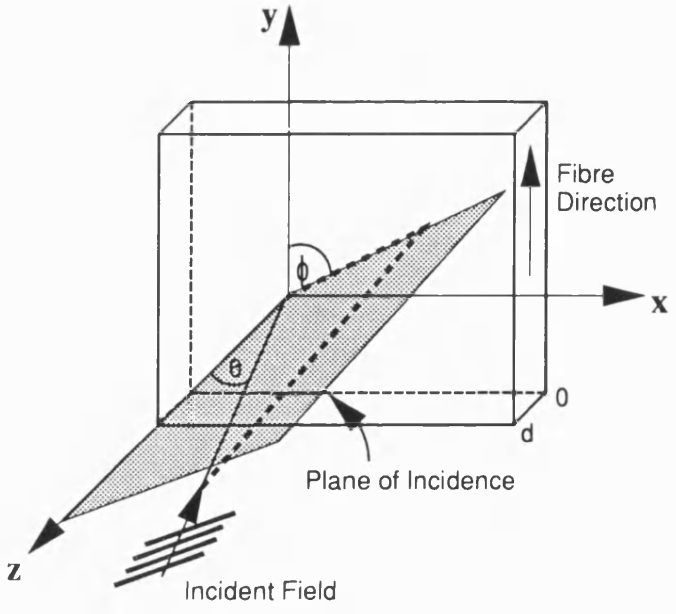

Figure 6.7 Variation of plane wave transmission loss (dB) with frequency and incident angle (θ) for the three planes of incidence at $\phi = 90°, 45°$ and $0°$ to the fibre direction.

(a) $\phi = 90°$

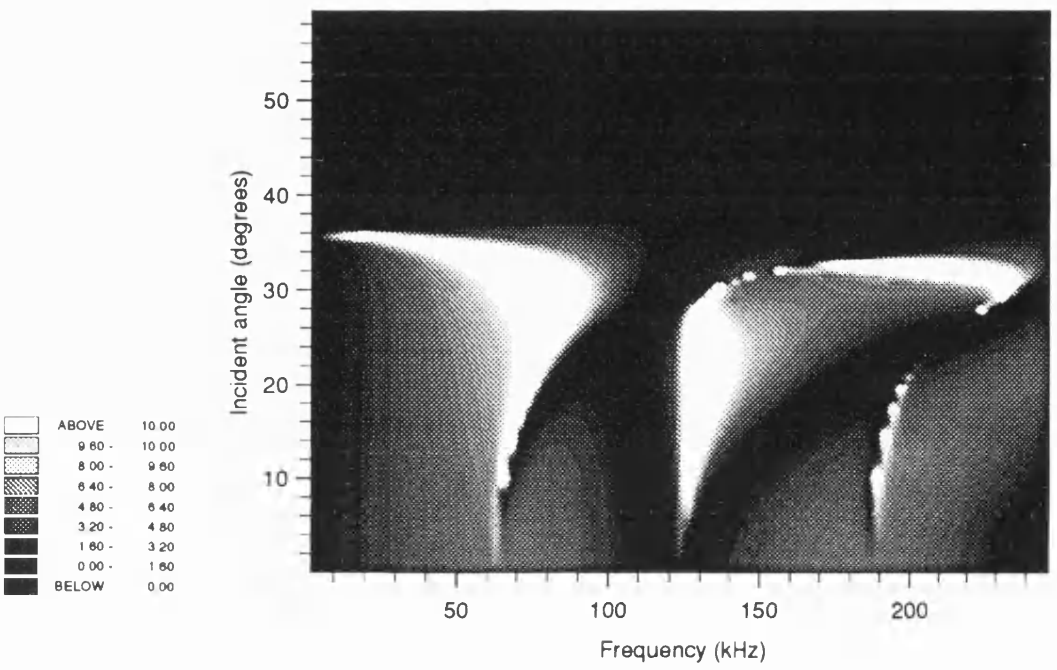

(b) $\phi = 45°$

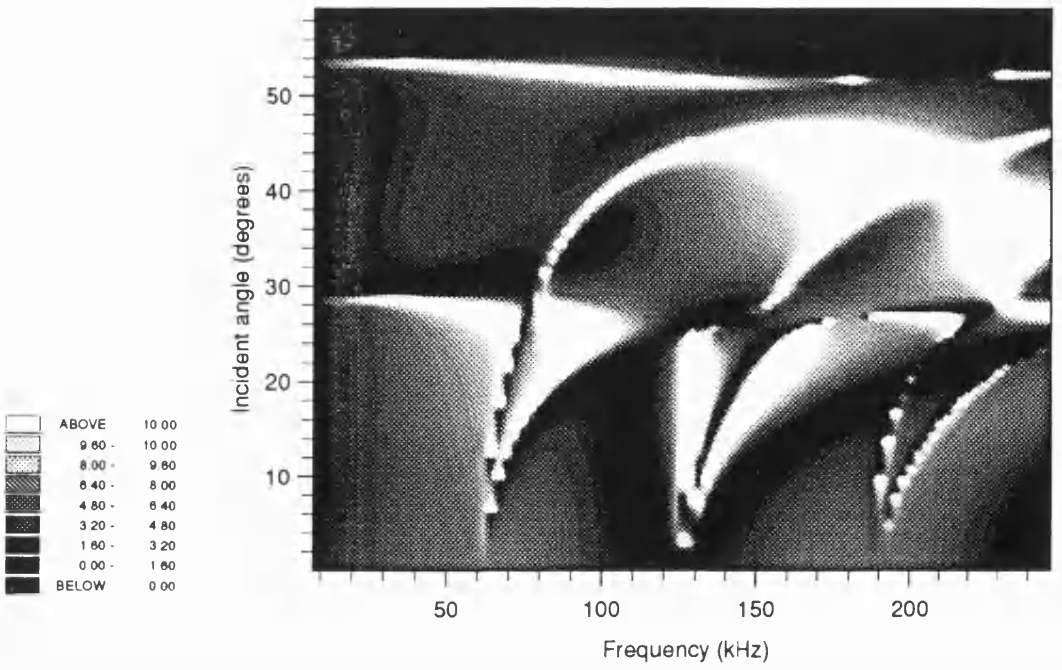

(continued)

(c) $\phi = 0°$

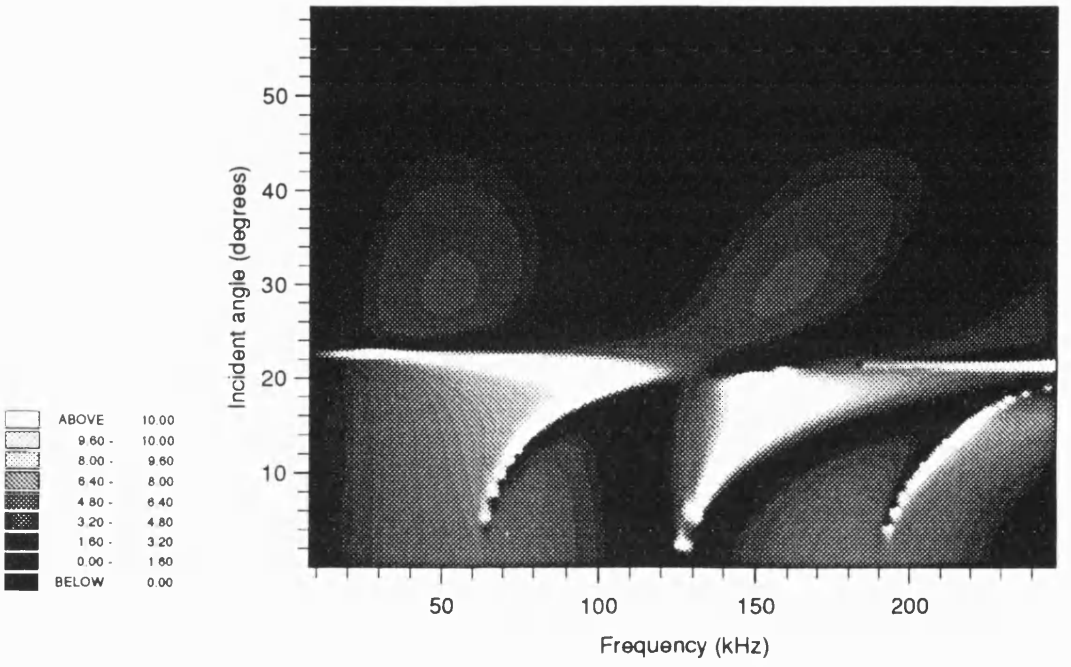

Figure 6.8 Computed dispersion curves for the free modes of vibration of the layer; mode propagation in the three directions $\phi = 90°, 45°$ and $0°$.

(a) $\phi = 90°$

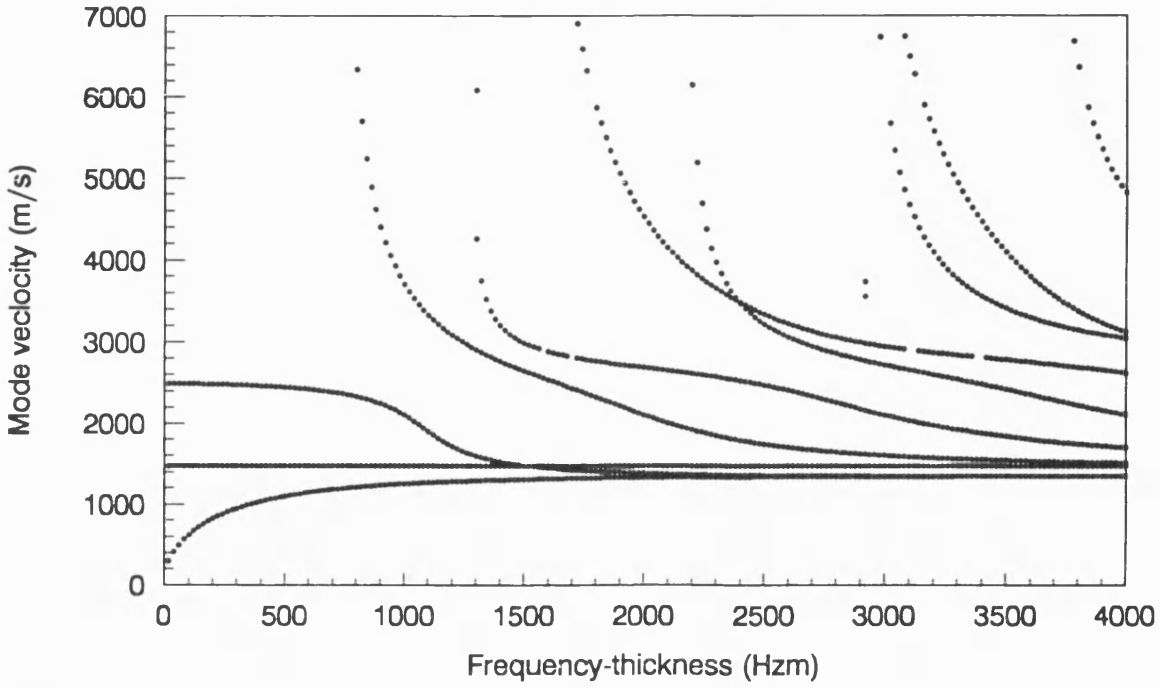

(b) $\phi = 45°$

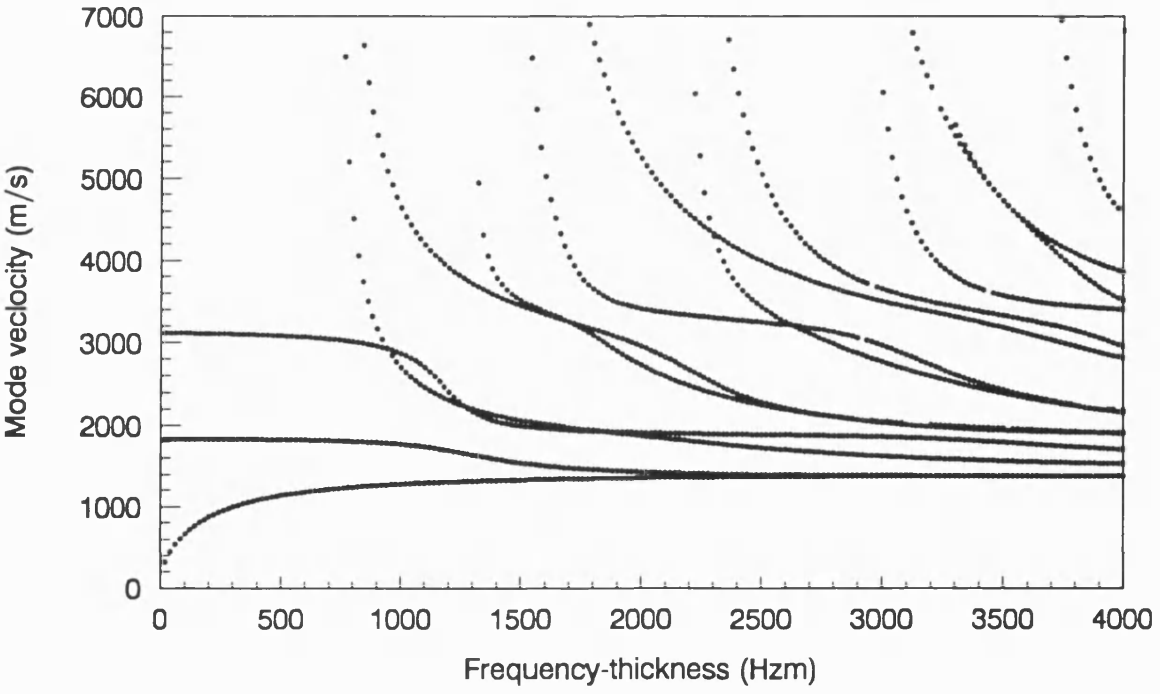

(continued)

(c) $\phi = 0°$

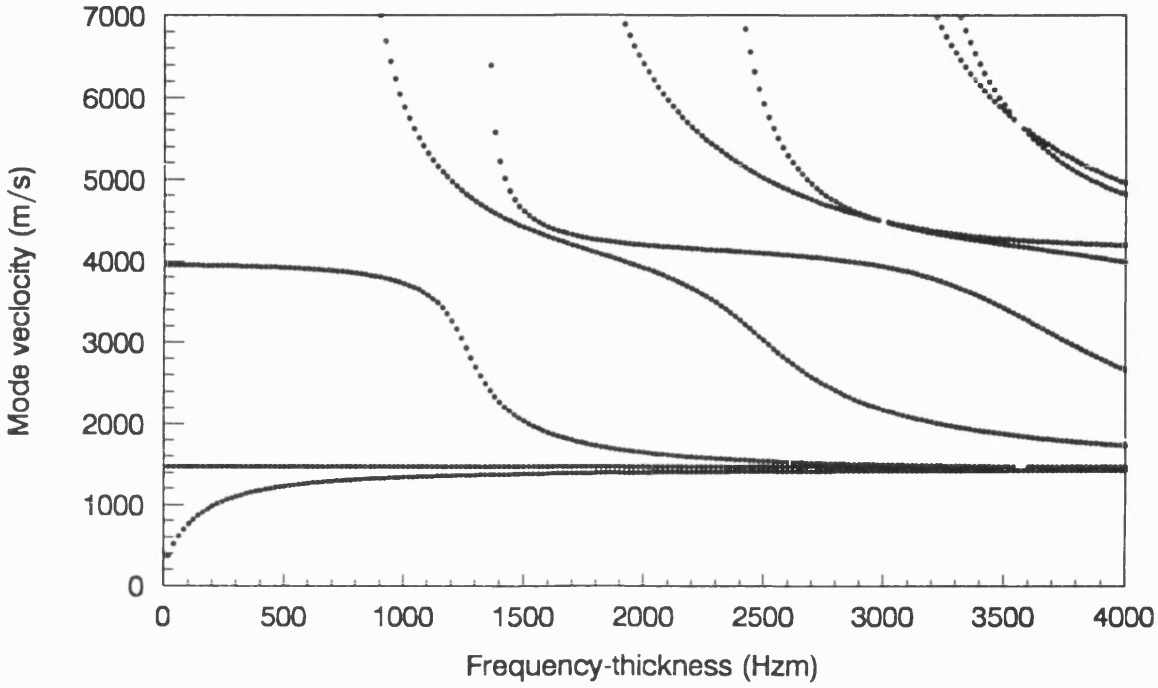

Figure 6.9 Experimentally measured transmission loss for the three planes of incidence orientated at $\phi = 90°, 45°$ and $0°$ to the fibre direction.

(a) $\phi = 90°$

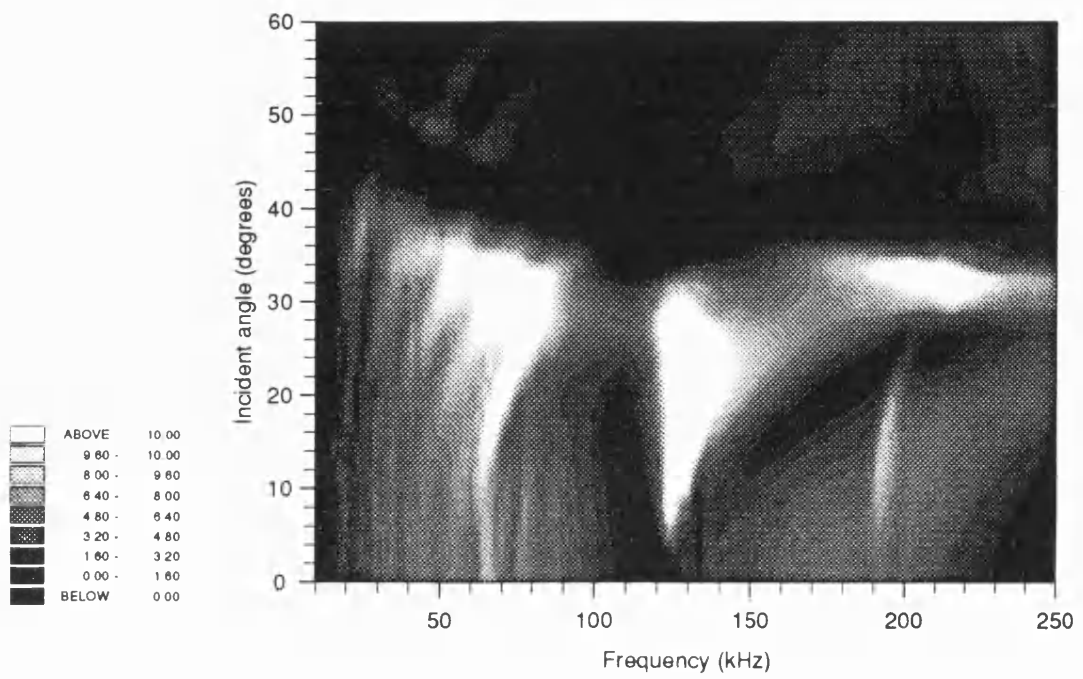

(b) $\phi = 45°$

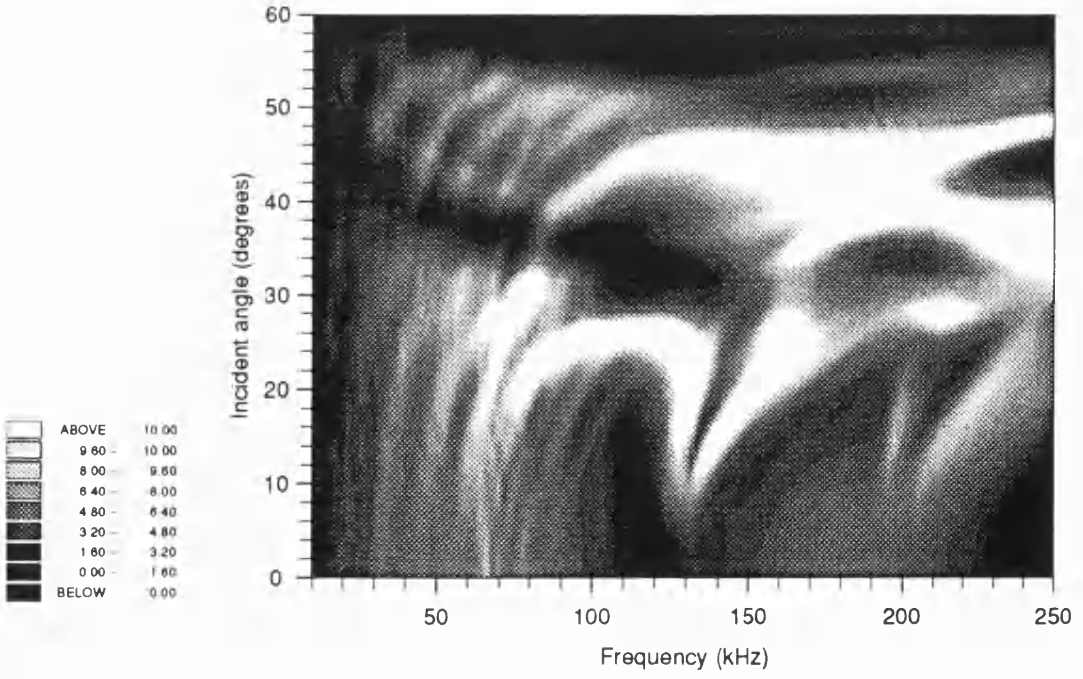

(continued)

(c) $\phi = 0°$

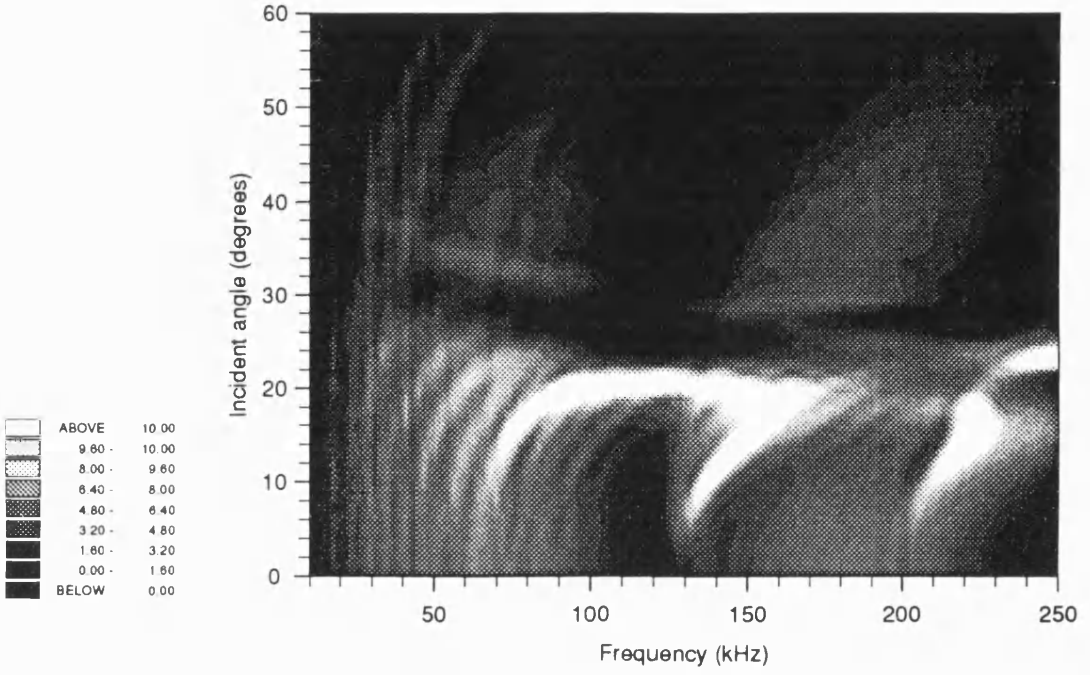

Figure 6.10 Geometry used in the calculation of the plane wave spectrum of the parametric source using the line array model.

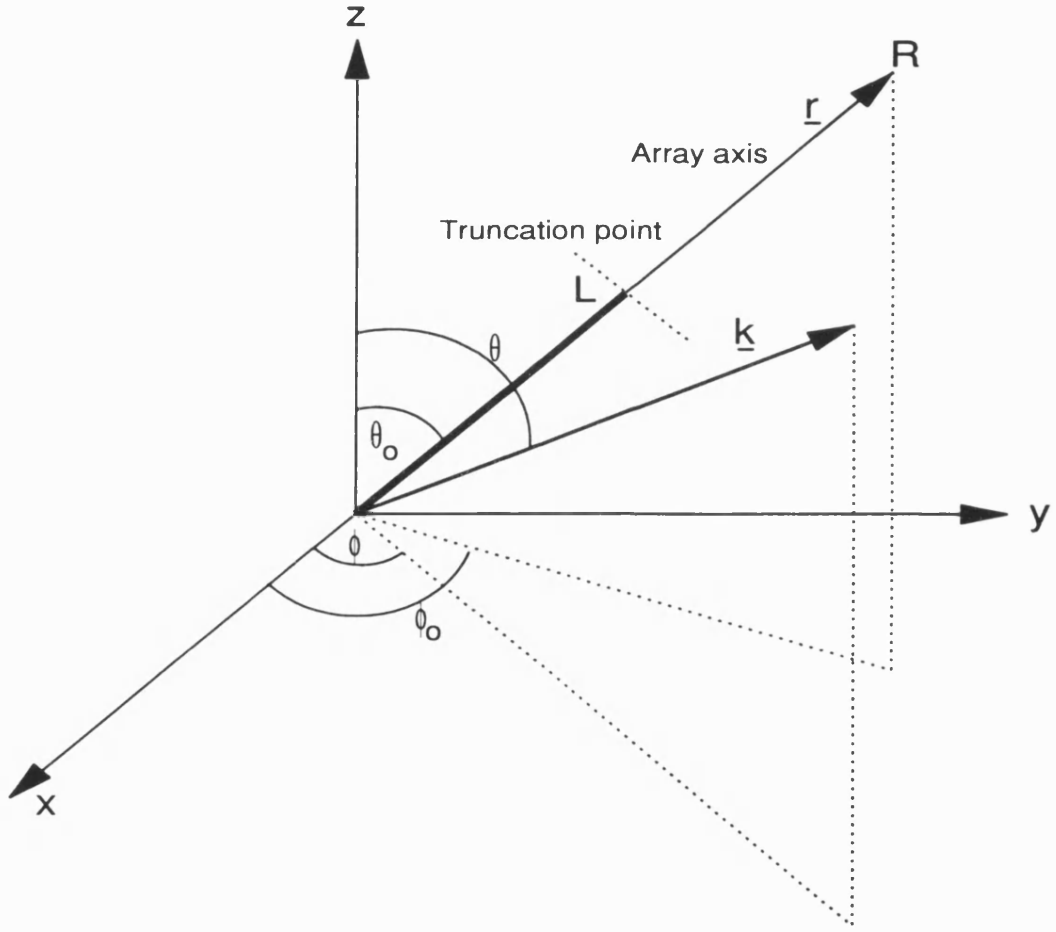

Figure 6.11 Theoretical predictions of transmission loss after the plane wave spectrum of the parametric array is included; propagation in the planes $\phi = 90°, 45°$ and $0°$.
(a) $\phi = 90°$

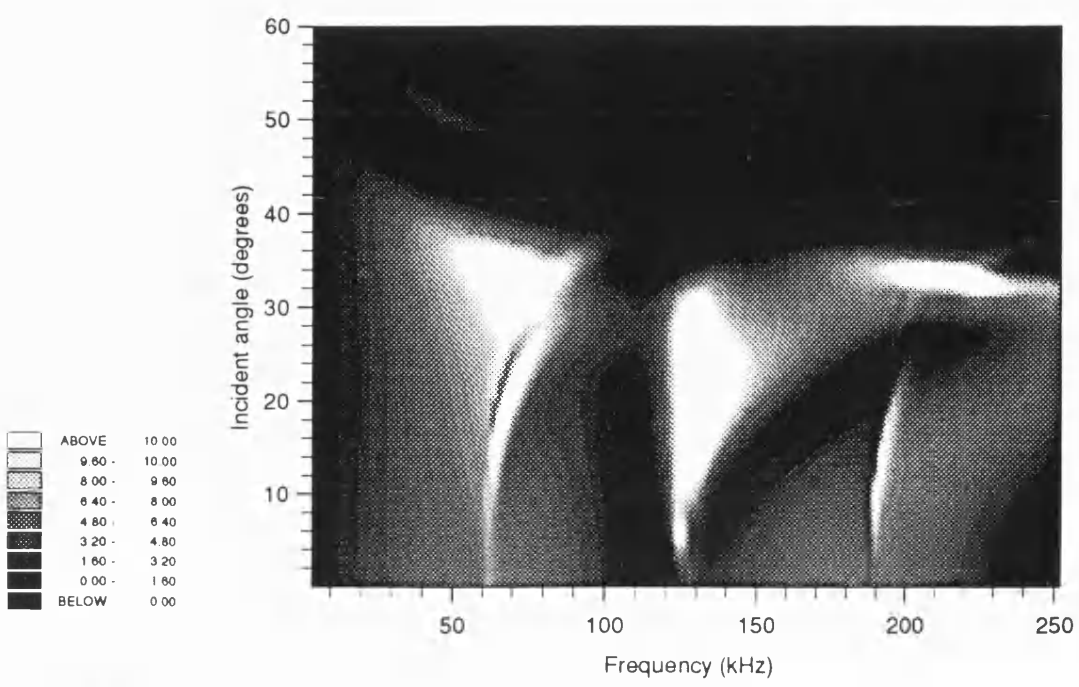

(b) $\phi = 45°$

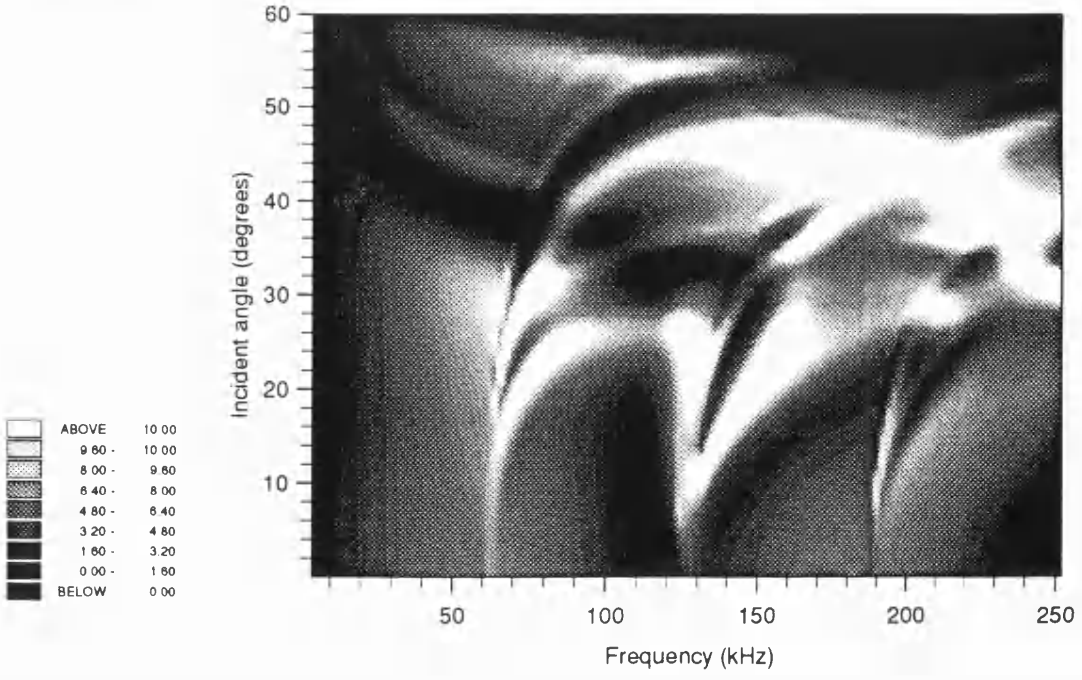

(continued)

(c) $\phi = 0°$

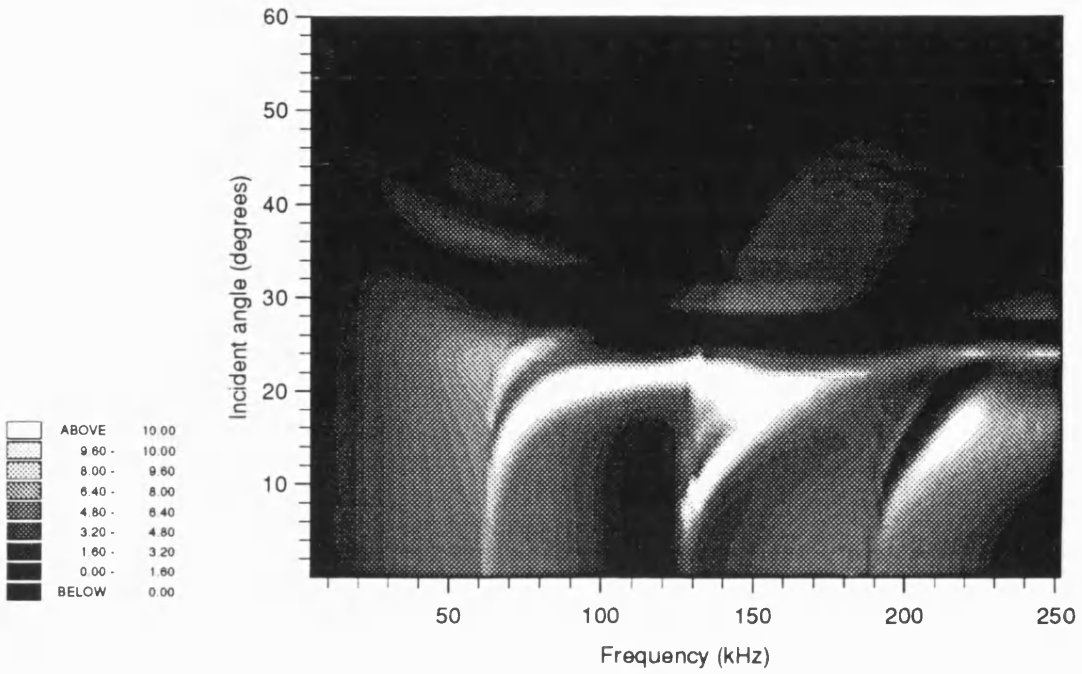

Figure 6.12 Variation of transmission loss with incident angle (θ) at a frequency of 150.4*kHz*; comparison of experimental results with both plane wave theory and predictions incorporating the plane wave spectrum of the parametric array.

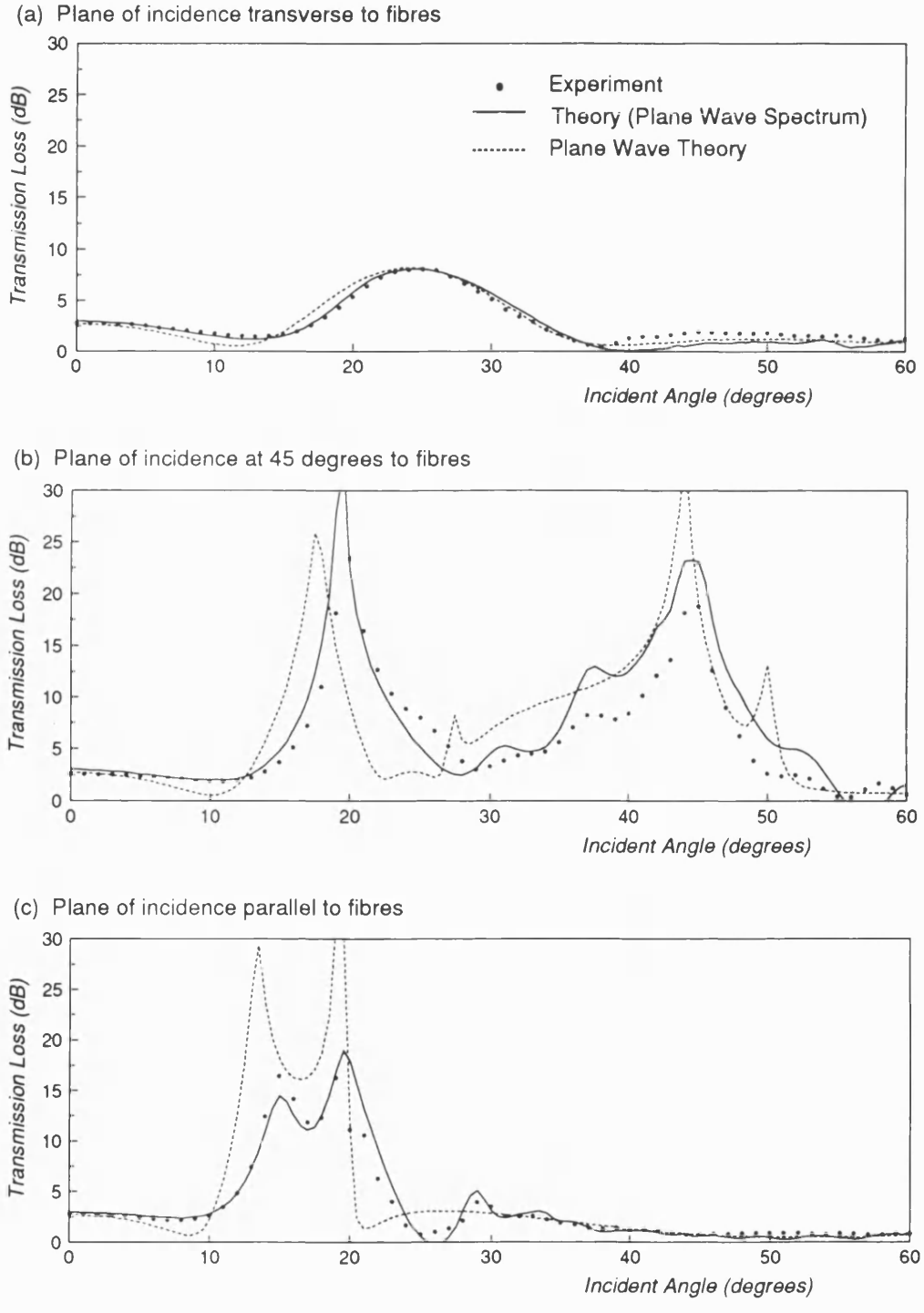

7 Summary and conclusions

This thesis has examined experimental and theoretical approaches to scattering involving objects of complex geometry and material properties. Attention has focussed on two particular areas of interest; the introduction of anisotropic reinforcement into the infinite planar elastic layer, and perturbations in the shape of normally insonified cylindrical shells. In this chapter the work is summarized, some general conclusions drawn, and a few recommendations made regarding the direction that future investigation should take.

The acoustic behaviour of the planar isotropic layer and the cylindrical shell of circular cross-section were briefly discussed in Chapter 2, as a prelude to the main body of work. The resonances of a scatterer were seen to be of particular importance in determining the acoustic response of an object to an incident wave. Simple theoretical models were presented and the acoustics was illustrated with predictions for these simple geometries.

The use of a Schlieren visualization technique for imaging two-dimensional acoustic fields has been investigated. A theory has been presented that successfully predicts the optical distribution obtained with an ideal Schlieren system. This model allows investigations into the effects of optical spatial filtering and acoustic pressure amplitude to be made. Preliminary theoretical investigations suggest that for zeroth order filtering and low acoustic pressures the image obtained is proportional to the square of the acoustic pressure amplitude. A comparison with experimental measurements indicated that the relationship between optical and acoustic fields is not as simple as was previously thought; probably because the actual pressures present in the experimental measurements are too high for the above approximation to be made. Independent measurements of the acoustic pressure amplitude within cylindrical shells have not been attempted and so exact comparisons cannot be made. The use of zeroth order filtering was found to produce optical images that are far more representative of the acoustic field than knife-edge filtering does (although knife-edge filtering is known to have other advantages over zeroth order filtering).

The use of the Schlieren technique for locating, identifying and imaging the fluid column resonance modes of cylindrical shells and cavities has been described. Results were presented for circular and non-circular geometries. High frequency resonances showed hybridization of modes (due to overlapping) and resulted in standing wave-fields having new and unexpected symmetries. The system has been shown to have great potential for studying the resonance behaviour of other cylindrical structures, including those of more complex geometry. Complementary to the main programme of work, results have been presented for the 'stadium' shaped cavity.

The fluid column modes of a flooded brass cylindrical shell of circular cross-section were located with the Schlieren system and the effects of 'deforming' the shell into the more general elliptical geometry studied. Many more resonance modes were observed, some of which closely resembled the modes of the circular sample, while others did not. A theoretical model for the fluid column modes of the elliptical cavity was developed. This model involved the solution of the wave equation in elliptical coordinates, with rigid boundary conditions being applied at the inner interface between the fluid and the shell. This model was used to calculate the resonance frequencies and acoustic fields within elliptical cavities of different eccentricities. Many mode splittings and level crossings were observed in the variation of modal frequency with eccentricity. The experimental data obtained with five samples of brass shell of different eccentricities gave reasonable agreement with the model, allowing the measured modes to be properly identified and classified. Both theory and experiment showed approximately twice the number of modes than exist in the circular case. The models were improved by allowing for the finite impedance of the shell; both for the circular geometry and for the general elliptical geometry. Very close agreement was obtained between theory and measurement for all but the most highly deformed sample (whose shape was not truly elliptical).

A second experimental facility was used to make backscattering measurements on the elliptical cylinder. An existing parametric array facility was adapted to allow broad-band measurements to be made over a wide range of incident angles, automatically, in a short period of time. This is a necessary requirement when studying

scattering from complex objects whose acoustic response is sensitive to several orientations, or incident angles. The use of *asymmetrical* pulses in the transmitting system has been investigated and found to permit measurements to be made over a wider range of frequencies than previously obtained using symmetrical pulses. Preliminary results for the backscattering by a single elliptical shell have been presented. Significant differences were observed between these measurements and those of a circular sample. Backscattering by non-circular cylinders and shells is an area that requires further investigation.

The parametric array facility has also been used to measure the transmission properties of fibre-reinforced layers. A theoretical model for wave propagation involving anisotropic layered media was presented, and results compared with experimental measurements of the transmission loss of a single uniaxial glass-reinforced plastic panel. The model was extended to account for the non-planar wave-field of the parametric source and good agreement obtained, thus validating the theoretical approach. This part of the study showed the transmission properties of the layer to vary considerably with *both* angles of incidence. Differences between the acoustics of the isotropic and anisotropic layers are attributed, in part, to the different free modes of vibrations of the layer that can be excited in the two cases. This is a factor which could possibly be exploited in the design of underwater structures using composite materials.

The work described in this thesis has not attempted to answer one particular question, but rather has sought to extend our understanding and knowledge in several areas; developing parallel theoretical and experimental techniques and procedures, and building up a knowledge and expertise of several key issues (perturbations in shape and material anisotropy) that will be needed in future studies involving complex scattering arrangements. The studies described in this thesis are part of a wider programme of work, in which the author is involved, aimed at considering many other complexities in scattering systems.

The ultimate aim of the work currently under way is to introduce anisotropy into

the cylindrical geometry. However, we are interested not only in man-made structures, but also naturally occurring scatterers - such as sediments - which can conveniently be studied using scale modelling in the laboratory. The aims of the research programme are to build upon the work involving simple structures by considering other complexities in scattering geometry. Other aspects that have been considered, or could be investigated in the future, include the following:

- Anisotropic reinforcement of panels and cylindrical shells with rib stiffeners
- Fibre-reinforced cylindrical shells
- *Irregularly* deformed cylindrical shells (and other, 3-dimensional, scatterers)
- Air-filled structures
- Objects having edges, corners, and facets (such as the cube)
- Surface roughness
- Multiple scattering between discrete objects (cylinders, spheres etc)
- The effects of inhomogeneities and defects in fibrous composites

In particular, with regards the deformation of cylindrical shells (both in a regular and an irregular manner) it would seem sensible to use thinner, less resonant shells in the scattering studies. The use of the *cubic* scatterer may be particularly informative as the edges and corners can be easily removed to see what effect they have upon the scattering by such particles.

The introduction of complexity of any kind into the idealistic model scattering geometries (simple structures) results in many kinds of practical and theoretical complications and problems; in particular with regards the fabrication of suitable targets (scale models) for experimental testing. For the simple geometries and materials previously studied; such as aluminium plates, steel cylindrical shells and spheres, high quality samples are readily available. There is a tendency to think that small perturbations in shape and material properties of an object require only a small increase in the computational effort needed to produce accurate theoretical predictions, and in the

technical expertise and cost of fabricating test objects. This is not so.[1] Also, in the case of fibrous materials, fabrication methods are such that many factors *not* associated with anisotropy, such as voids, defects and uneven lay-up, may need to be considered, in addition to the effects of anisotropy. With theoretical models it can be easy to exploit some physical property of a structure, such as anisotropy, in the design of structures having optimal acoustic performance. Often, however, some other (unforeseen) aspect of the design can have a significant effect upon the acoustic behaviour of the structure that is actually built. This highlights the enormous importance of good parallel theoretical and experimental investigations, such as this programme of work attempts to achieve. Good experimental techniques must also be accompanied by a thorough understanding of the character and limitations of a measurement technique if results obtained with it are to be meaningfully interpreted. In this thesis this is of particular relevance to the parametric array (with regards the effect of non-planar wave-fields) and the Schlieren system (with regard to the interpretation of the optical image).

Although the Schlieren studies have great potential, there is no plan to significantly extend this work any further. The main limitation of the Schlieren technique is that quantitative information cannot easily be extracted from the system (as it is presently configured). The advantages of Schlieren lie in the fact that acoustic waves and scattering phenomena can be 'seen'; and that which can be seen can be better understood and interpreted. The insight into resonance phenomena gained with Schlieren is remarkable considering the qualitative nature of the results obtained. If the system could be calibrated in some fashion, allowing acoustic pressures to be obtained, the Schlieren technique would be a very powerful tool in the study of many aspects of wave phenomena - not just those of interest in underwater acoustics. The early results obtained with the 'stadium' shaped cavity have attracted the interest of researchers involved in studying the eigenstates and scattering behaviour of two-dimensional chaotic systems (Smilansky, 1991). Also, the kind of laboratory scale modelling of scattering

1 As is evidenced in the difficulty of boring *non-circular* holes for example (although perversely, some of the easiest targets to make are the hardest to model; e.g. the cube, which contrary to intuition is very difficult to model).

and resonance phenomena that is possible with Schlieren potentially allows complex geometries to be investigated where numerical solution is extremely difficult, if not impossible. Another valuable use for the technique is as an educational tool - again because wave phenomena can actually be seen. Finally, studies undertaken with Schlieren have an *aesthetic* appeal; an often neglected factor of no minor importance in research.

A carefully designed Schlieren system, based upon the current design, but with improvements aimed at removing some of the current limitations, could have enormous potential for research in acoustics, and wave physics in general.

8 Bibliography

Abramowitz M. and Stegun I.A. (Eds) (1972), *Handbook of mathematical functions* (Dover Publications, Inc. New York).

Aldoshina I.A. and Olyushin M.V. (1992), *Resonance frequencies and structures of sound fields in the enclosures of acoustical systems*, Sov. Phys. Acoust. **38**(6) 529-534.

Auld B.A. (1990), *Acoustic Fields and Waves in Solids*, 2nd ed Vols 1 and 2 (Krieger).

Baskar S., Varadan V.V. and Varadan V.K. (1984), *Thin shell theories and acoustic wave scattering by infinitely long cylindrical shells of arbitrary cross section*, J. Acoust. Soc. Am. **75**(6) 1673-1679.

Beckett C. (1992), *Studies of acoustic scattering using a parametric array*, Ph.D. thesis, University of Bath.

Beckett C. and Humphrey V.F. (1989), Private communication; exposition of the theory predicting the optical image in the Schlieren system.

Beckett C. and Humphrey V.F. (1989), *Experimental form function determination for normally and obliquely incident wave-fields on a solid cylinder*, Ultrasonics International 89 Conference Proceedings (Butterworths), 382-387.

Berktay H.O. (1965), *Possible exploitation of non-linear acoustics in underwater transmitting applications*, J. Sound Vib. **2**(4) 435-461.

Berry M.V. (1981), *Regularity and chaos in classical mechanics, illustrated by three deformations of a circular 'billiard'*, Eur. J. Phys. **2** 91-102.

Bjørnø L. (1975), *Underwater applications of non-linear ultrasound*, in Ultrasonics International 1975 Conference Proceedings (IPC Science and Technology Press), edited by Z. Novak, 238-244.

Boasman P. (1991), Private communication regarding wave functions of the stadium.

Borovikov V.A. and Veksler N.D. (1985), *Scattering of sound waves by smooth convex elastic cylindrical shells*, Wave Motion **7** 143-152.

Bowman J.J., Senior T.B.A. and Uslenghi P.L.E. (eds) (1987), *Electromagnetic and Acoustic Scattering by Simple Shapes* (Hemisphere Publishing Corporation).

Brekhovskikh L.M. (1980), *Waves in Layered Media*, 2nd Edition (Academic Press)

Brigham G.A., Libuha J.J. and Radlinski R.P. (1977), *Analysis of scattering from large planar gratings of compliant cylindrical shells*, J. Acoust. Soc. Am. **61**(1) 48-59.

Burke J.E. (1964) *Low-frequency approximations for scattering by penetrable elliptic cylinders*, J. Acoust. Soc. Am. **36**(11) 2059-2070.

Burke J.E. and Twersky V. (1966), *On scattering of waves by the infinite grating of elliptic cylinders*, IEEE Trans. Antennas Propag. **AP-14** 465-480.

Chalmers D.W. (1988), *The properties and uses of marine structural materials*, Marine Structures **1** 47-70.

Chedid-Helou F.A. and Hemann J.H. (1991), *Mathematical modelling of wave propagation in anisotropic media*, Materials Evaluation, June 1991.

Chinnery P.A. (1990), *Resonances within deformed cylindrical cavities, experimental observations and simple theoretical model,* University of Bath report (unpublished).

Chinnery P.A. (1991), *The transmission loss of layered anisotropic panels measured with a parametric source, Part I: theory*, University of Bath report (unpublished).

Chinnery P.A. (1992), *The transmission loss of layered anisotropic panels measured with a parametric source, Part II: experimental results - three fibre-reinforced panels*, University of Bath report (unpublished).

Chinnery P.A. (Ed) (1993), *Acoustics of Advanced Materials for Underwater Applications*, Proc. I.O.A. Vol 15 Pt 6.

Chinnery P.A. and Humphrey V.F. (1994), *Resonances in acoustic scattering by cylindrical objects*, Proc. I.O.A. Vol 16 Pt 6 51-58.

Chinnery P.A. and Humphrey V.F. (1995), *Experimental visualization of acoustic resonances within the stadium*, submitted to Phys. Rev. Lett. Included here as Appendix A2.

Dardy H.D. et al (1987), *Acoustically induced stresses in elastic cylinders and their visualization*, J. Acoust. Soc. Am. **82**(4) 1378-1385.

DiPerna D.T. and Stanton T.K. (1994), *Sound scattering by cylinders of noncircular cross section: a conformal mapping approach*, J. Acoust. Soc. Am. **96**(5) 3064-3079.

Doron E., Smilansky U. and Frenkel A. (1990), *Experimental demonstration of chaotic scattering of microwaves*, Phys. Rev. Lett. **65** 3072-3075.

Fiorito R., Madigosky W. and Überall H. (1979), *Resonance theory of acoustic waves interacting with an elastic plate,* J. Acoust. Soc. Am. **66**(6) 1857-1866

Flax L., Dragonette L.R. and Überall H. (1978), *Theory of elastic resonance excitation by sound scattering*, J. Acoust. Soc. Am. **63**(3) 723-731.

Flax L., Gaunaurd G.C. and Überall H. (1981), *Theory of resonance scattering*, in *Physical Acoustics Vol. XV* edited by Mason W.P. and Thurston R.N. (Academic Press) 191-294.

Freedman A. (1982), *On the "overlapping resonances" concept of acoustic transmission through an elastic plate, I and II*, J. Sound Vib. **82**(2) 181-213.

Gaunaurd G.C. (1989), *Elastic and acoustic resonance wave scattering*, Appl. Mech. Rev. **42**(6) 143-192.

Goel G.C. and Jain D.L. (1981), *Scattering of plane waves by a penetrable elliptic cylinder*, J. Acoust. Soc. Am. **69**(2) 371-379.

Gustafsson G. (1987), *Experiments on shock-wave focusing in an elliptical cavity*, J. Appl. Phys. **61**(11) 5193-5195.

Gutzwiller M.C. (1990), *Chaos in Classical and Quantum Mechanics* (Springer-Verlag).

Harumi K. (1961), *Scattering of plane waves by a rigid ribbon in a solid*, J. Appl. Phys. **32**(8) 1488-1497.

Hosten B. (1991), *Reflection and transmission of acoustic plane waves on an immersed orthotropic and viscoelastic solid layer*, J. Acoust. Soc. Am. **89**(6) 2745-2752.

Humphrey V.F. (1981), *The measurement of acoustic properties of specimens of limited size by use of a parametric source*, Ultrasonics International 81 Conference Proceedings (IPC Science and Technology Press Ltd) edited by Z. Novak, 360-365.

Humphrey V.F. (1983), *The measurement of acoustic properties of specimens of limited size by use of a parametric source*, University of Bath report (unpublished).

Humphrey V.F. (1985), *The measurement of acoustic properties of limited size panels by use of a parametric source*, J. Sound Vib. **98**(1) 67-81.

Humphrey V.F., Anastadiasis K. and Dyer C. (1992), Private communication regarding laboratory measurements using a parametric array.

Humphrey V.F. and Beckett C. (1990), *The application of a parametric array to scattering studies in the laboratory*, in *Frontiers of Nonlinear Acoustics: Proceedings of 12th ISNA* (Elsevier), edited by M.F. Hamilton and D.T. Blackstock, 265-270.

Humphrey V.F. and Beckett C. (1994), *Experimental studies of acoustic scattering by cylindrical objects*, Proc. I.O.A. Vol 16 Pt 6 43-50.

Humphrey V.F. and Berktay H.O. (1985), *The transmission coefficient of a panel measured with a parametric source*, J. Sound Vib. **101**(1), 85-106.

Humphrey V.F. and Hsu C.H (1980), *Non-linearity of cylindrical hydrophones used for the measurement of parametric arrays*, in *Transducers for sonar applications*: Institute of Acoustics conference, University of Birmingham, December 1980.

Humphrey V.F., Knapp S.M. and Beckett C. (1990), *Laboratory studies of acoustic scattering*, Proc. I.O.A. Vol 12 Pt 1 91-98.

Humphrey V.F., Knapp S.M. and Beckett C. (1991), *Visualization of the resonances of a fluid-filled cylindrical shell using a low frequency Schlieren system*, in *Physical Acoustics*, edited by O. Leroy and M.A. Breazeale (Plenum) 371-376.

Humphrey V.F., Murphy C. and Moustafa A.H.A. (1987), *Wideband backscattering measurements using a parametric array*, Ultrasonics International 87 Conference Proceedings (Butterworths), 265-270.

Humphrey V.F., Simmonds D.J. and Green M. (1994), *Large area PVDF coaxial cable hydrophones*, in Proceedings of the 2nd European Conference on Underwater Acoustics (European Commission), edited by L. Bjørnø, Vol. 1 567-572.

James J.H. (1990), *Acoustics of orthorhombic planar layered media*, Admiralty Research Establishment Gosport (UK) report: ARE TR90303 (HMSO London).

James J.H. (1993), *Low frequency acoustics of laminated composite axisymmetric structures*, Defence Research Agency Gosport (UK) Report: DRA-TM(USGR)93302 DRIC-BR-316760.

Klein W.R. and Cook B.D. (1967), *Unified approach to ultrasonic light diffraction*, IEEE Trans. Sonics Ultrasonics, SU-**14** 123-134.

Knapp S.M. (1987), *Schlieren studies of acoustic backscattering; Report no. 2 - Experimental arrangement and preliminary results*, University of Bath report (unpublished).

Knapp S.M. (1988), *Schlieren studies of acoustic backscattering; Report no. 3 - Theoretical study of acousto-optic interaction and practical limitations at low frequencies*, University of Bath report (unpublished).

Knapp S.M. (1988), *Schlieren studies of acoustic backscattering; Report no. 4 - Variation of the Schlieren image with acoustic pressure*, University of Bath report (unpublished).

Knapp S.M. (1988), *Schlieren studies of acoustic backscattering; Report no. 5 - Visualization of low frequency acoustic fields*, University of Bath report (unpublished).

Knapp S.M. (1989), *Schlieren studies of acoustic backscattering; Report no. 7 - Aperture enlargement and system limiting factors*. University of Bath report (unpublished).

Knapp S.M. and Beckett C. (1989), *Acoustic backscattering from specific targets; Report No. 6 - Experimental and theoretical observation of cylinder resonances*, University of Bath report (unpublished).

Knapp S.M., Beckett C. and Humphrey V.F. (1995), *Schlieren observation of the resonances of a fluid filled shell*, in preparation for J. Acoust. Soc. Am.

Knapp S.M and Humphrey V.F. (1989), *Schlieren visualization of low frequency ultrasonic fields*, in Ultrasonics International 89 Conference Proceedings (Butterworths) 1089-1094.

Li Y. and Thompson R.B. (1990), *Influence of anisotropy on the dispersion characteristics of guided ultrasonic plate modes*, J. Acoust. Soc. Am. **87**(5) 1911-1931.

Mal A.K. and Ting T.C.T. (Eds) (1988), *Wave Propagation in Structural Composites*, Proceedings of the joint ASME/SES applied mechanics and engineering sciences conference, Berkeley, California 1988 (The American Society of Mechanical Engineers, New York).

Maze G., Izbicki J.L. and Ripoche J. (1986), *Acoustic scattering from cylindrical shells: guided waves and resonances of the liquid column*, Ultrasonics **24** 354-362.

Maze G. and Ripoche J. (1983), *Méthode d'isolement et d'identification des résonances (MIIR) de cylindres et de tubes soumis à une onde acoustique plane dans l'eau,* Revue Physique Appl. **18** 319-326.

McLachlan N.W. (1947), *Theory and Application of Mathieu Functions,* (Clarenden Press, Oxford).

Moffet M.B. and Blue J.E. (1980), *Hydrophone non-linearity measurements,* N.U.S.C Technical memorandum 801150.

Morse P.M. and Feschbach H. (1946), *Methods of Theoretical Physics* (parts I and II) (McGraw Hill, New York).

Musgrave M.J.P. (1954), *On the propagation of elastic waves in aeolotropic media, I: General principles*, Proc. Roy. Soc. London **A226** 339-355.

Musgrave M.J.P. (1954), *On the propagation of elastic waves in aeolotropic media, II: Media of hexagonal symmetry*, Proc. Roy. Soc. London **A226** 356-366.

Musgrave M.J.P. (1970), *Crystal Acoustics* (Holden-Day).

Nayfeh A.H. and Chimenti D.E. (1988), *Ultrasonic wave reflection from liquid-coupled orthotropic plates with application to fibrous composites*, J. Appl. Mech. **55** 863-870.

Nayfeh A.H. and Chimenti D.E. (1991), *Elastic wave propagation in fluid-loaded multiaxial anisotropic media*, J. Acoust. Soc. Am. **89**(2) 542-549.

Neubauer W.G (1973), *Observation of acoustic radiation from plane and curved surfaces*, in *Physical Acoustics Vol. X* edited by W.P. Mason and R.N. Thurston (Academic Press) 61-126.

Newman D.R. (1973), *Observations of cylindrical waves reflected from a plane interface*, J. Acoust. Soc. Am. **53** 1174-1176.

Pillai T.A.K. et al (1983), *Acoustic wave scattering by elastic cylindrical shells in water*, J. Acoust. Soc. Am. **74**(2) 619-624.

Pillai T.A.K., Varadan V.V. and Varadan V.K. (1982), *Sound scattering by rigid and elastic infinite elliptical cylinders in water,* J. Acoust. Soc. Am. **72**(3) 1032-1037.

Plona T.J., Behravesh M. and Mayer W.G (1975), *Rayleigh and Lamb waves at liquid-solid boundaries*, Ultrasonics, July 1975 171-174.

Radlinski R.P. and Simon M.M. (1993), *Acoustic and elastic wave scattering from elliptic-cylindrical shells*, J. Acoust. Soc. Am. **93**(5) 2443-2453.

Raman C.V. and Nath N.S.N. (1935), *The diffraction of light by sound waves of high frequency, parts I-V* in Vols. 2 & 3 of Proc. Indian Acad. Science.

Raman V. and Venkataraman K.S. (1939), *Determination of the adiabatic piezo-optic coefficient of liquids*, Proc. Roy. Soc. A **171** 137-147.

Randall C.J. (1991), *Modes of noncircular fluid-filled boreholes in elastic formations,* J. Acoust. Soc. Am. **89**(3) 1002-1016.

Scott D.C. and Wilcox D. (1992), *A quantitative study of ultrasonic resonances within cylindrical shells using the Schlieren technique,* University of Bath undergraduate project reports (unpublished).

Simon M.M. and Radlinski R.P. (1982), *Elastic wave scattering from elliptical shells*, J. Acoust. Soc. Am. **71**(2) 273-281.

Sittig E.K. and Coquin G.A. (1970), *Visualization of plane-strain vibration modes of a long cylinder capable of producing sound radiation*, J. Acoust. Soc. Am. **48**(5) 1150-1159.

Skelton E.A. (1993), *Theoretical models for predicting the acoustic characteristics of fibre-reinforced materials*, in *Acoustics of Advanced Materials for Underwater Applications,* edited by P.A. Chinnery, Proc. I.O.A. Vol 15 Pt 6 13-26.

Skelton E.A. and James J.H (1992), *Acoustics of anisotropic layered media,* J. Sound Vib. **152**(1) 157-174.

Smilansky U. (1991), Private communication.

Smith C.S. (1990), *Design of marine structures in composite materials* (Elsevier Science).

Solie L.P. and Auld B.A. (1973), *Elastic waves in free anisotropic plates,* J. Acoust. Soc. Am. **54**(1) 50-65.

Stepanishen P.R. and Ramakrishna S. (1994), *Acoustic radiation impedances and impulse responses for elliptical cylinders using internal source density and singular value decomposition methods*, J. Sound Vib. **176**(1) 49-68.

Sutton G. and Ryall D.B. (1986), *Ultrasonic velocity measurements in non-isotropic materials using an immersion method*, University of Bath undergraduate project reports (unpublished).

Tawil E.P (1930), *Ultrasonic stationary waves in gasses rendered visible by the method of striae*, Comptes Rendus **191** p92.

Tewary V.K. (1978), *Mechanics of Fibre Composites* (Wiley Eastern).

Toepler A. (1867), Ann. Chim. Phys. **131** 33-35.

Trusler J.P.M. (1991), *Physical acoustics and metrology of fluids* (IOP Publishing Ltd).

Tsui C.Y., Reid G.N. and Gaunaurd G.C. (1986), *Resonant scattering by elastic cylinders and their experimental verification*, J. Acoust. Soc. Am. *80*(2) 382-390.

Van Den Abeele K. and Leroy O. (1990), *Light diffraction by ultrasonic pulses: analytical and numerical solutions of the extended Raman-Nath equations*, J. Acoust. Soc. Am. **88**(5) 2298-2315.

Varadan V.K. and Varadan V.V. (Eds) (1980), *Acoustic, electromagnetic and elastic wave scattering - focus on the T-matrix approach* (Pergamon Press).

Varadan V.K., Varadan V.V. and Tsao S.J. (1982), *Scattering of acoustic waves by rigid cylindrical objects with sharp corners*, J. Acoust. Soc. Am. **72**(6) 1957-1964.

Veksler N.D. (1993), *Resonance Acoustic Spectroscopy* (Springer-Verlag)

Werby, M.F. et al (1990), *Acoustic resonance spectroscopy for elastic spheroids of varying aspect ratio, and the level crossing phenomena,* J. Acoust. Soc. Am. **88**(6) 2822-2829.

Westervelt P.J. (1957), *Scattering of sound by sound*, J. Acoust. Soc. Am. **29**(2) 199-203.

Westervelt P.J. (1963), *Parametric acoustic array,* J. Acoust. Soc. Am. **35**(4) 535-537.

Appendix A

In Chapter 3 high frequency fluid column resonance modes of the circular cylindrical shell are presented and evidence of periodic orbits, or 'ray paths' observed. In the first part of this Appendix (A1) the concept of rays and orbits is discussed within the context of two-dimensional cavities of various geometry. The second part of this Appendix (A2) is a reproduction of a paper dealing specifically with the stadium shaped cavity.

A1 Ray dynamics

In Chapter 3 some fundamental differences in the resonance patterns of the circular cylindrical shell are observed as we move from the low to the high frequency domain. These differences are attributed to hybridization of eigenstates in the resonances. The appearance of some of these hybrid states reminds us of one significant conceptual difference between these two domains; the applicability of the 'ray' construction. We now discuss in more detail the formulation of wave-fields in terms of classical ray paths.

By associating rays with wave-fronts - each ray being normal to the wave-front - the wave function at a point ($\psi(r)$) can be written as a sum over classical rays passing through that point, $\psi(\underline{r}) = \sum_j A_j e^{iS_j/\hbar}$, where A_j is the amplitude of the j^{th} path (A^2 is the classical probability) and S_j is its *action* $S(\underline{r}) = \int \underline{p} \cdot d\underline{r}$. The momentum ($p$) and wavelength ($\lambda$) are related by the familiar formula $p = h/\lambda$, where h is Planck's constant.

The association of rays with wave-fronts is the essence of the semi-classical approach to wave physics and is obviously only applicable in the high frequency (short wavelength) domain. We will now discuss the behaviour of these rays when confined to motion within boundaries of different shapes.

It is the shape of a boundary that determines the behaviour of the wave, or ray, that is incident upon it. We saw in Chapter 3 two different kinds of trajectory within a circular boundary, giving rise to two different kinds of orbit. We shall now discuss the idea of classical orbits within boundaries in more detail and introduce the concept of *chaotic* orbits (Berry, 1981) which must be considered in the context of *non*-circular cavities.

Let us assume the boundary to be totally rigid and imagine an 'orbit' to be that of a particle bouncing around, as in a 'billiard'. Any orbit can be described as a succession of reflections, each characterized by a position coordinate (s) and a momentum coordinate (p). These coordinates define a single *point* in phase space. The term 'billiards' is often used to describe the succession of reflections of a particle (or ray) with a boundary. For example, in the circular billiard the coordinate (s) is the arc length measured around the boundary, and the momentum (p) is the cosine of the angle that the trajectory makes with the boundary tangent at the point of impact, as illustrated below.

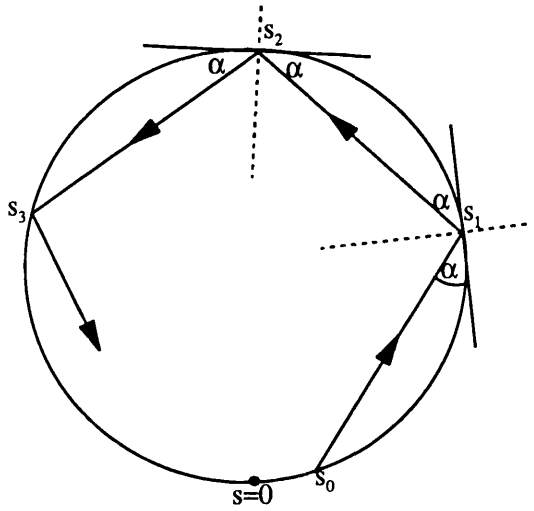

Typical orbit trajectory in a circular billiard

A succession of impacts (s,p) produces an orbit whose nature is critically dependent upon the shape of the boundary. The concept of orbits is usually understood to describe motion in phase space, but here we shall describe them within coordinate space. In general, three very different kinds of orbit are possible:

- A *closed* orbit of n bounces (phase space contains a finite set of points (s_1,p_1) ..... (s_n,p_n) which are repeatedly encountered). The 'stability' of a closed orbit is defined in terms of the behaviour of an orbit that begins with a position and/or momentum very close to that of the closed orbit[1]: if the deviations (after n impacts) of this neighbouring orbit from its initial position remain bounded and oscillate about zero, the closed

1 A 'neighbouring' point in phase space.

orbit is said to be *stable*; if the deviations increase exponentially with repeated iterations of the orbit, it is said to be *unstable*; if the deviations increase linearly, the orbit is *neutrally* stable. The 'isolation' of a closed orbit describes the orbits relation to its neighbours: an *isolated* closed orbit having no neighbouring orbits that are closed; a *non-isolated* closed orbit being one of a family of closed orbits that can be transformed into one another by rotation or translation (thereby filling an invariant curve in phase space).

- A general orbit that never repeats (is not closed) yet has a constant of motion (a conserved quantity, i.e. the motion is integrable and the solution separable[2]). In this case phase space contains a smooth curve, known as an invariant curve. In the case of the circular billiard the constant of motion is $p = \cos\alpha$ where α is, for a given orbit, the (unchanging) angle of impact at the boundary.
- A *chaotic* orbit that eventually explores every point of the boundary with every possible momentum (hence every angle α). In this case the whole two-dimensional area of phase space is eventually filled by the orbit[2]. When an orbit is chaotic, the initial conditions (starting position and momentum) are extremely important in determining the detailed structure of the orbit: any two chaotic orbits whose initial conditions are close will rapidly deviate from each other. In fact unless, the two neighbouring orbits have initial conditions that are equal to infinite precision then rapid divergence of the orbits is inevitable - this is the nature of chaos.

The circular, elliptical and stadium geometries with which this thesis is concerned each support different kinds of orbit.

The possible trajectories within a *circular* billiard belong to the first two kinds of orbit mentioned above. The periodic orbit illustrated in section 3.7.1 is a non-isolated closed orbit of neutral stability[3]. The other orbit shown in section 3.7.1 is of the second kind; the caustic corresponding to the invariant curve in phase space and being

1 For a discussion of integrability and separability see Gutzwiller (1990).

2 This is as close as we shall come here to a definition of *ergodicity*.

3 Similar orbits can be found in any position rotated with respect to the first.

dependent on the (constant) momentum ($\cos\alpha$).

The *elliptical* geometry is also an integrable kind of boundary problem, possessing orbits of the first and second kind only. The invariant curves in phase space correspond to the existence of two kinds of caustic in coordinate space that are repeatedly touched by the non-periodic orbits: a family of ellipses and a family of hyperbolae. The closed orbits fall into two distinct groups; those that are non-isolated (as in the circular case) and those which are isolated. The isolated orbits are the diametrical orbits ($n = 2$): the orbit along the major axis being unstable and that along the minor axis being stable. The caustics that result from the non-closed orbits within the ellipse have clearly been seen in the resonance patterns of the elliptical cylinder in the high frequency domain where classical interpretation is meaningful - they are not, however, presented here.

The *stadium* geometry is totally chaotic; almost all trajectories eventually explore every point on the boundary with every momentum.

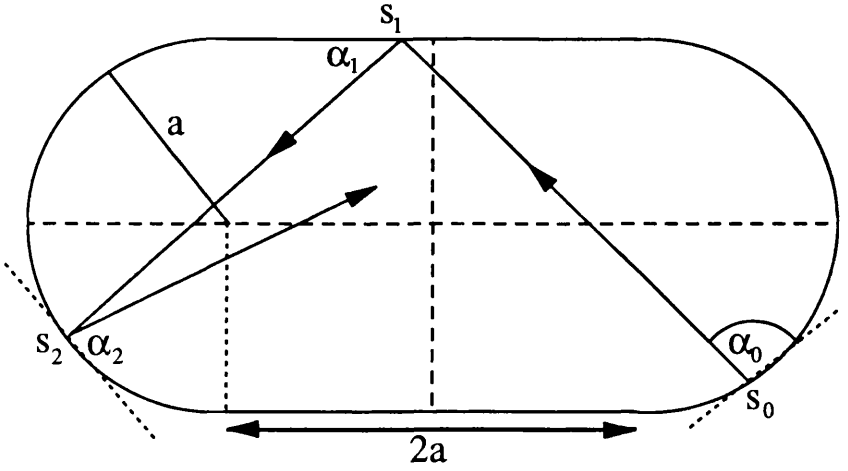

The stadium

That is to say that every point in phase space is accessed eventually (if enough iterations are permitted). This follows from the fact that there are *no* conserved quantities (constants of motion) in the stadium. Exceptional closed orbits do exist however. Firstly are the $n = 2$ orbits that bounce back and forth between the flats of the stadium and which are non-isolated. These orbits are known as 'bouncing ball' orbits and have the peculiar property that small deviations from these closed orbits result in trajectories

that zigzag around in the neighbourhood of the closed orbit for a large number of bounces before becoming unstable and exploring all other regions of the boundary (as they must inevitably do). This peculiarity lies in a consequence of the 'ergodic theorem' which states that an orbit averages equal time in equal areas of phase space; here requiring that the orbit, having left the zigzag region around the closed orbit, will not enter that region again for a long time (a large number of reflections)[1]. The remaining closed orbits are all isolated and unstable.

The periodic orbits discussed here can clearly be associated with the acoustic resonance behaviour of the circular cavity at high frequencies (as discussed in Chapter 3). Also in Chapter 3 (Figure 3.10) is shown a mode of the 'stadium' cavity which can be associated with a bouncing ball orbit. The stadium geometry is of interest because, like the elliptical geometry, it is a deformation of the circular geometry; but unlike the ellipse, which is separable, the stadium dynamics are largely chaotic. The possibility of visualizing the modes of cavities whose dynamics are chaotic, and of obtaining their spectra lead us to investigate the acoustics of the stadium using the Schlieren system. Of particular interest is the influence that the periodic orbits have on the resonances. Some preliminary results of this study are given in the paper included here in Appendix A2.

A2 Acoustic resonances within the stadium

The following paper is in preparation for Physical Review Letters and provides a more detailed investigation into the use of Schlieren for studying the acoustics of the stadium (and two-dimensional cavity resonances in general).

1 Conversely, an orbit beginning *far* from the bouncing ball orbit will not enter the neighbourhood of that closed orbit for a long time. This is of importance when considering the method of excitation of acoustic resonances within the stadium.

Experimental visualisation of acoustic resonances within the stadium

P. A. Chinnery and V. F. Humphrey
School of Physics, University of Bath, Bath BA2 7AY, UK

Acoustic resonances of an insonified water-filled "stadium" cavity are located and visualised in a non-invasive manner using a Schlieren technique. The chaotic nature of the geometry is seen to effect the form of the resonance patterns observed. Individual eigenstates of the cavity can be resolved at low frequencies; in particular the "bouncing ball" modes. In the high frequency (overlapping resonance) regime, nodal patterns are reminiscent of the "scarlets" predicted by P. O'Connor, J. Gehlen and E. J. Heller [Phys. Rev. Lett. 58, 1296 (1987)].

The solutions of the Helmholtz equation are of great importance in acoustic, electromagnetic, water-wave and quantum contexts. Recent interest in the spectra and eigenfunctions of two dimensional cavities, or "billiards", arose out of semiclassical studies of quantum systems whose classical mechanics is chaotic, such as the stadium of Bunimovich [1–4]. It is known that the *shape* of the boundary is of great importance in determining the behaviour of the system; integrable or non-integrable, regular or chaotic motion. The equivalence of the time independent Schrodinger equation and the Helmholtz equation would seem to suggest that phenomena discovered in the quantum context can be sought in other fields.

The study of chaotic systems is important in all fields since such systems are ubiquitous in realistic scattering situations; integrable systems are the exceptions not the rule. The spectra of non-integrable chaotic systems can be described by GOE (Gaussian orthogonal ensemble) random matrix statistics [5,3], unlike the spectra of integrable systems (circular, elliptical, rectangular geometries etc) which obey Poisson statistics. Also unlike integrable systems, the eigenfunctions of chaotic systems are characterised by nodal lines that meander around with few crossings; eigenfunctions of integrable systems have families of nodal lines with many perpendicular crossings (Ref. [4] Ch. 15).

The classical trajectories of a completely chaotic system, such as the stadium, access every region of phase space, and it was conjectured [6] that the eigenstates of such systems are governed by the random superposition of plane waves, all having the same wavevector magnitude but differing amplitude, phase and direction. Such a superposition was shown [7] to result not in a "speckle pattern", but in a wavefield characterised by a network of ridges which have since become known as "scarlets" [8]. In the stadium these ridges appear to be localised along classical periodic orbits, manifesting themselves as enhanced (or diminished) amplitude; they are known as "scars" of the periodic orbit. The importance of the periodic orbits was shown by Gutzwiller [9] who expressed the density of states as a sum over the classical periodic orbits. More recently Doron and Smilansky [10] have extended the summation approach to *scattering* systems. Many theoretical predictions of scarred eigenstates have been presented in the literature (see for example Ref. [2] and references therein). Scars have been identified in even quite low energy states [11]; scars and scarlets are thought to be a general wave phenomena. Scars have been observed in the high frequency vibrations of stadium shaped plates [12].

The little published experimental work concerning itself with non-integrable systems and chaotic scattering has mainly involved microwave cavities [13,11], although the manifestation of scarlets and scars have been nicely demonstrated for water surface waves by Blümel [14]. Stöckman and Stein have used microwave resonators to obtain spectra of both the stadium and the Sinai billiard [15] and have obtained wavefunctions for the stadium [16] which give good agreement with Gutzwiller's semiclassical representation, convincingly demonstrating the influence of the periodic orbits on the wavefunctions.

In this letter we describe an experimental arrangement which permits the location and visualisation of the wavefunctions of two dimensional acoustic cavities. By using a Schlieren technique we are able to study the fluid-column resonances within insonified cylindrical cavities of "stadium" cross-section, and compare them with the resonances of a circular cavity. This technique has previously been used to successfully locate and image the resonances within submerged circular and elliptical cylindrical shells [17,18] and to study the scattering of pulses by various objects and geometries [19]. The extension of this technique to the study of *non-integrable* systems seems a natural one. To our knowledge this is the first application of acoustics to the determination of the wavefunctions of two dimensional cavities having non-integrable topology.

The pressure (ψ) within the fluid column of a cylindrical shell satisfies the Helmholtz equation $(\nabla^2 + k^2)\psi = 0$ with impedance boundary conditions. For a shell presenting an *infinite* impedance to the cavity, this is just the requirement that the normal derivative of the pressure field vanish at the boundary (Neuman boundary conditions), and the resonant frequencies constitute the spectrum of eigenvalues of the cavity. However, an *insonified*

shell having *finite* impedance constitutes a true scattering problem and yields a *resonance* spectrum characterised by resonances of finite width which may overlap at high frequencies. Of particular interest in the circular geometry is the hybridization of eigenstates in the overlapping resonance regime, and the effect this has on the resonance patterns, many of which exhibit new symmetries of great aesthetic appeal.

One advantage of this technique is that it is non-invasive and permits wavefields to be recorded instantly on film or video (with a resolution limited only by that of the film), or analysed by computer using an image-grabbing system. This allows resonance modes to be rapidly identified as the frequency is swept. A disadvantage of the present experimental arrangement is the low Q-factor of the acoustic system which prevents individual resonances from being resolved at high frequency (although the semiclassical regime *is* one of overlapping resonances [20].)

The experimental arrangement is shown in Fig. 1 and has been described in detail elsewhere [17,19]. The principle upon which Schlieren operates is that light is *diffracted* during its passage through an acoustic field in a fluid; the diffracted light containing information about the spatial distribution of the acoustic field. Light from a high power light emitting diode is focused onto a pinhole, or an array of pinholes having a random basis. The resultant light beam is collimated by the first parabolic mirror and passed through a glass walled tank containing the acoustic field. In the present application a transducer placed in the tank, with its axis perpendicular to the light beam, insonifys a cylinder suspended with its axis parallel to the light beam. The light emerging from the tank is brought to a focus by the second parabolic mirror: the resultant diffraction pattern contains the light which has passed straight through the acoustic field undiffracted (zeroth order) and the diffracted light (higher orders). By removing a part of the light in the diffraction pattern and allowing the remainder to recombine in a still camera or video, an "image" of the acoustic field is obtained. The optical distribution in the image has, in general, a complicated dependence on the spatial filtering arrangement and the pressure amplitude in the acoustic field. However, it has been shown [21] that for *low* acoustic pressures and zeroth order filtering, the optical distribution approximates the *square* of the acoustic pressure distribution. As any variations in the acoustic field *along* the light path are integrated out, the system is restricted to the visualisation of resonances of bodies having translational symmetry.

The cylinder used in these experiments was a stadium shaped cavity in an aluminium block, the semi-circular ends of the cavity had radii (a) $12.7mm$ and the straight sections of the cavity were of length $2a$. The cylinder was $100mm$ long and could be insonified at various angles to the minor axis of the stadium (see Fig. 1). The transducer was driven in continuous mode, and by sweeping the frequency and altering the angle of insonification, resonances within the cavity were easily located and recorded on film. The current experimental arrangement incorporates parabolic mirrors of focal length 1.8m, has an aperture of approximately $25cm$, and can be used to visualise acoustic fields down to about 100kHz. The upper frequency limit of the visualisation system is unlimited, although individual wavefronts cannot be resolved at very high frequencies (above several megahertz).

The ability to resolve individual modes of the cavity depends upon the density of resonances and the Q-factor of the scattering system; in this case influenced by the losses from the cavity due to the finite impedance of the shell, and the method of excitation. For a truly bound system (discrete eigenvalues) the average density of states of a cavity of area A is given by

$$\overline{\rho}(\nu) = \frac{2\pi A\nu}{c^2} \tag{1}$$

where c is the speed of sound in water and ν is the frequency. The average separation of states is $1/\overline{\rho}(\nu)Hz$ and it follows that Q-factor's of the order

$$Q = \frac{\nu}{\Delta\nu} = \overline{\rho}(\nu)\nu = \frac{2\pi A}{c^2}\nu^2 \tag{2}$$

are necessary for individual states to be resolved at a frequency ν. The average number of states with a frequency *less* than ν is given by

$$\overline{N}(\nu) = \frac{\pi A}{c^2}\nu^2 \approx \frac{Q}{2}. \tag{3}$$

For our stadium ($A = (4+\pi)a^2$, $c = 1480$) the 1000th eigenstate exists around 800kHz and a Q of about 2000 would be required to resolve these 1000 states; the Q of our present system is *not* that high. The overlapping resonance regime begins at around several hundred kilohertz, in the megahertz region we have *many* overlapping states and the consequences of their interference must be considered when interpreting the resonance patterns obtained with the system.

At the lowest frequencies analysed with this system the cavity resonances are clearly resolved in frequency. Fig. 2(a) shows a typical low frequency resonance found at 150.9 kHz. The "bouncing ball" (BB) periodic orbit can be associated with this mode which is confined to the portion of the cavity between the flat sides, avoiding the semi-circular ends. Such resonance modes are the most easily excited and identified; by insonifying the stadium at 'normal incidence', members of the family of BB resonances can be isolated and visualised over a wide frequency range; a mode found at 720.2 kHz is shown in Fig. 2(b). The resonance shown in Fig. 2(c) was found at 261.1 kHz and has an altogether different appearance. Unlike the BB modes, a significant portion of the disturbance is present in the semi-circular ends, and the

focusing effect of these ends is clearly seen. At 664.8 kHz a wave function is shown (Fig. 2(d)) that can be associated with the "double-diamond" periodic orbit. The resonance widths have become significant at this frequency; modes are thought to overlap and the appearance of the wavefield alters as the incident angle is varied.

Fig. 2(e) shows a typical wavefield observed at very high frequency (2.5 MHz). The network of ridges is reminiscent of the "scarlets" predicted in [7] and observed in water surface waves [14]. In the acoustic case presented here there are many overlapping resonances contributing to the wavefunction at this frequency and varying the angle of the incident beam causes the pattern to change, although the ridge structure remains. There is some evidence in this image that the scarlets are aligning themselves along the trajectory of a periodic orbit.

For comparison we present results for an insonified *circular* shell; a geometry that is integrable. The shell is made of brass, and has inner and outer radii of $14.25mm$ and $15.85mm$. In the low Frequency regime we again see isolated resonance modes (n,m) whose wave functions are of the form $J_n(k_{n,m})cos(n\phi)$; the separable nature of this geometry reflects itself in the presence of nodal line families which intersect perpendicularly. Fig. 3(a) shows the (2,4) fluid column resonance. At a higher frequency of 2.5 MHz where resonances overlap, the nodal crossings are, in places, destroyed and new symmetries appear (Fig. 3(b)); in this case a five-pointed star is clearly evident. Many such patterns of great aesthetic beauty can be observed within the circular cylindrical shell. Similar effects are to be expected in the overlapping resonance regime of the stadium cavity.

The ease with which the resonance modes can be located and visualised over a wide range of frequencies makes the Schlieren system a valuable tool for studying the eigenfunctions, and to a limited extent the *spectra*, of 2-dimensional cavities. The main disadvantage of the current experimental setup is the low Q-factor of the acoustic system, preventing spectra from being obtained at high frequencies. It is proposed that alternative acoustic arrangements, perhaps involving excitation of fluid filled shells *in air*, would yield significantly higher Q-factors, permitting a greater number of resonance modes to be resolved and spectra obtained. A preliminary study undertaken by the authors has demonstrated that such a technique could, with care, be incorporated into the Schlieren visualisation system.

The association of periodic orbits with the acoustic wavefunctions of the stadium has been demonstrated, and the appearance of scarlets at higher frequencies noted. The importance of considering the effects of overlapping resonance states in realistic scattering systems has been noted.

We gratefully acknowledge important discussions and the interest in this work shown by U. Smilansky. We are also grateful to M. Berry for suggesting this study, and to P. Boasman and E. Doron for discussions and comments upon the work.

[1] E. J. Heller and S. Tomsovic, Phys. Today July 1993, p. 38.
[2] *Chaos and Quantum Physics*, edited by M.-J. Giannoni, A. Voros and J. Zinn-Justin, Les Houches Session LII, 1989 (Elsevier, Amsterdam, 1991).
[3] M. V. Berry, Proc. R. Soc. Lond. A **413**, 183 (1987).
[4] M. C. Gutzwiller, *Chaos in Classical and Quantum Mechanics* (Springer-Verlag, New York, 1990).
[5] E. Ott, *Chaos in Dynamical Systems* (Cambridge University Press, 1993).
[6] M. V. Berry, in *Chaotic Behaviour of Deterministic Systems*, edited by G. Iooss, R. H. G. Helleman and R. Stora, Les Houches Session XXXVI, 1981 (North-Holland, 1983), p. 171.
[7] P. O'Connor, J. Gehlen and E. J. Heller, Phys. Rev. Lett. **58**, 1296 (1987).
[8] E. J. Heller, in Ref. [2], Course 9, Ch. 5.
[9] M. C. Gutzwiller, J. Math. Phys. **12**, 343 (1971), and references therein.
[10] E. Doron and U. Smilansky, Phys. Rev. Lett. **68**, 1255 (1992).
[11] S. Sridhar and E. J. Heller, Phys. Rev. A **46**, R1728 (1992).
[12] O. Legrand, C. Schmit and D. Sornette, Europhys. Lett, **18** (2), 101 (1992).
[13] S. Sridhar, Phys. Rev. Lett. **67**, 785 (1991).
[14] R. Blümel *et al.*, Phys. Rev. A **45**, 2641 (1992).
[15] H. -J. Stöckmann and J. Stein, Phys. Rev. Lett. **64**, 2215 (1990).
[16] J. Stein and H. -J. Stöckmann, Phys. Rev. Lett. **68**, 2867 (1992).
[17] V. F. Humphrey, S. M. Knapp and C. Beckett in *Physical Acoustics*, edited by O. Leroy and M. A. Breazeale (Plenum Press, New York, 1991), p. 371.
[18] P. A. Chinnery and V. F. Humphrey, in *Proceedings of the Second European Conference on Underwater Acoustics, Vol. 1*, edited by L. Bjørnø(European Commission, Luxembourg, 1994), p. 159.; *Proceedings of the Institute of Acoustics, Vol. 16, Pt. 6* (1994).
[19] S. M. Knapp and V. F. Humphrey, in *Ultrasonics International 89 Conference Proceedings* (Butterworths, 1989), p. 1089.
[20] R. Blümel, B. Dietz, C. Jung and U. Smilansky, J. Phys. A: Math. Gen. **25**, 1483 (1992).
[21] S. M. Knapp, P. A. Chinnery and V. F. Humphrey, University of Bath Reports (unpublished).

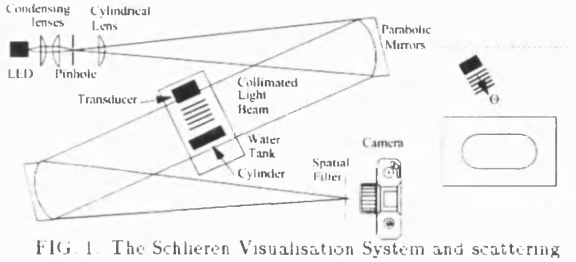

FIG. 1. The Schlieren Visualisation System and scattering geometry (inset)

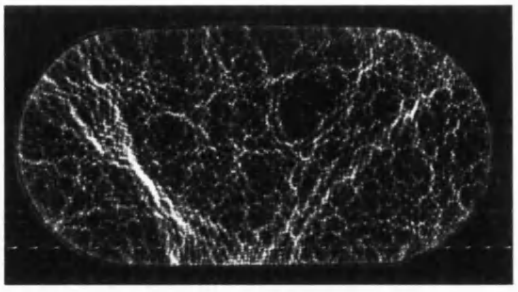

FIG. 2. Acoustic wavefields within the stadium cavity. Frequencies are (a) 150.9kHz, (b) 720.2kHz, (c) 261.1kHz, (d) 664.8kHz and (e) 2.5MHz. Different angles of the incident beam (not shown) were used to excite each resonance [see Fig. 1 (inset)]

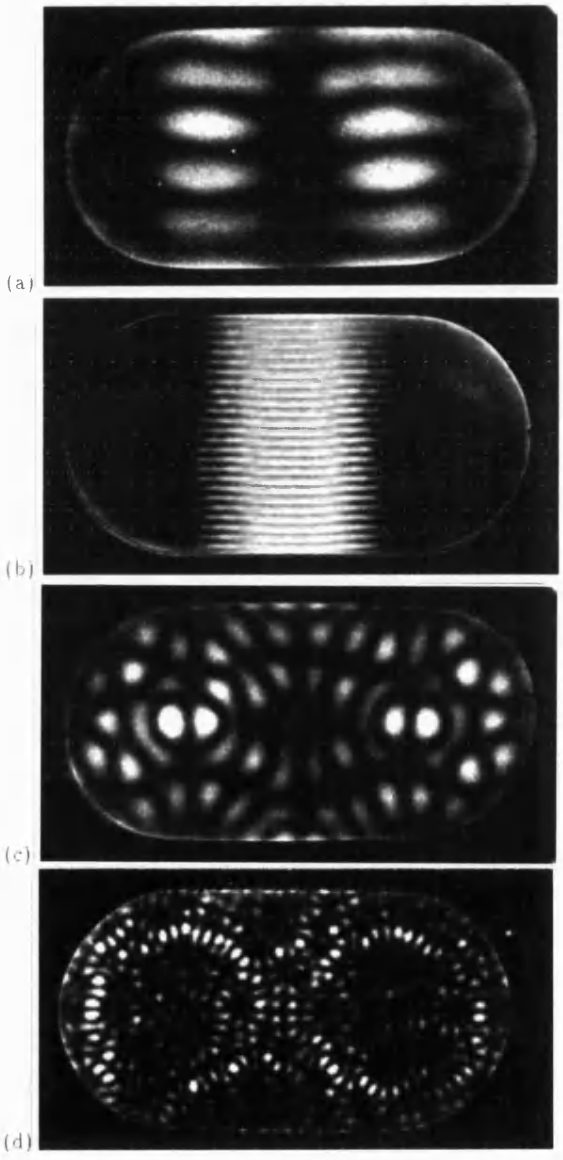

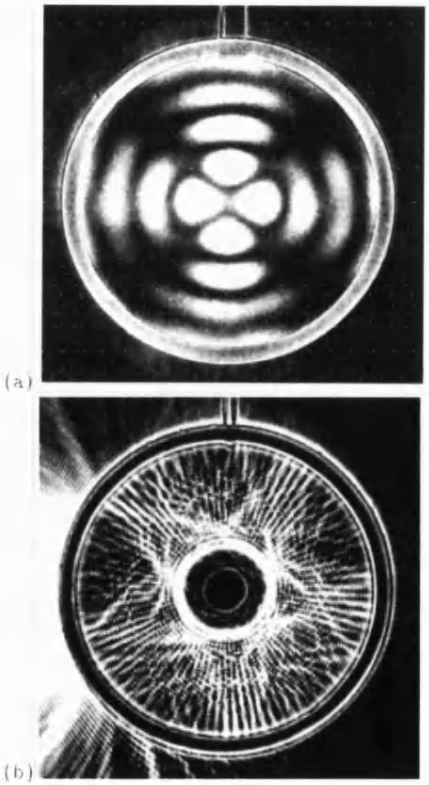

FIG. 3. Wavefields within the circular cavity (a) 218kHz and (b) 2.5MHz

Appendix B

Details of the elliptical coordinate system and Mathieu's equations are given. Further details can be found in Morse & Feschbach (1946), McLachlan (1947) and Abramowitz & Stegun (1972).

B1 Elliptical coordinate systems

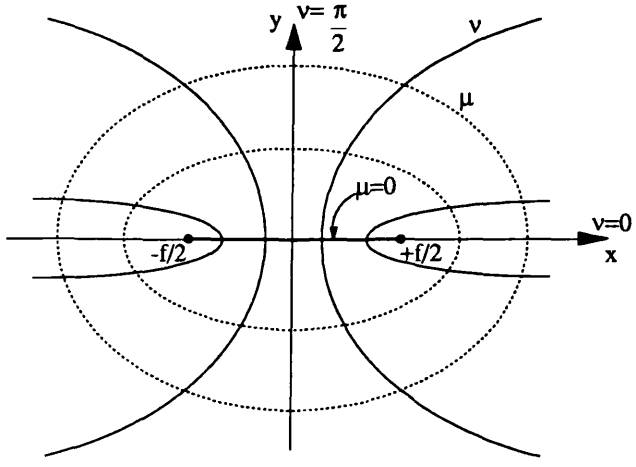

The elliptical coordinate system is shown above. The coordinate μ represents a family of confocal ellipses;

$$\frac{x^2}{\left(\frac{f}{2}\right)^2\cosh^2\mu} + \frac{y^2}{\left(\frac{f}{2}\right)^2\sinh^2\mu} = 1 \qquad \text{(B1.1)}$$

with foci at $\pm f/2$ and is described as the 'radial' coordinate. The elliptical coordinate ν represents a family of confocal hyperbolae;

$$\frac{x^2}{\left(\frac{f}{2}\right)^2\cos^2\nu} + \frac{y^2}{\left(\frac{f}{2}\right)^2\sin^2\nu} = 1 \qquad \text{(B1.2)}$$

with the same foci and is described as the 'angular' coordinate. The μ and ν intersect everywhere orthogonally and define a coordinate system whose relation to the cartesian coordinates (x, y) is given by

$$x = \frac{f}{2}\cosh\mu\cos\nu \qquad \textit{and} \qquad y = \frac{f}{2}\sinh\mu\sin\nu. \tag{B1.3}$$

There are in fact an infinity of elliptical coordinate systems corresponding to the different values of f.

The circular limit is obtained as $\mu \to \infty$ and $f \to 0$. In this limit we then have the relation

$$\frac{f}{2}\cosh\mu \;\to\; \frac{f}{2}\sinh\mu \;\to\; r \qquad \text{as} \quad f \;\to\; 0 \tag{B1.4}$$

where r is the radial polar coordinate. In this same limit the hyperbolae (ν) become straight lines, passing through the origin (the point at which the two foci coalesce), and inclined at an angle ϕ to the major axis;

$$\nu \;\to\; \phi \qquad \text{as} \qquad f \;\to\; 0 \tag{B1.5}$$

where ϕ is the angular polar coordinate. We have therefore recovered the circular polar coordinate system from the elliptical system in the above limit.

An ellipse of semi-major axis l and semi-minor axis s can be described by a single coordinate μ_0,

$$\mu_0 \;=\; \tanh^{-1}\left(\frac{s}{l}\right). \tag{B1.6}$$

This is a dimensionless quantity; the actual 'size' of the ellipse depends upon the interfocal distance f. The eccentricity (e) of such an ellipse is given by

$$e \;=\; sech\,\mu_0\,. \tag{B1.7}$$

If the shape of an ellipse is changed in such a way that its circumference ($\mathcal{L}_c$),

$$\mathcal{L}_c \;=\; \pi(s+l),$$

remains constant and equal to that of a circle of radius b, then the dimensions of the major and minor axis are related by

$$b = \frac{l+s}{2}. \tag{B1.8}$$

B2 Mathieu's equations

The two-dimensional wave equation in elliptical coordinates separates into two equations; Mathieu's equation and Mathieu's Modified equation. Mathieu's equation,

$$\frac{\partial^2 \Theta}{\partial \nu^2} + (\iota - 2q\cos 2\nu)\Theta = 0 \tag{B2.1}$$

has solutions of period π, and solutions of period 2π; each of which can have even (e) or odd (o) symmetry about $\nu = 0$. These solutions are the 'Mathieu functions';

$$\begin{aligned}
\Theta = ce_{2n}(\nu, q) &= \sum_{r=0}^{\infty} A_{2r}^{2n} \cos(2r\nu) && (e, \pi) \\
\Theta = ce_{2n+1}(\nu, q) &= \sum_{r=0}^{\infty} A_{2r+1}^{2n+1} \cos((2r+1)\nu) && (e, 2\pi) \\
\Theta = so_{2n}(\nu, q) &= \sum_{r=0}^{\infty} B_{2r}^{2n} \sin(2r\nu) && (o, \pi) \\
\Theta = so_{2n+1}(\nu, q) &= \sum_{r=0}^{\infty} B_{2r+1}^{2n+1} \sin((2r+1)\nu) && (o, 2\pi).
\end{aligned} \tag{B2.2}$$

Recursion relations exist between the coefficients (A and B). The corresponding separation constants, or 'characteristic values', (ι), are labelled a_{2r}, a_{2r+1}, b_{2r} and b_{2r+1} respectively and are each the roots of 'continued fraction' equations given below.

The following definitions are made;

$$D_r = \frac{(1-r^2)}{q} \tag{B2.3}$$

$$Ge_r = \frac{A_r}{A_{r-2}} \qquad \text{and} \qquad Go_r = \frac{B_r}{B_{r-2}}, \tag{B2.4}$$

and each of the four solutions given in turn;

$\underline{ce_{2n}}$

a_{2r} is the root of

$$D_0 - \frac{2}{D_2 -} \frac{1}{D_4 -} \frac{1}{D_6 - \ldots} \ldots = 0$$

and the coefficients given by

$$Ge_2 = D_0 \qquad Ge_4 = D_2 - \frac{2}{Ge_2}$$

$$Ge_r = \frac{1}{D_r - Ge_{r+2}} \qquad r \geq 4$$

with the normalization condition

$$A_0^2 + \sum_{n=1}^{\infty} A_{2n}^2 = 1$$

$\underline{ce_{2n+1}}$

a_{2r+1} is a root of

$$D_1 - 1 - \frac{1}{D_3 -} \frac{1}{D_5 -} \frac{1}{D_7 - \ldots} \ldots = 0$$

and the coefficients given by

$$Ge_3 = D_1 - 1 \, , \; Ge_r = \frac{1}{D_r - Ge_{r+2}} 34 r \geq 3$$

with normalization

$$\sum_{n=0}^{\infty} A_{2n+1}^2 = 1$$

$\underline{se_{2n}}$

b_{2r} is a root of

$$D_2 - \frac{1}{D_4 -} \frac{1}{D_6 - \ldots} \ldots = 0$$

and the coefficients given by

$$Go_4 = D_2$$

$$Go_r = \frac{1}{D_r - Go_{r+2}} \qquad r \geq 4$$

with normalization

$$\sum_{n=1}^{\infty} B_{2n}^2 = 1$$

$\underline{se_{2n+1}}$

b_{2r+1} are the roots of

$$D_1 + 1 - \frac{1}{D_3 -} \frac{1}{D_5 -} \frac{1}{D_7 - \ldots} \ldots = 0$$

and the coefficients given by

$$Go_3 = D_1 + 1 \, , \; Go_r = \frac{1}{D_r - Go_{r+2}} r \geq 3$$

with normalization

$$\sum_{n=0}^{\infty} B_{2n+1}^2 = 1$$

(B2.5)

Radial Mathieu functions

The Modified Mathieu's equation is

$$\frac{\partial^2 j}{\partial \mu^2} - (\iota - 2q\cosh\mu)j = 0, \tag{B2.6}$$

whose solutions are the Modified Mathieu functions;

$$\begin{aligned}
j &= je_{2n}(\mu, q) = \sum_{r=0}^{\infty} A_{2r}^{2n} \cosh(2r\mu) && (e, \pi) \\
j &= je_{2n+1}(\mu, q) = \sum_{r=0}^{\infty} A_{2r+1}^{2n+1} \cosh((2r+1)\mu) && (e, 2\pi) \\
j &= jo_{2n}(\mu, q) = \sum_{r=0}^{\infty} B_{2r}^{2n} \sinh(2r\mu) && (o, \pi) \\
j &= jo_{2n+1}(\mu, q) = \sum_{r=0}^{\infty} B_{2r+1}^{2n+1} \sinh((2r+1)\mu) && (o, 2\pi)
\end{aligned} \tag{B2.7}$$

The coefficients (A, B) and separation constants (ι) are the same as for the corresponding Mathieu functions given previously.

There are also a second set of solutions to the Modified Mathieu's equation, but these are not needed for the field *inside* an elliptical boundary.

Appendix C

C1 Reduced subscript notation

Symmetry properties of the forth-rank stiffness tensor of an elastic medium allow it to be written as a *matrix* using the reduced subscript notation whereby the following *pairs* of subscripts are replaced by single subscripts;

$$11 \rightarrow 1, \quad 22 \rightarrow 2, \quad 33 \rightarrow 3, \quad 23 \rightarrow 4, \quad 13 \rightarrow 5, \quad 12 \rightarrow 6.$$

Using the same notation the second rank stress and strain tensors are written as *vectors*.

C1.1 Differential operators

The differential operators applied to variables written in reduced subscript notation are,

$$\nabla = \begin{pmatrix} \frac{\partial}{\partial x} & 0 & 0 \\ 0 & \frac{\partial}{\partial y} & 0 \\ 0 & 0 & \frac{\partial}{\partial z} \\ 0 & \frac{\partial}{\partial z} & \frac{\partial}{\partial y} \\ \frac{\partial}{\partial z} & 0 & \frac{\partial}{\partial x} \\ \frac{\partial}{\partial y} & \frac{\partial}{\partial x} & 0 \end{pmatrix} \qquad \nabla\cdot = \begin{pmatrix} \frac{\partial}{\partial x} & 0 & 0 & 0 & \frac{\partial}{\partial z} & \frac{\partial}{\partial y} \\ 0 & \frac{\partial}{\partial y} & 0 & \frac{\partial}{\partial z} & 0 & \frac{\partial}{\partial x} \\ 0 & 0 & \frac{\partial}{\partial z} & \frac{\partial}{\partial y} & \frac{\partial}{\partial x} & 0 \end{pmatrix} \tag{C1.1}$$

C1.2 Bond stress transformation matrix

In the reduced subscript notation the stiffness matrix in a rotated coordinate system (x', y', z') is given by

$$C' = M\, C\, M^t \tag{C1.2}$$

where M is the Bond stress transformation matrix,

$$M = \begin{pmatrix} a_{xx}^2 & a_{xy}^2 & a_{xz}^2 & 2a_{xy}a_{xz} & 2a_{xz}a_{xx} & 2a_{xx}a_{xy} \\ a_{yx}^2 & a_{yy}^2 & a_{yz}^2 & 2a_{yy}a_{yz} & 2a_{yz}a_{yx} & 2a_{yx}a_{yy} \\ a_{zx}^2 & a_{zy}^2 & a_{zz}^2 & 2a_{zy}a_{zz} & 2a_{zz}a_{zx} & 2a_{zx}a_{zy} \\ a_{yx}a_{zx} & a_{yy}a_{zy} & a_{yz}a_{zz} & a_{yy}a_{zz}+a_{yz}a_{zy} & a_{yx}a_{zz}+a_{yz}a_{zx} & a_{yy}a_{zx}+a_{yx}a_{zy} \\ a_{zx}a_{xx} & a_{zy}a_{xy} & a_{zz}a_{xz} & a_{xy}a_{zz}+a_{xz}a_{zy} & a_{xz}a_{zx}+a_{xx}a_{zz} & a_{xx}a_{zy}+a_{xy}a_{zx} \\ a_{xx}a_{yx} & a_{xy}a_{yy} & a_{xz}a_{yz} & a_{xy}a_{yz}+a_{xz}a_{yy} & a_{xz}a_{yx}+a_{xx}a_{yz} & a_{xx}a_{yy}+a_{xy}a_{yx} \end{pmatrix} \quad \text{(C1.3)}$$

and where the a_{ij} are elements of the coordinate transformation matrix. For example, rotation through an angle θ about the x-axis is described by

$$a = \begin{pmatrix} 1 & 0 & 0 \\ 0 & \cos\theta & \sin\theta \\ 0 & -\sin\theta & \cos\theta \end{pmatrix}. \quad \text{(C1.4)}$$

C2 Christoffel matrix for orthotropic media

If the differential operators ∇ and ∇• act upon displacements of the form $e^{i(k_x x + k_y y + k_z z - \omega t)}$, they reduce to

$$\nabla \rightarrow i\begin{pmatrix} k_x & 0 & 0 \\ 0 & k_y & 0 \\ 0 & 0 & k_z \\ 0 & k_z & k_y \\ k_z & 0 & k_x \\ k_y & k_x & 0 \end{pmatrix} \quad \text{(C2.1)}$$

and

$$\nabla\bullet \rightarrow i\begin{pmatrix} k_x & 0 & 0 & 0 & k_z & k_y \\ 0 & k_y & 0 & k_z & 0 & k_x \\ 0 & 0 & k_z & k_y & k_x & 0 \end{pmatrix}. \quad \text{(C2.2)}$$

Using these operators, and the *orthotropic* stiffness matrix (C_{ij}), in the Christoffel equation (6.10) the Christoffel matrix elements for orthotropic media are found to be

$$\begin{aligned}
\Gamma_{11} &= C_{11}\hat{k}_x^2 + C_{66}\hat{k}_y^2 + C_{55}\hat{k}_z^2 & \Gamma_{12} &= (C_{12}+C_{66})\hat{k}_x\hat{k}_y \\
\Gamma_{22} &= C_{66}\hat{k}_x^2 + C_{22}\hat{k}_y^2 + C_{44}\hat{k}_z^2 & \Gamma_{13} &= (C_{13}+C_{55})\hat{k}_x\hat{k}_z \\
\Gamma_{33} &= C_{55}\hat{k}_x^2 + C_{44}\hat{k}_y^2 + C_{33}\hat{k}_z^2 & \Gamma_{23} &= (C_{23}+C_{44})\hat{k}_y\hat{k}_z
\end{aligned} \qquad \text{(C2.3)}$$

where $\hat{k}_i$ are the direction cosines of the wave.

C3 Spectral displacements within the layer

Spectral variables, such as the spectral displacement vector ($\overline{U}_i$), are defined by relations of the form

$$U_i(x,y,z) = \frac{1}{4\pi^2}\int\int \overline{U}_i(k_x,k_y,z)e^{i(xk_x+yk_y)}dk_xdk_y \qquad \text{(C3.1)}$$

$$\overline{U}_i(k_x,k_y,z) = \int\int U_i(x,y,z)e^{-i(xk_x+yk_y)}dxdy. \qquad \text{(C3.2)}$$

With this definition the spectral form of equation (6.10) becomes, after lengthy algebra,

$$\left[D_{ij}\frac{\partial^2}{\partial z^2} + iB_{ij}\frac{\partial}{\partial z} + A_{ij}\right]\overline{U}_j = 0 \qquad i,j = 1,2,3 \qquad \text{(C3.3)}$$

where, for orthotropic media, the matrices A, B and D have non-zero elements;

$$\begin{aligned}
A_{11} &= C_{11}k_x^2 + C_{66}k_y^2 - \rho\omega^2 & B_{13} &= B_{31} = -(C_{13}+C_{55})k_x \\
A_{12} &= A_{21} = (C_{12}+C_{66})k_xk_y & B_{23} &= B_{32} = -(C_{23}+C_{44})k_y \\
A_{22} &= C_{66}k_x^2 + C_{22}k_y^2 - \rho\omega^2 & D_{11} &= -C_{55}, \quad D_{22} = -C_{44} \\
A_{33} &= C_{55}k_x^2 + C_{44}k_y^2 - \rho\omega^2 & D_{33} &= -C_{33}.
\end{aligned} \qquad \text{(C3.4)}$$

Equation (C3.3) is a second order differential equation whose solutions are of the form

$$\overline{U}_j(k_x,k_y,z) = \overline{U}_j(k_x,k_y)e^{i\gamma z}. \qquad \text{(C3.5)}$$

Substituting this solution back into (C3.3) leads to an equation in the unknowns γ;

$$[-\gamma^2 D_{ij} - \gamma B_{ij} + A_{ij}]\overline{U}_j(k_x, k_y) = 0, \tag{C3.6}$$

requiring

$$|\gamma^2 D + \gamma B - A| = 0, \tag{C3.7}$$

which is cubic in γ^2;

$$\gamma^6 + b_1\gamma^4 + b_2\gamma^2 + b_3 = 0 \tag{C3.8}$$

where

$$b_1 = -\frac{(A_{11}D_{22}D_{33} + D_{11}(A_{22}D_{33} + A_{33}D_{22}) + D_{11}B_{23}^2 + D_{22}B_{13}^2)}{D_{11}D_{22}D_{33}}$$

$$b_2 = \frac{A_{11}(A_{22}D_{33} + A_{33}D_{22} + B_{23}^2) + A_{22}A_{33}D_{11} - A_{12}^2 D_{33} + B_{13}^2 A_{22} - 2A_{12}B_{13}B_{23}}{D_{11}D_{22}D_{33}} \tag{C3.9}$$

$$b_3 = \frac{A_{12}^2 A_{33} - A_{11}A_{22}A_{33}}{D_{11}D_{22}D_{33}}.$$

The six roots of this equation (eigenvalues of (C3.7)) are labelled γ^l ($l = 1 \rightarrow 6$) and the corresponding eigenvectors $\overline{U}_j = \overline{W}_j^l$ are found, by solution of equation (C3.6), to be

$$\begin{pmatrix} \overline{W}_x^l \\ \overline{W}_y^l \\ \overline{W}_z^l \end{pmatrix} = \begin{pmatrix} (A_{33} - D_{33}\gamma^{(l)2})(A_{22} - D_{22}\gamma^{(l)2}) - B_{23}^2\gamma^{(l)2} \\ B_{23}B_{13}\gamma^{(l)2} - A_{12}(A_{33} - D_{33}\gamma^{(l)2}) \\ -B_{23}A_{12}\gamma^l + B_{13}(A_{22} - D_{22}\gamma^{(l)2})\gamma^l \end{pmatrix}, \tag{C3.10}$$

for non-degenerate eigenvalues γ^l, and

$$\begin{pmatrix} \overline{W}_x^m \\ \overline{W}_y^m \\ \overline{W}_z^m \end{pmatrix} = \begin{pmatrix} -B_{23} \\ +B_{13} \\ 0 \end{pmatrix} \quad \text{and} \quad \begin{pmatrix} \overline{W}_x^n \\ \overline{W}_y^n \\ \overline{W}_z^n \end{pmatrix} = \begin{pmatrix} -B_{13}\gamma^n \\ -B_{23}\gamma^n \\ -\gamma^{(n)2}(B_{13}^2 + B_{23}^2)/(A_{33} - D_{33}\gamma^{(n)2}) \end{pmatrix}, \tag{C3.11}$$

for eigenvalues γ^m and γ^n that are equal.

The general solution is a linear combination of these six eigenvectors;

$$\overline{U}_j(k_x,k_y,z) \;=\; L^l\,\overline{W}^l_j\,e^{i\gamma^l z} \qquad \begin{matrix} l=1\to 6 \\ j=x,y,z \end{matrix} \tag{C3.12}$$

where the L^l are unknown coefficients.

C4 Spectral stresses within the layer

An expression for the spectral stresses within the layer is now derived. The spectral forms of the stress-strain equation (6.2) and the strain-displacement equation (6.3) together relate the spectral stresses ($\overline{\mathcal{T}}$) to the spectral displacements ($\overline{U}$) in the layer;

$$\overline{\mathcal{T}}_i \;=\; C_{ij}\,\nabla_{jk}\,\overline{U}_k\,. \tag{C4.1}$$

Substituting the expression for the spectral displacements (C3.12) gives

$$\overline{\mathcal{T}}_i(k_x,k_y,z) = L^l\,\overline{Q}^l_i e^{i\gamma z} \tag{C4.2}$$

where

$$\overline{Q}^l_i = C_{ij}\,\nabla_{jk}\,\overline{W}^l_k \quad [{}^{k=1\to 3}_{i,j,l=1\to 6}]. \tag{C4.3}$$

Of these *six* components of stress, only those three that apply to planes of constant z are required, that is ; $\mathcal{T}_{zx}\equiv\mathcal{T}_5$, $\mathcal{T}_{zy}\equiv\mathcal{T}_4$, $\mathcal{T}_{zz}\equiv\mathcal{T}_3$. The corresponding elements of $\overline{Q}$ are found to be

$$\begin{pmatrix} \overline{Q}^l_3 \\ \overline{Q}^l_4 \\ \overline{Q}^l_5 \end{pmatrix} \;=\; \begin{pmatrix} i\left(C_{13}k_x\overline{W}^l_x + C_{23}k_y\overline{W}^l_y + C_{33}\gamma\overline{W}^l_z\right) \\ iC_{44}\left(k_y\overline{W}^l_z + \gamma\overline{W}^l_y\right) \\ iC_{55}\left(k_x\overline{W}^l_z + \gamma\overline{W}^l_x\right) \end{pmatrix}. \tag{C4.4}$$

We have therefore found both the spectral displacements (C3.12) and spectral stresses (C4.2) at the surfaces of the layer in terms of six unknown constants L^l.

C5 Spectral stiffness relation

A 'stiffness' relation between surface spectral stresses and displacements is derived. We firstly form a vector of interfacial displacements $\overline{u} \equiv [\overline{U}^1, \overline{U}^2]$ whose components are vectors of the displacement at the first (1) and second (2) interfaces of the layer (Figure 6.5);

$$\overline{U}^1 = \begin{pmatrix} \overline{U}_x(d) \\ \overline{U}_y(d) \\ \overline{U}_z(d) \end{pmatrix} \qquad \overline{U}^2 = \begin{pmatrix} \overline{U}_x(0) \\ \overline{U}_y(0) \\ \overline{U}_z(0) \end{pmatrix} \tag{C5.1}$$

For each of these displacements the corresponding stresses in the elastic layer, $\overline{T} \equiv [\overline{T}^1, \overline{T}^2]$, are written

$$\overline{T}^1 = \begin{pmatrix} \overline{T}_{zx}(d) \\ \overline{T}_{zy}(d) \\ \overline{T}_{zz}(d) \end{pmatrix} \qquad \overline{T}^2 = \begin{pmatrix} \overline{T}_{zx}(0) \\ \overline{T}_{zy}(0) \\ \overline{T}_{zz}(0) \end{pmatrix}. \tag{C5.2}$$

These components of displacement and stress at the first ($z = d$) and second ($z = 0$) surfaces of the layer can be deduced from equations (C3.12) and (C4.2) to be

$$\begin{aligned} \overline{u}_M(k_x, k_y) &= R_M^i L^i \\ \overline{T}_N(k_x, k_y) &= P_N^l L^l , \end{aligned} \tag{C5.3}$$

where

$$\begin{aligned} R_1^i &= \overline{W}_x^i e^{i\gamma^i d} & P_1^l &= \overline{Q}_3^l e^{i\gamma^l d} \\ R_2^i &= \overline{W}_y^i e^{i\gamma^i d} & P_2^l &= \overline{Q}_4^l e^{i\gamma^l d} \\ R_3^i &= \overline{W}_z^i e^{i\gamma^i d} & P_3^l &= \overline{Q}_5^l e^{i\gamma^l d} \\ R_4^i &= \overline{W}_x^i & P_4^l &= \overline{Q}_3^l \\ R_5^i &= \overline{W}_y^i & P_5^l &= \overline{Q}_4^l \\ R_6^i &= \overline{W}_z^i & P_6^l &= \overline{Q}_5^l . \end{aligned} \tag{C5.4}$$

The unknown coefficients (L^i) can be eliminated between the two equations in (C5.3). Multiplying the first by R^{-1} gives

$$[R^{-1}]_l^M \overline{\mathcal{U}}_M = [R^{-1}]_l^M R_M^i L^i = \delta_{li} L^i = L^l, \tag{C5.5}$$

with which the second can be written

$$\overline{\mathcal{T}}_N(k_x, k_y) = [P_N^l]\,[R^{-1}]_l^M \overline{\mathcal{U}}_M(k_x, k_y), \tag{C5.6}$$

or, in matrix form,

$$\begin{pmatrix} \overline{\mathcal{T}}^1 \\ \overline{\mathcal{T}}^2 \end{pmatrix} = \begin{pmatrix} \mathcal{S}_{11} & \mathcal{S}_{12} \\ \mathcal{S}_{21} & \mathcal{S}_{22} \end{pmatrix} \begin{pmatrix} \overline{U}^1 \\ \overline{U}^2 \end{pmatrix}, \tag{C5.7}$$

where $\mathcal{S}_{ij}$ are 3×3 submatrices of PR^{-1}, that is;

$$\begin{pmatrix} \mathcal{S}_{11} & \mathcal{S}_{12} \\ \mathcal{S}_{21} & \mathcal{S}_{22} \end{pmatrix} = \underset{(6\times6)}{P \times R^{-1}}. \tag{C5.8}$$

This then is the relationship between the stresses in the layer at interfaces and the displacements of these interfaces. At a given frequency ω and given wave numbers (k_x and k_y), the elements of the matrix $\mathcal{S}$ (the spectral 'stiffness coupling matrix') are functions of the elastic constants, density and thickness of the layer material.

C6 Fluid loading

Similar relationships between stress and displacement can be derived for the fluid half spaces that bound the elastic layer (Figure 6.5). The geometry is such that a common factor of $e^{i\alpha x}$ can be omitted from all equations. In a fluid, waves of the form

$$P = A_+ e^{i\gamma z} + A_- e^{-i\gamma z} \tag{C6.1}$$

can propagate, where P is the acoustic pressure. The component of displacement normal to the layer is given by

$$U_z = \frac{1}{\rho_f \omega^2}\frac{\partial P}{\partial z} = \frac{i\gamma}{\rho_f \omega^2}(A_+ e^{i\gamma z} - A_- e^{-i\gamma z}). \tag{C6.2}$$

In the upper half-space waves will propagate in the $+z$ direction due to the motion of the upper interface; hence $A_- = 0$ and

$$P^1 = A_+ e^{i\gamma d} \quad , \quad U_z^1 = \frac{i\gamma}{\rho_f \omega^2} A_+ e^{i\gamma d} \tag{C6.3}$$

from which

$$P^1 = -\frac{i\rho_f \omega^2}{\gamma} U_z^1. \tag{C6.4}$$

Similarly, in the lower half-space waves will propagate in the $-z$ direction only, giving

$$P^2 = \frac{i\rho_f \omega^2}{\gamma} U_z^2. \tag{C6.5}$$

These equations relate the normal stresses ($T_{zz} = -P$) in the fluid to the normal displacements of the interfaces, just as (C5.7) does for the elastic layer. The fluid cannot support shear deformation and so there are no relations between tangential displacements of the interfaces and stresses in the fluid. Writing the equations in matrix form gives, for the upper (1) and lower (2) half-spaces respectively,

$$\begin{aligned} T^1 &= -S_f U^1 \\ T^2 &= +S_f U^2 , \end{aligned} \tag{C6.6}$$

where

$$S_f = \begin{pmatrix} 0 & 0 & 0 \\ 0 & 0 & 0 \\ 0 & 0 & -\dfrac{i\rho_f \omega^2}{\gamma} \end{pmatrix}. \tag{C6.7}$$

Appendix D Publications

During the course of the programme of research described in this thesis, several international conferences were attended, and some of the work described here was presented. The published papers arising from these conferences are listed below.

• **Anisotropy in the acoustic transmission properties of fibre-reinforced laminates,** *V. F. Humphrey and P. A. Chinnery*
in Ultrasonics International 93 Conference Proceedings, 387-390 (1993).

• **Resonances of deformed cylindrical shells - experimental visualization and identification,** *P. A. Chinnery and V. F. Humphrey*
in Proceedings of the 2nd European Conference on Underwater Acoustics,
Vol. 1 159-164 (1994).

• **Measurement and calculation of the acoustic characteristics of fibre-reinforced panels - the influence of anisotropy,** *V. F. Humphrey and P. A. Chinnery*
in Proceedings of the 2nd European Conference on Underwater Acoustics,
Vol. 1 279-284 (1994).

• **Resonances in acoustic scattering by cylindrical objects,**
P. A. Chinnery and V. F. Humphrey
in Proceedings of the Institute of Acoustics, Vol. 16 Pt. 6 51-58 (1994).

Also, currently in preparation (for Physical Review Letters) is a paper entitled;
Experimental visualization of acoustic resonances within the stadium,
which is included in this document as Appendix A2.

In an attempt to further advance the research in the area of complex materials, the author also organised a one day conference entitled '*Acoustics of Advanced Materials for Underwater Applications*' (Chinnery, 1993). This conference, organised on behalf of the Institute of Acoustics, brought together researchers working on other aspects of the problems being dealt with in the present programme of work.

Appendix E Nomenclature

The symbols used in the *main body* of this document are listed here with their meanings. Some of the symbols have different meanings in the appendices and these shall not be listed. Throughout the document, subscripts and superscripts are sometimes dropped where the meaning is clear, and other diacritics must be used.

The main subscripts and superscripts used to label the variables associated with different wave-fields or media are listed here:
Subscripts:

ex	total external field (scattered plus incident fields)
f	fluid parameter (water in all cases in this document)
fl	field in the fluid *column*
in	incident field
l	longitudinal (compressional) wave parameter
s	transverse (shear) wave parameter
sc	scattered (reflected) field
tr	transmitted field

Superscripts

$X^{1,2}$	quantity at top/bottom (front/back) interface of layer
X^*	complex conjugate of X
X'	derivative of X with respect to its *argument*
$\dot{X},\ddot{X}$	time derivatives of X
$X^{e,o}$	solutions of even/odd symmetry
$\overline{X}$	spectral form of variable X (defined in Appendix C3)

Note: the wave numbers for an *isotropic* elastic media are denoted $k_{l,s}$, and (in Chapter 6 only) those in *anisotropic* media are denoted k *(no* subscript). The wave number for a *fluid* is also denoted k, its meaning being clear from the context in which it appears.

Roman symbols

a	outer radius of the cylindrical shell
A_n	coefficient in Normal Mode Series for the field in the fluid column
A_i	antisymmetric Lamb waves
b	inner radius of the cylindrical shell
B_n	coefficient in Normal Mode Series for the scattered field

c_f, c_l, c_s	speed of sound in fluid (f) and isotropic media (l,s)
c_{ijkl}	stiffness tensor
ce_n	Mathieu functions of order n; even solutions
C	stiffness matrix for elastic media
d	thickness of planar or cylindrical layer
dn	normal to ellipse
e	eccentricity of ellipse (deformed shell)
$E(\underline{r},t)$	optical field after passing through acoustic field
E_o	amplitude of optical field
$E_I(\underline{r},t)$	optical field in the image plane of the Schlieren system
$E_T(\eta,t)$	optical field in the diffraction (transform) plane of Schlieren the system
$E_{T'}(\eta,t)$	optical field after spatial filtering
f, f_a, f_b	interfocal distance; of outer (a) and inner (b) elliptical boundaries
$f(r,\phi)$	form function
$F^{1,2}$	external forces (stresses) applied to the interfaces of the layer
$\mathcal{F}$	vector of interfacial applied forces (F^1, F^2)
h	focal length of the mirrors in the Schlieren system
h_μ	metric in elliptical coordinate systems
$H_n^1(kr)$	Hankel function
$I(\underline{r},t)$	intensity in the image plane of the Schlieren system
$\Im(\eta)$	spatial filter function (Schlieren)
$j(\mu)$	pseudo-radial part of the pressure in elliptical coordinates
je_n	radial Mathieu functions of order n; even solutions
jo_n	radial Mathieu functions of order n; odd solutions
$J_n(kr)$	Bessel function of order n
k, k_l, k_s	wave numbers in fluid and elastic media (see note above)
l	semi-major axis of ellipse (at inner surface of shell)
ℓ	separation of orders in diffraction plane of the Schlieren system
L	interaction length in the Schlieren system truncation length of the parametric array
M_{ij}	elements of the Bond transformation matrix
$p(\underline{r})$	spatial part of the acoustic pressure field in the Schlieren model
$P_{in,sc,fl,tr,ex}$	pressure fields in fluid media
P_{lay}	pressure in an 'acoustic' layer (shell)

p_n, q_n, r_n, s_n	products of Bessel functions and derivatives (Abramowitz, 1972 pg. 361)
q, q_b	parameters in Mathieu's equation and its solutions
r, R	radial polar coordinate (range from cylinder centre, point in the field of the parametric array)
$\Re$	reflection coefficient of an elastic layer
s	semi-minor axis of ellipse (inner surface of shell)
s	$= \kappa(\partial\mu/\partial p)_s L$; constant in Schlieren model
so_n	Mathieu functions of order n; odd solutions
S_n, S_r	slowness; normal to layer (n), and in the plane of the layer (r)
S_i	symmetric Lamb waves
S_f	'stiffness' matrix for fluid half-spaces
S	stiffness matrix for *system* (layer and fluid half-spaces)
$\mathcal{S}$	stiffness coupling matrix for an elastic layer
t	time
T_i	Love waves
$T^{1,2}$	stresses in *fluid* at interfaces of the planar layer
$\mathcal{T}$	stress vector (or tensor) for elastic material
U	displacement
$\mathcal{U}$	vector of interfacial displacements (U^1, U^2)
V	particle velocity
V^n	phase velocity of plate waves in planar layer
w	vector potential in isotropic media
X_{inp}	closely related to Z_{inp} $(h_\mu X_{inp} = Z_{inp})$
$Y_n(kr)$	Bessel function of second kind
Z_{inp}	surface input impedance of layer (planar or circular)
Z_{circ}	surface impedance of circular shell
Z_L	$= \rho c_l$; impedance of layer *material* (planar or circular)
Z_w	impedance of external fluid (planar or circular)
$\aleph_{ij}$	function involving spatial filter ($\Im$) and products of Bessel functions
$\left(\frac{\partial\mu}{\partial p}\right)_s$	adiabatic piezo-optic coefficient

Greek symbols

α	x –component of wave number in the plane of the layer
β	y –component of wave number in the plane of the layer
γ	component of wave number *normal* to layer

	percentage deformation of cylindrical shell
Γ	Christoffel matrix
δ_{ij}	Kroneker delta
δ	phase of acoustic pressure field in Schlieren model
ε_n	Neumann function; $\varepsilon_n = 1$ *if* $n = 0$, 2 *if* $n > 0$
ζ	scalar potential in isotropic media
$\underline{\eta}$	spatial coordinate vector in diffraction plane of Schlieren system
θ	angle of incidence (for planar layer and elliptical shell)
$\Theta(\nu)$	'angular' part of pressure field in elliptical coordinates
ξ^n	*in-plane* wave numbers of plate waves in elastic layer
ι	separation constant in Mathieu's equations
κ	optical wave number
Λ	function of θ, θ_o, ϕ and ϕ_o in expression for parametric source
μ	pseudo-radial coordinate (elliptical systems)
μ_o	pseudo-radial coordinate of inner and outer surfaces of deformed shell
ν	'angular' elliptical coordinate
ν_o	Raman-Nath parameter
Π	plane wave transmission coefficient of elastic layer
$\tilde{\Pi}$	plane wave transmission coefficient modified to account for layer
Π_{pws}	transmission coefficient measured with a *parametric* source
ρ_f, ρ	density of fluid/elastic media
σ	phase variations of light wave passing through the acoustic field
Σ	strain tensor/vector
τ_{ij}	submatrices in stress-displacement relation for an isotropic layer
ϕ	azimuthal incidence angle for anisotropic layer (angle with fibre direction)
	angular polar coordinate for cylindrical geometries
χ	ratio of impedances $= Z_w/\rho c_l$
ψ, ψ_o	field of a parametric array with/without panel present
ω	angular frequency
$\Omega(\theta, \phi)$	plane wave spectrum of parametric array